Arumugam, Puvaneswaran (2013) Design and modelling of permanent magnet machine's windings for fault-tolerant applications. PhD thesis, University of Nottingham.

Access from the University of Nottingham repository:
http://eprints.nottingham.ac.uk/13457/1/Design_and_modelling_of_PM_machine%27s_windings.pdf

Copyright and reuse:

The Nottingham ePrints service makes this work by researchers of the University of Nottingham available open access under the following conditions.

- Copyright and all moral rights to the version of the paper presented here belong to the individual author(s) and/or other copyright owners.
- To the extent reasonable and practicable the material made available in Nottingham ePrints has been checked for eligibility before being made available.
- Copies of full items can be used for personal research or study, educational, or not-for-profit purposes without prior permission or charge provided that the authors, title and full bibliographic details are credited, a hyperlink and/or URL is given for the original metadata page and the content is not changed in any way.
- Quotations or similar reproductions must be sufficiently acknowledged.

Please see our full end user licence at:
http://eprints.nottingham.ac.uk/end_user_agreement.pdf

A note on versions:

The version presented here may differ from the published version or from the version of record. If you wish to cite this item you are advised to consult the publisher’s version. Please see the repository url above for details on accessing the published version and note that access may require a subscription.

For more information, please contact eprints@nottingham.ac.uk

Design and Modelling of Permanent Magnet Machine's Windings for Fault-tolerant Applications

Puvaneswaran Arumugam B.Eng (Hons)

Thesis submitted to the University of Nottingham for
the degree of Doctor of Philosophy

The University of Nottingham

UNITED KINGDOM · CHINA · MALAYSIA

Acknowledgements

“One of the joys of completion is to look over the journey past and remember all the people who have helped and supported along this long”

My first debt of gratitude must go to Professor Chris Gerada, Professor Patrick wheeler, who gave me the great opportunity to start this journey.

I would like to express my heartfelt gratitude to my mentors Professor Chris Gerada and Dr. Mohand Hamiti (Tahar), who are inspirational, supportive, and patient. They patiently provided the vision, encouragement and advice necessary for me to proceed through the research and complete my thesis.

I would also like to thank my examiners, Professor Mark Sumner and Dr. Smail Mezani, who provided encouraging and constructive feedback. I am grateful for their thoughtful and detailed comments.

I would like to thank my friends Karen Eveson and Ingrid vella, who are given support in thesis proof reading. Also I would like to thank my friends Nirmal Perumal, Tao Yang, Tahar Hamiti and his family, Jiri Dusek, Yusuke Zushi, Christopher Brunson, Ralph Feldman, Chintan Patel, Elisa Rispetto, Prof. Kino Hitoshi, V, Kelly, Emmanuel, Fyn Musonga, Sakthy, George Anna and Leroy Hill for all the great time that we have shared and always takes part in my good and bad times.

I am deeply thankful to my Mum, Dad, Luximi and Arumugam for their love, support, and sacrifices. Without them, this thesis would never have been written. I am grateful to my big brother Sureshkanth, who always believed in me and encouraged me to follow my dreams. Thanks Anna again. Finally, I would like to thank my sisters and other family members for their love and support.

Abstract

The research described in this thesis focuses on the mitigation of inter-turn short-circuit (SC) faults in Fault-Tolerant Permanent Magnet (FT-PM) machines. An analytical model is proposed to evaluate the inter-turn SC fault current accounting for the location in the slot of the short-circuited turn(s). As a mitigation strategy to SC faults at the design stage, a winding arrangement called VSW (Vertically placed Strip Winding) is proposed and analysed. The proposed analytical model is benchmarked against finite element (FE) calculation and validated experimentally. The results demonstrate that the proposed winding arrangement in the slot improves the fault tolerance (FT) capability of the machine by limiting the inter-turn SC fault current regardless the fault location in the slot.

Electromagnetic and thermal studies are conducted to verify the merits and drawbacks of the proposed winding compared to the conventional winding using round conductors (RCW). The study shows that the proposed winding scheme, in addition to being fault-tolerant, has an improved bulk radial conductivity, can achieve a good fill factor, but has a significantly higher frequency-dependent AC copper loss. To predict the AC losses an analytical model based on an exact analytical 2D field solution is proposed. This model consists of first solving the two-dimensional magneto-static problem based on Laplace’s and Poisson’s equations using the separation of variables technique. Then, based on that solved solution, by defining the tangential magnetic field (H_t) at the slot opening radius, Helmholtz’ equation is solved in the slot subdomain.

Subsequently, an FE and MATLAB® coupled parametric design is undertaken to maximise the VSW-wound machine’s efficiency whilst maintaining its FT capability. The proposed analytical models for prediction of the SC fault current and AC copper losses are integrated into the coupled optimisation. It is shown that the effective losses of the VSW can be minimised through design parametric design while maintaining the required level of machine performance. Using an existing FT-PM machine of which the rotor is kept unchanged two stators were designed, manufactured and wound with RCW and VSW respectively and experimental tests are carried out to validate the analytical models and the new winding concept.

Content

LIST OF SYMBOLS AND ABBREVIATION

Symbols

A - z-component of the magnetic vector potential, cross sectional area of conductor

B_r ,B_θ - radial and tangential flux density components

B_{rem} - remanence flux density of the magnet

I - current

L_s, L_h, L_m - inductances

$\overline{D_j}$ - interface boundary

D_o, D_i - Diameter – outer, inner

J_c - source current density

J_e - eddy current density

M_r - radial magnetization of the magnets

N - number of turns

Nc - number of turns per coil

N_s - number of shorted turns

Q - number of stator slots

R - radius, resistance

R_1 - inner radius of the rotor yoke

R_2 - outer radius of the PM surface

R_3 - stator inner radius

R_4 - outer radius of the slot-opening

R_5 - stator outer radius

P - number of pole pairs

S - number of stator slots

S_w - slot width

l_{stk} - axial length

r_{c1}, r_{c2} - inner and outer radius of a conductor

α - magnet span, slot wedge angle

Δ - rotor position

δ - slot width angle

β - slot opening angle

θ_i - angular position

θ_{c1}, θ_{c2} - angular position of a conductor

ω - angular frequency, rated speed

ω_e - electrical speed

σ - electric conductivity of the winding material

ρ - electric resistivity of the winding material

μ_o - permeability of the air

μ_r - relative recoil permeability

Φ_g - magnetic flux

Ψ - flux linkage

Ψ_m - flux linkage due to magnet

f - frequency

k_w - winding factor

κ - $\sqrt{-j\omega\sigma\mu_o}$

b_o - slot opening

h_s slot height

h_t tooth-tip height

k, m, n - order of harmonic

n. m, N_{ph} - number of phases

J_x - Bessel function of the first kind with order x

Y_x - Bessel function of the second kind with order x

I, II , i, j - PM, air gap, slot-opening and slot regions, respectively

Notations

$$P_z(x, y) = \left(\frac{x}{y}\right)^z + \left(\frac{y}{x}\right)^z$$

$$E_z(x, y) = \left(\frac{x}{y}\right)^z - \left(\frac{y}{x}\right)^z$$

Abbreviation

AC	Alternating Current
DC	Direct Current
DSP	Digital Signal Processing
EMA	Electro Mechanical Actuator
EMF	Electro Motive Force
FE	Finite Element
FT	Fault Tolerant
HSW	Horizontally placed Strip Winding
MMF	Magneto Motive Force
PDE	Partial Differential Equation
PM	Permanent Magnet
PWM	Pulse Width Modulation
RCW	Round Conductor Winding
SC	Short-Circuit
SR	Switch Reluctance, Split Ratio
TR	Tooth-width to tooth-pitch Ratio
VA	Volt-Ampere
VSW	Vertically placed Strip Winding

List of figures

List of tables

CHAPTER

1

Introduction

1.1. **Introduction to fault tolerant drive system**

The current shift towards more electrical transport has significantly increased the requirements for safety and reliability of electrical systems. Examples of safety critical applications include fuel pumps and actuators for aerospace applications and electrical steering for automotive applications. In such applications, it is essential to ensure that the drive is capable of continuing operation in the event of any failure. Such a drive system is known as a fault tolerant drive system.

Switched Reluctance (SR) machines and Permanent Magnet (PM) machine drives are the preferred choice for fault tolerance drive systems, each having certain advantages and disadvantage depending on the application. Due to their robustness, ease of manufacture and low magnetic interaction between phases, SR machines constitute a good choice for fault tolerant drives [1, 2]. However, these qualities are overshadowed by a relatively high torque ripple and acoustic noise. Consequently, PM machines have become more popular when compared to SR machines in safety critical applications due to their greater torque density and subsequent higher power density. This is a crucial advantage, especially in the aircraft industry since a reduction in weight increases fuel efficiency, reducing the aircraft's environmental impact.

One of the key concerns about PM machines, especially in safety-critical applications, is the issue of fault-tolerance as the PMs cannot be de-excited [3]. As a result a single fault in such drives can cause catastrophic damage, with potentially significant cost and safety implications. Hence, more reliable, safe and secure PM machine drive systems are required for safety critical applications.

1.1.1. Faults in the drive system

Generally, the faults in typical drive systems are categorised into two main groups: mechanical faults and electrical faults. The most common mechanical faults in machine drives are: rotor eccentricity, bearing faults, shaft misalignment and load related faults. These have not been considered in this study as the possibility of mechanical faults occurring in the system is very low compared to electrical faults. The electrical faults can be characterised into four groups according to where the faults arise in the drive system, as shown in Figure 1.1.

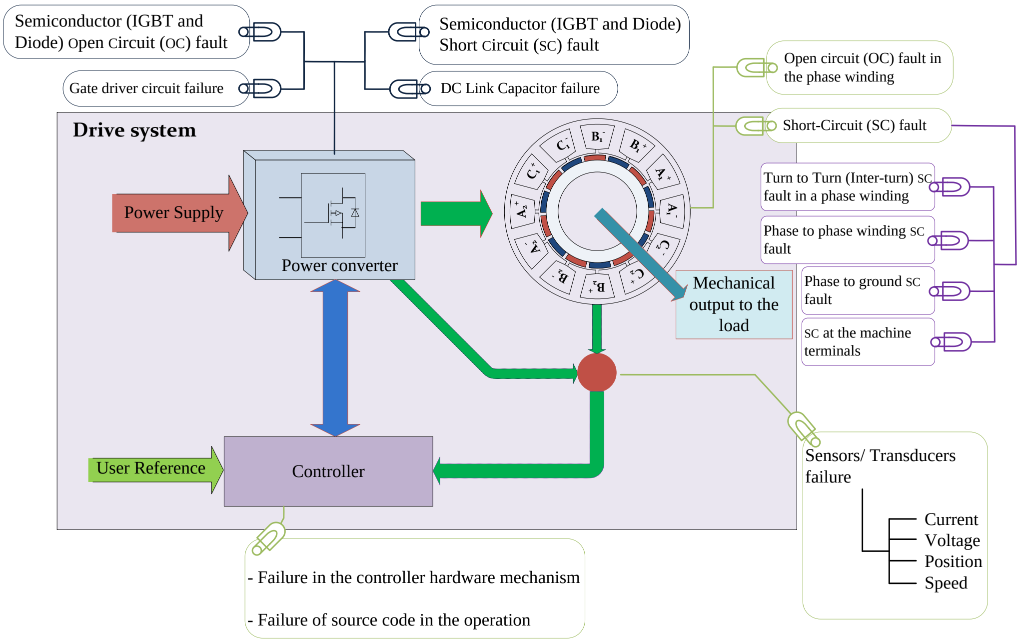

Figure 1.1 Drive system's fault

A Fault Tolerant (FT) drive system should have the ability to detect and accommodate any of these faults and to support continuous operation until a solution or repair is available. In early years, due to a lack of control methodology the entire drive system was completely shutdown in the event of failure and fault tolerance was achieved through entire drive redundancy. This caused increased overall system weight and component count. In recent years, the concept of fault tolerance has been advanced rapidly with improvement in power electronics devices and significant changes in the control topologies and machine topologies, allowing the drives to meet the fault tolerance requirements for each type of potential fault.

1.1.2. Established fault tolerant PM drive system

A typical fault-tolerant PM drive topology includes a number of design features to facilitate a level of operation when faults ensue. These can be categorized as follows:

a) Isolation/Fail-safe
b) Performance
c) Fault detection and post-fault control strategy
d) Redundancy and Reliability

a) Isolation/Fail-Safe

Isolation in the drive system is an important pre-fault remedial measure which reduces the possibilities of fault occurrence. There are four isolation methods commonly considered in drive systems. These are: electrical, magnetic, thermal and physical isolation.

Electrical isolation between the phases is achieved by employing a separate voltage-fed inverter for each phase or group of phases. This has the effect of doubling the amount of power electronics components. However, the total VA (volt-ampere) rating also increases slightly since the converter only supplies the phase voltage rather than line-to-line voltage.

Additional isolation is achieved through physically and magnetically separating the drive phase windings using a concentrated winding. Consequently, a fault that occurs in one phase will not spread to adjacent phases. Hence, the fault is confined in an individual slot and the resulting temperature rise in the slot can be cooled effectively by adopting a cooling method for the outer surface of the stator. It is worth noting that the physical separation between the phases allows the control of each phase without any interaction since the mutual coupling between them is negligible.

Although isolation between the phases can be accomplished effectively in the drive system, the turn-turn Short-Circuit (SC) fault that occurs inside the slot cannot be segregated from the phase windings. The SC faults are severe and produce excessive current in the shorted turns. This leads to localised heating in the slot and possibly catastrophic failure in the plant. Thus, the machine's winding has to be designed with one per unit self-inductance[1] [4] to limit this excessive SC current while applying post-fault control strategy [5] i.e. short-circuiting the respective phase through the separated H-bridge converter switches. As an alternative, other post-fault control strategies [1, 6, 7] can also be considered. A fault-tolerant drive system may be required to provide for such a fault scenario depending on the reliability requirements of the application at hand.

b) Performance

The machine drive is able to produce rated power continuously in the event of failure by overrating the machine and converter design to handle the increased current loading during faulty operation. This can be done by designing the machine with multiple phases. The choice of the number of phases will determine the machine's overrating factor [2], which is inversely proportional to the number of phases. However, a small number of phases ensures a better reliability and simplifies the system. A thermal design exercise is required when

---

[1] the self-inductance that limits phase SC current value equivalent to rated current is called one per unit inductances

sizing such machines to determine the ultimate winding temperatures reached when the specific control algorithm is applied. Apart from the additional copper losses as a result of the increased current loading, additional iron and magnet losses due to the unbalanced fields also need to be accounted for.

c) Fault detection and post-fault control strategy

Fast and effective fault detection techniques [8-15] and remedial actions via a post-fault control strategy are vital in the event of failure in a FT drive system. This is particularly important for turn-turn SC faults since the turn-turn SC fault is one of the most harmful faults in the drive system. There is no doubt that it is desirable to detect incipient faults and to utilize the correct algorithm which can be implemented on the system so as to protect the system and ease the damage.

d) Redundancy and Reliability

In safety critical applications, rated or reduced operation of the drive must be ensured even after a fault. After a fault happens the system is also often required to reach a certain reliability level. As a result parallel redundancy is often employed despite the higher cost. However, in order to achieve the necessary system reliability level, including a reduced overall system weight and component count, without replicating the complete drive system, different redundancy methods [16, 17] are also considered.

From the above stated fault tolerant features, it can be clearly seen that although such a machine drive topology, if appropriately designed, can potentially tolerate converter failures, winding open circuit failures and terminal SC failures, a winding turn-turn SC fault remains problematic since the fault is located in the slot which cannot be entirely eliminated. If an SC fault, or more importantly, an inter-turn (a single turn) fault is left undetected and uncorrected, the resulting current of the fault becomes excessively high due to its low impedance. A potential consequence is a winding open circuit fault. The condition of a larger faulted current will affect the remaining windings and ground wall insulation and eventually lead to a ground wall puncture and forced outage of the machine. Often this type of fault can cause fire or an explosion in a short period of time. Therefore the machine has to be stopped or remedial action needs to be employed very quickly in order to avoid damage to the equipment and/or human lives.

1.2. Root causes of the inter-turn SC fault

The main cause of the winding failure is deterioration of the insulation property. This has been clearly reported in industrial surveys related to the failures [18]. Also it has been stated in the report published by “BAKER maintenance technology” [19], that 30% of motor failures are due to insulation failure, 60% of which are caused by overheating. The report shows that for every 10^{O} C of additional heat to the windings, the insulation lifetime is halved [19]. However it is worth noting that the severity of deterioration of the winding depends on the insulation thickness and the operating environment.

In normal operation, the turn/strand insulation experiences mechanical and electrical stresses as well as thermal stress. As a result of these stresses, the insulation can be damaged by one of the following mechanisms: voltage surge related puncture, partial discharge and aging due to overheating. Poor cooling due to high ambient temperature, clogged ducts are typical examples of non-electrically induced temperature stresses on both the motor and insulation system. Chemical abrasive substances in the air, wet operation, and high altitude operation are a few common environmental stresses which also influence the insulation deterioration.

1.3. Simple analysis of the inter-turn SC fault

An inter-turn SC fault causes a change in winding resistance, inductance and also the electrical circuit of the winding. During a turn-turn SC fault, the healthy and the shorted turns behave as two separate circuits which are magnetically coupled, but electrically isolated [20], as illustrated in Figure 1.2.

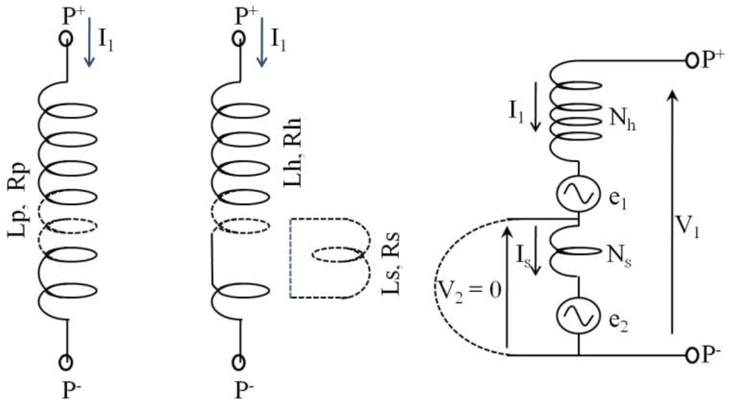

(a) (b) (c)

Figure 1.2 (a) A healthy phase winding (b) a phase winding under a SC fault condition (c) equivalent circuit of a FT-PM machine under turn-turn SC condition

Since the mutual coupling between phases for a properly designed FT-PM machine can be neglected [3], the differential equations (1.1) and (1.2) governing a faulty phase circuit allow computation of the SC current.

$$V_1(t) = I_1(t) R_h + L_h \frac{dI_1}{dt} + L_m \frac{dI_s}{dt} + e_1(t) \tag{1.1}$$

$$0 = I_s(t) R_s + L_s \frac{dI_s}{dt} + L_m \frac{dI_1}{dt} + e_2(t) \tag{1.2}$$

where,

- e_1: EMF in the healthy (N_h) turns;
- e_2: EMF (N_s) turns;

- I_1: phase current;
- Is: induced current in the shorted (N_s) turns;
- Lh: self inductances of healthy (N_h) turns;
- Ls: self inductances of shorted (N_s) turns;
- Lm: mutual inductance between N_h and N_s turns.

From (1.1) and (1.2) it can be seen that knowledge of the resulting self and mutual inductances is necessary to examine the drive behaviour under SC faults. These values are strongly dependent on the location of the fault within the slot and slot geometry [21]. Since the inter-turn SC current is inductance-limited at rated speed, an accurate knowledge of the different inductances will facilitate the correct evaluation of the SC current and thus, the steady state SC current can be represented in the following form.

$$I_s = -\frac{e_2(\omega)}{R_s + j\omega L_s} - \frac{j\omega L_m}{R_s + j\omega L_s} I_1(\omega) \qquad (1.3)$$

From (1.3), it is clearly evident that the magnitude of the fault current highly depends on the phase current, rate of flux change due to the PMs, impedance of the shorted turn and mutual inductances between the faulty and remaining healthy turns. Although the supply is disconnected, the SC fault current cannot be eradicated in PM machines and this is maintained until the machine stops due to the PM’s flux. This resultant SC fault current highly depends on the impedance of the shorted turn and thus, it becomes critical in the event of single turn fault.

1.4. **Problem description**

The common and conventional method to limit the SC fault current is shorting the whole phase through the power converter switches [5]. This force all the turns in the phase to share the net winding magneto motive force (mmf). As a result the current in the shorted turn reduces and the magnitude of the SC current is accommodated equivalent to the rated current by designing the machine to have one per unit inductances. However, in the case of an inter-turn SC fault where the inductances are dominant, the magnitude of the SC current becomes critical since the fault is highly position dependent [22]. This is due to the slot leakage-flux which has significant influence on the inductances of the phase coil; the self inductance of both healthy and faulty turns and mutual inductances between them. Under a SC fault, these inductances are varied according to the amount of slot leakage-flux associated with them. As a result a significantly high fault current compared to the rated current can persist [22]. This can be overcome by designing the machine with even higher than per unit inductance. Whilst possible to achieve, this would result in a poorer power factor and a significant reduction in the torque density achievable. Hence, necessary corrective actions are required in either the design stage or post-fault control stage, or both, to mitigate the position dependent inter-turn SC fault current effectively.

1.5. **Aim and objectives**

The main purpose of this work is to investigate inter-turn SC fault behaviour, including position dependency, in the FT-PM machine, adopting an analytical tool, and to develop a solution at the design stage to mitigate the impact of such faults. The key objectives of the thesis can be summarised as follows:

- Investigate position dependent inter-turn SC fault behaviour for different winding configurations (i.e. conventional round conductor and bar type winding) using an analytical model and propose a solution to the SC fault

- Analyse the dynamic, electromagnetic and thermal behaviour of the winding configurations under healthy, inter-turn SC fault and post-fault control operations and verify the effectiveness and advantages and disadvantages of the proposed solution

- Develop a 2D exact analytical model that enables fast computation of eddy current losses in order to study the eddy current phenomena resulting for the design of the machine to satisfy fault-tolerance requirements (high eddy current losses due to high slot leakage).

- Optimise and design a FT-PM machine for safety critical applications using both developed analytical methods and FE (Finite Element) methods

- Validate the proposed design solution for the inter-turn SC Fault experimentally

1.6. Novelty of the thesis

The thesis presents:

- a vertically placed rectangular/ foil winding concept as a solution to the position dependency in the inter-turn SC fault
- an analytical model to predict the inter-turn SC fault for two different concentrated winding configurations, i.e. horizontally (bar type winding) and vertically placed (foil/ rectangular) conductors
- an analytical model to estimate the eddy current losses including eddy current reaction effect
- a study on electromagnetic, thermal and dynamic behaviour of the vertical winding

1.7. **Thesis outline**

The thesis is divided into the following chapters 2-7:

Chapter 2 presents a review of the FT aspects of synchronous PM machines, including proposing various design methods and strategies which have more emphasis on the inter-turn SC fault. It examines techniques proposed in recent literature, presenting trade-off studies of the methods.

Chapter 3 presents an analytical model used to investigate the SC current behaviour resulting from an inter-turn fault. The methodology presented is based on the computation of different inductances: self inductances of healthy and faulty turns and the mutual inductances between them. Two different concentrated winding configurations, horizontally and vertically placed conductors in the slot, are considered. The proposed model is verified with FE analysis and validated experimentally.

Chapter 4 investigates the thermal behaviour of a fault-tolerant, permanent magnet motor adopting a vertically placed conductor proposed in chapter 3. The generated winding losses and thermal behaviour of the winding are studied and compared with conventional round conductors winding. The advantages and disadvantages of the windings are discussed.

Chapter 5 presents an analytical model based on a sub domain field model to calculate eddy current loss in a vertically placed conductor wound, surface mounted radial flux PM machine, considering the eddy current reaction effect. Initially, the model solves the two-dimensional problem based on Laplace and Poisson’s equations using the separation variables technique for each sub domain: PM, airgap, slot opening and slot. Then, based on the obtained solution, the eddy current reaction field in the slot is calculated by solving a complex Helmholtz’s equation. The validity and accuracy of the model is verified using FE analysis. The limitations of both FE and analytical methods are discussed.

Chapter 6 looks at a systematic investigation of split ratios to minimize the AC losses of a vertically placed conductor in concentrated-wound surface mounted PM synchronous machines with FT capability. The repeated numerical design optimization is carried out in FE to achieve the required torque and FT capabilities for the minimum level of electromagnetic losses. In addition, the influence of the tooth width to slot pitch ratio, slotting effects and tooth height are investigated.

Chapter 7 experiments an existing machine prototype having vertical conductor and round conductor winding configurations to validate the proposed analytical models. Inter-turn SC fault current and AC loss are measured and compared with analytically calculated ones.

This thesis concludes with a summary of the project, highlights of suggested project improvements and achievements obtained in the course of the project.

CHAPTER

2

Fault tolerant permanent magnet machines

2.1. **Introduction**

With the increase in interest in Permanent Magnet Synchronous Machines in safety-critical applications, due to their ability of producing greater torque density (and subsequently higher power density), concern with fault tolerance in these machines is becoming more and more important. One of the key concerns about PM machines, especially in safety-critical applications, is that the field produced by the permanent magnet cannot be de-excited. Many studies have been carried out to improve fault tolerance in electrical machines and to devise strategies for mitigating faults to fail safely or to maintain operation.

This chapter provides a review of the fault tolerant aspects of synchronous PM machines and includes various proposed methods and strategies which have more emphasis on the inter-turn SC fault. The proposed methods in the literature are categorised into two main parts: machine design methodologies and control methodologies. Machine design methodologies cover various techniques considered in the machine's design to prevent a fault whilst post-fault strategies include techniques which can be used to operate the machine under faulty conditions Fault detection is generally central to any fail-safe or continuous operation strategy. Several comprehensive studies have been carried out to understand failure mechanism in electrical drives and to devise strategies for detecting incipient failures. However, in this chapter importance is not given to detection methods [8-11, 13, 15, 23-26], key importance is given to the proposed fault-tolerant methods for SC faults in the literature and their trade-off.

2.2. **Control Strategies**

These methods are well known as post-fault active control. In [5], a possible post-fault control strategy has been proposed for PM machines. It has been identified that the machine needs to meet the fault tolerance requirements [2] including having magnetic, electric, thermal and physical isolation between the adjacent phases, for continuous operation under faults. To achieve magnetic isolation, a fractional slot concentrated winding has been proposed making the magnetic coupling between the phases negligibly small. By employing a separate two-leg H-bridge inverter for each phase (controlled by the separated drive as a module), electric isolation has been achieved. As a result the machine can be safely operated under faults with the loss of the faulty phase. To obtain a satisfactory level of performance a higher number of phases is proposed, where the basic criterion is that the drive should continue to produce rated power in the event of the failure of one phase. Hence, if there are n phases, each phase must be overrated by a fault-tolerant rating factor, F [4]

$$F = \frac{n}{n-1} \tag{2.1}$$

For instant, if there are three phases, each drive must be overrated by 50% in order to give full capability when faulted. Hence, F falls as the number of phases rises, but this must be balanced against the increasing complexity of a high phase number and the inevitably greater chance of a failure.

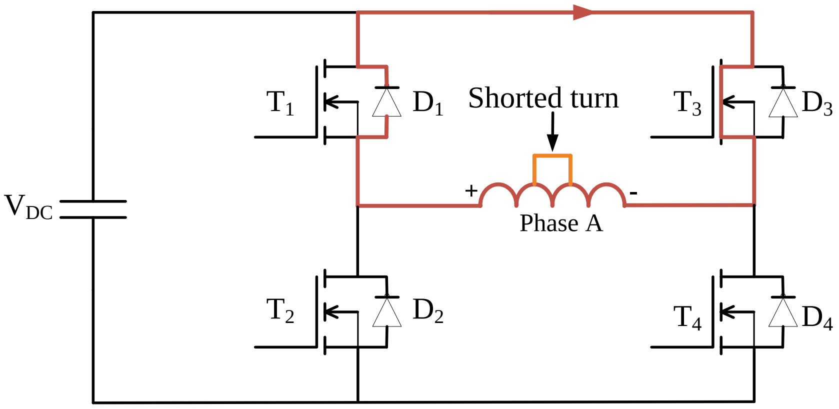

Figure 2.1 Illustration of proposed post-fault control strategy in [5]

Different types of faults are addressed and a post-fault control strategy is proposed for critical SC fault as shown in Figure 2.1 where the respective faulty phase is short-circuited through the separated H-bridge converter switches (T_1, T_3 are ON stage and T_2, T_4 are OFF stage) under the SC fault. In fact the field produced by the PM is almost equally shared by whole turns in the faulty winding and thus the current will be limited. However, it is worth noting that the magnitude of the induced current in a shorted turn depends on the winding inductance and thus, the machine has to be designed with 1.0 per unit inductance to maintain a current equivalent to the rated/excitation current. However, this approach is not always valid since the inductances are position dependent [27] and are considerably lower for the turn located closer to the slot opening region. As a result the current in the shorted turn will be large, leading to unacceptable local heating in the faulty coil.

Based on [5], redundancy in the fault-tolerant control methodology is implemented by a dual three-phase modular solution [16, 17, 28-31] instead of the separated multi singe-phase system. The modular solution has two (or more than two) separate three-phase windings in the stator, for instance A_1-B_1-C_1 and A_2-B_2-C_2, each supplied by a separate converter. Thus, the VA rating of the converter corresponds to half the motor VA rating during normal operation. In the event of failure of one of the dual three phase windings or the corresponding converter, the respective unit is disconnected or short–circuited as explained in Figure 2.2 and thus, the machine can then be operated with the remaining healthy unit. The loss of output power can be compensated for by increasing the current loading. Of course the machine and converter have to be overrated at the design stage to handle the current loading in the event of failure. Clearly, the design has to be overrated by 100% since a three-phase set completely shut down during the fault in a phase. However, this method has a simpler control approach since dual three-phase sets control by separated controller where not necessary to modify the control methodology under a SC fault. Another advantage of this method is that torque ripple and unbalanced radial forces under faulty operating conditions are less than for the separated multi-phase modular approach.

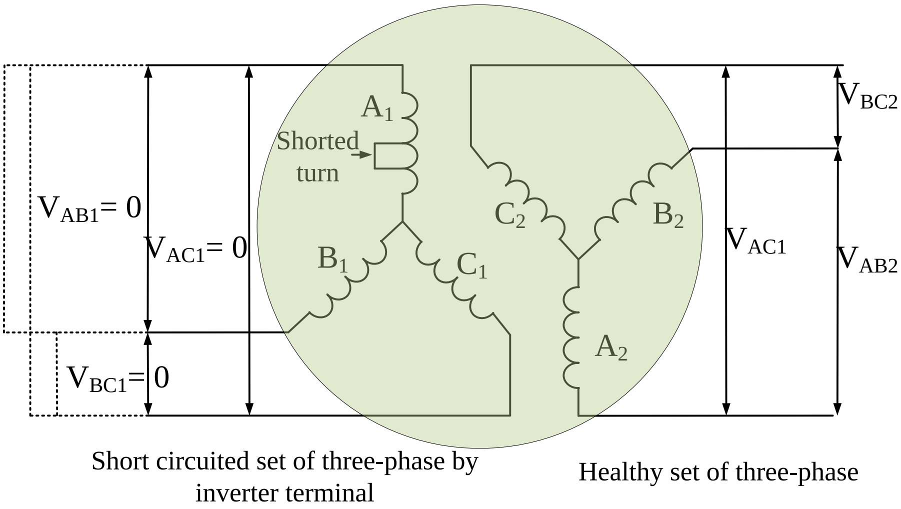

Figure 2.2 Schematic of post-fault control stagey in a dual-three phase machine drive

In [6], a PM machine with centre-split stator winding has been investigated under SC fault conditions. Each of the stator phases is split at the centre into two windings each having an equal number of turns with both split windings having a common magnetic axis as shown in Figure 2.3. The phases are controlled by separate H-bridge inverters as explained in [2]. Auxiliary switches are used to break the fault current path or to isolate the faulty winding. During the fault the current in the healthy half of the phase winding is controlled and is used to cancel the rotor magnetic flux linking in the shorted turns of the second half. Consequently the fault current is reduced which allows the drive to continue operation with a fault. Even though the study claims that the method guarantees continuous operation under various SC fault conditions, no results or convincing discussion is presented for the inter-turn SC fault. This method would not be effective for the inter-turn SC fault since the half of the phase winding is under control; consequently it may induce excessive current in the shorted turn by acting as a single phase transformer.

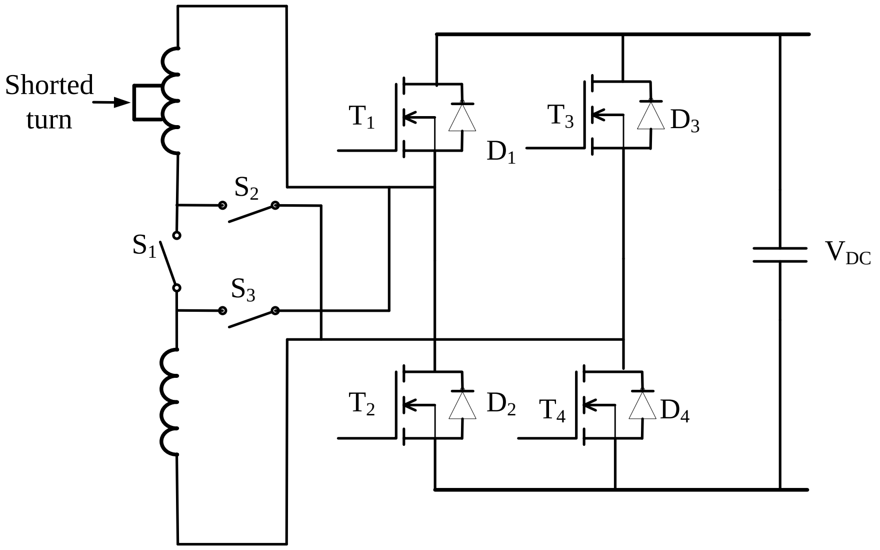

Figure 2.3 Illustration of centre-split winding arrangement [6]

A similar concept has been proposed in [1]. It was shown that the inter-turn fault current in an open slot, bar wound, large PM machine is mitigated by injecting a d-axis current. The injected current must be at the same phase angle as the terminal SC current (90° lagging relative to the back-EMF) and the magnitude of injected current is greater than the terminal SC (complete phase short-circuited) current whilst considerably smaller than the single turn SC current. It was demonstrated that the method would not be effective in the case of a semi-open slot since the required current for the injection is greater than the single turn SC current.

In a similar way to [1], a flux nulling control strategy is proposed for Interior Permanent Magnet (IPM) machines in [7, 32] to improve steady-state response under short-circuit fault conditions. In this method, the flux is nulled by setting the d-axis current to the motor's characteristic current without a q-axis current, thus reducing the breaking torque during a SC fault. However, this method would not be effective for the inter-turn fault since the field produced by the d-axis current may create excessive current in the shorted turn, as explained beforehand. It also requires a significant amount of current in the remaining healthy phases to produce the opposing flux due to weak magnetic coupling among the phases. Moreover, each of the current components used to produce the opposing flux will interact with the rotor magnetic field and produce pulsating torque [6].

2.3. **Machine design strategies**

In earlier sections, it was reported how the control method can be adapted to accommodate the SC fault. In this section, proposed design elements including magnetic circuit structure and windings that can be modified in the electrical drive systems to mitigate the fault are discussed. Proposed methods are categorised into three parts in terms of design aspects: electromagnetic, mechanical and thermal.

2.3.1. Electromagnetic design

As discussed in section 2.2, the FT-PM machine should have an effective d-axis inductance of one per unit to limit the steady-state SC fault current to the rated current. Thus, the thermal limit of the faulted winding will not be exceeded and the SC can be accommodated over an extended period. The key to achieving these requirements is to design a machine with a large leakage inductance by controlling the depth and width of the slot opening [4]. The slot opening depth is designed to be approximately one-half of the tooth-width to avoid undue saturation due to the magnet flux which normally passes through the tooth after the application of remedial action [5] under the SC fault. The main disadvantages of this design are poor power factor and increased eddy current losses due to slot leakage flux. However, these flux can be used to filter the motor current of the Pulse Width Modulated (PWM) AC drives.

In [33], a new approach is presented for selecting slot and pole number combinations for FT-PM machine which satisfies the fault tolerant features proposed in [4]. It is shown that certain combinations of slot and pole numbers force the coupling between phases to essentially be zero, regardless of magnet depth and other design details. Thus, the preferred slot and pole number combinations facilitate accommodation of the fault in the phase without influencing adjacent phases. It is explained that the choice of slot and pole combinations can be used to eliminate low pole number armature Magneto Motive Force (MMF). Consequently this reduces the vibration and stray loss present during normal operation. It is worth noting, however, that the design has to meet one per unit inductance to mitigate a SC fault.

In [34], feasible slot and pole number combinations for multiple two and three phase FT-PM machines has been investigated and the relative merits are discussed via a design case study. A winding SC fault detection technique based on search coils wound around the stator teeth is also presented, and its performance is assessed in FE. It is shown that the proposed detection technique can reliably detect any type of SC fault under all load conditions however nothing is suggested as to what action is to be taken to limit the fault current.

In [35], a spacer tooth arrangement (Figure 2.4) between the phases has been proposed to improve the physical, electrical, magnetic and thermal isolation. It was demonstrated that a narrower spacer tooth than the coil/winding tooth provides a greater magnetic flux-linkage in the winding and thus increasing Electro Motive Force (EMF) within the corresponding winding. This spacer tooth arrangement is further investigated in [36] for a 50kW integrated fault-tolerant PM motor drive as shown in Figure 2.5. However, this spacer tooth arrangement reduces the overload capability of the machine as spacer tooth starts to saturate earlier than the wound tooth.

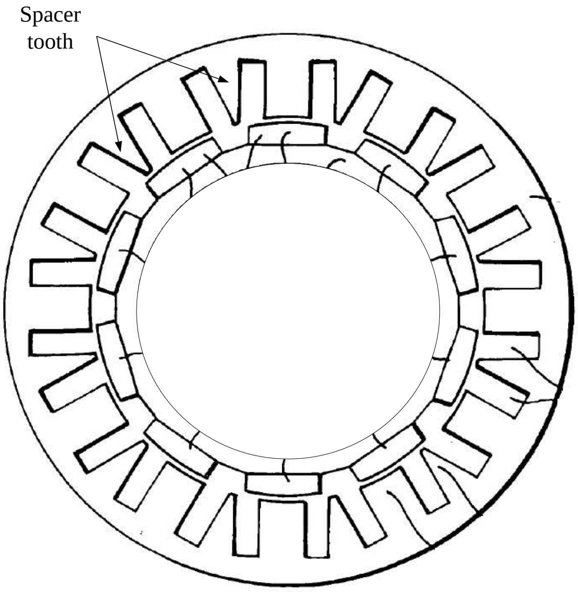

Figure 2.4 Phase windings are separated by spacer tooth [35]

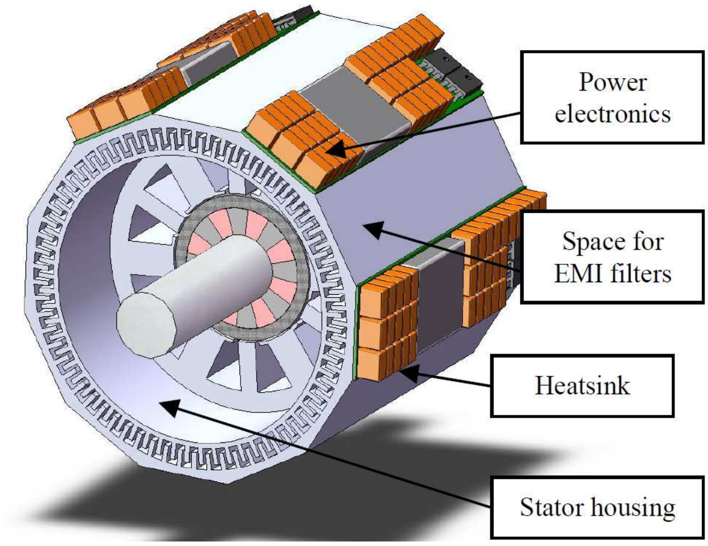

Figure 2.5 Integrated power converter and machine having spacer tooth [36]

2.3.1.1. Machine types and applications

Generally surface mount PM (SPM) machines are the preferred choice and widely used in safety critical areas since the design, which has surface mounted magnets combined with a retaining sleeve, reduces the air gap component of the armature reaction field, so the mutual coupling is insignificant. Several other PM machine topologies including Interior Permanent Magnet (IPM) machines, doubly salient PM machines and flux switching PM machines have also been considered for safety critical applications since they have inherent fault tolerant and flux weakening capabilities. In this sub-section different FT machine types are reviewed.

In [37], SPM machines which satisfy the fault-tolerant requirements identified in [4] have been tested under possible fault scenarios. The design of a fault tolerant SPM machine drive based on a 16 kW, 13000 rev/min, six-phase aircraft fuel pump specification was presented. It was shown that undetected turn to turn faults will result in the flow of currents many times larger than the rated current in the faulted winding. If no action is taken the fault is likely to propagate rapidly. A single shorted turn can be detected by monitoring the sampled current in each PWM cycle. Shorting the phase reduces the fault current to rated value. A shorted power device results in very large shoot through currents when the healthy power device in the faulted limb is turned on. Shoot-through current can be detected within the SC withstand time of the power device and the healthy device turned off again. Finally the results showed that the healthy phases are capable of compensating for the torque loss resulting from the failure [37] in the event of each fault.

In [38], the fault tolerant control architecture for an electric actuator has been investigated. A triple three phase drive architecture has been developed and implemented, including fault tolerance of the SPM motor, power electronic converter, position feedback sensors and DSP (Digital Signal Processing) controller. It was explained that the system is able to accommodate any of the failures automatically and ensure that rated torque is maintained at all rotor positions when stationary or when rotating at low speed, with the mean torque demand being met at high speed. A detailed approach to weight-optimise an Electro Mechanical Actuator (EMA) for helicopter primary flight control system was presented in [39]. Importance was given to the SPM machines as a major component in the system. In order to achieve the redundancy the study considered both circumferential and axial machine segmentation. Finally, the importance of low inertia design and machine operation in magnetic saturation due to high peak-to-rated torque ratio and acceleration requirements was shown.

Figure 2.6 Modified slot-opening arrangement for iron loss reduction [40]

In [41] a modular drive, four phase, fault tolerant system was designed to meet the specifications with a fault in any one of the phases for an aircraft main engine fuel pump. The motor used has a permanent magnet rotor with the magnets arranged in a Helbach array to maximise the air-gap flux density. Exceptionally high electric loadings are obtained by flooding the entire motor with aircraft fuel, which acts as an excellent cooling agent. The design has been tested under un-faulted drive operation and with one of several fault scenarios. The results showed that the flooded fuel has excellent performance without introducing significant drag on the rotor. The slot-opening arrangement of this design has been modified in [40] to reduce the iron losses as shown in Figure 2.6. It was shown that iron loss can be reduced significantly by design. However, the resulting copper losses increase due to the slot-leakage flux increase.

Another application where fault tolerant machines have been gaining a lot of interest is automotive [42-47] where IPM machines have been widely used due to their advantages: ease of magnet retention, less prone to demagnetisation and better field weakening capability. The major disadvantage of these machines is the higher torque pulsations. In [48], a five-phase IPM motor with low torque pulsations was discussed. A control strategy that provides fault tolerance to five-phase PM motors was introduced. It was shown that the control scheme facilitated the operation of a five-phase system continuously and safely under a loss of up to two phases without any additional hardware connections.

In [49], a novel five-phase fault tolerant IPM motor drive with higher performance and reliability for use in fuel cell powered vehicles was presented. A new machine design along with an efficient control strategy was developed for fault tolerant operation of an electric drive without severely compromising the drive performance. Fault tolerance was achieved by employing a five phase fractional-slot concentrated winding configuration IPM motor drive, with each phase electrically, magnetically and physically independent of all others. It was shown that the electric drive system has higher torque density, negligible cogging torque and about ±0.5% torque ripple. Finally it was confirmed that the terminal SC current is about 0.88 per unit rated current which guarantees the operation of the system after isolation of a fault.

Another type of machine considered where fault tolerance is required, is from the family of switched reluctance machines. One of the members is a doubly salient PM machine whose topology combines the features of the switched reluctance and brushless DC machines. The machine has a PM in the stator counterpart as shown in Figure 2.7. This machine provides superior performance over switch reluctance machines in terms of efficiency, torque density, torque to current ratio, and torque to inertia ratio. A new type of doubly salient machine was presented in [50] where the field excitation of the machine is provided by the PM. The flux wakening capability of the machine was discussed in [51] where various methods have been proposed.

In [52], a field winding (as shown in Figure 2.8) was introduced in the doubly salient PM machine to improve the field wakening. The machine topology was improved in [53] by replacing the magnets in the stator teeth as shown in Figure 2.9. It was shown that the topology reduces the acoustic noise considerably and also improves the torque density with reduced cogging torque. The performance of the machine was investigated in [54-62] for automotive applications.

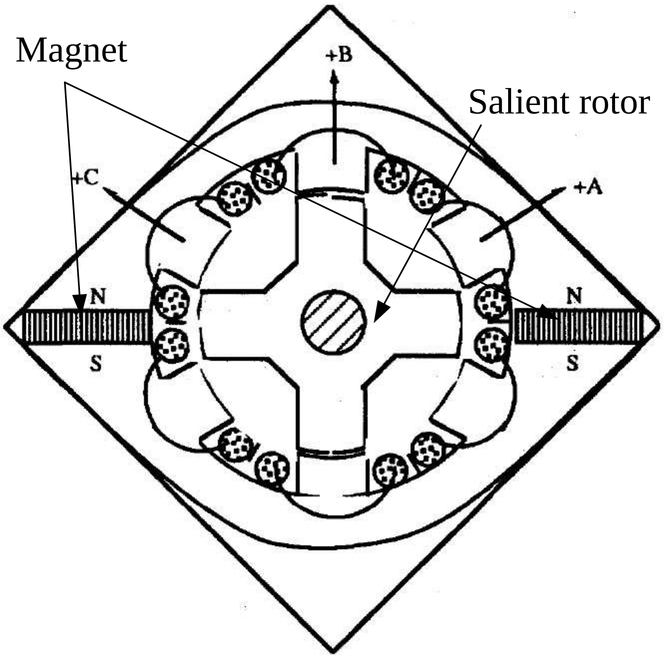

Figure 2.7 Structure of doubly salient machine PM machine [50]

In [63], a new fault-tolerant flux-Mnemonic doubly-salient permanent-magnet motor was presented. The motor consists of aluminium-nickel-cobalt (AlNiCo) PMs and small magnetizing windings in the inner-layer stator, salient poles wound with armature windings in the outer-layer stator and solid-iron salient poles in the outer rotor as shown in Figure 2.10. The armature current controller utilizes a five phase full-bridge inverter to achieve independent control among phases, while the magnetizing current controller adopts an H-bridge converter to generate a temporary current pulse, controllable in both magnitude and direction, to magnetize or demagnetize the AlNiCo PMs. The motor drive works in a remedial magnetizing mode during open-circuit fault, and a remedial demagnetizing mode during short-circuit fault. However the additional field windings generate additional losses which require an extra H-bridge module; this consequently increases the weight.

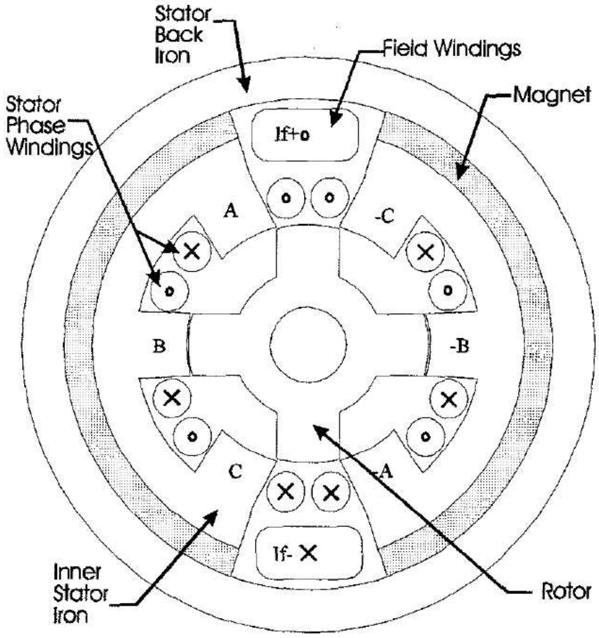

Figure 2.8 Doubly salient machine PM machine with field winding [52]

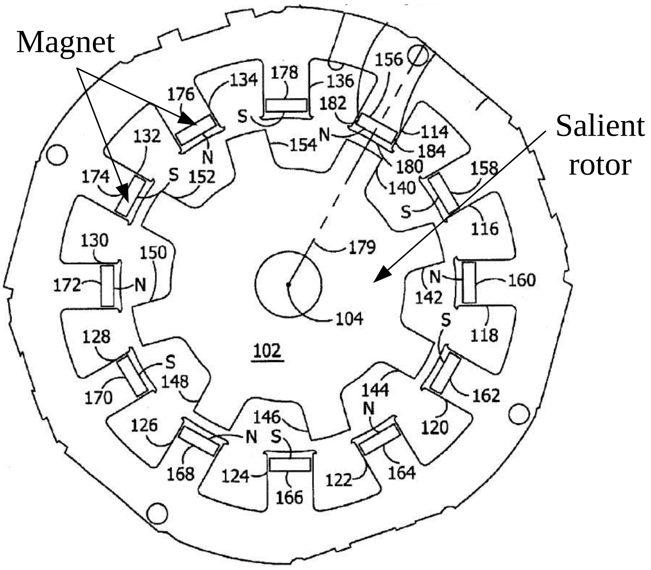

Figure 2.9 Structure of doubly salient machine PM machine having PM in stator teeth [53]

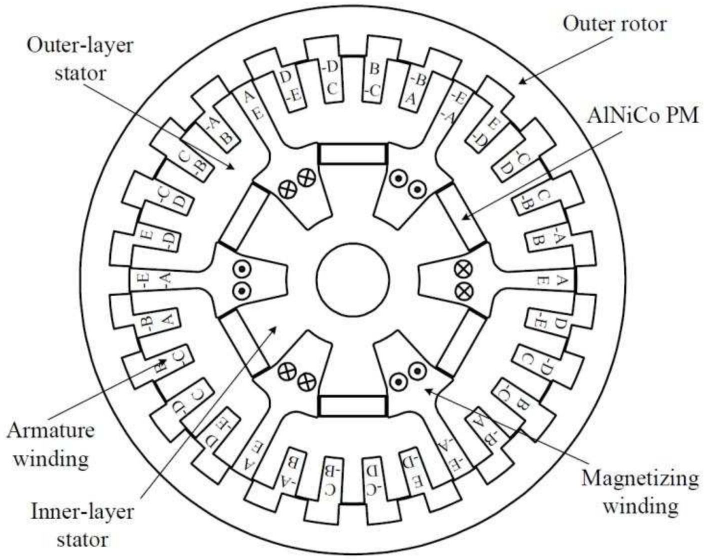

Figure 2.10 Fault-tolerant flux-Mnemonic doubly-salient PM motor [63]

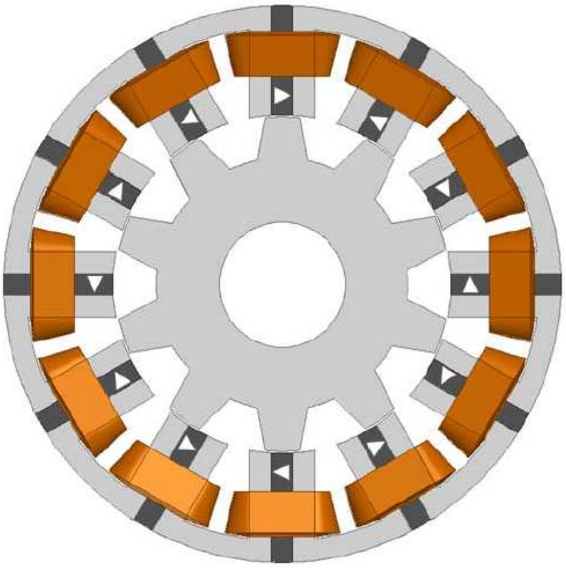

Figure 2.11 Structure of twelve slot ten pole flux switching PM machine [64]

Another family of switch reluctance machines that has been investigated for safety critical applications in the literature is the flux switching PM machines. The PM flux switching machine is an interesting topology as it can be seen as a hybrid of the switch reluctance and PM-AC machine topologies (as illustrated in Figure 2.11). Its rotor is similar to that of a switched reluctance machine; its windings are concentrated and it has permanent magnets embedded in the stator. The benefits of adopting this topology are the robust nature of the rotor (with no need for magnet retention) and the lower resistance thermal path for the magnet-induced losses [65]. In its basic form this topology has limited fault-tolerant capabilities. Several design modifications have been presented in [64, 66-77] including multi-phase [71], thermal isolation [77] and redundancy [66] to improve its fault-tolerant properties.

2.3.1.2. Winding design

As stated previously, fault tolerance in PM machines can be achieved by altering the winding arrangements. Generally a higher number of phases are adopted with concentrated winding arrangements to improve independence between the slots. The winding has been investigated and compared with the distributed winding in [78] and it was proved in [5] that the optimal for fault-tolerant variants is the concentred winding type.

A design consideration on the fractional number of slots per pole per phase concentred winding was studied and analysed in [79] for fault-tolerant synchronous motors. It was demonstrated that the configuration produces a smooth torque, because of the elimination of the periodicity between slots and poles, and improves the FT capability, making the machine able to work even in faulty conditions. Although this is beneficial for fault tolerance of the machine, it produces high numbers of MMF harmonics that may cause an unbalanced saturation and thus an unbearable torque ripple. A method to design fractional numbers of slots per pole per phase motors was proposed considering both double–layer and single–layer winding arrangements. In the study, an analytical computation was extended to determine the distribution of the MMF harmonics and their effect was highlighted in isotropic as well as anisotropic motors. Suitable slot pole combinations were reported to avoid the mutual coupling amongst the phases.

The fractional slot fault-tolerant PM motors were tested and compared in [80]. Two different fault-tolerant PM motors: five-phase and dual three-phase motor drives were considered. The performances of both machines were presented under both open circuit and SC faulty operating conditions. The advantages and disadvantages of both machines were discussed and noted. It was shown that with regard to the behaviour under fault, better results in terms of average torque and torque smoothing can be achieved with a five–phase motor drive. However, this drive requires a non-standard motor as well as a non-standard converter.

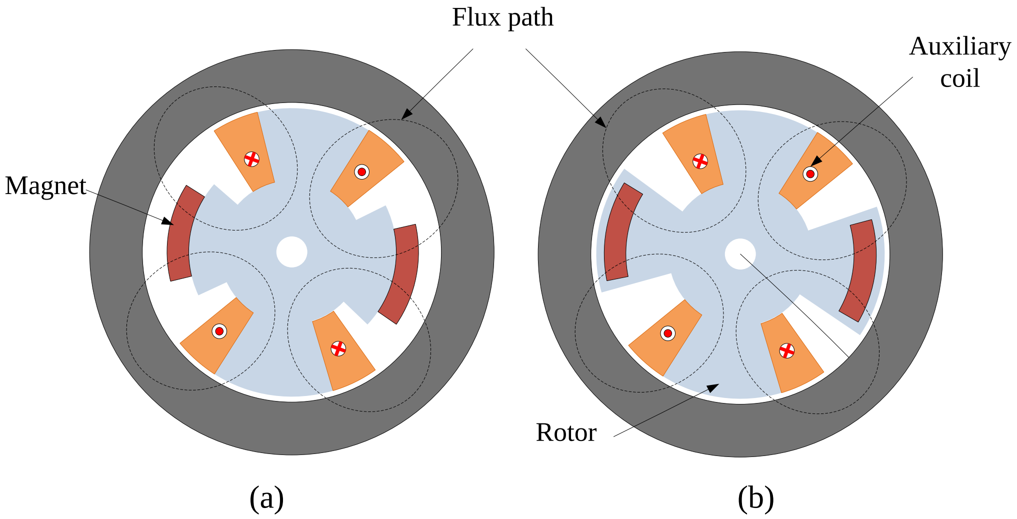

Figure 2.12 Cross sectional view of the proposed machine in (a) [81] and (b) [82]

In [81] a method has been proposed for brushless SPM machines with an auxiliary winding in the rotor (Figure 2.12a) to null the magnet flux during the fault. A start-up winding known as an auxiliary (Direct Current - DC) winding is used to create the torque needed to start. This winding is also often used to completely nullify the magnet flux in case of fault in the flux weakening applications. The method has been improved in [82] for IPM machines (Figure 2.12b). The winding is not only used to weaken the flux but also to regulate the flux in the machine. The drawback of this method is that the DC windings require either brushes and slip rings or rotating diodes, in addition to the separate power supply, since the winding is situated in the rotor. Also this method imposes significant reliability issues.

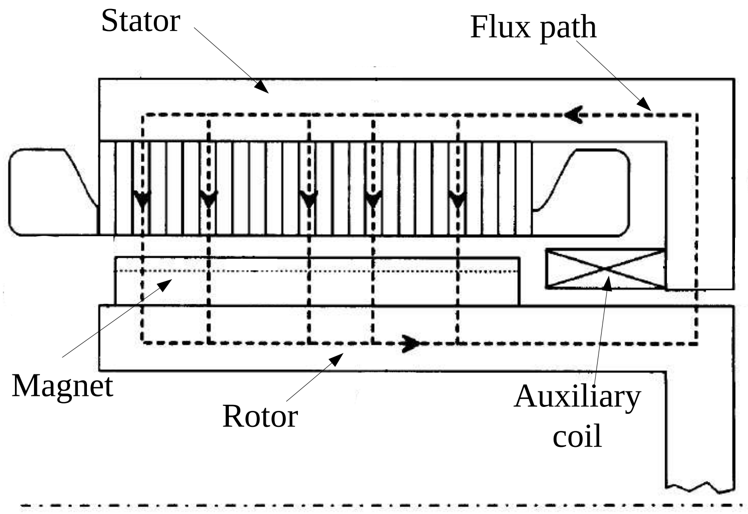

Figure 2.13 Cross sectional view of auxiliary coil placed in the rotor end region [83]

In order to null the magnet flux within the machine a similar auxiliary coil has been introduced in [83] for the rotor end region of homo-polar generators. The coil placement in the machine is shown in Figure 2.13. This arrangement allows for increasing the number of turns; consequently the excitation current is reduced and thus, it facilitates the reduction of loss and weight of the auxiliary winding including the auxiliary power supply.

The same idea is adopted for the radial [84, 85] and axial [86-88] flux consequent pole PM machine (as shown in Figure 2.14 and Figure 2.15, respectively) using auxiliary windings on the stator side. Even though the machine configurations allow control of the airgap flux level without any demagnetization risk, it reduces the power density since the windings are placed in the stator.

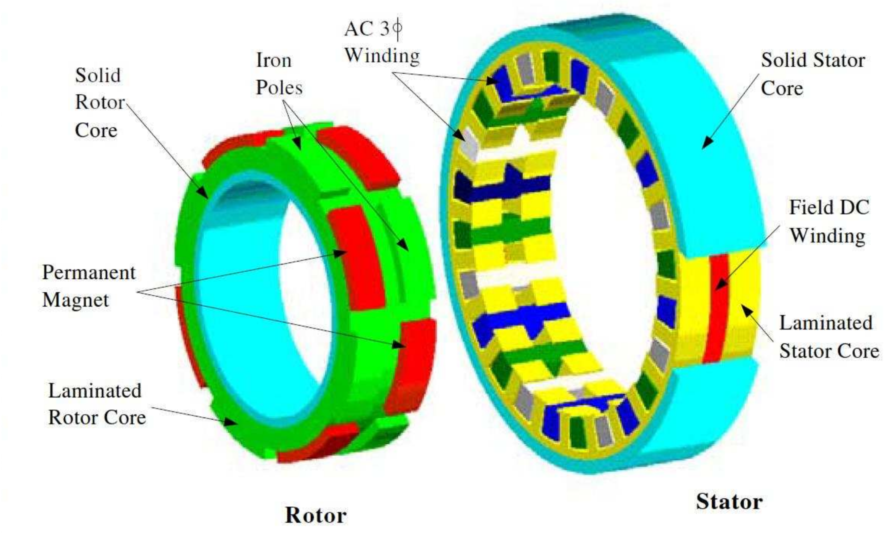

(a)

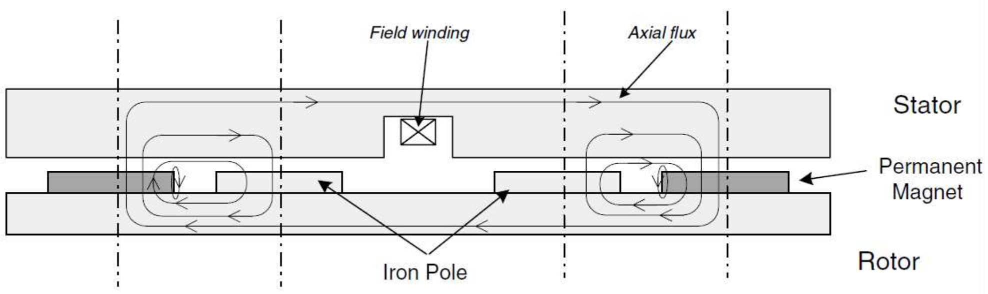

(b)

Figure 2.14 (a) Structure (b) two pole extended magnetic circuit of the radial-flux consequent pole PM machine [84]

In [89], a winding arrangement including primary and secondary windings in the stator side has been proposed for outer rotor PM machines as shown in Figure 2.16. There is a transformer effect between the primary and secondary coils. Under normal operation both the primary and secondary windings (in a shorted cage) act like a shorted transformer. During fault conditions, the current in the secondary winding increases, consequently these windings turn into open circuited winding. This can be done by using fuses or switches. Hence, the current in the primary windings can be limited by transformer effect. However, it is worth noting that this is not reliable and is also very difficult to guarantee since the method depends on the switches. Also the additional windings in the stator side will result in extra copper losses.

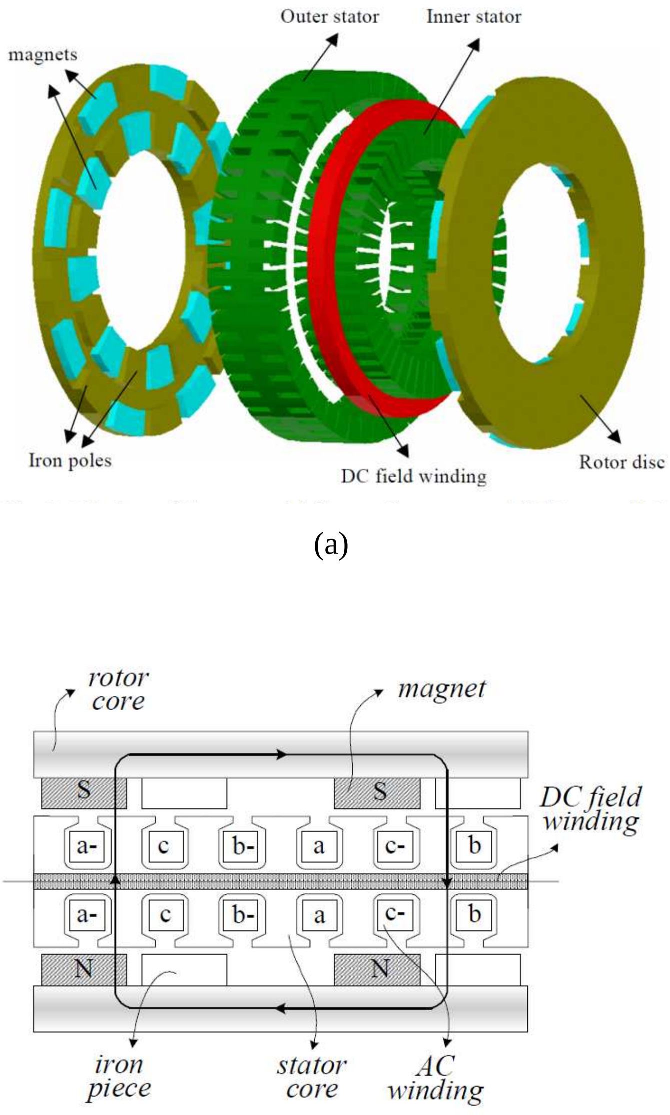

(b)

Figure 2.15 (a) Structure (b) two pole extended magnetic circuit of the axial-flux consequent pole PM machine [88]

In [90], a damper bar winding has been proposed for PM salient-pole synchronous machines in order to avoid the PM's demagnetisation under SC fault. It is shown that irreversible demagnetization might arise in the PM under three-phase SC fault due to the very large field and armature current. Employing damper bars in the machine the demagnetization of the PM is avoided as shown in Figure 2.17. However, the excessive fault current remains in the winding and thus an additional post-fault control approach is required.

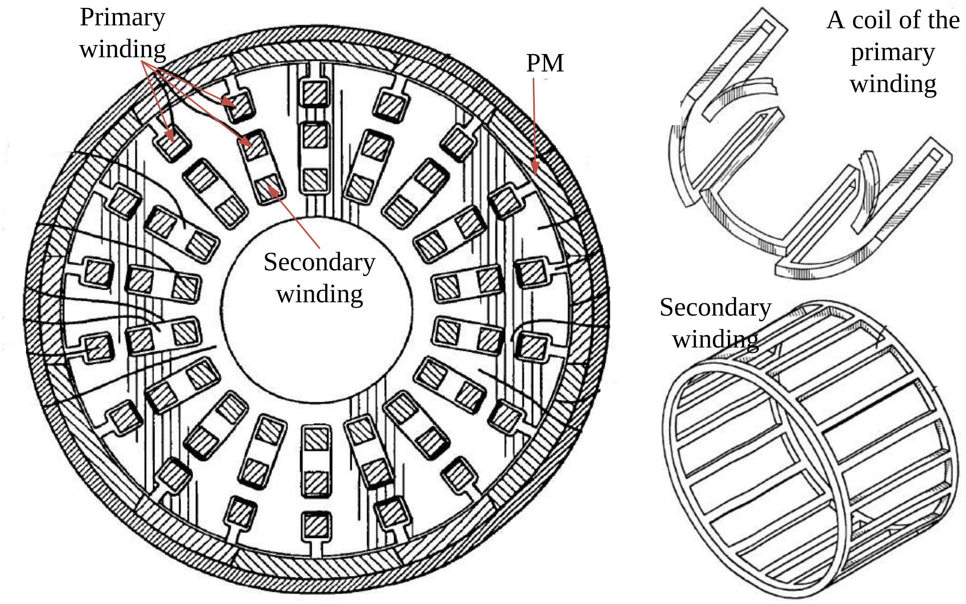

Figure 2.16 A winding arrangement in the stator of outer rotor PM machines providing transformer effect [89]

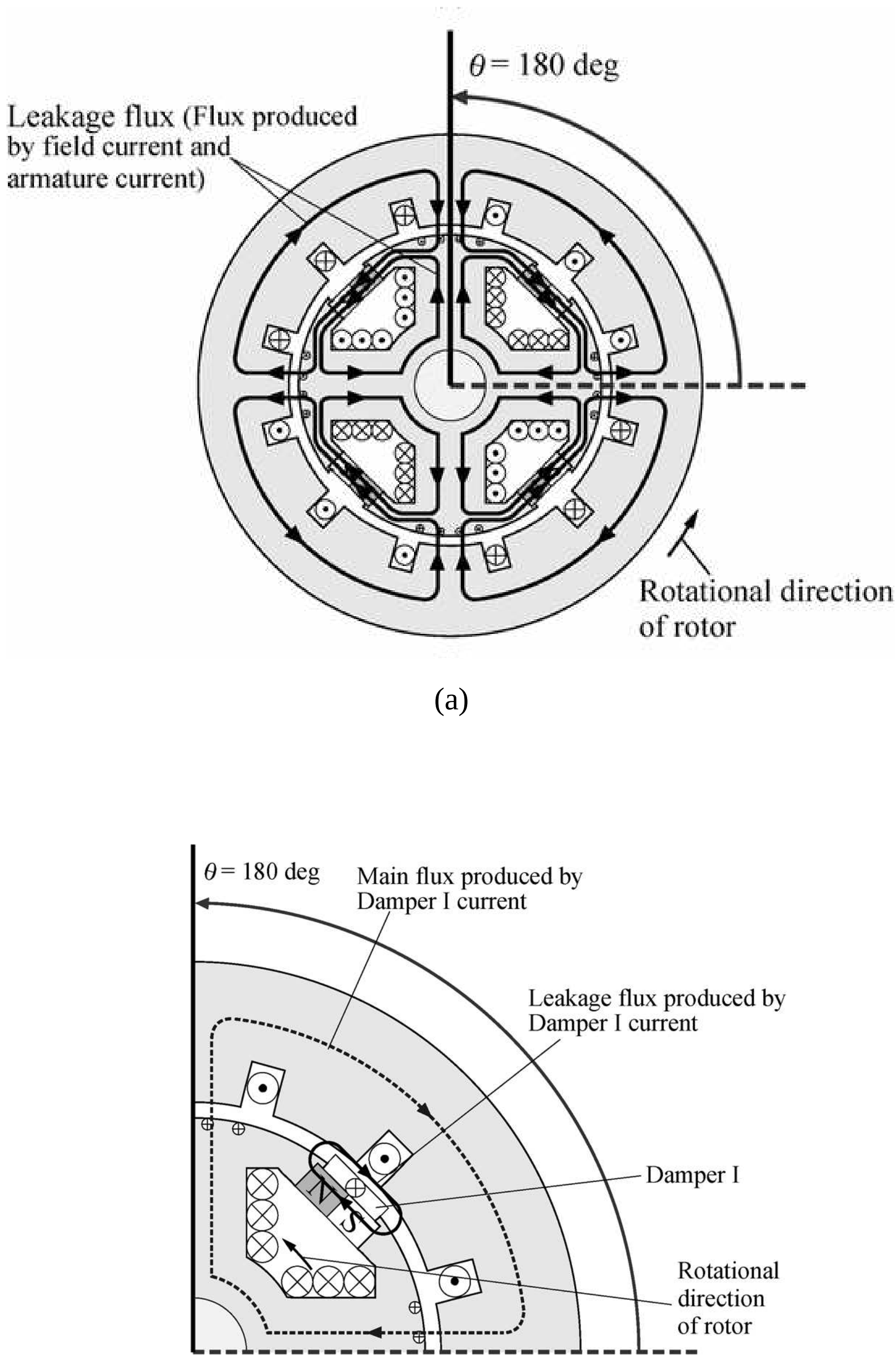

(a)

(b)

Figure 2.17 Cross sections and schematic flux lines of a four-pole PM salient-pole machine under (a) three phase SC fault operation (b) three phase SC fault operation with dumber bars [90]

2.3.1.3. *Stator shunts*

The same shunt concept in [89] is adopted in the stator side in [50, 53] by placing the thin solid copper/ N number of turns winding at the slot opening region as shown in Figure 2.18. During normal operation, thin solid copper is fed by a DC supply forming a coupling between the stator and the rotor due to the saturation at the slot opening. Under faulty operation the supply is disconnected, consequently the flux produced by the magnet is shorted through the slot opening. The main disadvantage of the method is that the thin copper requires a high amount of MMF in order to saturate the region resulting in excessive copper losses.

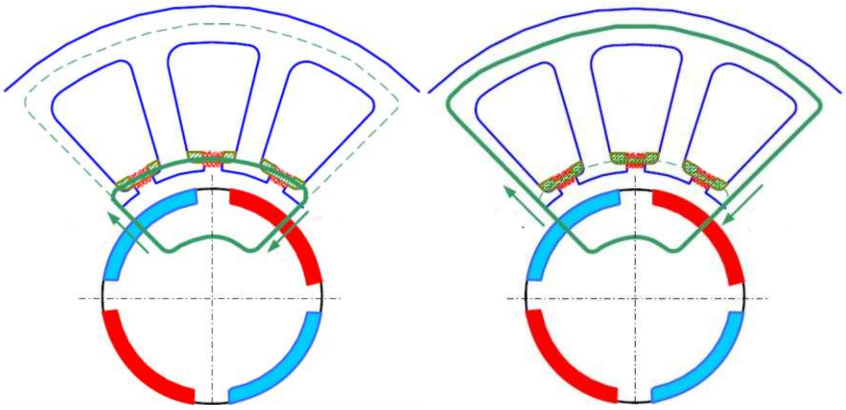

(a) **(b)**

Figure 2.18 Electrical shunt – (a) shorting the flux via slot opening under the fault (b) saturated slot opening region under healthy operation [50]

2.3.1.4. *Rotor shunts*

In [91], a magnetic shunt arrangement was proposed for the PM alternator to provide the desired wave shape. The shunts are placed between the pole pieces as shown in Figure 2.19. The winding on each flux shunt generates flux in the shunt proportional to the supplied current. The flux through the stator winding is controlled by increasing or reducing the shunt flux and thus it controls the amount of flux diverted from the magnets through the shunt. In the case of fault the windings around the shunt are de-excited, thus, a large portion of the magnet flux is shorted through the shunt. As discussed earlier in section

2.3.1.2, the additional winding causes extra losses and increases the total weight.

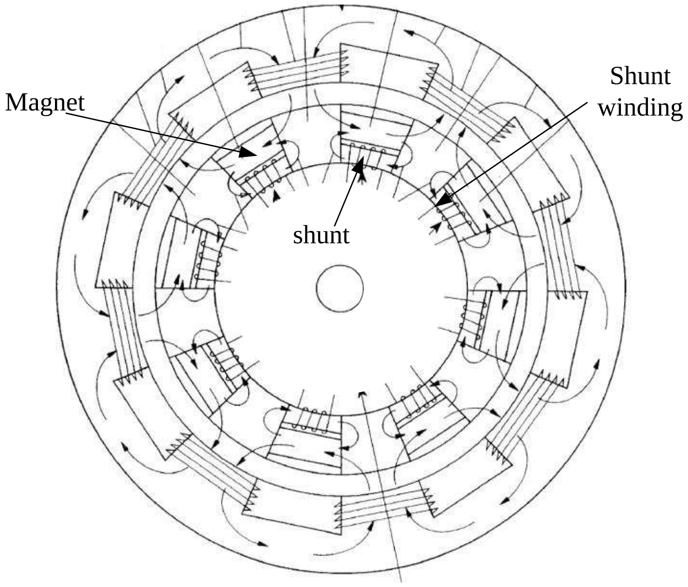

Figure 2.19 Shunt arrangement in PM machines [91]

2.3.2. Mechanical design

Several mechanical designs were proposed to weaken the magnet flux during the SC fault. The key challenges and issues of mechanical designs are: reliability, additional weight and latency in triggering the mechanism.

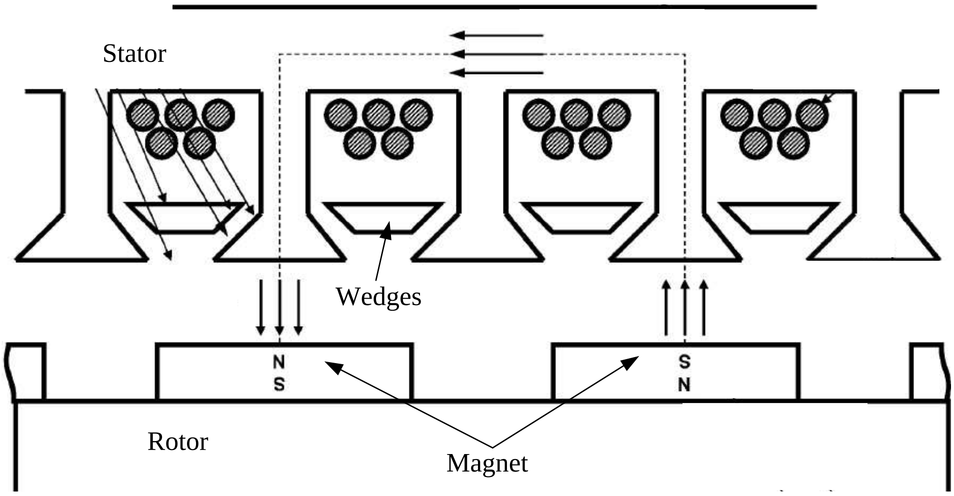

Figure 2.20 Shunting the flux via slot-opening under SC fault [92]

The same concept as the electromagnetic shunt, mechanical shunt mechanism also can be used to weaken the flux in the magnet under fault conditions. In [92], a spring loaded shunt mechanism was proposed to decouple the rotor flux via slot opening as shown in Figure 2.20. Under healthy operation the slot-opening region is open and thus it provides a strong magnetic coupling between the stator winding and the rotor magnetic flux. Under fault, the slot-opening is closed using the magnetic wedges. Hence, most of the magnet flux is shorted through the slot-opening, reducing the coupling between the stator winding and the magnet flux. Additional systems in the mechanism to open and close the wedges will increase the system's weight. Reliability of this closing method and the time which is taken to react are also of concern.

A similar shunting concept has been applied in [93] using adjustable magnetic sleeves while rotor and sleeves are rotating. The sleeve has spaced ferromagnetic bridges as shown in Figure 2.21. The sleeve can be shifted with respect to the rotor angularly. It changes the amount of flux that passes through the bridges. It is shown that the reposition of the sleeve provides a more constant output voltage during the load from the alternator and increases efficiency by diminishing the eddy current losses. This method has the same disadvantages as the previous one.

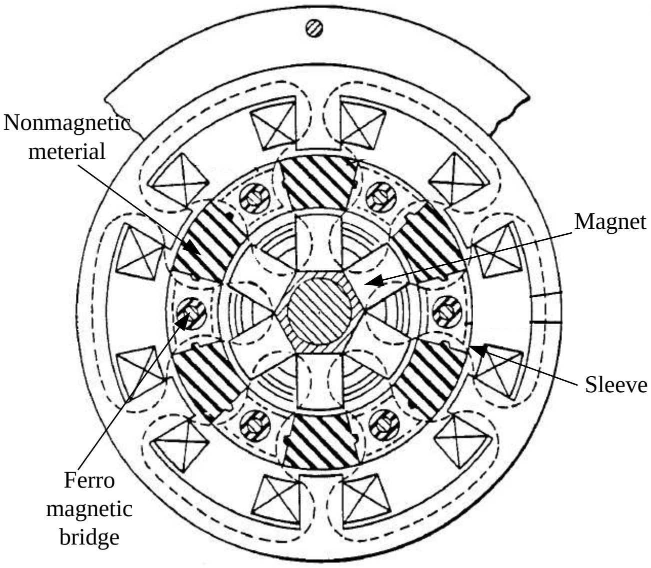

Figure 2.21 Shunting the flux via sleeve [93]

In [94], a method has been proposed for an axial flux PM machine to achieve constant-power operation over a wide speed range. It was shown that adjusting the phase displacement between the two PM rotor discs weakens the machine flux linkage as required, as illustrated in Figure 2.22. The phase shift is managed using a speed dependent mechanical device. As the desired phase displacement between the rotor discs does not produce a variation of the airgap flux density, this can be accomplished with no energy demand and a simple and cost effective speed-dependent mechanical regulator can be used [94]. However, reliability is the key concern of this method.

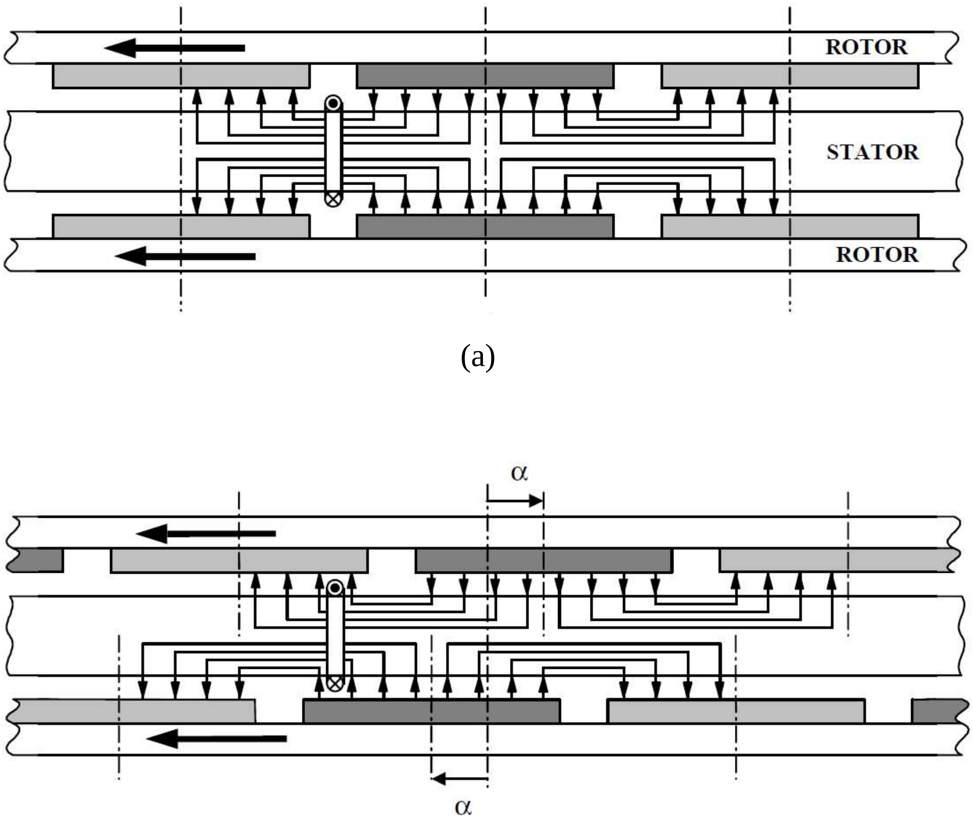

(a)

(b)

Figure 2.22 Mechanical weakening of the flux linkage via the regulation of the angular phase displacement between the two PM rotor discs - (a) aligned (b) shifted by α [94]

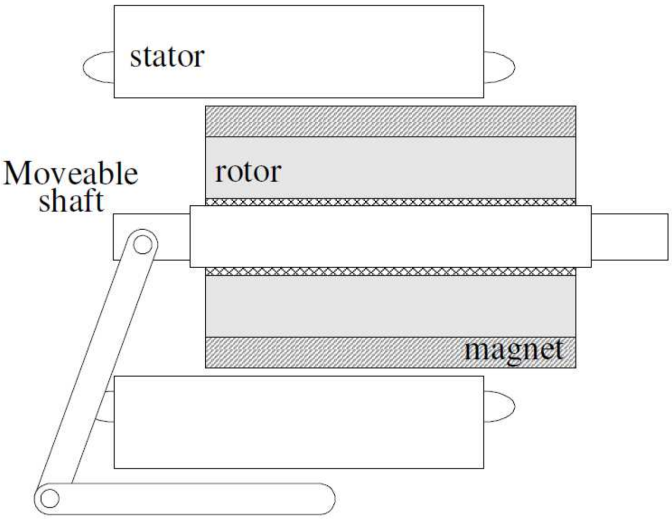

Figure 2.23 Magnet flux weakening using misalignment between rotor and stator **[95]**

In [95], field weakening is introduced in the PM machine using axial misalignment between rotor and stator. PMs are supported on the inner surface of an axially movable cylindrical shell as shown in Figure 2.23. Under normal operation both stator and rotors are aligned perfectly. In the event of failure the rotor is moved in an axial direction outside the rotor. In this case the reliability of the method is greatly dependent on the capability of bearings and the response time which it takes to move the rotor.

In [96], a method has been proposed to weaken the flux by varying the airgap under SC fault conditions. The design has a fixed rotor and an adjustable/ moveable stator. The stator is divided into two parts and held by screws at both ends as shown in Figure 2.24. Under healthy operation, the machine is operated with a fixed airgap. In the event of fault the stator is moved away from the rotor; consequently the airgap is increased and so the SC current reduces due to less coupling between the stator and PM rotor. As explained beforehand, reliability is the key concern.

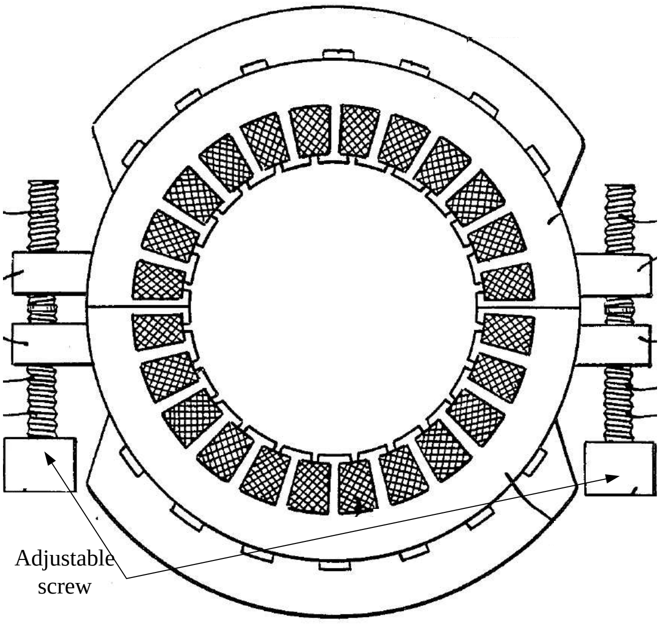

Figure 2.24 Magnet flux weakening by varying airgap[96]

2.3.3. Thermal design

In [97], a method has been proposed for a machine designed for a safety critical application where parallel redundancy is employed (as shown in Figure 2.25). The stator and rotor are constructed using iron/ferrite material. In the case of fault, the stator and the rotor material heat up due to generated high fault current. External heaters sense the fault condition and are used to speed up the heating process of the material. As a result the material becomes non-magnetic and thus the machine is prevented from further failure. During the cooling process the material regains it magnetic properties. The disadvantages of the method are: poor magnetic properties of iron resulting in poor power density, poor thermal constant, and the risk that heat in the faulty machine may spread requiring additional heat contamination. The key concern is how fast the material becomes non-magnetic.

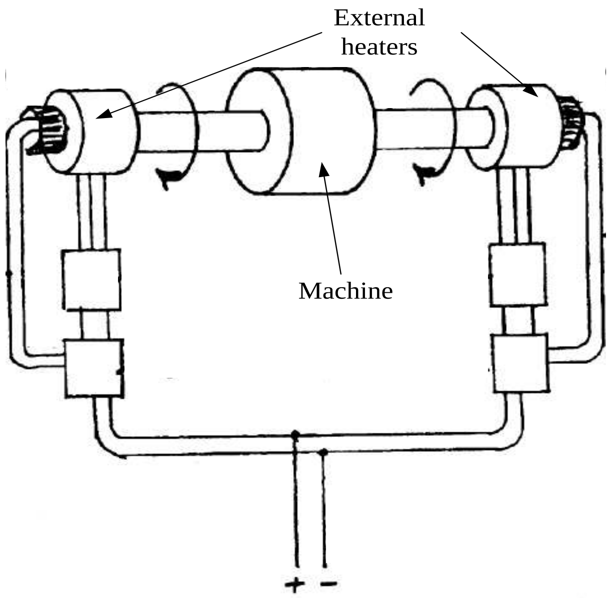

Figure 2.25 PM machine with external heaters [97]

2.4. **Fault control methods and comparison**

Table 2-1 shows a comparison between the various methods mentioned above. From Table 2-1, it can be seen that shorting the phase scheme is the most attractive method in terms of the cost, weight and reliability.

SC CONTROL METHODS	WEIGHT	COST	RELIA-BILITY	LOSS/EFFICIENCY
1. Shorting the faulty phase	☑	☑	☑	☒
2. Current injection	☑	☑	☒	☒
3. Auxiliary winding	☒	☒	☒	☒
4. Mechanical design	☒	☑	☒	☒
5. Thermal design	☒	☒	☒	☒

Table 2-1 Comparison of various methods

2.5. **Conclusion**

In this chapter, fault tolerant aspects in the synchronous PM machines, including various proposed methods and strategies with more emphasis on inter-turn SC fault, have been discussed. The advantages and disadvantages of the proposed methods are also examined. The key conclusion is that there are no ideal solutions for fault tolerance with regards to either design or control mechanisms. There are many trade-offs involving reliability, performance (torque density, power density, and efficiency), cost, weight, etc to accomplish the required level of fault tolerance. It is shown that shorting the faulty phase through the inverter terminal scheme is the most attractive method.

In the next chapter, the shorting terminal of the faulty phase scheme is adopted to investigate the inter-turn SC fault. An analytical model is established to improve computational time.

CHAPTER

3

Analytical prediction of inter-turn SC fault current

3.1. Introduction

This chapter describes an analytical method that can predict the inter-turn SC fault current considering the fault location in the slot of FT-PM machines. Since the winding inductances are directly related to the flux, the self-inductance of both healthy and faulty turns accommodated in a phase coil as well as the mutual inductance between them can be evaluated by quantifying the slot-leakage and air-gap fluxes. The evaluation of inductances as a function of the fault position can be used to determine the SC current before and after the application of remedial action which consists of short-circuiting the faulted phase terminals as discussed in chapter 2.

3.2. Why do we need an analytical model?

Modelling the machine including the fault is the first step in the development of fault analysis. There are two methods commonly used: FE method and analytical method. These methods always have a trade-off between time and accuracy. FE method is a numerical technique used to solve field problems of structures with any complex geometries and non-linear material properties. It is done by dividing the entire region of analysis into smaller finite elements which are connected to the adjacent elements by two or more nodes. A main disadvantage of this method is that the accuracy is directly proportional to the computation time and which can be varied according to the choice of mesh size. Furthermore, it's relatively difficult to implement the drive control algorithms in an FE environment. Hence, recent interest in development of analytical methods is increasing as they can provide faster solutions with sufficient accuracy.

There are few analytical methods proposed in the past for prediction of the SC fault current based on the lumped-parameter model [98, 99] and equivalent circuit model based on parameters calculated using either experiment or FE [100, 101]. The lumped-parameter model is based on the analogy between magnetic and electric circuits, where the machine is represented as a reluctance network with its associated magneto-motive sources. Although the modelling and computational time of this methods is much shorter than that required by FE ones, the modelling accuracy of the method highly depends on the number of nodes and related reluctance paths. Furthermore, the model becomes more complex in the case of single turn fault where each turn is represented by an equivalent reluctance. A FE based equivalent circuit model can be used as an alternative, however taking considerable amount of time for geometry formation and the parameter computation. Hence, a complete analytical model which can estimate the SC current effectively with less computation time is very useful.

3.3. An analytical model based on flux maps

In section 1.2, we have shown that the current in the shorted turn(s) is dependent on its (their) relative position in the slot where the phase winding is housed, and the slot-leakage flux associated with these turns has a significant influence on the magnitude of the SC current when a remedial action is applied (short-circuiting the phase terminals methodology). Hence, an accurate knowledge of these slot-leakage fluxes will facilitate the computation of different inductances: inductance of the SC turn, inductance of the remaining healthy turns and mutual inductances between them; consequently the SC current.

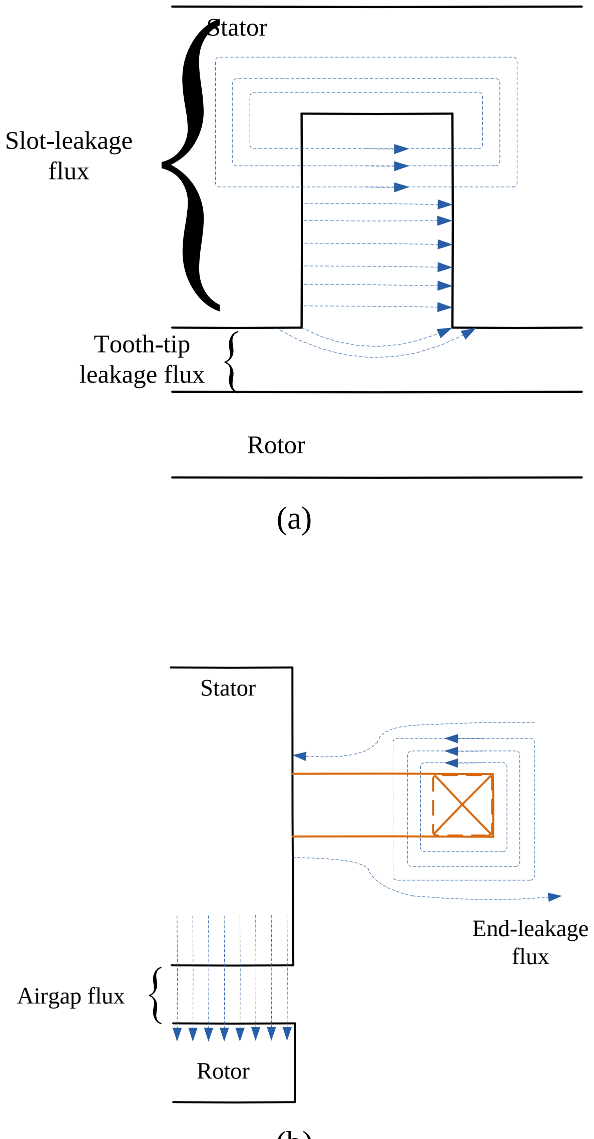

Figure 3.1 Flux components of a concentrated winding contained in a slot: (a) view of the slot area and (b) view of the end winding area

The flux associated to the winding inductances can be divided into two parts: main airgap flux and leakage flux, as shown in Figure 3.1. Furthermore, the leakage flux in electrical machines can be divided into two parts: the air gap flux leakage (e.g. zigzag leakage flux, skew leakage flux [102]) and the flux leakage components that do not cross the air gap. The leakage flux crossing the air gap is included in the main air gap flux. The flux components that do not cross the air gap can be separated according to their location within the slot. Those are:

1. the slot leakage flux;
2. the tooth-tip leakage flux;
3. the end-winding leakage flux.

Since these leakage fluxes are directly related to inductances (i.e. flux linkage for a unit current), by considering the above leakage fluxes and the main air gap flux, the associated inductances can be calculated. The total phase inductance is obtained by summing the different inductances. However, calculation of the leakage fields is difficult since the geometry is quite complex; the end winding leakage inductance is particularly difficult to compute. Thus, several assumptions will be made to simplify the computation process. These are explained in the next section.

3.3.1. Computation of SC inductances

Computation of indactances for a traditional (strand) Round Condutor Winding (RCW) is dificult and complex. Hence, a modelling approch proposed in [22, 103] is used with some modifications to suit fault tolerant machines. Initially, the flux distribution of a circumferentially arranged rectangular bar-type winding and RCW are investigated in FE by injecting a current in a turn whilst the remaining turns are open circuited as shown in Figure 3.2. Since both windings have similar flux distribution in the slot, the bar-type winding can be adopted in the modelling instead of RCW. Considering this arrangement of the conductors in the slot, the bar-type winding is named as Horizontally placed Strip Winding (HSW) throughtout this chapter.

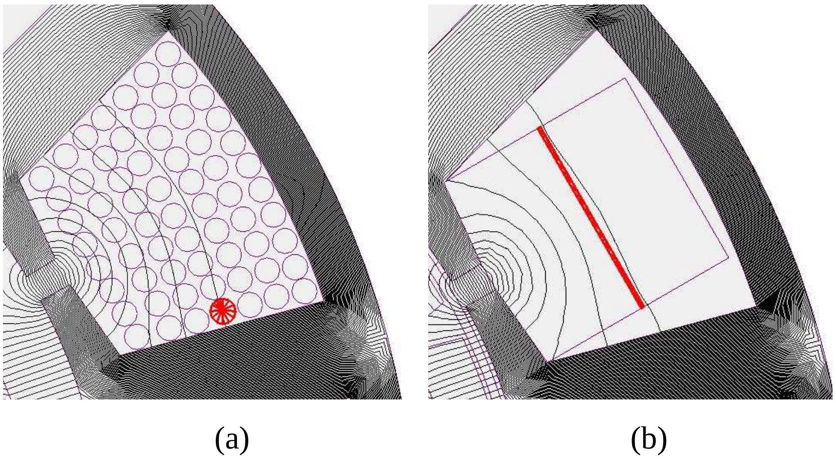

Figure 3.2 Flux maps of the (a) RCW, (b) HSW in a slot of FT-PM machine

Figure 3.3 shows the considered slot geomery of the machine having HSW, where the short-circuited adjacent turns (N_s) are sandwiched by the remaining healthy turns (N_a and N_b). x represents the position of the shorted turns. Thus, the different inductances of both healthy (N_a and N_b) and faulty (N_s) turns as well as the mutual inductance between them can be estimated with respect to the fault location by quantifying the associated slot-leakage flux.

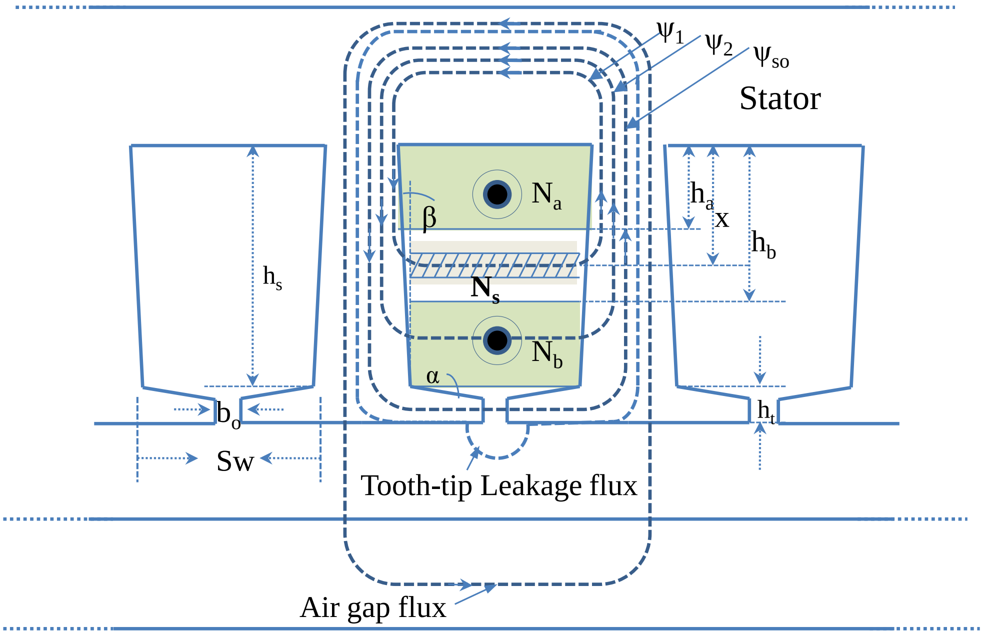

Figure 3.3 Flux representation used in the modeling of horizontal winding

In the modeling process, the following assumptions were made:

1. the laminated magnetic material has an infinite permeability;
2. the concentrated winding is placed horizontally and uniformly in the slot;
3. the slot-leakage flux is always parallel to circumferential direction as shown in Figure 3.3;
4. The end-leakage flux is negligible.

As shown in Figure 3.3 to calculate the self inductance of N_s shorted turns, the total leakage flux can be divided into five parts:

A. the slot leakage flux (Ψ_{so}) linking the slot wedge and the slot opening associated to the shorted turns;

B. the slot leakage flux (Ψ_1) linking the height (h_b-h_a) associated to the shorted turns;

C. the slot leakage flux (Ψ_2) linking the height (h_s-h_b) associated to the shorted turns;

D. the leakage flux associated to the tooth-tip and air gap.

A. Flux (Ψ_{so}) linking the slot wedge and the slot opening

The flux (Ψ_{so}) linking the slot wedge and the slot opening associated to the shorted turns can be estimated by quantifying the permeance (P_s) of a rectangular slot opening and a trapezoidal slot wedge [103]. Hence, the flux (Ψ_{so}) is given as follows:

$$\begin{aligned}\Psi_{so} &= P_s N_s^2 I \\ &= \mu_o l_{stk}\left[\frac{h_t}{b_o}+\frac{1}{2}\tan(\alpha)\ln\left(\frac{S_w}{b_o}\right)\right]N_s^2 I\end{aligned} \tag{3.1}$$

where:

l_{stk} : axial length of the laminated core

μ_o : permeabilty of air

b_o : the slot opening

S_w : the slot width

h_t : the tooth-tip height

α : the slot wedge angle

I : the current

N_s : the number of shorted turns

B. *Flux (*Ψ_1) linking the height (h_b-h_a)

The total flux linking the width (h_b-h_a) of the shorted turns (N_s) can be evaluated by integrating the flux density over the corresponding area A. Applying Ampere's law, the flux density can be written as:

$$B = \mu_o H = \mu_o \frac{N_s I}{l} \tag{3.2}$$

and the flux increment can then be written as:

$$d\Psi = B\,dA = \mu_o \frac{N_s^2 I}{l} l_{stk}\, dx \tag{3.3}$$

with dx being the length increment along the slot depth, (l) the flux path length across the slot width and (N_s) the number of shorted turns. Assuming a trapezoidal slot geometry and uniformly distributed turns along the slot height, l and Ns can thus equal to:

$$l = S_w + 2\left(h_s - x\right)\tan\left(\beta\right) \tag{3.4}$$

$$N_s = \frac{N}{h_s}\left(x - h_a\right) \tag{3.5}$$

By integrating (3.3) the total flux linking the height (h_b-h_a) of the N_s shorted turns is

$$\begin{aligned}\Psi_1 &= \int_{h_a}^{h_b} d\Psi \\ &= \int_{h_a}^{h_b} \mu_o\, l_{stk}\, I \left(\frac{N}{h_s}\right)^2 \left[\frac{\left(x-h_a\right)^2}{S_w+2\left(h_s-x\right)\tan\left(\beta\right)}\right] d\,x\end{aligned} \tag{3.6}$$

The integration can be done numerically using a methamatical software (i.e. MathCad, Maple, Matlab).

C. Flux (Ψ_2) linking the height of (h_s-h_b)

The flux linking the height (h_s –h_b) associated to the shorted turns can be estimated by quantifying the corresponding trapezoidal slot permeance (P_t) [103]:

$$P_t = \mu_o\, l_{stk} \frac{1}{2\tan\left(\beta\right)} \ln\left[\frac{S_w+\left(2\tan\left(\beta\right)\left(h_s-h_b\right)\right)}{S_w}\right] \tag{3.7}$$

and the resulting flux linkage is given by:

$$\Psi_2 = P_t\, N_s^2\, I \tag{3.8}$$

The total slot leakage flux linking the shorted turns is:

$$\Psi_s = \Psi_{so} + \Psi_1 + \Psi_2 \tag{3.9}$$

Using the same derivation process, the slot-leakage flux (Ψ_h) linking all the healthy turns as well as the mutual flux (Ψ_m) between the healthy and the shorted turns can be evaluated. The equations of these fluxes are given in Appendix B.

D. Flux associated to the tooth-tip and the air gap

The tooth-tip leakage flux and the air gap flux can be calculated by quantifying the tooth-tip leakage permeance P_{al} and the air gap permeance P_a as follows [103]:

$$P_{al} = \mu_o l_{stk} \left[\frac{5\left(l_g + h_m\right)/b_o}{5 + \left(4\left(l_g + h_m\right)/b_o\right)} \right] \tag{3.10}$$

$$P_a = \mu_o l_{stk} \left[\frac{\theta}{\ln\left(1 + \left(\left(l_g + h_m\right)/r\right)\right)} \right] \tag{3.11}$$

where, r,l_g,θ and h_m represent respectively the rotor radius, the air gap length, the slot pitch angle and the magnet depth.

Hence, self and mutual inductances under fault conditions can be calculated respectively from the following equations:

$$L_s = P_a N_s^2 + N_Q \left(P_{al} N_s^2 + \frac{\Psi_s}{I} \right) \tag{3.12}$$

$$L_h = P_a N_h^2 + N_Q \left(P_{al} N_h^2 + \frac{\Psi_h}{I} \right) \tag{3.13}$$

$$L_m = P_a N_h N_s + N_Q \left(P_{al} N_h N_s + \frac{\Psi_m}{I} \right) \tag{3.14}$$

where, N_Q is number of slots per phase coil. For a concentrated wound single layer winding, the slot-leakage and tooth-tip leakage fluxes are doubled since there are two slots per phase coil ($N_Q = 2$).

3.3.2. Computation of inter-turn SC current

The resistance (R) and the back electromotive force (e) of both healthy and shorted turns can be determined as follows [28]:

$$R = N \rho \frac{l}{A} \tag{3.15}$$

$$e = \sqrt{2}\pi \; f \; N \, k_w \, \Phi_g \tag{3.16}$$

where, N, ρ, l, A, k_w, f and Φ_g represent respectively the number of the considered turns, the resistivity of the conductors, the length of one turn, the cross section area of one conductor, the fundamental winding factor, the operating frequency and the fundamental air gap magnetic flux amplitude. The resistance of the winding is calculated at temperature of 20°C neglecting eddy current effects and it is assumed to be constant under fault conditions. The back-emf is calculated at no load and assumed to be sinusoidal and phase shifted between the phases by 120 electrical degrees. It is assumed that the induced emf in the shorted turn(s) due to the rotor excitation field is exactly aligned with its phase and that there is no load dependency. In realty the back-emf magnitude will reduce as a function of the armature reaction flux due to saturation. However this is in general expected not to have a major influence on the approach undertaken as will be shown further on in the next section when saturable FE models are adopted and compared to the analytical solution.

As described in section 1.2, the transient SC current can be obtained by the differential equations (3.17).

$$\begin{bmatrix} \dfrac{dI_1}{dt} \\ \dfrac{dI_s}{dt} \end{bmatrix} = \begin{bmatrix} L_h & Lm \\ Lm & Ls \end{bmatrix}^{-1} \begin{bmatrix} V_1 - e_1 - I_1 R_h \\ -e_2 - I_s R_s \end{bmatrix} \qquad (3.17)$$

Assuming that the machine is sinsodially fed, the steady state SC current I_s can be obtained by replacing the time derivatives by $j\omega$ in (3.17). Thus, I_s can be simplified as follows:

$$I_s = -\frac{e_2(\omega)}{R_s + j\omega L_s} - \frac{j\omega L_m}{R_s + j\omega L_s} I_1(\omega) \qquad (3.18)$$

where, I_1 is assumed to be still under control during a fault condition. Once an inter-turn SC fault is detected, the phase terminals of the faulty phase are shorted as part to the fault tolerant control strategy; this current is computed in steady-state by (3.19)

$$\begin{aligned} I_s = {} & \frac{j\omega L_m}{R_s R_h + \omega^2 (L_m{}^2 - L_s L_h) + j\omega(R_h L_s + R_s L_h)} . e_1 \\ & - \frac{j\omega L_h + R_h}{R_s R_h + \omega^2 (L_m{}^2 - L_s L_h) + j\omega(R_h L_s + R_s L_h)} . e_2 \end{aligned} \qquad (3.19)$$

3.3.3. Horizontal winding configuration - comparison with finite element calculations

A three phase, 12 slots and 14 pole concentrated wound FT-PM machine (Figure 3.4) is considered. The specifications of the machine are given in Table 3-1. Each phase has two coils connected in series, each having 65 turns which are wound around the respective teeth as shown in Figure 3.5.

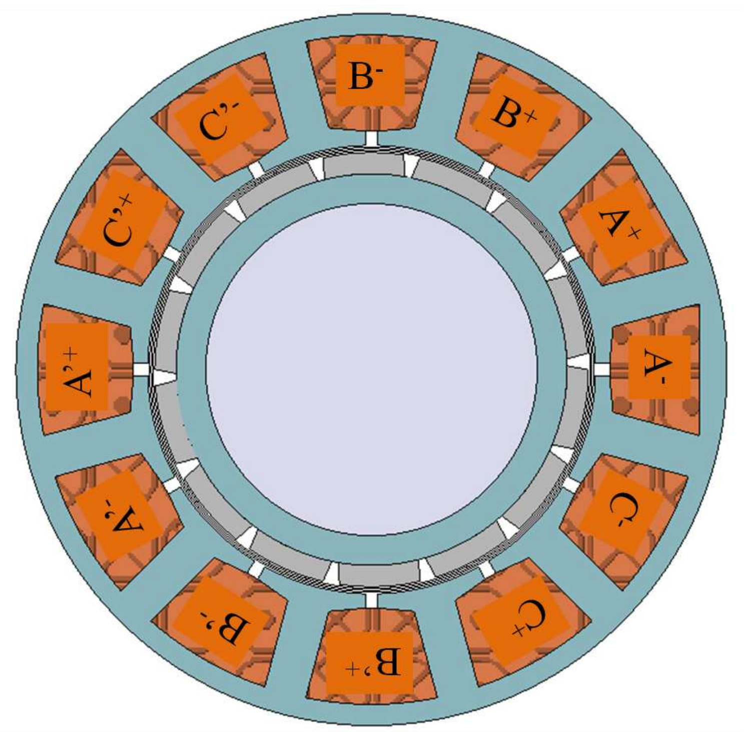

Figure 3.4 Cross sectional view of a 12slot 14 pole FT-PMSM

Specification	Value
Rated Speed (ω_{rm})	2000 rpm
Rated Output Power (P_o)	2062 W
Rated Current (Peak)	10 A
Phase Resistance (R_s)	0.45058 Ω
Slot Height (h_s)	12.5 mm
Magnet Height (h_m)	3 mm
Air gap Length (includes h_m)	4 mm
Slot Opening (b_o)	1.65 mm
Slot Width (S_w)	Inner 12 mm, Outer 18.5 mm
Tooth Shoe Height (h_t)	2 mm
Slot Wedge Height (h_w)	1 mm
Rotor Radius (r_{rot})	27.5 mm

Table 3-1 Specification of the three phase FT-PM machine

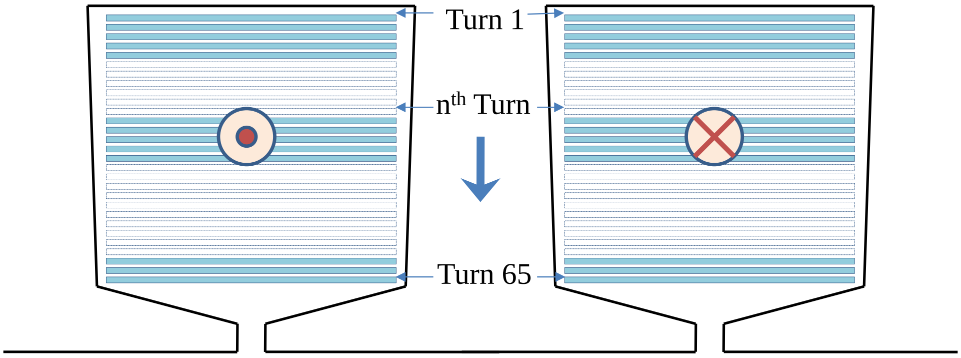

Figure 3.5 Representation of HSW configuration

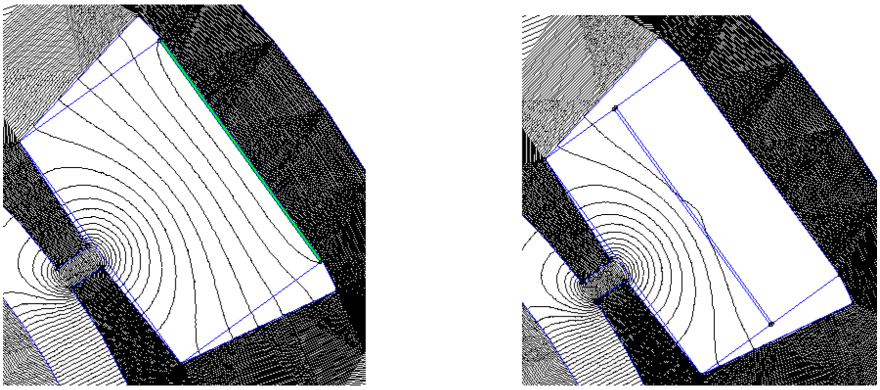

(a) (b)

Figure 3.6 Flux maps of the HSW in one slot for two different shorted turn positions: (a) at the inner most (b) at middle

Firstly, the resulting SC current when different numbers of inter-turn faults occur was investigated with the analytical model then compared with FE [104]. FE nalysis is performed using linear magnetic material ($\mu_r = 2000$). In addition, FE analysis using non linear magnetic material (M250-35A) is used as a benchmark. The numbers of shorted turns considered were 1, 5, 10, 15, 20, 25, 30, 45 and 60. Analytical and FE calculated steady state SC currents after the application of the remedial control strategy are given in Figure 3.7 where it can be seen that the single turn fault is the worst case scenario. Since the single turn SC is the worst case the resulting SC currents for various single turn faults but at different positions will be considered. The associated inductances for various single turns at different locations, which correspond to the following positions in the coil of the shorted turn: 1, 13, 26, 33, 39, 52 and 65. The different inductances computed with the analytical model are compared to the ones calculated by FE and the obtained results are shown in Figure 3.8.

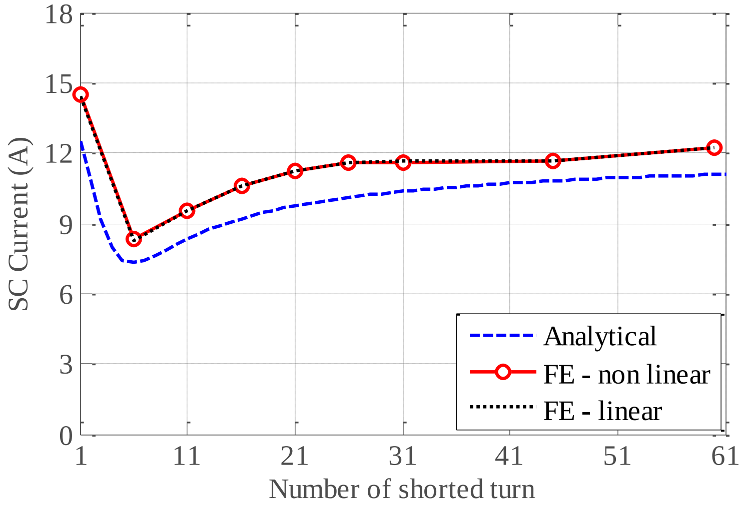

Figure 3.7 SC current vs. the number of shorted turns after application of the remedial action

The analytically calculated inductances are in good agreement with the FE ones. However, it can be seen from Figure 3.8 that the analytically calculated inductances are slightly higher (with error of 2% – 5%) than the FE ones; this is mainly due to the assumption of the flux paths being only parallel to the circumferential direction. This can be observed from Figure 3.6. It is also interesting to highlight the fact that the resulting SC current in the healthy turns, when the phase coil is short circuited as part of the remedial control strategy, is out of phase with the back-emf as the coil impedance is inductance limited [4]. This results in an equivalent negative d-axis current which drives the iron out of saturation, thus making the analytical modeling method a valid approach.

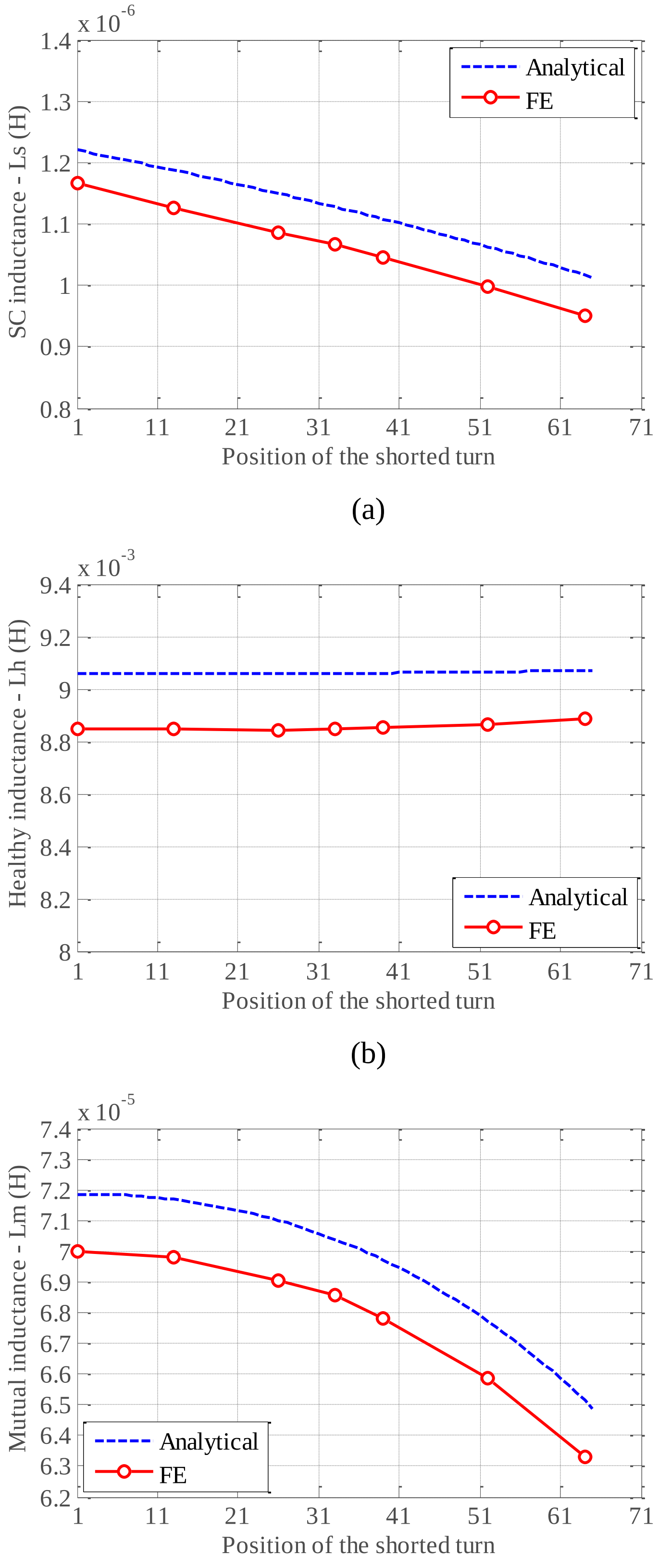

(a)

(b)

(c)

Figure 3.8 Comparison of analytical and FE results of (a) SC (b) Healthy (c) Mutual Inductances for the HSW

Figure 3.9 shows the computed steady state SC current compared to FE results when the remedial action has been applied (ie. applying a terminal SC). As it can be seen, the results are in good agreement. The error between the two methods is less than 2.3%. The SC current reaches its maximum value when the fault is located close to the slot opening. This is the worst scenario of this type of winding.

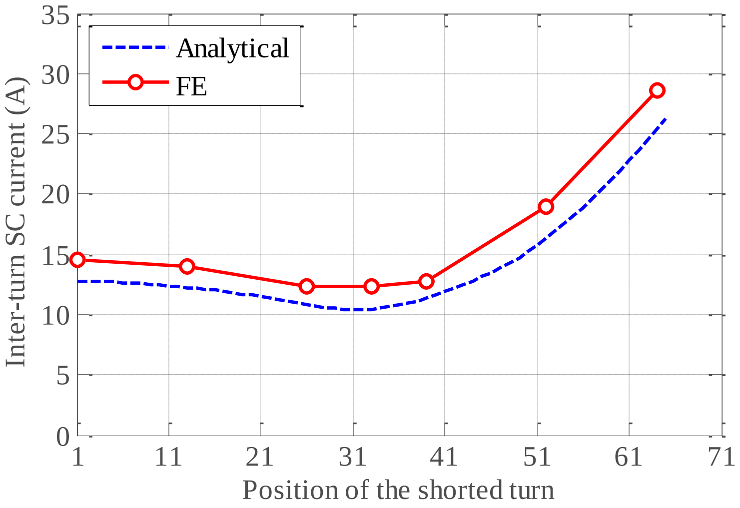

Figure 3.9 Current in the shorted turn after application of the remedial action for the HSW

3.3.4. Model verification for RCW

In order to verify the usefulness of the proposed analytical tool, the SC current in the RCW is computed in FE assuming that the fault is located at various positions within the slot of the same FT-PM machine, as shown in Figure 3.10. The turn-turn SC current of a corresponding HSW for a number of fault positions along the coil are calculated analytically.

Figure 3.11 shows the steady-state SC current of the turns depicted above and the corresponding current in HSW configurations were adopted for a fault in the same position. The results are for when the remedial action has been applied. It can be observed that the induced current in the RCW reaches over four times the nominal current when the fault is located in the bottom of the slot due to low inductance. Also it can be seen that the predicted magnitude of the SC currents are identical for the turns located at the same radial position (turns 1-2-3, 4-5-6 and 7-8-9 for instance). This is due to the assumption that the flux is invariable along the tangential direction.

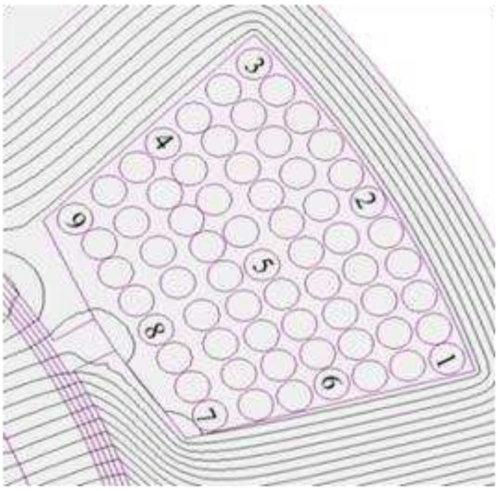

Figure 3.10 Representation of the SC fault location in traditional stranded winding

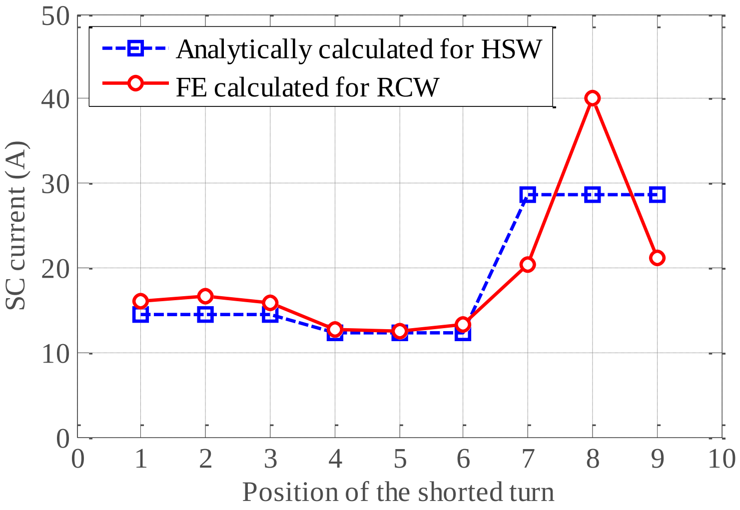

Figure 3.11 Comparison of the SC current in RCW and HSW configurations under fault at 9 different locations when remedial action being employed

The results obtained for RCW are in good agreement with the calculated ones everywhere in the slot except where the fault is located closest to the slot opening. The proposed analytical method underestimates the SC current at middle of the slot-opening (at position 8) while overestimates it at position 7 and 9. This is due to the fact that the slot-leakage flux lines close to the slot opening are not exactly in the circumferential direction. However, this analytical method is completely valid for bar-type winding. Thus, the method can be used as a reference for RCW.

3.4. Solution to inter-turn SC fault

One way of overcoming this serious over current is to design the machine with a larger inductance which can be even higher than unity per unit inductance. Whilst possible, this would result in a poorer power factor and a significant reduction in the torque density achievable [3]. Due to these negative merits of this design approach, as a solution to the serious over current, a Vertically placed Strip conductor Winding (VSW) configuration is proposed as a solution and analysed hereafter.

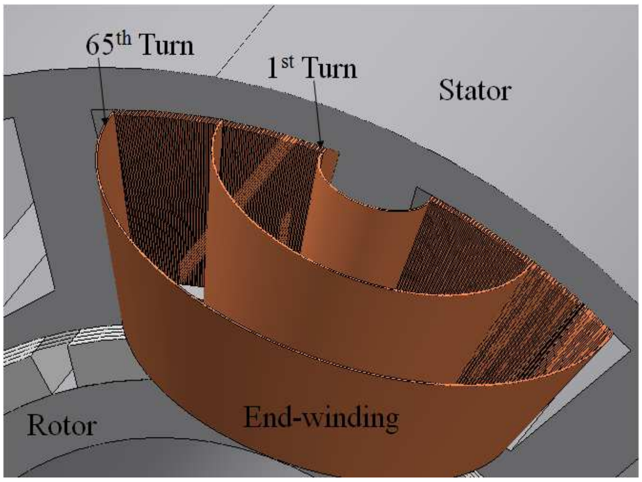

Figure 3.12 Perspective view of the VSW

Figure 3.12 shows the prespective view of the concentrated wound VSW. This winding is placed in the slot vertically and is made of thin copper foil or strip or solid rectangular conductor depending on the required number of turns per slot. In next section, an analytical model is proposed to compute the inductances of VSW.

3.5. Inductances compuatation of the proposed vertical conductor winding

In order to compute the inducances, the flux map in the slot containing the VSW were first obtained using FE for different faulty turn placements in the slot. Different placements of faulty turn are investigated by injecting a current whilst the remaining turns are open circuited. It was observed, as shown in Figure 3.13, that the flux lines across the slot are parallel to the vertical conductors. This assumption is valid under SC fault conditon since the relatively high induced current in the shorted turn which results in an increase of the SC MMF. Thus, the inductances can be evaluated by assuming that the flux lines are parallel to the conductors.

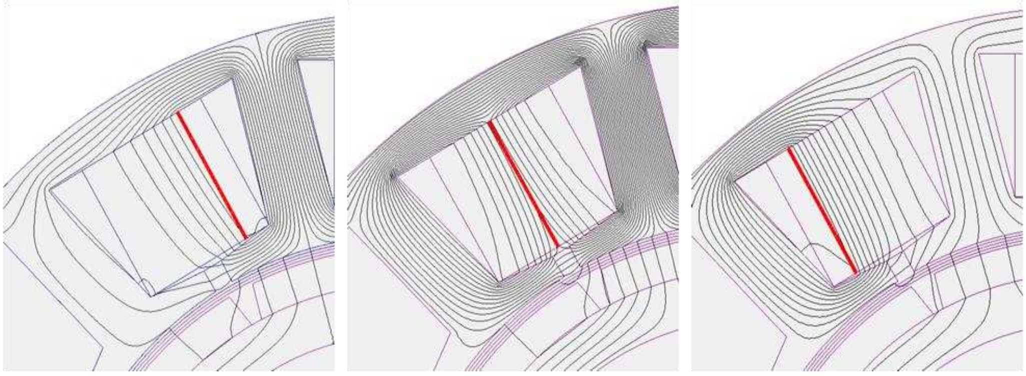

(a) (b) (c)

Figure 3.13 Flux maps in one slot of the VSW for three different positions of one shorted turn. (a) One shorted turn in the left side of the slot (b) One shorted turn in the middle of the slot. (c) One shorted turn in the right side of the slot

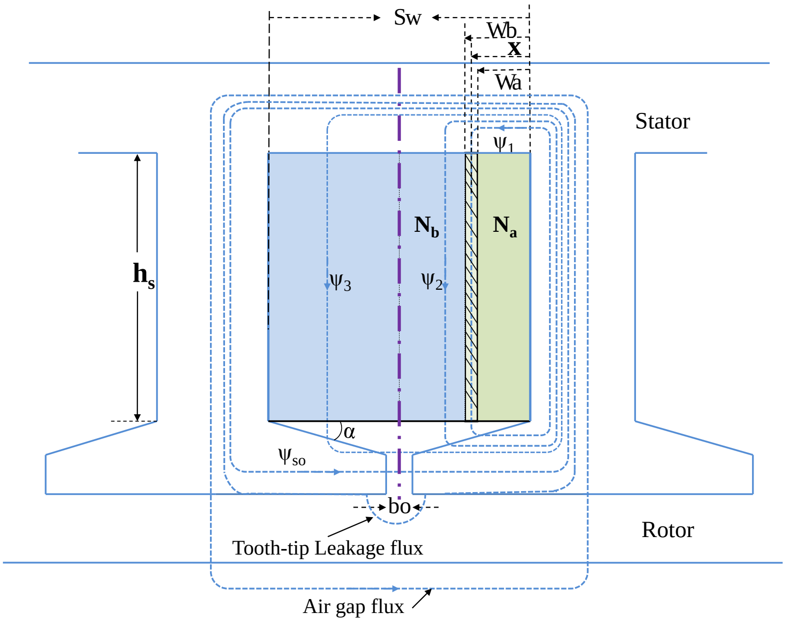

Figure 3.14 Flux representation used in the modelling of the VSW

The following assumptions are made in the modeling process:

1. The slot has a rectangular shape, as shown in Figure 3.14;
2. The laminated magnetic material has infinite permeability;
3. The concentrated winding is placed vertically and uniformly in the slot;
4. Under fault conditions, due to the relatively high induced SC current, the flux lines across the slot are parallel to the conductors, as illustrated in Figure 3.14;
5. the end effects are negelected.

Furthermore, for the modeling purposes, the slot is split in the middle as shown in Figure 3.14. With respect to the position of the shorted turns, being characterized by the lengths W_a and W_b, three conditions were made for the inductances calculation process. These conditions are:

1. $$\begin{cases} \text{if } W_a < W_b < \dfrac{S_w}{2} \text{ then,} \\ \qquad \Psi_{a1} = f(N, x), \; x \in \left[0, \dfrac{S_w}{2}\right] \end{cases}$$

2. $$\begin{cases} \text{if } W_b > W_a > \dfrac{S_w}{2} \text{ then,} \\ \qquad \Psi_{a2} = f(N, S_w - x), \; x \in \left[\dfrac{S_w}{2}, S_w\right] \end{cases}$$

3. $$\begin{cases} \text{if } W_a < \dfrac{S_w}{2} < W_b \text{ then, } \Psi_{a3} = \dfrac{\Psi_{a1} + \Psi_{a2}}{2} \end{cases}$$

Where, the slot leakage fluxes (Ψ_{a1}, Ψ_{a2}, Ψ_{a3}) are estimated with respect to the shorted turns' number N_s and their position (x) as will be detailed in the following section.

To calculate the self inductance of N_s shorted turns, as shown in Figure 3.14, the slot-leakage flux can be divided into four parts:

A. the slot leakage flux (Ψ_{so}) linking the slot opening;
B. the slot leakage flux (Ψ_1) linking the width ($W_b - W_a$);
C. the slot leakage flux (Ψ_2) linking the width ($S_w/2 - W_b$);
D. the slot leakage flux (Ψ_3) linking the width ($S_w - S_w/2$) respectively.

A. Flux *linkage (Ψ_{so})* associated with the slot opening

The flux (Ψ_{so}) linking the shorted turns and associated to the slot opening can be estimated by quantifying the permeance of the slot opening (P_{so_v}):

$$\begin{aligned} \Psi_{so} &= P_{so\_v} N_s^2 I \\ &= \mu_o l_{stk} \left[\frac{h_t}{b_o}\right] N_s^2 I \end{aligned} \tag{3.20}$$

B. *Flux (Ψ_1)* linking the width (W_b – W_a)

The total flux linking the width (W_b – W_a) of the shorted turns (N_s) can be evaluated by integrating the flux density over the corresponding area (A). Applying Ampere's law, the flux density can be written as:

$$B = \mu_o H = \mu_o \frac{N_s I}{l} \tag{3.21}$$

where,

- $l = h_s + x \tan(\alpha)$ is the leakage flux path length
- $N_s = N(x-W_a)/S_w$ is the number of shorted turns occupying the width (W_b – W_a)

Hence, the flux increment can be written as:

$$d\Psi = B\,dA = \mu_o \frac{N_s^2 I}{l} l_{stk}\, dx \tag{3.22}$$

and the associated flux linking the width (W_b – W_a) of the shorted turns is given by (3.23).

$$\begin{aligned} \Psi_1 &= \int_{W_a}^{W_b} d\Psi \\ &= \int_{W_a}^{W_b} \mu_o\, l_{stk}\, I \left(\frac{N}{S_w}\right)^2 \left[\frac{(x-W_a)^2}{h_s + x\tan(\alpha)}\right] d\,x \end{aligned} \tag{3.23}$$

C. *Flux (Ψ_2)* linking the width ($S_w/2$ – W_b)

The flux linking the width ($S_w/2$ – W_b) associated to the shorted turns can be estimated by quantifying the corresponding slot permeance (P_{s2}):

$$P_{s2} = \mu_o \, l_{stk} \left[\frac{S_w - 2W_b}{2(h_s + W_b \tan(\alpha))} \right] \tag{3.24}$$

and the resulting flux is given by:

$$\Psi_2 = P_{s2} \, N_s^2 \, I \tag{3.25}$$

D. Flux (Ψ_3) linking the width ($S_w - S_w/2$)

In a similar way as for (Ψ_2), the permeance (P_{s3}) associated to the width ($S_w - S_w/2$) and the corresponding flux is given by:

$$\begin{aligned} \Psi_3 &= P_{s3} \, N_s^2 \, I \\ &= \frac{1}{2} \mu_o \, l_{stk} \left[\frac{2S_w h_s + 2S_w h_w - b_o h_w}{(h_s + h_w)(2h_s + h_w)} \right] N_s^2 \, I \end{aligned} \tag{3.26}$$

The total slot leakage flux linking the shorted turns is:

$$\Psi_s = \Psi_{so} + \Psi_1 + \Psi_2 + \Psi_3 \tag{3.27}$$

In the same manner, slot-leakage flux Ψ_h linking all the healthy turns as well as the mutual flux Ψ_m can be evaluated using the equations given in Appendix C. The tooth-tip leakage and air gap fluxes can be estimated using (3.10) and (3.11) and the corresponding SC, healthy and mutual inductances can be computed respectively from (3.12), (3.13) and (3.14).

3.5.1. Comparison with finite element calculations

In order to verify the proposed analytical tool, the same three phases, 12 slots and 14 poles concentrated winding FT-PM machine is considered. The inductances are evaluated under one turn SC fault condition for different locations (as shown in Figure 3.15), which correspond to the position in the slot of the shorted turn whose number is 1, 13, 26, 33, 39, 52 and 65 respectively. The different inductances computed with our model are compared to the ones calculated by FE and the results obtained are shown in Figure 3.16.

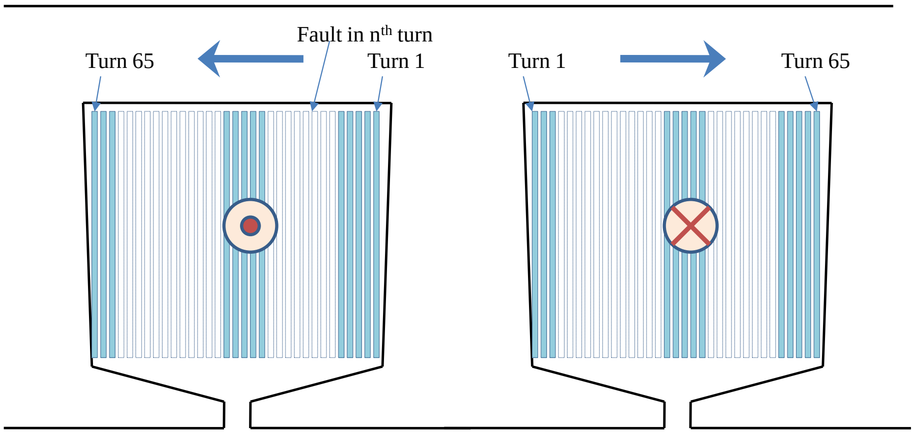

Figure 3.15 Representation of nth turn SC fault in the VSW

The results are in good agreement, but the analytically calculated values of inductances are slightly higher than the FE as for the horizontal winding. The error between the two methods is less than 5%. This is again likely due to the fact that linear iron is assumed in the analytical model and due to the fact that the flux lines are not strictly straight along the radial direction, as evident in Figure 3.13.

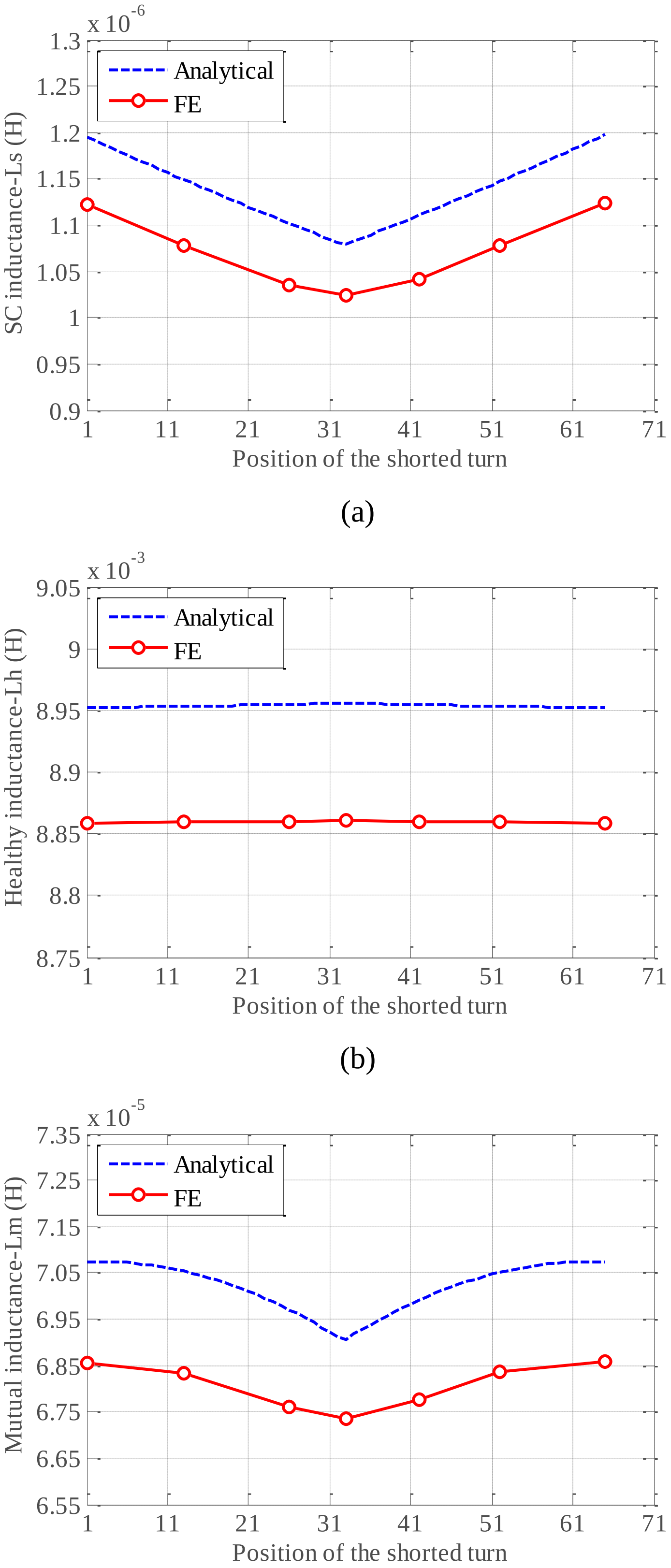

(a)

(b)

(c)

Figure 3.16 Comparison of analytical and FE results of (a) SC (b) Healthy (c) Mutual Inductances for the VSW

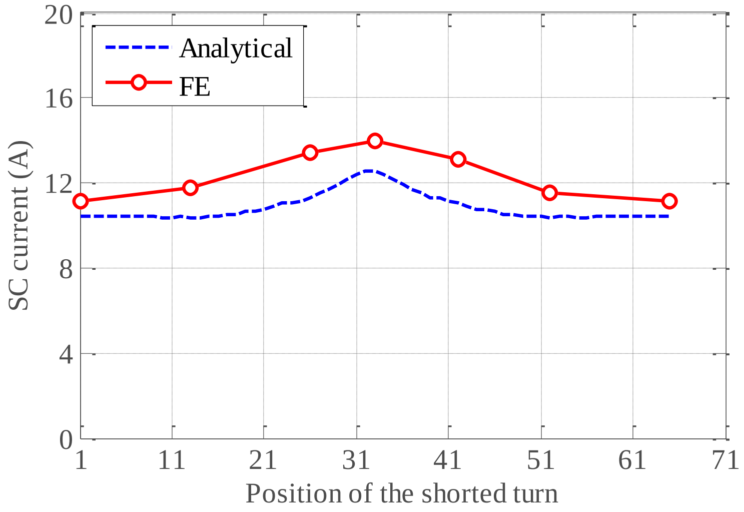

Figure 3.17 Current in the shorted turn after application of the remedial action for the vertical winding configuration

From Figure 3.17, it can be seen that the SC current results are in good agreement as well. The SC current reaches its maximum value when the fault is located in the middle of the slot. The comparison of analytically calculated and FE computed inductances and resulting SC currents were also carried out for different slot geometries and multi-turn SC faults. Similar characteristics were obtained.

3.5.2. Comparison of winding configurations with respect to inter-turn SC current suppression

Figure 3.18 shows the induced current in the HSW and VSW for different fault positions. Form Figure 3.18, it can be observed that the current variation with the faulted turn position can be neglected in the vertical winding configuration when compared to the horizontal winding. This result shows clearly that the vertical winding is intrinsically limiting the short-circuit current significantly compared to both RCW and HSW.

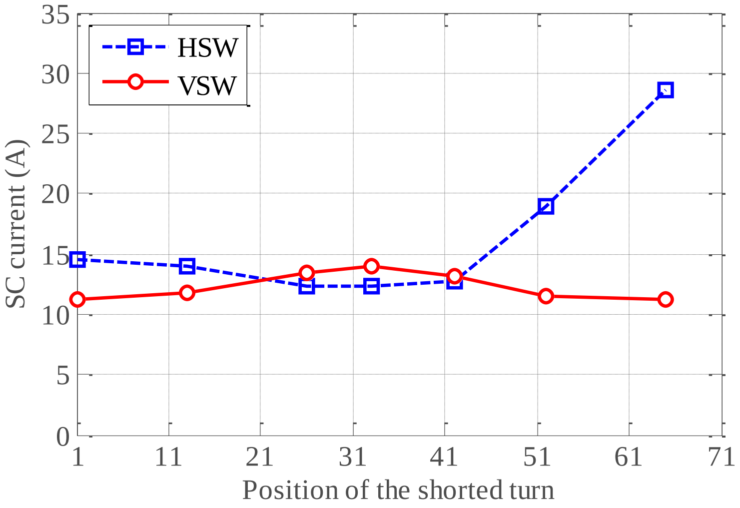

Figure 3.18 Comparison of the current in the shorted turn of HSW and VSW configurations after application of the remedial action

3.6. Experimental validation

Although a degree of confidence in the analytical methodology to calculate the resultant SC current is achieved through FE validation, experimental validation is also carried out on a purposely constructed stator core section (Figure 3.19). For simplicity of manufacturing, the stator core section is constructed using a solid material (low carbon 0.1-0.3% steel, specifications of which are given in the Table 3-2).

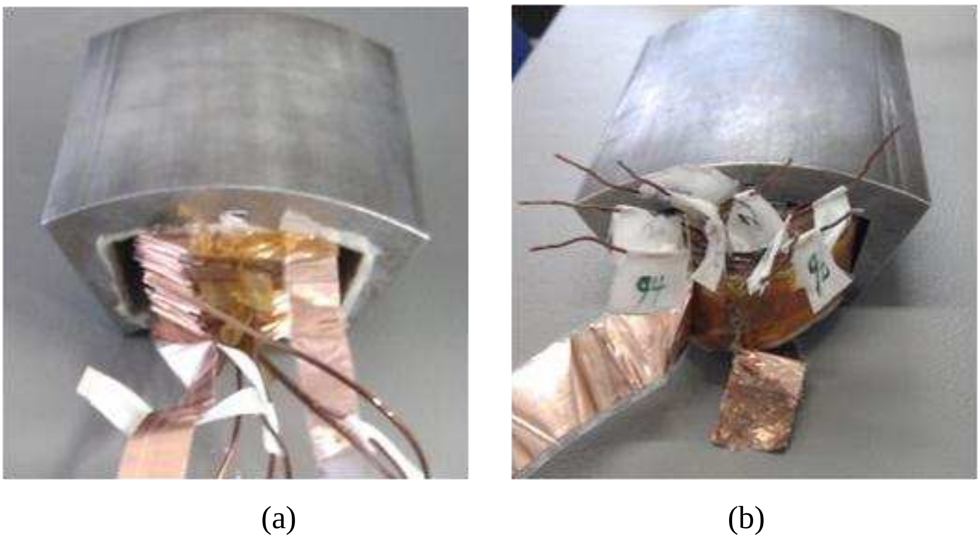
(a) (b)

Figure 3.19 Constructed stator core section with (a) HSW (b) VSW

The windings are placed in the slot horizontally with 50 turns (due to the folded end-winding), then vertically with 100 turns as shown in Figure 3.19a, b respectively. In both cases, to allow a satisfactory precision of measurement a five turn SC is considered. By considering that the fault occurs at positions 1, 15, 35 and 45 for the horizontal winding and 1, 21, 48, 71 and 95 for the vertical winding, the inductances of healthy and shorted turns were measured using an RLC meter.

SPECIFICATIONS	VALUE
Tooth Width (W_t)	24.7562 mm
Slot Height (h_s)	18 mm
Slot Opening (b_o)	0.82 mm
Slot Width (S_w)	Inner 18 mm, Outer 18 mm
Tooth Shoe Height (ht)	3 mm
Conductivity (σ)	5800000 S/m at 20ºC
Relative Permeability (μ_r)	200

Table 3-2 Specification of the prototype stator core

As shown in Figure 3.20 and Figure 3.21, the tendency of the measured results is in good agreement with both analytical and FE results, but the measured SC inductance shows a significant difference from the computed ones. This is due to the characteristic of the solid magnetic material which has a very low relative permeability ($\mu_r \approx 200$), which is confirmed by conventional experimental methods [105, 106]. The relative permeability of low carbon steel is confirmed using hysteresis loop measurements (remanence flux density $B_r = 1.2$ T and coercive force $H_c = 5320\text{Am}^{-1}$). For verification purposes, the obtained SC inductance with FE using similar material's properties is also given in Figure 3.20 and Figure 3.21. This is very close to the simulated value; however, the measured healthy inductance is slightly higher than FE under similar conditions. This may be caused by the end-leakage inductance that is not considered in FE analysis. However, this is much less significant in the case of few shorted turn, where the end-leakage inductance can be neglected.

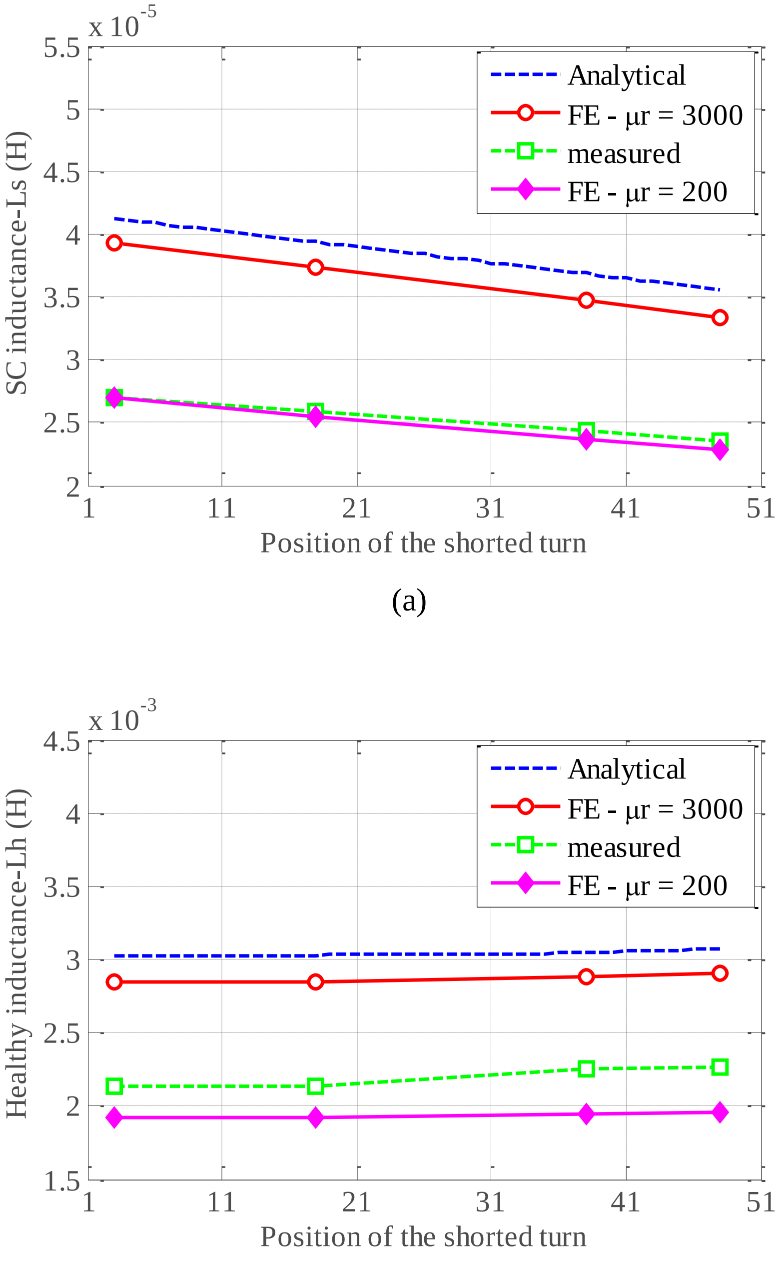

Figure 3.20 Comparison of measured and computed inductances: (a) SC inductance of the HSW and (b) healthy inductance of the HSW

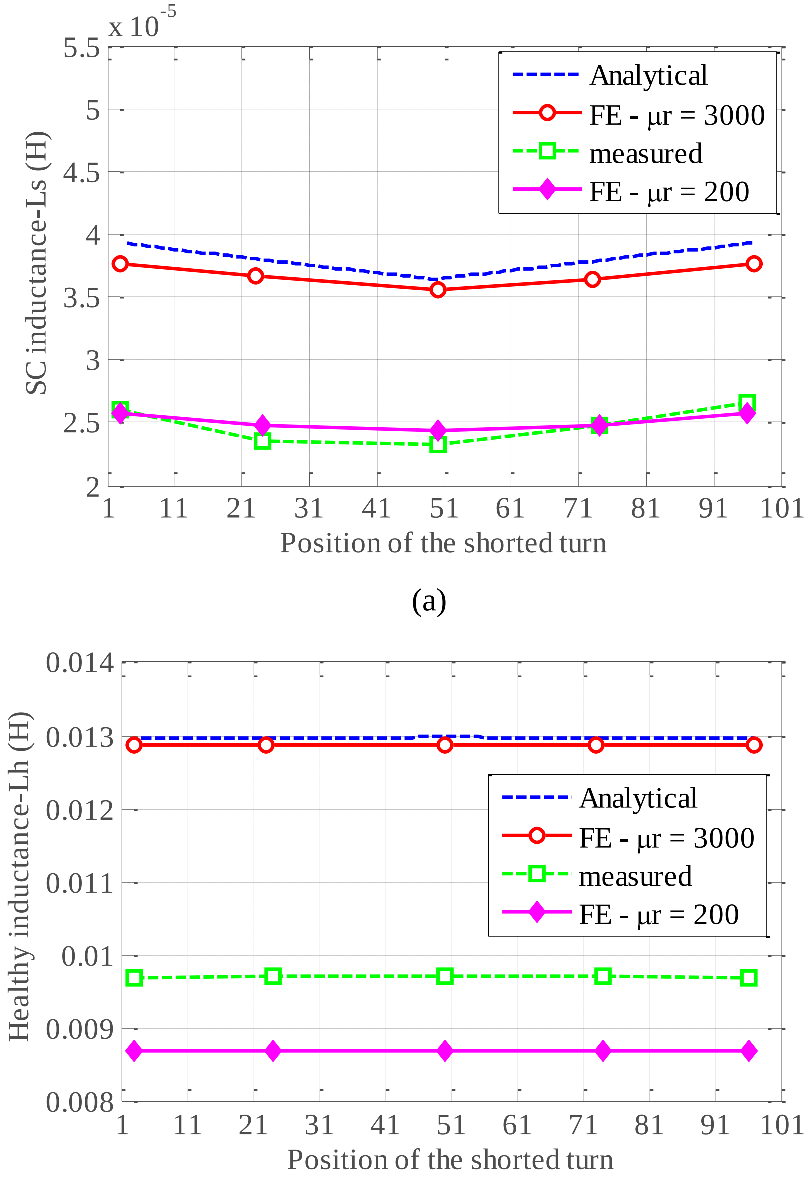

(a)

(b)

Figure 3.21 Comparison of measured and computed inductances: (a) SC inductance of the VSW and (b) healthy inductance of the VSW

The measured results clearly show that the SC inductances are position dependent in the slot and thus, the short circuit current is also position dependent and will be excessive if the fault occurs in the critical fault location (close to slot opening). The experimental results clearly show that the faulty turns' inductance position dependency in the vertical coil arrangement is very small. This results in an effective solution to mitigate the issue of large short circuit currents close to the slot opening in traditional coil arrangements.

3.7. **Conclusion**

This chapter has clearly highlighted the issues with the SC current magnitude as a result of the location of the fault within the coil. The study focused on concentrated coil structures often adopted in fault tolerant machines. It was observed that for stranded coils a single turn-turn fault close to the slot opening results in a worst-case SC current magnitude. An analytical model that can be used to evaluate inductances and subsequently calculate the fault currents for two different concentrated winding configurations under SC fault conditions has been proposed. Although this method, as any other analytical method, has some obvious limitations in terms of accuracy, it has a very fast computation time and can be effectively used at a design stage where much iteration is needed and where the modeling of individual turns in a FE package under fault conditions would be prohibitively time consuming. The modeling method is also very easy to integrate in dynamic simulations where the effect of faults on the system dynamics and converter control are also required.

CHAPTER

4

Comparative thermal analysis of RCW and VSW

4.1. **Introduction**

The conductors of the VSW being placed vertically in the slot are expected to experience a higher current re-distribution due to resulting eddy-currents. This is due to the main slot leakage crossing the slot in mostly a tangential direction. The issue is naturally more dominant at higher speeds (frequencies). There are two different phenomena that contribute to the total eddy-current effect: skin effect and proximity effect which is also named as double sided skin effect [103]. The skin effect is the tendency for very high frequency currents to flow in the surface of the conductor and the proximity is the tendency for current to flow in other undesirable patterns that form a localized current distribution in the slot due to the presence of an external field which can be produced by either the magnets or adjacent surrounding conductors [107, 108]. These effects are dependent on the physical structure of the winding, the length of the conductors, the slot dimensions and the operating frequency. Detailed analysis of these losses will be dealt with in the next chapter.

In this chapter, an investigation into the thermal behaviour of both VSW and RCW wound FT-PM machine is done under healthy and post-fault controlled operating conditions, i.e. shorting the phases via converter terminals.

Bulk thermal conductivity of copper windings is relatively low compared to solid copper [109]. This results in a considerable temperature gradient within the winding with the hot-spot determining the machine rating. The effective thermal conductivity is a function of the copper packing factor and the conductivity of the resin. In a VSW it is expected that this issue is somehow alleviated due to the fact that: a) higher copper packing factors can be achieved and, more importantly b) the radial conductivity of the winding is expected to approach that of pure copper. The latter should significantly improve the thermal management of exterior-cooled machines. Thus, a study carried out using FE [61] and a comparison between the two windings is done with a particular focus on the winding hot spot.

4.2. FE Copper losses evaluation

In order to evaluate frequency dependent copper losses an assumption is made that there are no changes in the effective resistance due to the temperature rise. The same FT-PM machine as the one considered in chapter 3 (see chapter 3 – section 3.3.3) is adopted for both winding configurations (RCW and VSW). In FE, both winding arrangements are modelled conductor by conductor, where RCW has diameter of 1.3819 mm whilst VSW has a height of 11.5 mm and a width of 0.13043 mm. The winding arrangement in the slot and the adopted mesh conditions for both VSW and RCW are given in Appendix D.1.

Figure 4.1 shows the ratio of AC (sum of DC and eddy-current losses) to DC losses against frequency. As can be seen, the two winding configurations have the same AC losses at low frequency while at rated frequency (233.33 Hz) the losses of the VSW are almost twice the value of those of RCW.

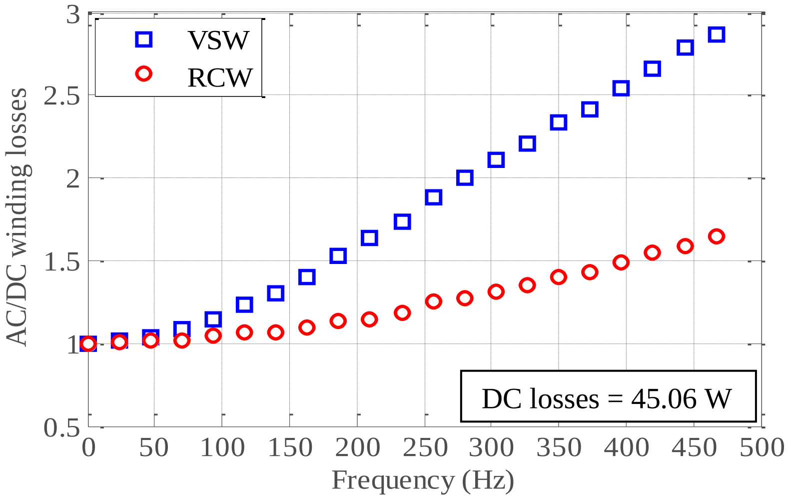

Figure 4.1 AC/DC loss ratio vs. frequency, Comparison between VSW and RCW

Since the cross section of the RCW is less than the skin depth for the range of frequencies considered, the additional losses are resistance limited. However, it is not the case of the VSW which has a larger skin depth in the radial direction as the height of its conductors is almost equal to the slot height and thus, both proximity losses and skin effect exist. This is further illustrated by the current density distribution plots shown in Figure 4.2.

From the obtained results, it is clearly evident that even though the VSW eliminates the SC current amplitude dependence on the position in the slot of the shorted turn, it increases eddy current losses.

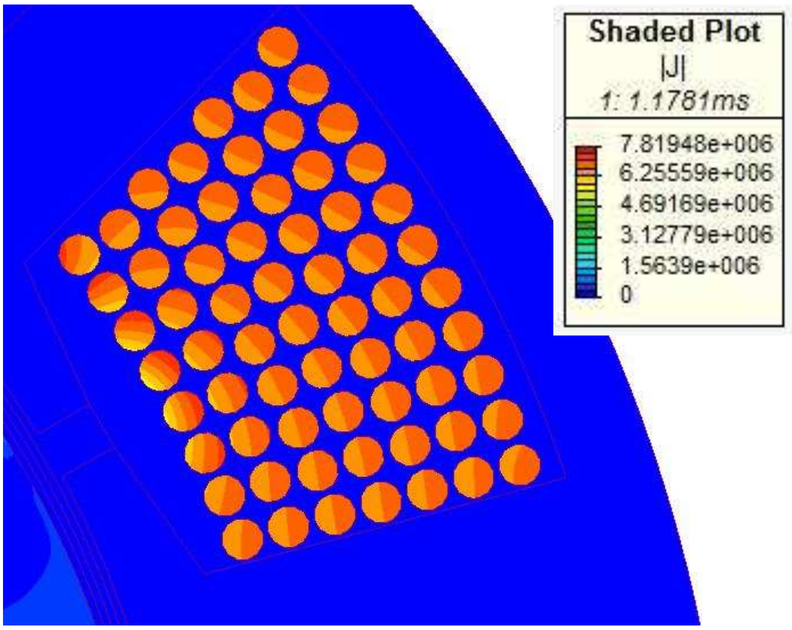

(a)

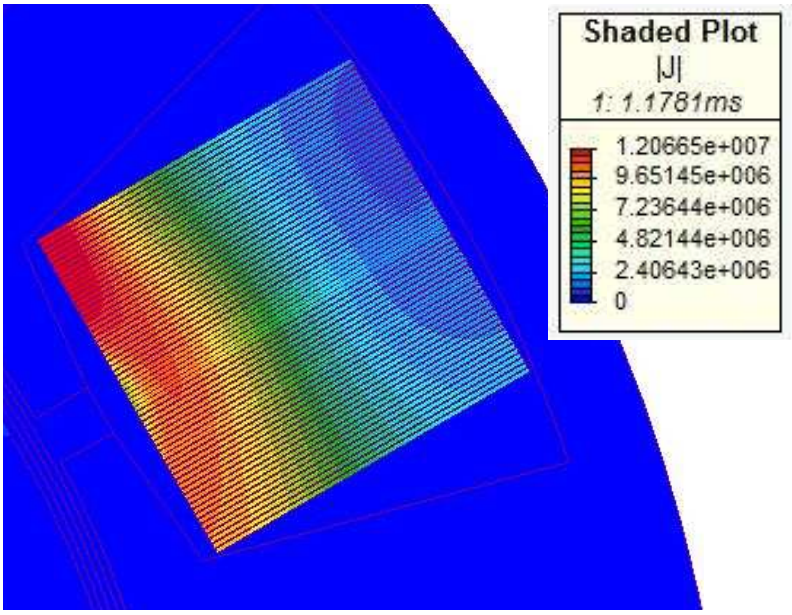

(b)

Figure 4.2 Current density distribution in the slot for: (a**)** RCW, (b) VSW

4.3. FE steady-state thermal behaviour

The temperature rise in the machine is a consequence of losses. The operating temperature must be monitored and controlled by adopting necessary cooling arrangement to continue the operation safely. Therefore, a comparative thermal analysis of both RCW and VSW windings is undertaken under healthy and faulty operating conditions.

To investigate the thermal behaviour of the proposed winding, a 2D FE thermal analysis is carried out to predict the temperature distribution in the slot under both healthy and faulty operation. The study is carried out in a weakly coupled electromagnetic and thermal FE simulation environment [110, 111]. Thermal 2D FE simulation is performed using the losses calculated from electromagnetic FE simulations at both healthy condition (ω_{rated} = 2000 rpm, I_{peak}=10A) and faulted condition with the remedial action (converter terminals SC) is being applied.

The same machine is used in this analysis, where the cross section area, insulation thickness, slot coating, slot dimensions and thermal boundaries (stator outer surface temperature is fixed to120 °C) are kept the same for both windings. Both windings are designed to have the same fill factor (K_f = 0.65). The insulation properties used in 2D thermal simulation are given in Table 4-1.

Description	Thermal Conductivity ($W.\ m^{-1}.C^{-1}$)	Thermal heat capacity ($J.\ kg^{-1}.C^{-1}$)
Winding insulation	0.22	1500
Slot wall insulation	0.25	1256
Slot insulation	0.10	1200

Table 4-1 Properties of the insulation material used in the thermal simulation

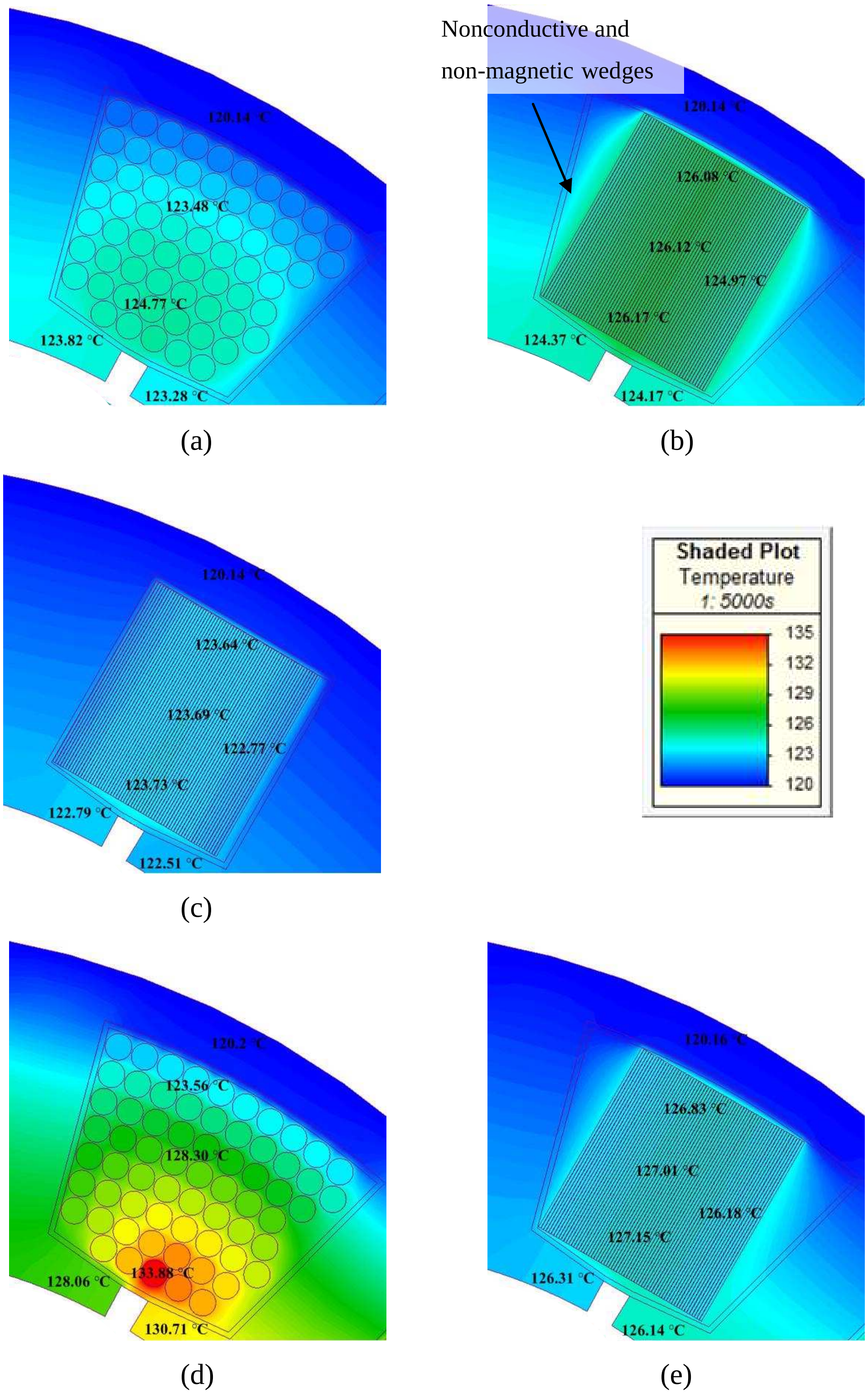

(a) (b)

(c)

(d) (e)

Figure 4.3 FE temperature distribution of: (a) RCW, (b) VSW, (c) modified slot for VSW at healthy operation and (d) RCW, (e) VSW at faulty operation (after application of the remedial action)

Figure 4.3a, b, c and Figure 4.3d, e show the slot temperature distribution for both windings during healthy operation (I = 10 A, ω_{rpm}= 2000 rpm) and faulty operation (after application of the remedial action), respectively. It can be seen that the VSW hotspot value (126.17 °C) is higher than that of RCW (124.77 °C). This is expected as the copper losses in the VSW for the machine adopted in this study are twice the ones of the RCW at rated speed (ω_{rpm} = 2000 rpm).

To overcome this problem, a solution exists to design the slot geometry with respect to the shape of the strip conductors so as to facilitate thermal conduction between the slot and the iron. Figure 4.3c shows the much improved scenario. The main advantage of the VSW in terms of heat transfer is that it has an equivalent winding radial conductivity which is close to that of copper. By doing so the temperature is limited to its equivalent excursion in RCW. The hot spot, which is towards the slot opening, is markedly higher in the stranded winding during faulty conditions, as can be seen in Figure 4.3d and e. From the obtained results, it is evident that the VSW has a better thermal path to the generated copper losses.

4.4. **Conclusion**

From the comparison between VSW and RCW, it can be seen that although the VSW improves fault-tolerant capability, the generated losses in the windings are significantly higher than those of RCW. Although these losses cannot be fully eliminated they can be limited to a reasonable value at design stage, since the AC/DC loss ratio is significantly dependent on the slot depth. Other possible design solutions to AC losses, along with a design parametric design procedure, are presented in chapter 6.

This chapter clearly outlined the advantages presented by the VSW in terms of it having a better thermal path to the generated copper losses.

CHAPTER

5

Analytical estimation of winding losses

5.1. Introduction

In the previous chapter, it has been shown that the VSW is highly influenced by frequency-dependant loss. To investigate this loss both FE [107, 112, 113] and analytical [114-120] methods can be used. FE method is the most popular and powerful for electromagnetic field computation due to its high accuracy and capability of catering for non-linear characteristics as shown in the loss results in the previous chapter. However, the method is highly time-consuming, and limits the flexibility of any parametric study; this is particularly true when conductive media are considered in a transient time-stepping simulation. Analytical tools can be alternatively adopted as they provide a faster solution despite their limitations.

In [121-125] proximity losses are investigated for round and rectangular conductors using a 1-D model. The 1-D model provides complementary results, but the results may be inaccurate particularly for semi-open slot machines. In [90], it is confirmed that the obtained losses are inaccurate for the conductors which are placed closer to slot-opening. This inaccuracy comes from the assumption made that the flux lines are one directional (circumferential); which is not valid in that region.

P.Reddy and et.al proposed an analytical method [114, 116, 126] to evaluate the resistance limited eddy current losses for single and double layer winding arrangements of round conductors based on flux density estimation. However, this method does not consider the eddy currents reaction field and assumes that the magnets field has no influence on the AC copper losses.

In [127, 128], a method has been proposed for estimation of the effective resistance of a rectangular conductor by solving a Phasor-form diffusion equation formulated in terms of current density and solved in Cartesian coordinates whereas a similar problem but in 1-D is solved in [103]. In both aforementioned references only a single slot is considered in the analysis and the influence of the PM field is not considered.

In [129-131], based on a vector potential formulation, sub-domains field solution is proposed to predict the performance of PM machines. Based on that solution, resistance limited eddy-current loss was calculated in [98, 118] for open slot configuration. This method was improved in [132] for semi-open slot configurations. These resistance limited eddy-current prediction methods which are only valid for round and bar type conductors are limited for resistance limited eddy-current loss and cannot be used to calculate inductance limited eddy-current loss. Thus, an accurate analytical model which accounts for AC losses are necessary, particularly for vertically placed conductors where the skin depth in the radial direction is smaller than the conductor height.

In this chapter, a novel analytical methodology is presented based on subdomain field model to calculate eddy current loss for both RCW and VSW in surface mounted, radial flux, PM machines considering eddy current reaction effect. The adopted approach consists to first solve the two-dimensional magneto-static problem based on Laplace’s and Poisson’s equations using the separation of variables technique for each of the following sub-domains: PM, air gap, slot-opening and slot. Then, based on that solved solution, by defining the tangential magnetic field (H_t) at the slot opening radius Helmholtz’ equation is solved in the slot sub-domain. The current density distribution is derived from the time-harmonic vector potential solution and the eddy current loss is consequently calculated. The validity and accuracy of the model is verified using FE analysis. Finally, we discuss the limitations of the proposed approach.

5.2. Resolution of the magneto-static field problem

A three-phase, 12-slot 14-pole concentrated wound FT-PM machine (Figure 5.1) is considered for illustration and as a case study. The geometrical parameters are the rotor yoke inner radius R_1, the permanent magnets outer surface radius R_2, the stator inner radius R_3 and the inner and outer radii of the slot R_4 and R_5, respectively.

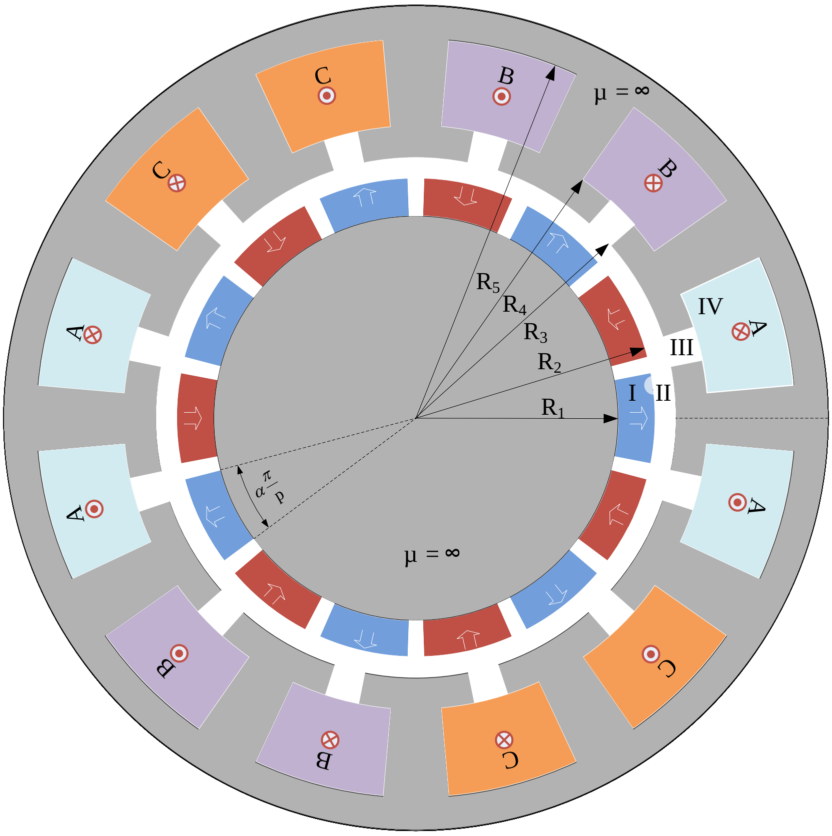

Figure 5.1 Geometric representation of the considered 12-slot/14-pole FT-PM machine

The machine has Q number of semi-open slots and each slot is represented with subscripts j and the related slot-opening is given with subscripts i. The subscripts i and j are always equivalent and they are given as follows:

i, i = 1, 2,..........Q

j, j = 1, 2,..........Q

The angular position of the ith slot-opening is defined as

$$\theta_i = -\frac{\beta}{2} + \frac{2\pi i}{Q} \quad \text{with } 1 \le i \le Q \tag{5.1}$$

where, β is slot-opening angle and other geometric parameters are represented in Figure 5.1.

The modelling methodology is built upon the following assumptions:

1. the machine has a polar geometry as shown in Figure 5.1;
2. the stator and rotor material has an infinite permeability and null conductivity;
3. the magnets are magnetized in the radial direction and their relative recoil permeability is unity ($\mu_r = 1$);
4. the end-effects are neglected and thus the magnetic vector potential has only one component along the z direction and it only depends on the polar coordinates r and θ.

In order to establish the exact analytical model, the cross-sectional area of the machine is divided into four sub-domains (Figure 5.1):

1. rotor PM sub-domain (A_I – region I)
2. air gap sub-domain (A_{II} – region II)
3. slot opening sub-domain (A_i – region III)
4. stator slot sub-domain (A_j – region IV)

where, A represents the Z-component of the magnetic vector potential .

The magneto-static partial differential equations (PDE) governing in the different sub-domains derived from Maxwell's equations and formulated in terms of vector potential are

$$\begin{cases} \frac{\partial^2 \mathrm{A_I}(\mathrm{r},\theta)}{\partial \mathrm{r}^2} + \frac{1}{\mathrm{r}}\frac{\partial \mathrm{A_I}(\mathrm{r},\theta)}{\partial \mathrm{r}} + \frac{1}{\mathrm{r}^2}\frac{\partial^2 \mathrm{A_I}(\mathrm{r},\theta)}{\partial \theta^2} = \frac{-\mu_\mathrm{o}}{\mathrm{r}}\frac{\partial \mathrm{M_r}(\theta)}{\partial \theta} \\ \frac{\partial^2 \mathrm{A_{II}}(\mathrm{r},\theta)}{\partial \mathrm{r}^2} + \frac{1}{\mathrm{r}}\frac{\partial \mathrm{A_{II}}(\mathrm{r},\theta)}{\partial \mathrm{r}} + \frac{1}{\mathrm{r}^2}\frac{\partial^2 \mathrm{A_{II}}(\mathrm{r},\theta)}{\partial \theta^2} = 0 \\ \frac{\partial^2 \mathrm{A_i}(\mathrm{r},\theta)}{\partial \mathrm{r}^2} + \frac{1}{\mathrm{r}}\frac{\partial \mathrm{A_i}(\mathrm{r},\theta)}{\partial \mathrm{r}} + \frac{1}{\mathrm{r}^2}\frac{\partial^2 \mathrm{A_i}(\mathrm{r},\theta)}{\partial \theta^2} = 0 \\ \frac{\partial^2 \mathrm{A_j}(\mathrm{r},\theta)}{\partial \mathrm{r}^2} + \frac{1}{\mathrm{r}}\frac{\partial \mathrm{A_j}(\mathrm{r},\theta)}{\partial \mathrm{r}} + \frac{1}{\mathrm{r}^2}\frac{\partial^2 \mathrm{A_j}(\mathrm{r},\theta)}{\partial \theta^2} = -\mu_\mathrm{o}\,\mathrm{J_c}. \end{cases} \tag{5.2}$$

(5.2) can be solved using the separation of variables technique [133]. For the sake of clarity the following notations are adopted henceforward.

$$\mathrm{P_z}(\mathrm{x, y}) = \left(\frac{\mathrm{x}}{\mathrm{y}}\right)^{\mathrm{z}} + \left(\frac{\mathrm{y}}{\mathrm{x}}\right)^{\mathrm{z}} \tag{5.3}$$

$$\mathrm{E_z}(\mathrm{x, y}) = \left(\frac{\mathrm{x}}{\mathrm{y}}\right)^{\mathrm{z}} - \left(\frac{\mathrm{y}}{\mathrm{x}}\right)^{\mathrm{z}} \tag{5.4}$$

5.2.1. Solution in the slot-opening sub-domain

As shown in Figure 5.2, in order to solve the governing Laplace's equation (5.5) in the i$^{\mathrm{th}}$ slot domain the boundary and interface conditions have to be defined.

$$\frac{\partial^2 \mathrm{A_i}(\mathrm{r},\theta)}{\partial \mathrm{r}^2} + \frac{1}{\mathrm{r}}\frac{\partial \mathrm{A_i}(\mathrm{r},\theta)}{\partial \mathrm{r}} + \frac{1}{\mathrm{r}^2}\frac{\partial^2 \mathrm{A_i}(\mathrm{r},\theta)}{\partial \theta^2} = 0 \ \text{ for } \begin{cases} \mathrm{R_3} \le \mathrm{r} \le \mathrm{R_4} \\ \theta_\mathrm{i} \le \theta \le \theta_\mathrm{i} + \beta \end{cases} \tag{5.5}$$

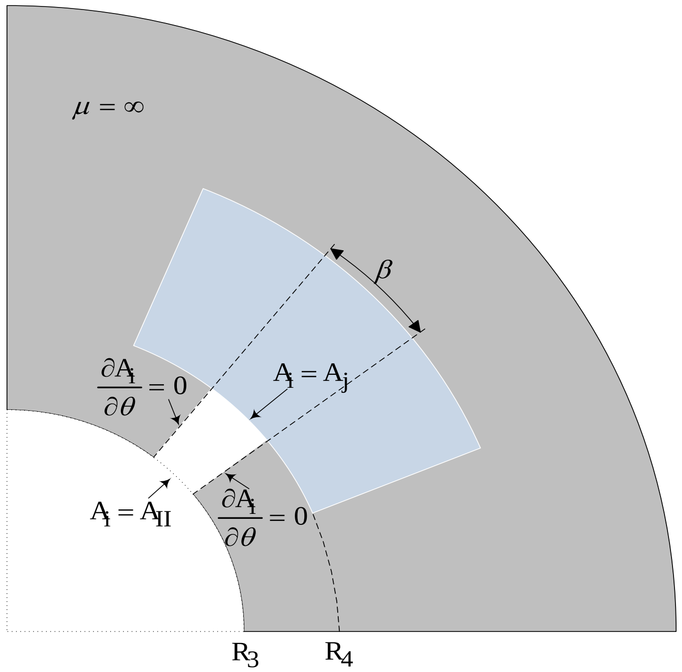

Figure 5.2 The slot-opening sub-domain and associated boundary conditions

The tangential component of the magnetic flux density at the walls of the slot-opening is null since the core permeability is assumed to be infinite. Hence, the associated boundary conditions are:

$$\left.\frac{\partial A_i(r,\theta)}{\partial \theta}\right|_{\theta = \theta_i} = 0$$

$$\left.\frac{\partial A_i(r,\theta)}{\partial \theta}\right|_{\theta = \theta_i + \beta} = 0 \tag{5.6}$$

The interface conditions between the slot sub-domain and the airgap sub-domain is:

$$A_I(R_3,\theta) = A_{II}(R_3,\theta)$$
$$A_I(R_4,\theta) = A_j(R_4,\theta) \qquad (5.7)$$

Now, (5.5) can be solved by the separation variable technique [133]. The principle of separation of variables technique consists to write the solution as a product of two functions:

$$A_I(r,\theta) = h(r)\,\xi(\theta) \qquad (5.8)$$

Introducing a separation constant (λ) [133] in (5.8) leads to the following two ordinary differential equations:

$$\xi'' - \lambda\xi = 0 \qquad (5.9)$$

$$r^2h'' + rh' + \lambda h = 0 \qquad (5.10)$$

Using the boundary conditions (5.6), the eigen values and the eigen functions of (5.9) can be evaluated [133]:

$$\lambda_0 = 0$$
$$\lambda_k = -\left(\frac{k\pi}{\beta}\right)^2 \text{ with } k = 1, 2.....K \qquad (5.11)$$

where, k represents the harmonic order. The eigen functions corresponding to λ_0, and λ_k are given as follows:

$$\xi_0(\theta) = 1$$
$$\xi_k(\theta) = \cos\left(\frac{k\pi}{\beta}(\theta - \theta_i)\right) \qquad (5.12)$$

Using λ_o, and λ_k, the solution of the differential equation (5.10) is given by:

$$\begin{aligned} h_0(r) &= A_o + B_o \ln(r) \\ h_k(r) &= A_k\, r^{-\frac{k\pi}{\beta}} + B_k\, r^{\frac{k\pi}{\beta}} \end{aligned} \tag{5.13}$$

Hence, the general solution of (5.5) can be obtained by multiplying (5.12) and (5.13).

$$\begin{aligned} A_I(r,\theta) = A_o^i + B_o^i \ln(r) + \sum_{k=1}^{\infty} \left(A_k^i\, r^{-\frac{k\pi}{\beta}} + B_k^i\, r^{\frac{k\pi}{\beta}} \right) \\ \times \cos\left(\frac{k\pi}{\beta} \left(\theta - \theta_i\right) \right) \end{aligned} \tag{5.14}$$

Taking into account the boundary conditions (5.6) the interface conditions (5.7) and adopting the notations (5.3) and (5.4) the general solution (5.14) can be written as:

$$\begin{aligned} A_I(r,\theta) = A_o^i + B_o^i \ln(r) \\ + \sum_{k=1}^{\infty} \left(A_k^i \frac{E_{k\pi/\beta}(r,R_4)}{E_{k\pi/\beta}(R_3,R_4)} - B_k^i \frac{E_{k\pi/\beta}(r,R_3)}{E_{k\pi/\beta}(R_3,R_4)} \right) \\ \times \cos\left(\frac{k\pi}{\beta} \left(\theta - \theta_i\right) \right) \end{aligned} \tag{5.15}$$

The constants A_o^i, B_o^i, A_k^i and B_k^i are evaluated using Fourier series expansions of the slot magnetic vector potential $A_j(r,\theta)$ and the airgap magnetic vector potential $A_{II}(r,\theta)$ over the slot-opening interval:

$$A_o^i + B_o^i \ln(R_3) = \frac{1}{\beta} \int_{\theta_i}^{\theta_i+\beta} A_{II}(R_3,\theta)\, d\theta \tag{5.16}$$

$$A_o^i + B_o^i \ln(R_4) = \frac{1}{\beta}\int_{\theta_i}^{\theta_i+\beta} A_j(R_4,\theta)\, d\theta \qquad (5.17)$$

$$A_k^i = \frac{2}{\beta}\int_{\theta_i}^{\theta_i+\beta} A_{II}(R_3,\theta)\cos\left(\frac{k\pi}{\beta}\left(\theta-\theta_i\right)\right) d\theta \qquad (5.18)$$

$$B_k^i = \frac{2}{\beta}\int_{\theta_i}^{\theta_i+\beta} A_j(R_4,\theta)\cos\left(\frac{k\pi}{\beta}\left(\theta-\theta_i\right)\right) d\theta \qquad (5.19)$$

In a similar manner the field equations (5.2) corresponding to other domains: airgap, slot and PM can be solved (see Appendix E). The expansions of the coefficients A_o^i, B_o^i, A_k^i and B_k^i are also given in Appendix E. The computation of the coefficients in the different sub-domains has been done numerically using Matlab® by solving a system of linear equations; the detailed solving process is given in Appendix E.

5.2.2. Eddy current loss calculation

The obtained magnetic vector potential in the slot sub-domain is used to predict the eddy current loss in each conductor. At this stage, an assumption is made that the windings conductors are designed to have a diameter less than the skin depth, and thus the induced eddy current in these conductor is only resistance limited. Hence, the eddy current density J_e in the conductor can be expressed as [117]

$$J_e = -\sigma \frac{\partial A_j}{\partial t} + C(t) \qquad (5.20)$$

where, σ is electric conductivity of conductive medium in the slot (in this case, it is copper, $\sigma = \sim 5.77 \times 10^7$ S/m) . The constant C which is a function of time is introduced to ensure that the total current flowing through each conductor is equal to the source current [117]. Hence, the total copper losses over a fundamental electrical period in a conductor can be obtained by

$$P = \frac{\omega l_{stk}}{2\pi\sigma} \int_{r_{c1}}^{r_{c2}} \int_{\theta_{c1}}^{\theta_{c2}} \int_{0}^{2\pi/\omega_o} \left(J_e + J_c\right)^2 r\, dt\, d\theta\, dr \tag{5.21}$$

where, ω is the electrical speed, l_{stk} is axial active length of the conductor and r_{c1}, r_{c2}, θ_{c1}, θ_{c2} are the inner and outer radius of the conductor and the angular position of the conductor tangential extremities, respectively.

SPECIFICATIONS	VALUE
Number of pole pairs (p)	7
Number of stator slots (Q)	12
Number of turns per phase (N_{ph})	90
Current density (J_{rms}) assuming a unity fill	1.89 A/mm^2
Remanence flux density of the PM (B_{rem})	1.08 T
Inner radius of the rotor yoke (R_1)	27.50 mm
Stator inner radius (R_3)	31.50 mm
Stator outer radius (R_5)	50.00 mm
Magnet depth (R_2-R_1)	3.00 mm
Tooth-tip height (R_4-R_3)	2.50 mm
Depth of stator back iron	4.00 mm
Axial length (l_{stk})	100.00 mm
Slot width angle *(δ)*	20
Slot opening angle *(β)*	3
Magnet span to pole pitch ratio *(α)*	0.85
Rated speed (ω)	2000 rpm

Table 5-1 Specifications of the 12-slot/ 14-pole PM machine

5.2.3. Results and comparison with FE calculation

In order to confirm the effectiveness of the analytical model, FE verification is carried out for a 12-slot/14-pole PM machine; its parameters are given in Table 5-1. In FE analysis, a nonlinear BH characteristic of non-oriented silicon steel (M250-35A) is used since the considered machine is not influenced by saturation at rated condition. The influence of non-linearity in the computation is discussed in section 5.3.4.2.

The mesh refinement has been done for each sub-domain until convergent results were obtained. 2D FE transient with motion simulations were carried out for the whole cross-section of the machine by imposing the rated current into each phase winding with its corresponding phase shift.

In the computation of the magnetic vector potential different numbers of harmonic terms were used for different sub-domains: n terms in the airgap and PM sub-domains, k terms in the slot-opening sub-domain and m terms in the slot sub-domain. Initially the analytical solution is computed with 100 harmonic terms for each sub-domain solution index. The accuracy of the solution depends on the finite number of harmonic terms. A good accuracy is obtained with 30 harmonic terms for each sub-domain solution index. A good accuracy is obtained with the adopted number of harmonic terms after a sensitivity analysis was performed.

Figure 5.3 shows the analytical and FE radial and tangential components of the flux density in the bottom of the slot sub-domain; the results are in a good agreement. However one can notice a slight discrepancy which may originate from numerical errors of the analytical tool. These issues are discussed in section 5.4.

The loss evaluation is carried out for both the RCW and VSW type windings. In order to evaluate the total copper losses in RCW the slot of the considered machine is segmented into N (N = 45) conductors of equal cross sectional area as illustrated in Figure 5.4. In turn, each conductor is divided equally into 7 segments radially and 7 segments tangentially (49 elements) and the vector potential in each sub-element is collected for numerical computation of the copper losses.

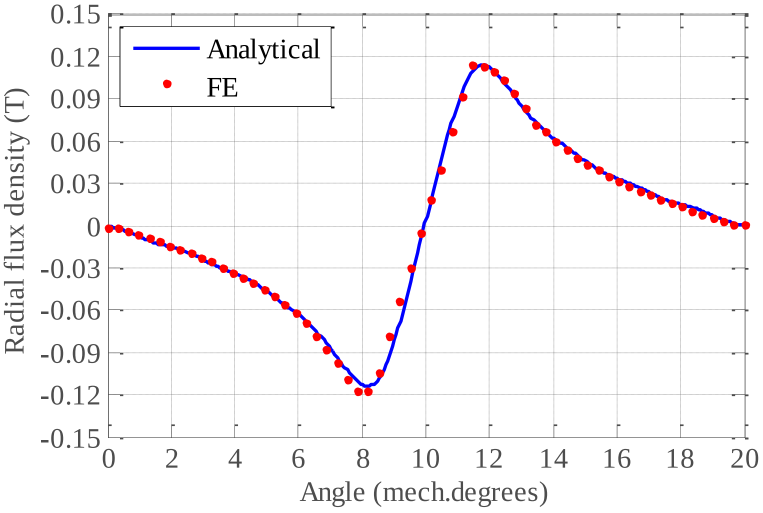

(a)

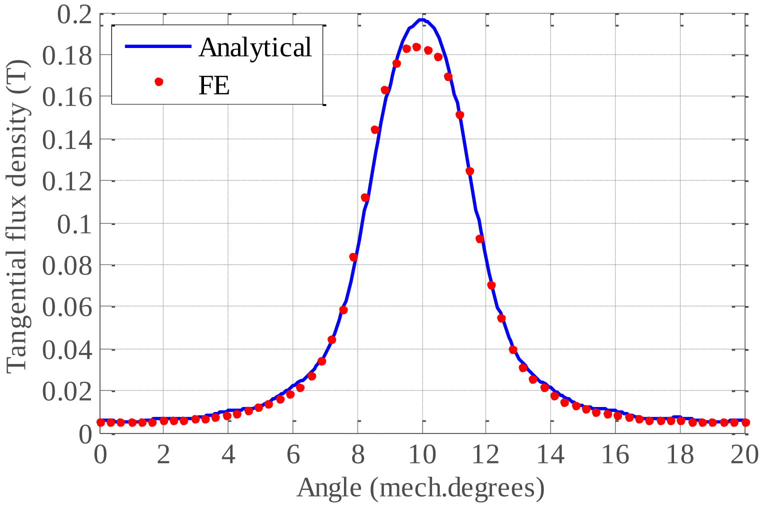

(b)

Figure 5.3 (a) Radial and (b) tangential component of the flux density in the bottom (r = 34.5mm) of the slot sub-domain at load condition (J_{rms} = 1.89 A/mm^2)

The calculated copper losses for different frequencies and its FE counterpart are plotted in Figure 5.5. The two results clearly show that there is a good agreement; however they start to diverge slightly above a certain frequency (~350Hz for the considered machine). This is due to the skin effect phenomena where the conductor’s depth exceeds the limit of the skin depth (3.5 mm) at the frequency of operation. In the operation over this frequency range, the eddy current reaction effect become significant and, in fact, slightly reduces the total copper losses as shown in Figure 5.5. For the studied machine the relative overestimation at twice the value of rated frequency (f_{rated} = 233.33 Hz) is 6% which is an acceptable value. However, this discrepancy depends on the depth of the conductor and thus, the loss prediction method is only valid if the diameter of the conductors is less than the skin depth within the operating frequency range.

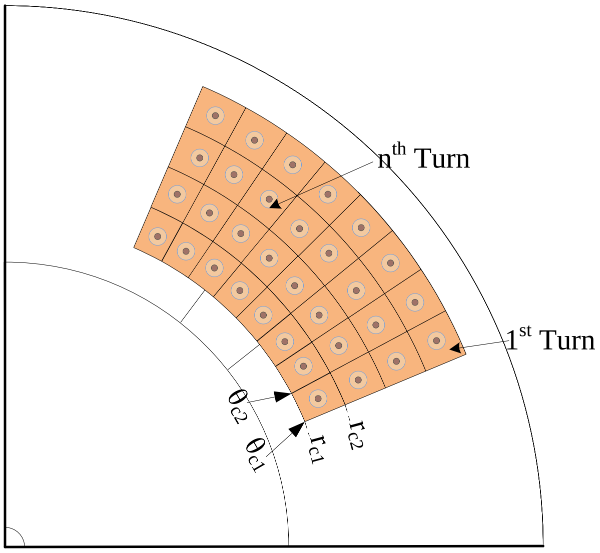

Figure 5.4 Representation of n numbers of RCW conductors in the j^{th} slot sub-domain

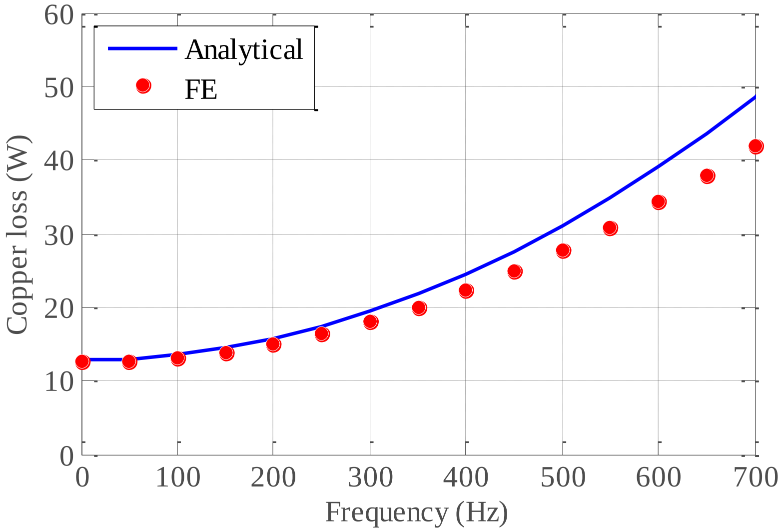

Figure 5.5 Magneto static field solution based and FE calculated RCW machine copper loss vs. frequency

For the VSW the slot of the considered machine is vertically segmented into N (N = 45) conductors. The segmentation of the VSW conductors is illustrated in Figure 5.6. Each conductor is divided equally into 50 segments radially and 3 segments tangentially (150 elements) and the vector potential in each element is collected for numerical computation of the copper losses.

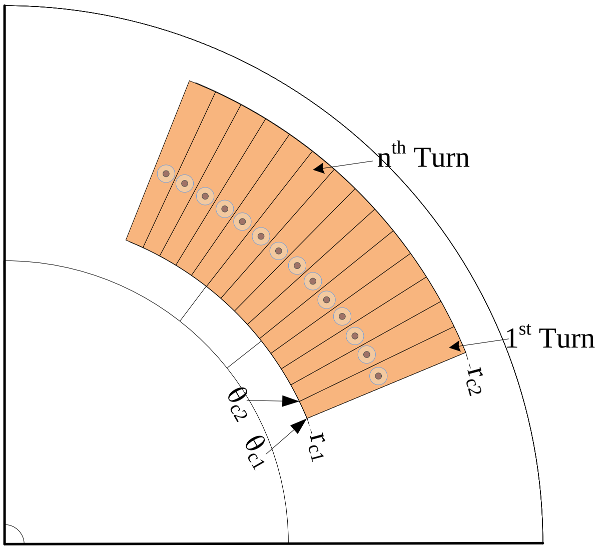

Figure 5.6 Representation of VSW in the j^{th} slot sub-domain

From Figure 5.7, it can be seen that the analytically calculated losses are in a good agreement with its FE counterpart at low frequency and then start to deviate from it beyond 150Hz. This is manifestly due to the eddy current reaction effect as the field produced by the eddy current opposes the field from which these eddy currents stem (Lenz's law). In fact this phenomenon reduces the total copper losses as can be noticed in Figure 5.7, It is clearly demonstrated that the eddy current reaction effect plays a vital role at high frequencies in such a winding structures since the conductors have a higher (depth of 11.5 mm) than the skin depth (5.4 mm) for the frequencies higher than the breakpoint between the analytical and FE results. It is worth noting that this breakpoint frequency (150Hz) is much lower than the one of the RCW (350Hz) for the machine considered while the nominal frequency is 233Hz. It is therefore well justified to investigate another approach of estimating analytically eddy currents in VSW; this is the subject of the next section.

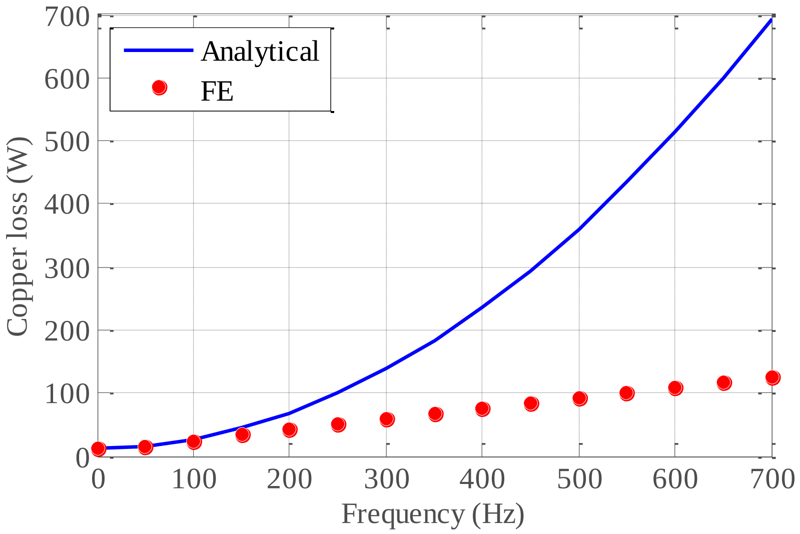

Figure 5.7 Magneto static field solution based and FE calculated VSW machine copper losses vs frequency

5.3. Resolution of the time harmonic diffusion equation in the slot domain

In order to estimate the copper losses considering high frequency eddy currents reaction effect when adopting the VSW, building upon the magneto-static field solution a time-harmonic problem (Phasor-form diffusion equation or Helmholtz' equation) is formulated in the domain of interest for copper losses calculation which is the slot domain. This approach uses to the solution of the magneto static problem at the slot opening upper radius ($r = R_4$) as the boundary condition ($\overline{D_j}$ in complex representation) of the time–harmonic problem in the slot domain, as illustrated in Figure 5.8. The boundary condition $\overline{D_j}$ represents in fact an equivalent current distribution across the slot opening. This approach assumes that the field in the slot domain is dominantly sinusoidal and so the effect of higher order field harmonics is negligible.

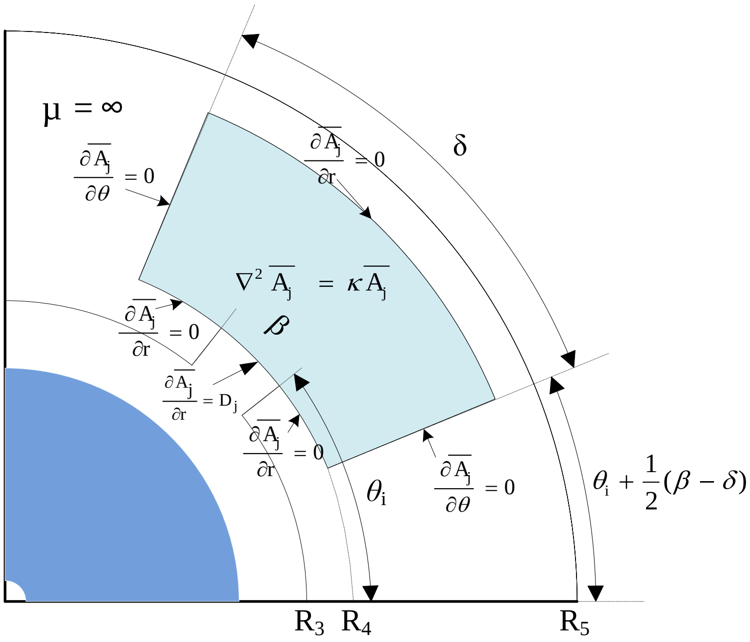

Figure 5.8 j^{th} slot sub domain and associated boundary conditions

Hence, eddy current distribution can be obtained by solving the Phasor-form diffusion equation only in the slot. At this stage, it is important to highlight that the slot conductive area is considered as a single bulk conductor. This assumption is quite plausible in the case of VSW (where each plate conductor occupies almost the entire height of the slot) as the leakage flux, responsible for eddy currents, crosses the conductors in the circumferential direction as they do across a bulk conductor as shown in Figure 5.9.

The following complex notation is used considering that the magnetic vector potential varies sinusoidally with time at an angular frequency ω:

$$d_j(R_4,\theta,t) = \mathrm{Re}[\overline{D_j}(R_4,\theta)e^{j\omega t}] \tag{5.22}$$

$$a_j(r,\theta,t) = \mathrm{Re}[\overline{A_j}(r,\theta)e^{j\omega t}] \tag{5.23}$$

where, Re denotes the real part of the complex number and j = √-1 .

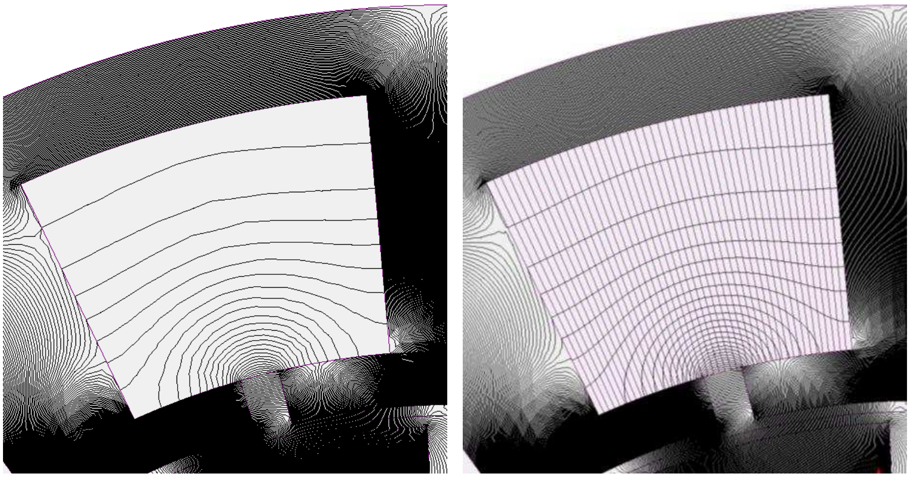

(a) (b)

Figure 5.9 Leakage-flux distribution across (a) a bulk conductor and (b) segmented VSW

5.3.1. Boundary condition from the quasi static solution

As can be seen in Figure 5.8, $\overline{D_j}$ corresponds to the continuity of the tangential component of the magnetic field between the j^th^ slot sub-domain and the i^th^ slot-opening sub-domain and thus, the boundary condition at $r = R_4$ is given by

$$\overline{D_j}(R_4,\theta) = \left.\frac{\partial \overline{A_j}}{\partial r}\right|_{r=R_4} = \begin{cases} \left.\dfrac{\partial A_i}{\partial r}\right|_{r=R_4} & \forall\ \theta \in [\theta_i, \theta_i+\beta] \\ 0 & \text{elsewhere} \end{cases} \qquad (5.24)$$

Hence, the boundary condition $\overline{D_j}$ can be written considering the magneto static field solution in the slot opening sub domain:

$$\overline{D_j}(R_4,\theta) = \frac{B_o^{\,i}}{R_4} + \sum_{k=1}^{\infty}\left(A_k^{\,i}\frac{2}{E_{k\pi/\beta}(R_3,R_4)} - B_k^{\,i}\frac{P_{k\pi/\beta}(R_4,R_3)}{E_{k\pi/\beta}(R_3,R_4)}\right) \times \cos\left(\frac{k\pi}{\beta}\left(\theta-\theta_i\right)\right) \qquad (5.25)$$

Here, it is worth noting that the boundary condition $\overline{D_j}$ can be obtained alternatively using the magneto-static solution in the slot sub-domain since the slot and slot opening sub-domains share a common interface at r = R4. The solution in the slot opening sub domain is chosen for simplicity.

5.3.2. Solution of the time-harmonic equation in the J^th slot

The jth slot domain and the associated boundary conditions are shown in Figure 5.8. The Phasor-form vector potential diffusion equation (Helmholtz' equation) in the slot domain is

$$\frac{\partial^2 \overline{A_j}}{\partial r^2} + \frac{1}{r}\frac{\partial \overline{A_j}}{\partial r} + \frac{1}{r^2}\frac{\partial^2 \overline{A_j}}{\partial \theta^2} - j\omega\sigma\mu_o \overline{A_j} = 0 \tag{5.26}$$

Since the stator iron has infinite permeability, the tangential components of the magnetic field at the slot walls are null. Hence, the boundary conditions are given by,

$$\left.\frac{\partial \overline{A_j}}{\partial \theta}\right|_{\theta = \theta_i + \frac{1}{2}(\beta - \delta)} = 0 \qquad \left.\frac{\partial \overline{A_j}}{\partial \theta}\right|_{\theta = \theta_i + \frac{1}{2}(\beta + \delta)} = 0 \tag{5.27}$$

$$\left.\frac{\partial \overline{A_j}}{\partial r}\right|_{r = R_5} = 0 \tag{5.28}$$

Taking into account the boundary condition (5.27) the general solution of (5.26) is given by [120]

$$\begin{aligned}\overline{A_j}(r,\theta) = {} & \overline{A_o}^{\,j} J_o(\kappa r) + \overline{B_o}^{\,j} Y_o(\kappa r) \\ & + \sum_{m=1}^{\infty}\left(\overline{A_m}^{\,j} J_{m\pi/\delta}(\kappa r) + \overline{B_m}^{\,j} Y_{m\pi/\delta}(\kappa r)\right) \\ & \times \cos\left(\frac{m\pi}{\delta}\left[\theta - \theta_i - \frac{1}{2}(\beta - \delta)\right]\right)\end{aligned} \tag{5.29}$$

where, $\kappa=\sqrt{-\mathrm{j}\omega\sigma\mu_{\mathrm{o}}}$, $\mathrm{J}_{\mathrm{m}\pi/\delta}$ is the Bessel function of the first kind, and order $\mathrm{m}\pi/\delta$ and $\mathrm{Y}_{\mathrm{m}\pi/\delta}$ is the Bessel function of the second kind.

Considering the boundary conditions (5.24) and (5.27), (5.29) can be simplified with two coefficients $\overline{\mathrm{C}_{\mathrm{o}}{}^{\mathrm{j}}}$ and $\overline{\mathrm{C}_{\mathrm{m}}{}^{\mathrm{j}}}$ as follows:

$$\begin{aligned}\overline{\mathrm{A}_{\mathrm{j}}}(\mathrm{r},\theta) = \overline{\mathrm{C}_{\mathrm{o}}{}^{\mathrm{j}}}\left(\frac{\mathrm{J}_{\mathrm{o}}(\kappa\mathrm{r}) - \overline{\mathrm{F}_1}\mathrm{Y}_{\mathrm{o}}(\kappa\mathrm{r})}{-\kappa\mathrm{J}_1(\kappa\mathrm{R}_4) + \kappa\overline{\mathrm{F}_1}\mathrm{Y}_1(\kappa\mathrm{R}_4)}\right) \\ + \sum_{\mathrm{m}=1}^{\infty}\overline{\mathrm{C}_{\mathrm{m}}{}^{\mathrm{j}}}\left(\frac{\mathrm{J}_{\mathrm{m}\pi/\delta}(\kappa\mathrm{r}) - \overline{\mathrm{F}_{\mathrm{m}}}\mathrm{Y}_{\mathrm{m}\pi/\delta}(\kappa\mathrm{r})}{\mathrm{J}'_{\mathrm{m}\pi/\delta}(\kappa\mathrm{R}_4) - \overline{\mathrm{F}_{\mathrm{m}}}\mathrm{Y}'_{\mathrm{m}\pi/\delta}(\kappa\mathrm{R}_4)}\right) \\ \times\cos\left(\frac{\mathrm{m}\pi}{\delta}\left[\theta - \theta_{\mathrm{i}} - \frac{1}{2}(\beta - \delta)\right]\right)\end{aligned} \tag{5.30}$$

where,

$$\overline{\mathrm{F}_1} = \frac{\mathrm{J}_1(\kappa\mathrm{R}_5)}{\mathrm{Y}_1(\kappa\mathrm{R}_5)} \tag{5.31}$$

$$\overline{\mathrm{F}_{\mathrm{m}}} = \frac{-\kappa\mathrm{J}_{1+\mathrm{m}\pi/\delta}(\kappa\mathrm{R}_5) + \dfrac{\mathrm{m}\pi}{\delta\mathrm{R}_5}\mathrm{J}_{\mathrm{m}\pi/\delta}(\kappa\mathrm{R}_5)}{-\kappa\mathrm{Y}_{1+\mathrm{m}\pi/\delta}(\kappa\mathrm{R}_5) + \dfrac{\mathrm{m}\pi}{\delta\mathrm{R}_5}\mathrm{Y}_{\mathrm{m}\pi/\delta}(\kappa\mathrm{R}_5)} \tag{5.32}$$

$$\mathrm{J}'_{\mathrm{m}\pi/\delta}(\kappa\mathrm{R}_4) = -\kappa\mathrm{J}_{1+\mathrm{m}\pi/\delta}(\kappa\mathrm{R}_4) + \frac{\mathrm{m}\pi}{\delta\mathrm{R}_4}\mathrm{J}_{\mathrm{m}\pi/\delta}(\kappa\mathrm{R}_4) \tag{5.33}$$

$$\mathrm{Y}'_{\mathrm{m}\pi/\delta}(\kappa\mathrm{R}_4) = -\kappa\mathrm{Y}_{1+\mathrm{m}\pi/\delta}(\kappa\mathrm{R}_4) + \frac{\mathrm{m}\pi}{\delta\mathrm{R}_4}\mathrm{Y}_{\mathrm{m}\pi/\delta}(\kappa\mathrm{R}_4) \tag{5.34}$$

The coefficients $\overline{\mathrm{C}_{\mathrm{o}}{}^{\mathrm{j}}}$ and $\overline{\mathrm{C}_{\mathrm{m}}{}^{\mathrm{j}}}$ are determined using a Fourier expansion of $\overline{\mathrm{D}_{\mathrm{j}}}$ (R_4,θ) over the slot-opening interval $(\theta_{\mathrm{i}},\ \theta_{\mathrm{i}}+\beta)$.

$$\overline{C_o^{\,j}} = \frac{1}{\delta}\int_{\theta_i}^{\theta_i+\beta} D_j\,(R_4,\theta)\; d\theta \tag{5.35}$$

$$\overline{C_m^{\,j}} = \frac{2}{\delta}\int_{\theta_i}^{\theta_i+\beta} D_j\,(R_4,\theta)\,\cos\left(\frac{m\pi}{\delta}\left[\theta-\theta_i-\frac{1}{2}(\beta-\delta)\right]\right)\; d\theta \tag{5.36}$$

The detailed expansions of the coefficients $\overline{C_o^{\,j}}$ and $\overline{C_m^{\,j}}$ are given in Appendix E.

5.3.3. Eddy current loss estimation from the time-harmonic field solution

The total current density in the conductor can be expressed from the complex magnetic vector potential as

$$\overline{J_t} = -\,j\omega\sigma\,\overline{A_j} \tag{5.37}$$

Thus, the total copper losses in a conductor from the complex current density can be re written as

$$P = \frac{l_{stk}}{2\sigma}\int_{r_{c1}}^{r_{c2}}\int_{\theta_{c1}}^{\theta_{c2}} \left(\overline{J_t}\right).\left(\overline{J_t}\right)^{*}\, r\, d\theta\, dr \tag{5.38}$$

where $\left(\overline{J_t}\right)^{*}$ represents the conjugate complex current density.

5.3.4. Results and comparison with FE

The analytical solution of the magneto static problem is computed with 30 harmonic terms for each sub-domain solution index while 15 harmonic terms are considered in the computation of time harmonic problem in the slot sub-domain. In order to verify the field distribution obtained from the analytical model, 2D time-harmonic FE simulation is carried out in a slot of the machine where the tangential field boundary (H_t) is assigned at the slot opening radius (r

= R_4) using the field obtained from the 2D static FE simulation. The slot opening boundary is segmented into 20 equal elements and each segmented part is considered to have a constant field within its length. The obtained results are compared with the ones analytically calculated.

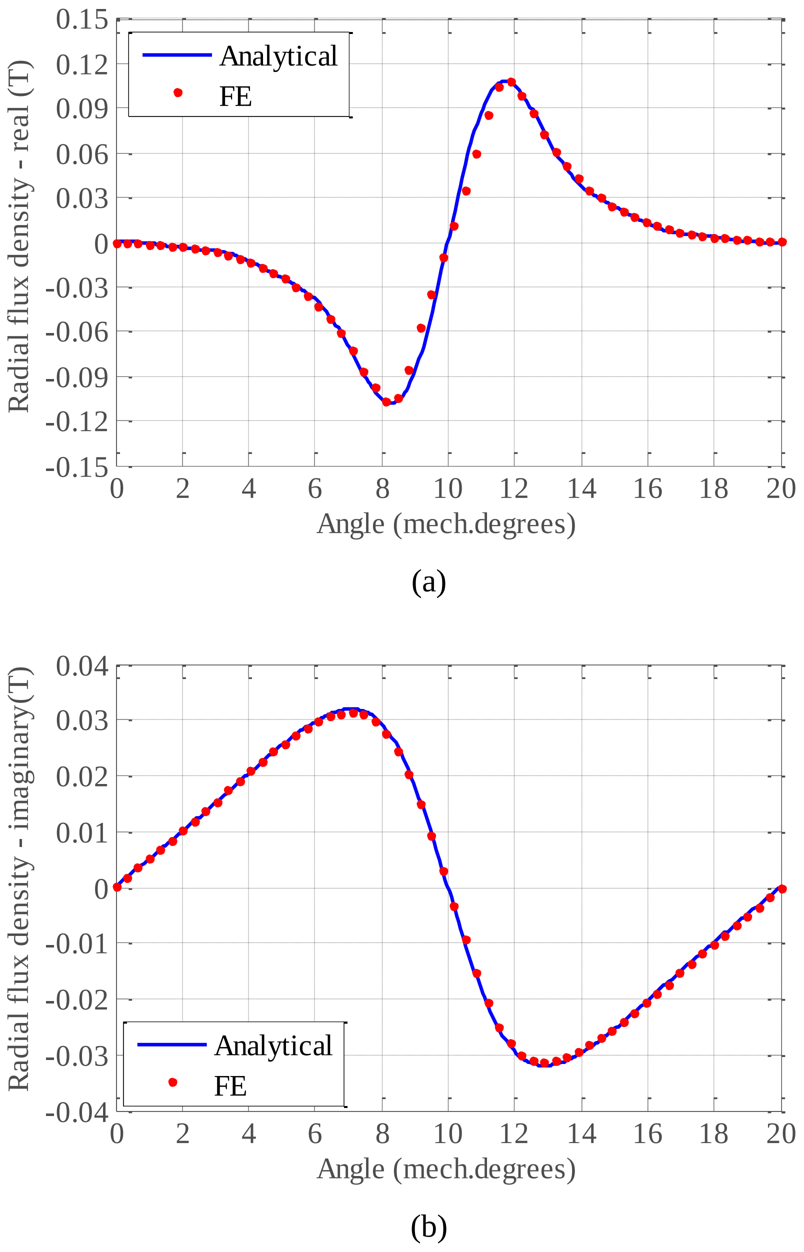

Figure 5.10 (a) Real and (b) imaginary parts of the radial flux density components in the bottom of the slot (r = 34.5mm) at frequency f = 700Hz

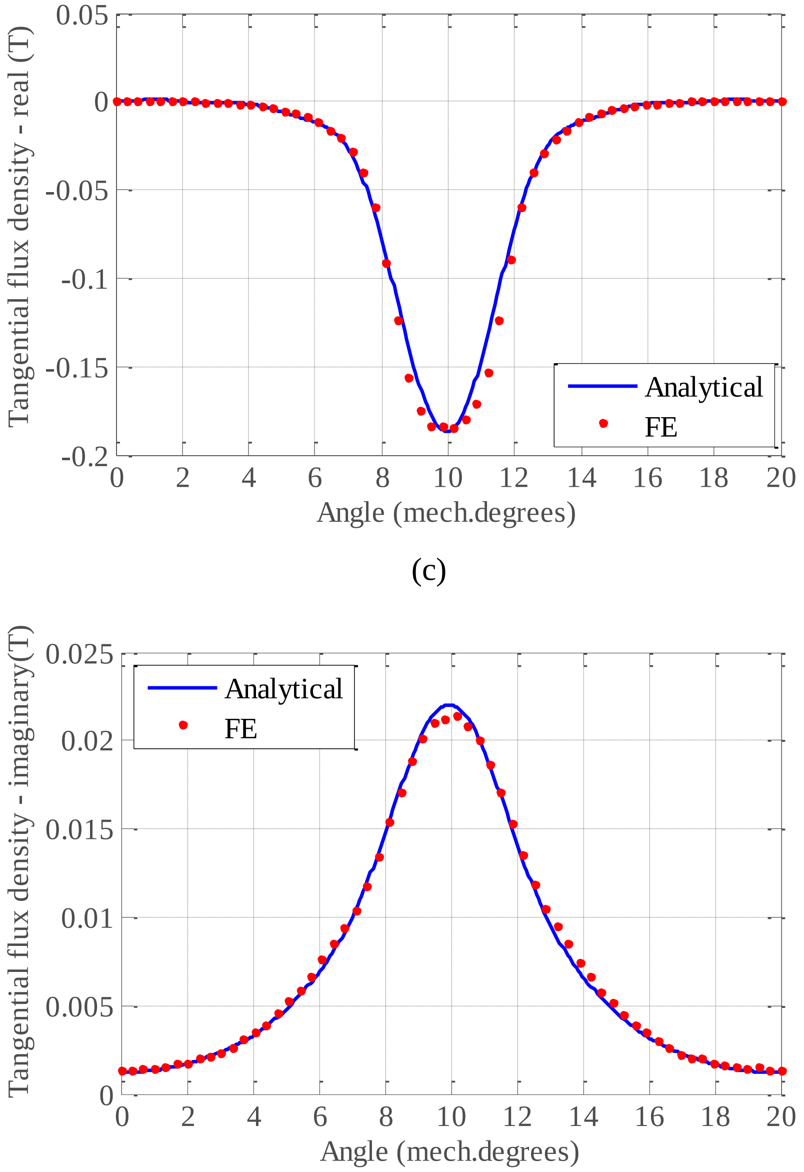

(c)

(d)

Figure 5.11 (a) Real and (b) imaginary parts of the tangential flux density components in the bottom of the slot (r = 34.5mm) at frequency f = 700Hz

Figure 5.10 and Figure 5.11 show both real and imaginary parts of the radial and tangential components of flux density in the bottom of a slot (r = 34.5 mm) of 12-slot 14-pole PM machine along the slot angle (δ) at an excitation frequency f = 700Hz. The obtained results have good agreement with results that were obtained in FE analysis. Fields for different slot position and different frequencies are also gathered and compared. Those results also match with FE. Those are added in the Appendix E.

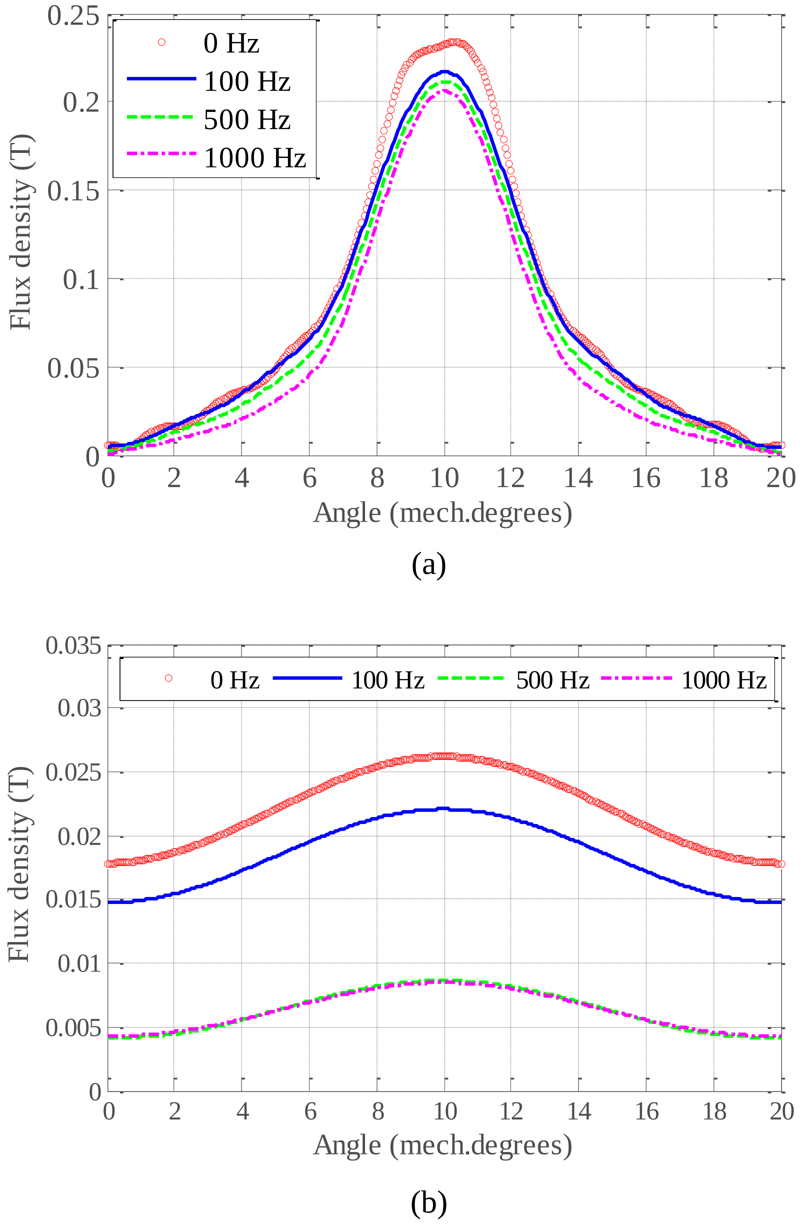

(a)

(b)

Figure 5.12 Time-harmonic field calculation based flux density module vs. frequency in the (a) the bottom (r = 34.5mm) and (b) the middle of the slot (r = 40mm)

Figure 5.12 compares the magnitude of the flux density components at the bottom (r = 34.5 mm) and the middle (r = 40 mm) of the slot for different frequencies. From Figure 5.12, it can be seen that the magnitude of the flux density dramatically decreases as frequency increases and there are not much further changes in the reaction effect after a certain frequency (i.e. ~500Hz). This might however vary with the specific geometry of the machine. These results clearly show that the reaction field is highly influential in the VSW type of winding and its limiting effect on the additional AC losses by opposing the slot leakage flux is significant.

In order to estimate the winding losses including the influence of the PM field as well as considering the conductors in the slot as separate conductive components, 2D FE transient with motion simulations were carried out for the whole cross-section of the machine by imposing the rated current into each phase winding with its corresponding phase shift. Obtained winding losses for different frequencies compared to analytically calculated ones are shown in Figure 5.13.

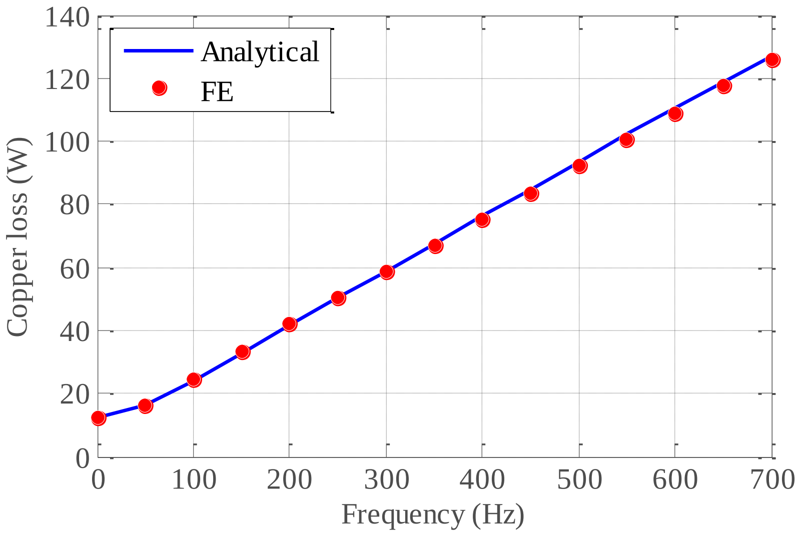

Figure 5.13 Time-harmonic field solution based and FE calculated VSW copper loss vs frequency for the 12-slot 14-pole PM machine

Obtained results have good agreement. The error between the two methods is less than one percent (~0.79%) at frequencies over 400Hz. From these obtained results it can be concluded that proposed analytical method for predicting eddy current losses is effective and quick whilst accounting for the eddy current reaction field. However, it is worth noting that the proposed model is only valid for VSW and cannot be applied for RCW since the AC field distribution of RCW is entirely different from that of VSW. In the computation of the eddy current loss (including skin effect) in RCW, it is necessary to take into account each conductor separately. In these studies importance is not given for the modelling of RCW including skin effect, since they have a depth less than the skin depth at the operating frequencies.

5.3.4.1. Influence of the slot opening

The influence of the slot opening on the losses of VSW is also investigated under nominal operation (ω = 2000rpm and J_{rms} = 1.89 A/mm^2). In FE the results are gathered for five different ratios between the slot opening's length and the complete slot's length. Where, three different conditions are considered: the winding losses due to the load (B_{rem} = 1.08 T and J_{rms} = 1.89 A/mm^2), the winding losses at no-load (B_{rem} = 1.08 T and J_{rms} = 0 A/mm^2) and the winding losses due to armature reaction alone (B_{rem} = 0 T and J_{rms} = 1.89 A/mm^2). In addition, the total winding losses are calculated analytically defining the interface boundary as an equivalent current sheet based on Ampere's theorem (H_t = NI). The obtained results are given in Figure 5.14.

From Figure 5.14, it can be clearly seen that the eddy current loss in the VSW is almost similar for any ratio of the slot opening if the rotor excitation field is neglected. However, the losses are significantly high particularly for large slot openings (i.e. ratio > 0.4) if the rotor excitation field is included. This is due to the increased leakage-flux by the PMs in the case of large slot opening.

The analytical model based on equivalent current sheet obtained from Ampere's theorem predicts the losses accurately for small ratios of slot opening.

However the model would not be effective for the VSW wound machines having larger slot opening since PM highly influences the VSW. These results validate that the proposed analytical model predicts the winding losses of VSW accurately considering PM's field.

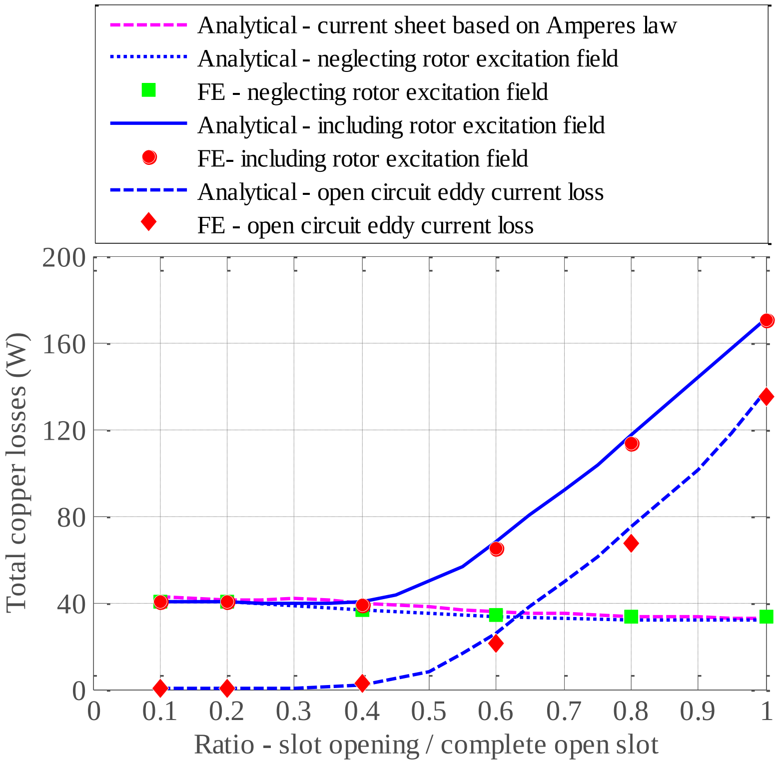

Figure 5.14 Total copper loss vs. slot opening to complete open slot ratio

5.3.4.2. Influence of the magnetic material non-linearity (saturation effects)

Figure 5.15 shows the obtained copper losses for different current loading at the nominal speed of 2000rpm. From the results, it can be seen that the proposed model predicts the losses accurately and the obtained losses starts to diverge at current loadings of five times higher than nominal where the machine heavily saturates. However, the model is applicable at rated operation where the saturation is less significant.

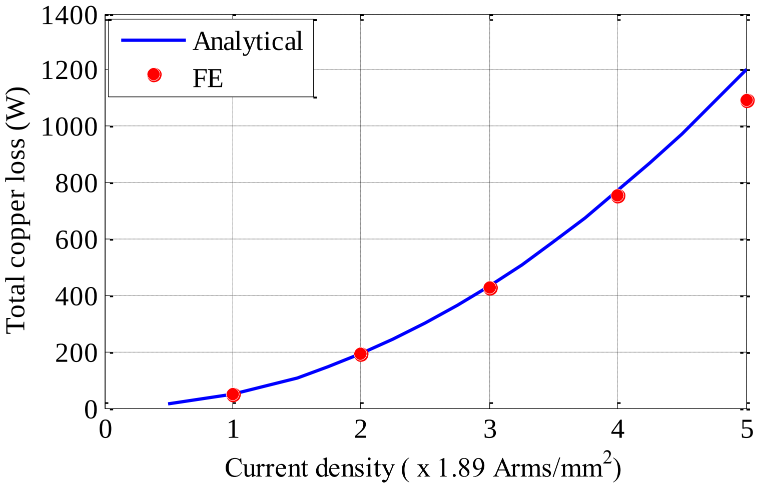

Figure 5.15 Total copper loss vs. current density

5.3.4.3. Influence of conductor segmentation/number of turns

Figure 5.17 show the winding losses obtained for different numbers of circumferential segmentation as illustated in Figure 5.16. In all the cases of segmentations, the DC current density is kept identical. From the results, it can clearly be seen that the obtained total copper losses for more than two segments are almost unchanged. However, the copper losses for a single conductor or two conductors show slightly higher losses than others. This is due to the skin depth of the conductor which induces additional losses. This influence of the skin depth becomes insignificant in the case of more than two turns. These results further validate the analytical model which considers the conductive slot area as a single bulk conductor.

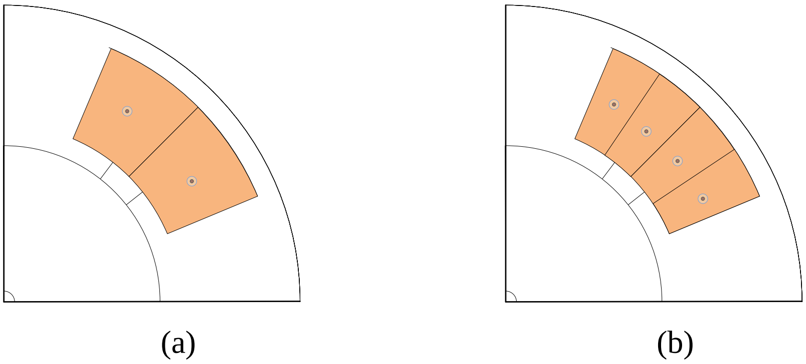
(a) (b)

Figure 5.16 Circumferential segmentation: (a) 2 turns and (b) 4turns

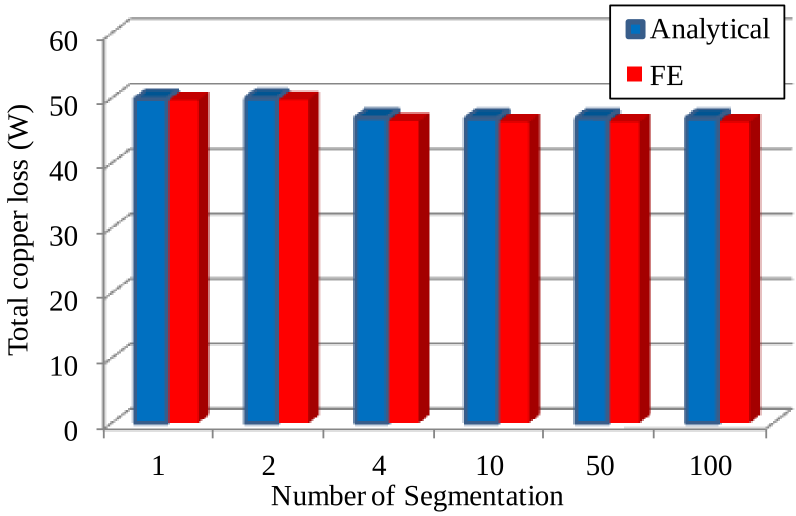

Figure 5.17 Total copper loss vs. numbers of conductor

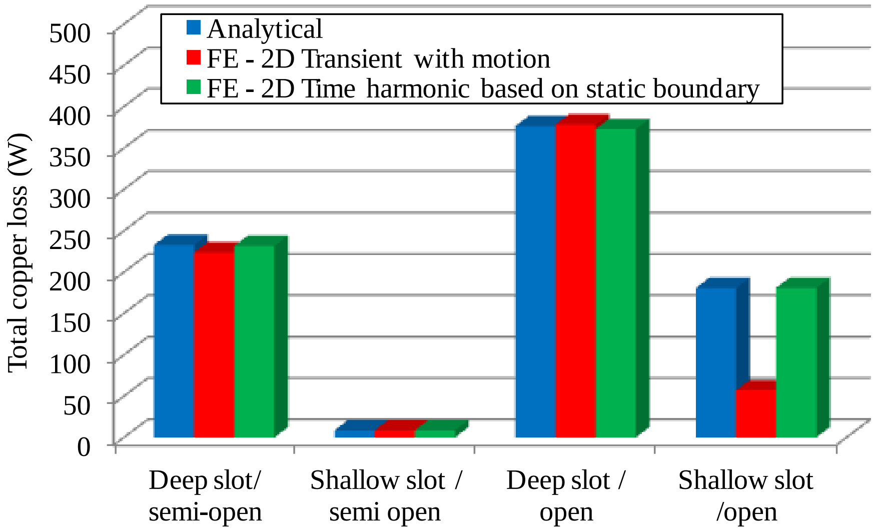

Figure 5.18 Total copper loss vs. different slot configurations

5.3.4.4. Influence of the slot depth

For further validation of the model two different slot geometries are considered: deep slot and shallow slot. The stator inner diameter and rotor geometry are kept identical whilst the outer radius of the stator is varied. In case of deep slot configuration, the slot height of 24 mm (R_5 = 62 mm) is considered whilst shallow slot height is 6mm (R_5 = 44 mm). The losses are calculated at nominal condition (ω = 2000rpm, J_{rms} = 1.89 A/mm^2) for two different slot opening ratios: semi open slot (*β*/*δ* = 0.15) and open slot (*β*/*δ* = 1). Obtained results are given in Figure 5.18.

Analytically calculated results have a good agreement with the solution obtained from 2D FE time harmonic solver considering the static boundary at r = R_4. These results are also in a good agreement with 2D FE transient with motion solution except the case of fully open shallow slot configuration where the analytical model overestimates the losses. This may come from the radial component which becomes significant in open shallow slot arrangement as shown in Figure 5.19.

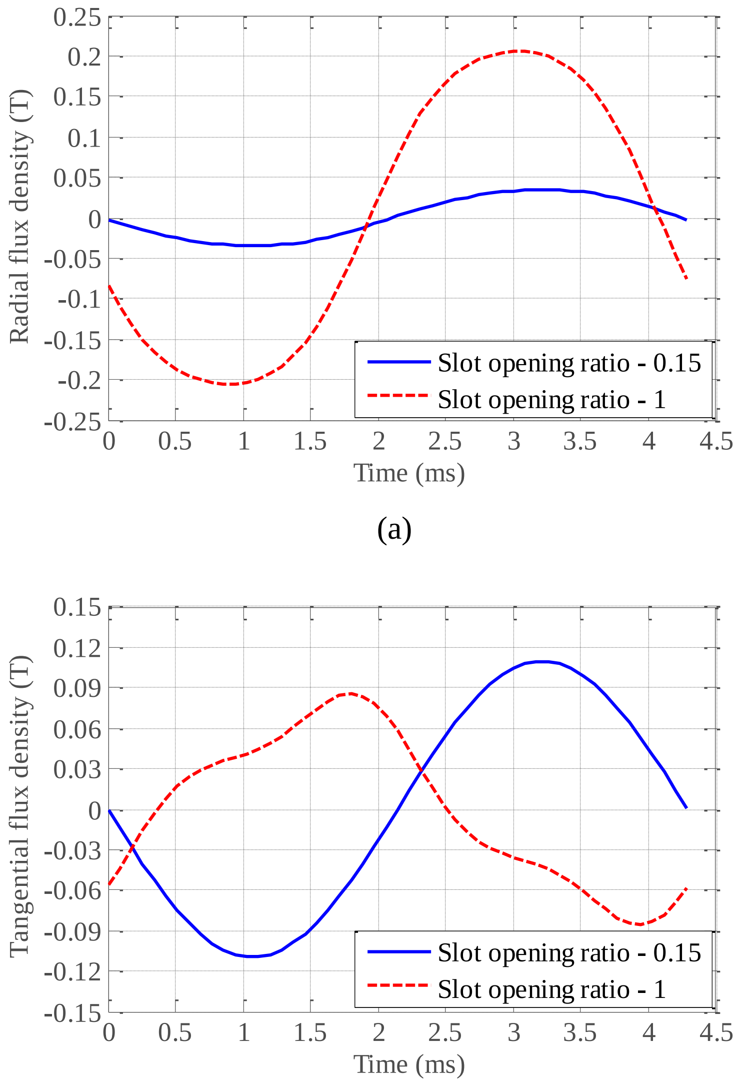

(a)

(b)

Figure 5.19 (a) Radial and (b) tangential flux density component at r = R4 along one electrical cycle for shallow slot configuration

5.4. Discussion on the limitations of the analytical method

It has been mentioned in section 5.3.4 that the accuracy of the results depends on the choice of number of harmonics accounted for. However, the choice of the number of harmonics is generally limited by the computational software capability. From (5.15), it can be seen that the slot boundary $\overline{D_j}$ depends on the slot-opening angle β. When the slot-opening becomes very small, so does the angle β. As a result the power exponent of the corresponding part of the equation gets to a very high value. Therefore, harmonic numbers have to be reduced to obtain a solution. Maintaining the same number of harmonics for very narrow slot-openings will result in non-convergence. The Bessel's function (which is introduced in the time-harmonic problem) also has similar non-convergence issue.

Although the analytical model has some limitations then FE, it provides an alternative solution within less computation time. For instance, calculation of the losses at a given frequency took 3.5s with the analytical model whilst it took over 2 hours with FE using the same computer. It is worth mentioning that the computational time of FE is highly dependent on the machine geometry, the number of mesh elements and the conductor structure (RCW or VSW) whereas the analytical model computational time depends only on the harmonic order, making it therefore fully scalable.

5.5. Conclusion

In this chapter, analytical models to evaluate eddy current loss in VSW surface mounted radial flux PM machines has been proposed. The effectiveness of the proposed method is corroborated by FE. The tool provides a considerable flexibility for parametric studies and design optimization of VSW machines.

In the next chapter, a design optimization of VSW wound PM machine to minimise the AC losses whilst still limiting the resulting SC currents after winding failure is presented. The proposed analytical tool is used to estimate the total copper loss whilst FE calculation is used for other magnetic losses including iron losses in the stator and rotor laminations and eddy current loss in the magnets.

CHAPTER

6

Feasible design solution to AC loss

6.1. **Introduction**

This chapter proposes feasible design solutions to minimise the generated excessive losses in VSW conductors. Two possible solutions are considered: different placement of the VSW conductors in the slot and a parametric design process. Initially, different placements of the VSW conductors are investigated since the AC copper losses can be reduced by avoiding the high flux density region. In addition, the influence of the slot geometry on AC copper losses is also considered.

As an alternative, a parametric design is considered to minimise AC copper losses of the VSW. The design optimization is carried out using both FE and the analytical models proposed in chapters 3 and 5. In the design routine, the analytical models are used to estimate the copper losses and SC fault current whilst FE calculates torque, iron losses and magnet losses. The obtained results are used to find an optimum considering copper losses and SC current limiting capability.

6.2. **Feasible solutions for AC copper losses minimization**

It was shown in chapter 4 (see section 4.2) that high frequency effects are more significant in the VSW due to its placement along the height of the slot;

consequently the losses are higher than for the RCW (assuming that nothing is gained or lost in terms of copper slot fill factor). However, the losses are frequency dependent and only critical at relatively high frequencies.

There are possibilities to diminish the high frequency losses relatively to RCW' losses by adequate machine design. The design possibilities are:

1. Placing the conductors in the slot with different winding arrangement;
2. Optimizing the slot dimensions along with the conductors' height and width.

6.3. Placing the conductors in the slot with different winding arrangement

The different vertical winding arrangements shown in Figure 6.1 are studied. To make a fair comparison, the analysis is carried out using FE since the arrangements SL3, SL4 and SL5 cannot be estimated using the analytical model. The same FT-PM machine considered in chapter 3 (see section 3.3.3) is used. All the configurations are designed to have the same number of turns (65 turns) and the same DC resistance, thus equal DC losses. The obtained results at rated condition (ω = 2000 rpm, I_{peak} = 10 A) are given in Table 6-1.

From the results, it is evident that placing the conductor in the slot with different winding arrangement has a significant influence on losses, especially for the VSW. The winding placement can be chosen to avoid the high flux density region which is nearer to the slot opening as in (SL2), or to minimize the conductor's height as in (SL3).

The results show that the SL3 arrangement has lower losses than SL2 due to the diminution in conductor's height. However, the magnitude of the SC current in both SL2 and SL3 configurations is higher than in SL1; there is a compromise between inter-turn SC current and eddy current losses.

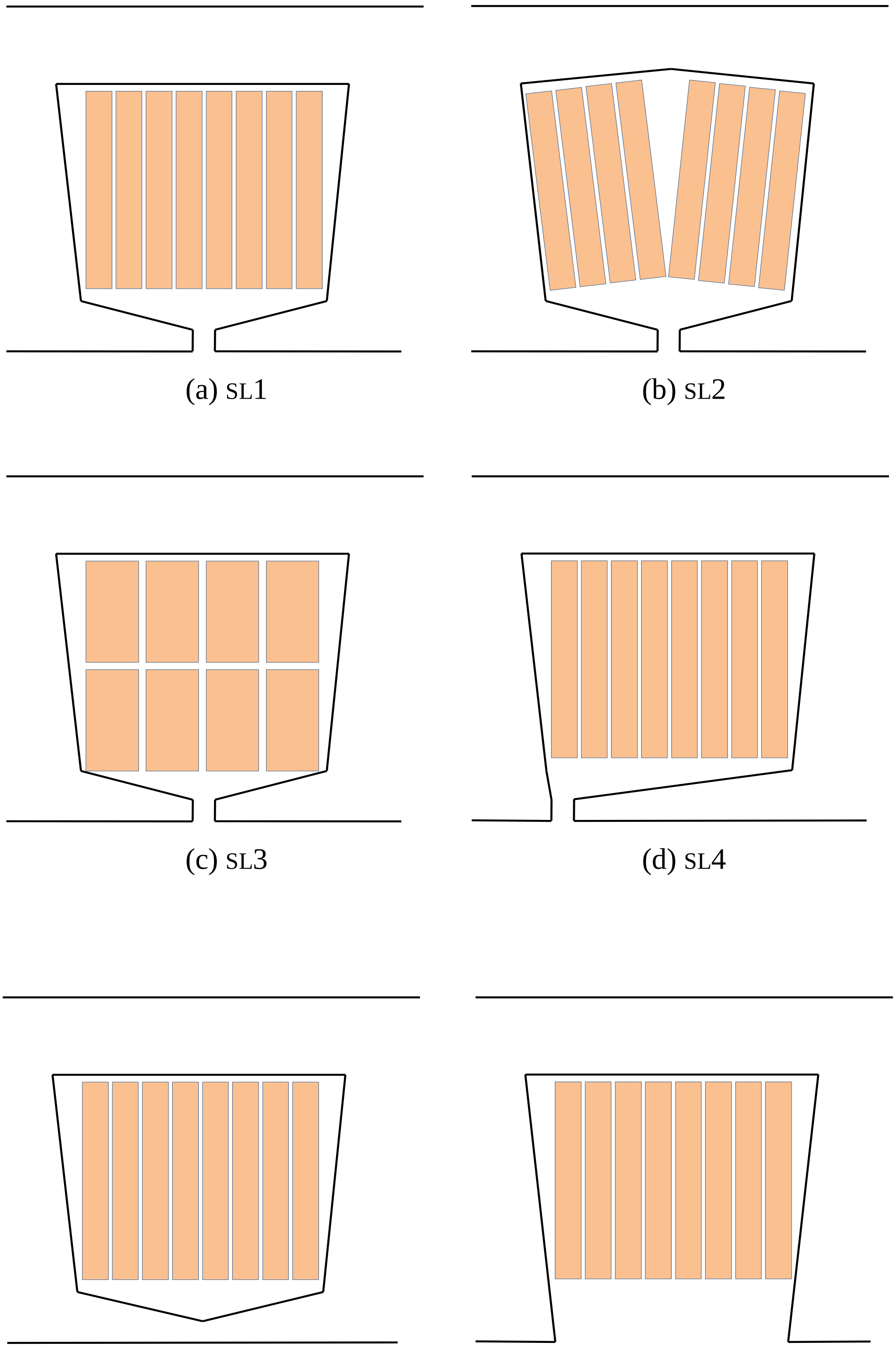
(a) SL1

(b) SL2

(c) SL3

(d) SL4

(e) SL5

(f) SL6

Figure 6.1 Illustration of single layer vertical winding arrangement: (a) standard design; (b), (c) modified winding; (d) modified slot; (e) closed slot; and (f) open slot.

Design	Copper loss (W)	Worst case inter–turn SC Current (A)	AVERAGED TORQUE (Nm)	TORQUE RIPPLE (%)
sl1	92.2	11.78	9.86	8.81
sl2	82.5	12.22	9.81	8.78
sl3	69.0	23.32	9.84	8.63
sl4	91.5	10.37	4.31	6.31
sl5	99.3	1.02	5.42	9.29
sl6	152.7	25.56	7.51	4.32
RCW	56.3	40.20	9.87	8.74

Table 6-1 Loss and SC current in different winding and design arrangements at 2000 rpm

As well as conductor's arrangement and structure, the slotting effect has a significant influence on losses. Thus, modified slot geometries are also considered for the vertical winding as shown in Figure 6.1d, e and f. In each design configuration, worst case a turn SC fault current and total copper losses are calculated.

The modified design SL4 gives more paths to leakage flux in the slot similar to SL1; consequently SL4 produces higher AC copper losses. Thus, the design SL4 can be a solution to further reduce SC current avoiding slot opening region, but it cannot be a solution to reduce AC losses, as evident in . Also it is worth noting that the modified slot geometry further reduces the averaged torque produced by the machine. This is due to the heavy saturation on the tooth.

6.3.1. Influence of the slot opening

The influence of slot opening on copper losses and SC current is clearly demonstrated in Figure 6.2. The closed slot configuration increases the leakage inductance consequently decreases dramatically the SC current. Where, the losses are lower due to reduction in the slot leakage flux density level whilst removing the rotor excitation field. However, the copper losses are significantly higher due to interaction of the rotor excitation field which produces uneven flux distribution in the slot as shown Figure 6.3. This results in large losses in the winding.

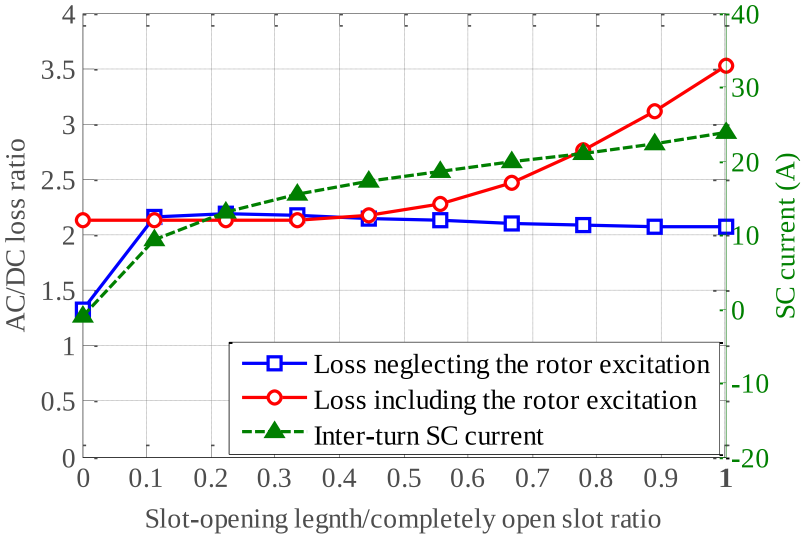

Figure 6.2 AC/DC copper loss ratio and SC current vs. slot opening

From the obtained results, it can be clearly seen that the VSW is sensitive to larger slot opening. Thus, the slotting effect on the losses can be avoided, if semi-open slots are adopted. It is clear that a good choice for the losses is a value less than 0.5.

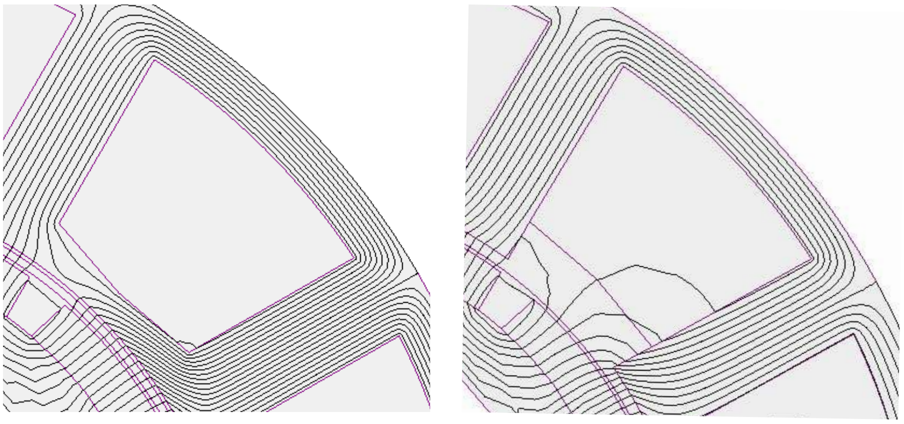

(a) (b)

Figure 6.3 Field distribution in the design of (a) closed slot (b) open slot

From the obtained results, it can be concluded that there is a trade-off between the induced SC current and the generated AC losses in the VSW. It also shows that standard (SL1) design is necessary to maintain the SC current at rated value. Thus, the parametric design technique can be taken for the VSW wound FT-PM machines to minimise the losses by acting upon the machine geometrical parameters: split ratio and tooth-width/slot pitch ratio which change the height of the VSW conductors.

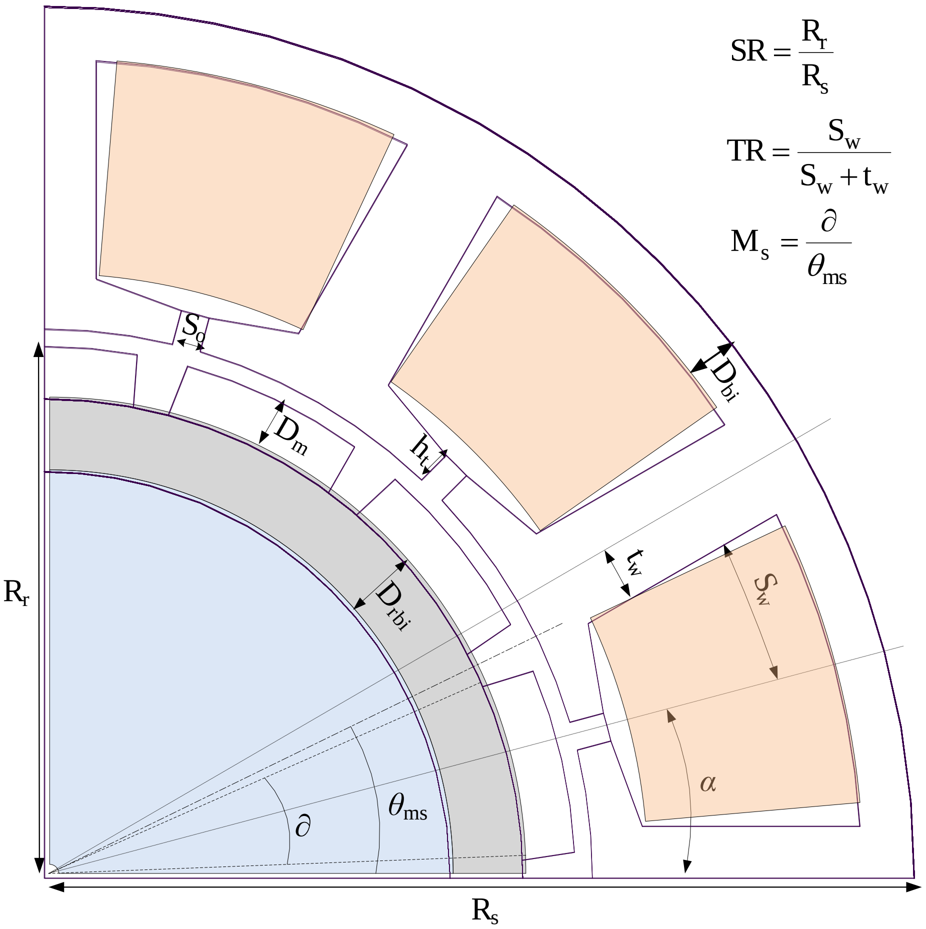

Figure 6.4 Illustration of the machine's design parameters

6.4. **Parametric Design**

The optimization is carried out using parameterized FE models which are coupled to MATLAB® to implement the optimization algorithm. The same 14-pole/12-slot surface mounted PM machine with single layer concentrated winding is considered. Outer diameter and axial length of the machine are fixed. Each phase consists of two coils and the windings are wound with the VSW conductors.

The geometry of the machine and the considered design parameters are illustrated in Figure 6.4, where t_w represents the tooth-width, S_w is the slot-width and R_s, R_r are the outer radius of the stator and the rotor respectively. The other geometrical parameters are indicated in Figure 6.4. The motor geometry is optimised for two major variable geometric parameters: Split Ratio (SR) which is the ratio of the rotor outer diameter and the stator outer diameter and Tooth-width to tooth-pitch Ratio (TR). The goals of the optimization are:

1. to achieve the required torque with minimum level of overall losses
2. to obtain a design that has fault-tolerant capability

Figure 6.5 shows the design process. The routine completes when the condition which fulfils the required torque (fixed as a constant) within the converter voltage limit is satisfied. It is important to highlight that the number of turns is included in the design routine to satisfy the inverter VA limits. The overall electromagnetic losses include iron losses in the stator and rotor laminations and eddy current loss in the magnets are calculated with FE whilst the winding losses produced in the machine are estimated using the analytical model proposed in chapter 5.

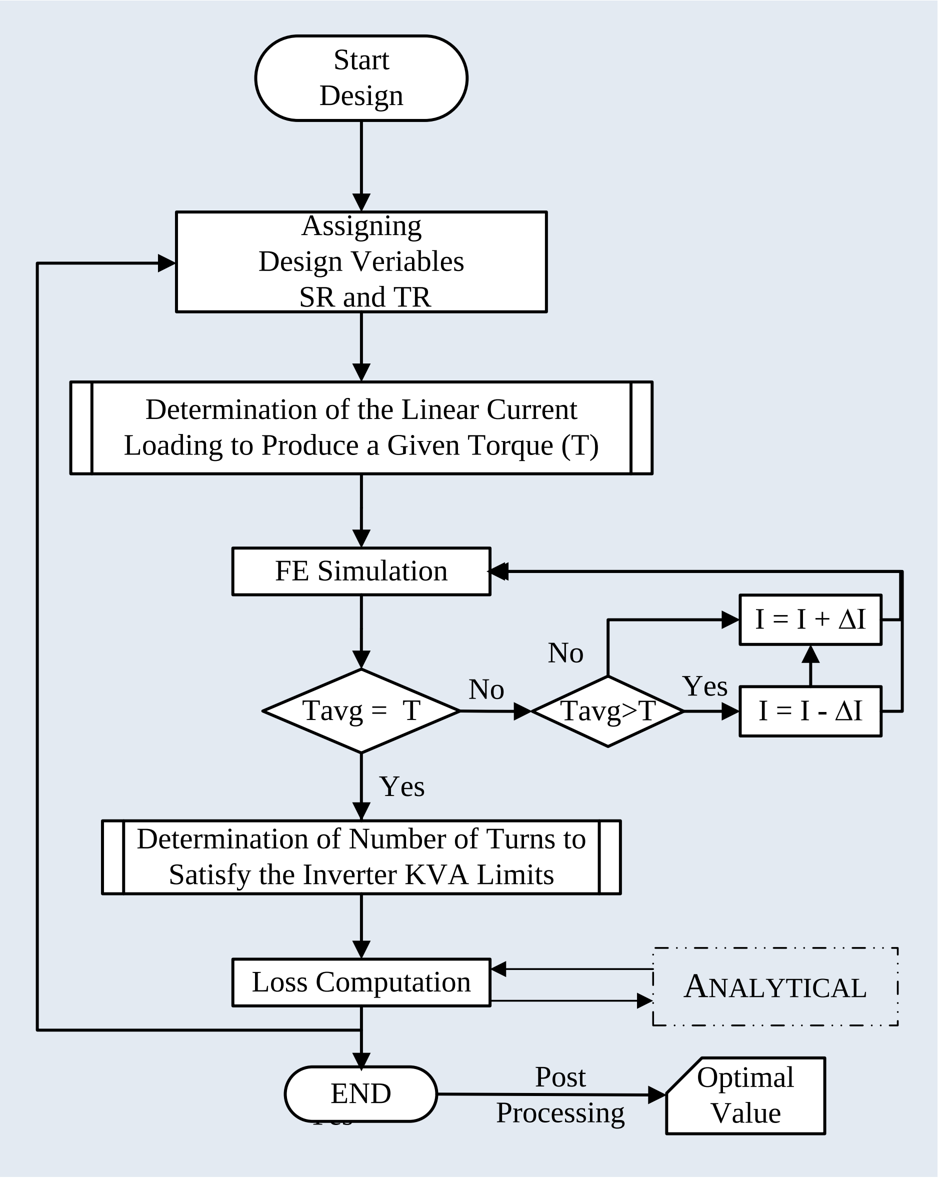

Figure 6.5 The optimization process

In addition the phase SC current is estimated by quantifying the induced current in both d and q axes from the following steady-state equations while the whole phase is short circuited.

$$I_{scd} = \frac{-L_s \omega_e^{2} \Psi_m}{R^2 + L_s^{2} \omega_e^{2}} \tag{6.1}$$

$$I_{scq} = \frac{-R\omega_e \Psi_m}{R^2 + L_s^2 \omega_e^2} \tag{6.2}$$

where, ω_e represents the electrical speed, Ψ_m is the magnet flux linkage, R is resistance and L_s is inductance of one phase. The magnitude of the induced current in the q axis can be neglected at high frequencies since the numerator of (6.2) is significantly smaller than (6.1). Hence, the magnitude of the SC current can be calculated as:

$$I_{sc} = \sqrt{I_{scd}^2 + I_{scq}^2} = I_{scd} \tag{6.3}$$

The worst case inter-turn SC current is also computed (using the model proposed in chapter 3) so as to assess the fault severity. At the post processing stage, the optimal SR and TR are obtained for minimum overall losses while the SC current is limited to its rated value. The parameters of the optimised machine are given in Table 6-2.

6.5. **Results and discussions**

From the results presented in Figure 6.6, it can be clearly seen that there is an optimal TR for different SR values. Figure 6.7 shows the total losses and SC current of a shorted phase against the two key variables, SR and TR. The optimal combinations of ratios are 0.65 and 0.45 respectively, which result in minimum overall losses of 115.15 W. Without including the eddy current effect in the conductor, a minimum loss of 83.5 W is obtained at optimal ratios 0.5 and 0.45 respectively. The results clearly show that eddy current loss is influencing design constraint, and thus it is an important aspect which cannot be neglected in the design stage.

GEOMETRIC PARAMETER OF THE MACHINE	VALUE
Number of poles (p)	14
Number of slots (S)	12
Number of phases (m)	3
Rated torque (T)	10 Nm
Rated speed (ω)	2000 rpm
Rated phase current (I_{rms})	13.2 A
Rated Phase Voltage (V_{rms})	84 V
Phase resistance (R_p)	45.9 mΩ
Self-inductance of a Phase (L_p)	5.2 mH
Number of turns per coil (N_C)	65
Worst case inter-turn SC current (I_s)	15.09 A
Stator outer diameter (D_o)	100 mm
Tooth shoe height (h_t)	2 mm
Slot wedge height	1 mm
Slot opening (S_o)	1.5 mm
Active length (l_{stk})	100 mm
Airgap (l_g)	1 mm

Table 6-2 Specification of the optimized PM machine

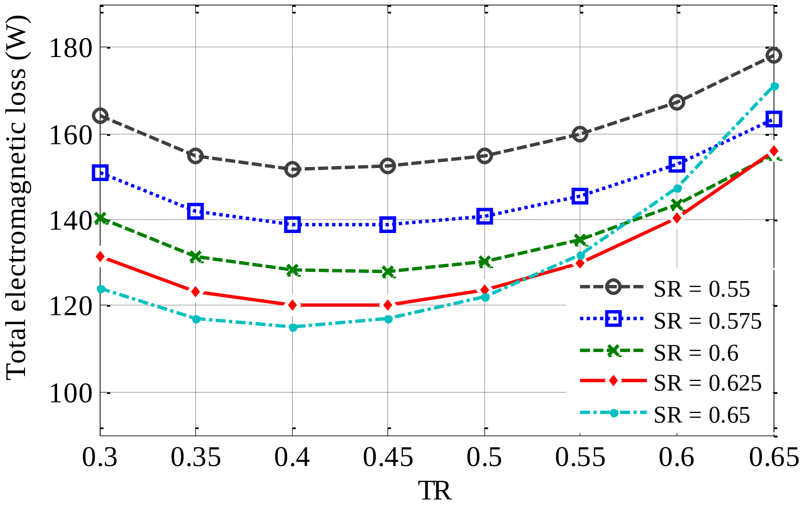

Figure 6.6 Overall losses vs. TR for different values of SR

To achieve the best design, a compromise which satisfies both SC current limiting capability and a reasonable amount of losses is required. For illustration purpose Figure 6.8 can be considered. It shows the area where SC current below the rated current is achievable for a given TR of 0.45. The best design for this particular TR is the one with minimum losses.

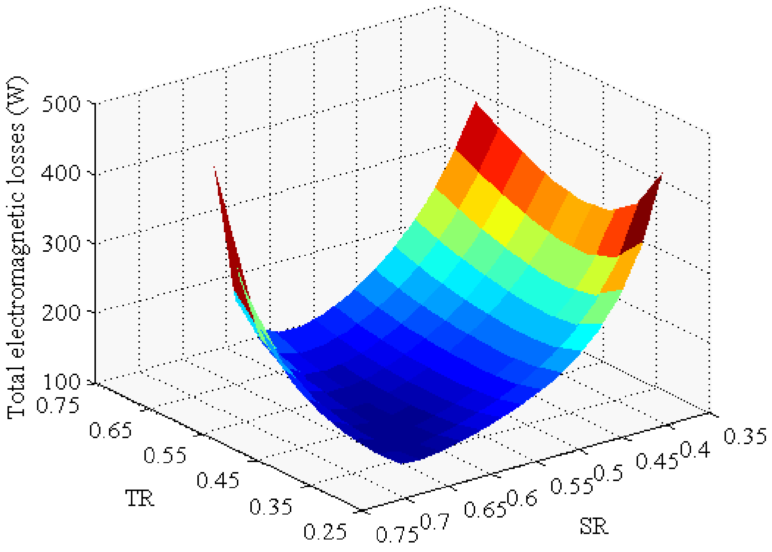

(a)

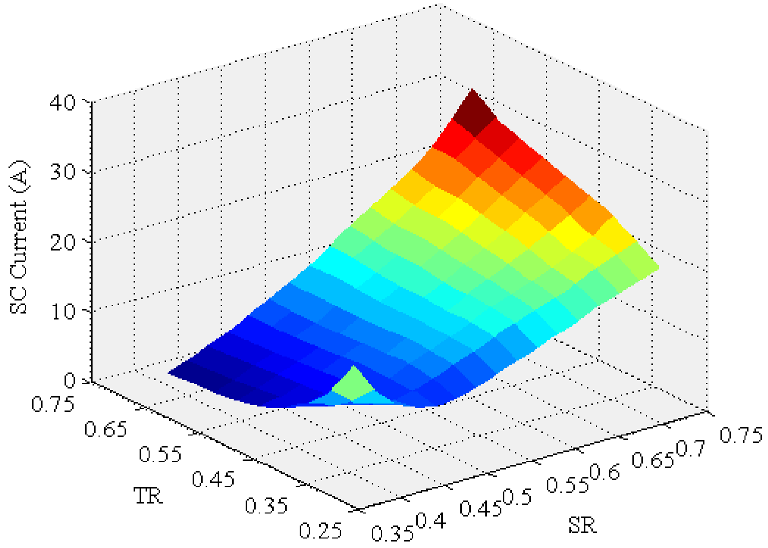

(b)

Figure 6.7 (a) Total losses (b) SC current vs. SR and TR

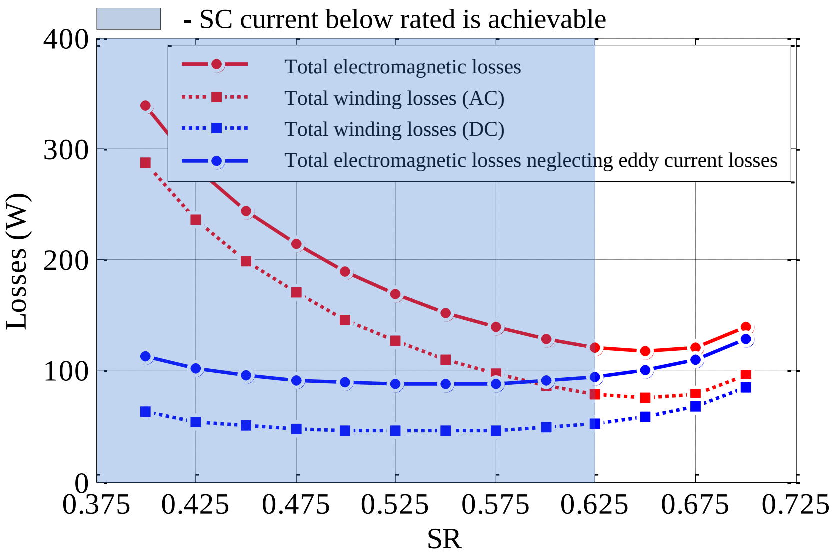

Figure 6.8 Comparison of losses vs. SR due to eddy current effect

The AC copper loss is relatively higher than DC copper loss in the winding when the SR is below 50%, as illustrated in Figure 6.8. When the split ratio is increased, as expected, the slot area is reduced and the AC loss converges to the DC loss value as the conductor height reduces. There is a point when the DC resistance will be such that the DC copper loss will have a steeper rate of increase with SR. From Figure 6.8, it can be seen that if fault tolerance is not considered the optimal split ratio is approx. 0.65.

The results above show that the split ratio has a significant influence not only on the DC copper loss and iron losses, but also on eddy currents loss. As well as SR, the slot opening also highly influences the AC copper loss generated in the VSW. Thus, a good choice of design parameters allow for diminishing AC loss at reasonable level whilst maintaining the fault tolerance capability of the PM machine. Design optimization is therefore necessary when adopting this type of winding, especially for high speed or high pole number applications.

6.6. Conclusions

The effects of VSW placement in the slot, split ratio and tooth width ratio on losses has been investigated in this chapter. It is shown that the AC loss can be reduced slightly by placing the conductor avoiding high flux density region. It is also shown that the split ratio has a significant influence not only on the DC copper loss and iron losses, but also on eddy currents loss. The optimization process allows for improving the electrical machine fault tolerance capability by using vertical conductors whilst maintaining the additional losses at a reasonable level.

CHAPTER

7

Experimental validation

7.1. Introduction

This chapter describes an experimental validation of the analytical models proposed for calculation of the inter-turn SC current and AC copper losses in chapters 3 and 5, respectively. For model validation an existing 12-pole/18-slot surface mounted PM machine is adopted. Considering an existing PM rotor, a new stator is designed to fit in the available envelope whilst the design satisfies the unity per unit inductance to meet fault tolerance criteria. Two different stator geometries are considered: one has a parallel slot to accommodate the VSW conductors and the other has a trapezoidal slot for RCW. The stator prototypes are manufactured and tested. The obtained results are compared with the analytically calculated ones and then discussed.

7.2. Description of the experimental setup

The specifications of the existing 12-pole/ 18-slot PM machine are given in Table 7-1. The Inner and outer diameters of the stator are fixed due to availability of the (surface mounted) rotor and the stator casing. Thus, the stator is designed to fit in the available envelope whilst the design satisfies the unity per unit inductance constraint to meet fault tolerance criteria. Technical drawings of the constructed stators and the existing rotor are given in Appendix F.

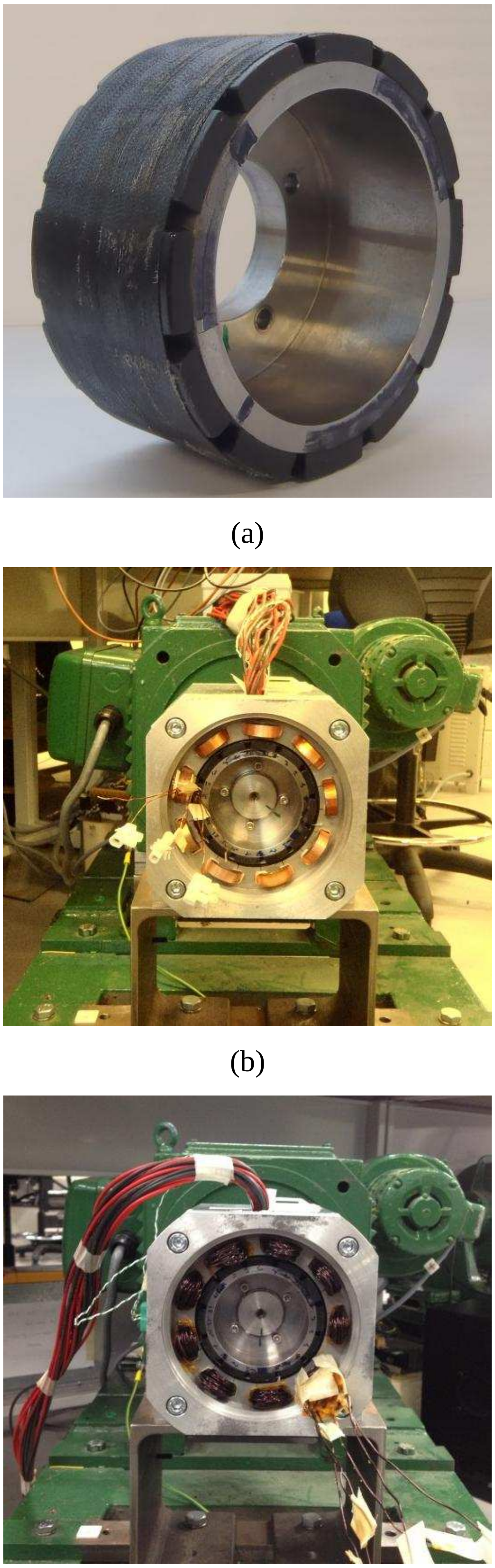

(a)

(b)

(c)

Figure 7.1 (a) 12-pole rotor (b) VSW wound and (c) RCW wound FT-PM machine

SPECIFICATIONS	VALUES
Rated speed (ω)	2000 rpm
Rated torque	6 Nm
Output Power	1.25 kW
Rated current (rms)	7.07 A
Back-emf (rms)	47.3 V
Number of phase (m)	3
Number of slot (S)	18
Number of pole (p)	12
Phase inductance (Lp)	2.1 mH
Phase resistance (Rp)	150 mΩ
Number of turns per coil (N_C)	40

Table 7-1 Specification of experimented PM machine

A hand winding method is chosen for both windings since the designed machine has small slot opening to achieve unity per unit inductance. In both designs, the DC resistance and the number of turns are kept identical. In order to introduce the inter-turn fault in the winding, external leads are connected to the end connections of the windings. Three different fault locations are considered. In the vertical conductor, the locations of the fault are introduced at the end turns of $14\frac{1}{2}$, $15\frac{1}{2}$, $19\frac{1}{2}$, $20\frac{1}{2}$, $34\frac{1}{2}$, $35\frac{1}{2}$ (e.g. $14\frac{1}{2}$ represents complete fourteen turns and a half turn) which correspond to the position of the shorted turns 15th, 20th and 35th, respectively. In the case of RCW, the fault is located at outer most, inner most and middle of the slot since it is difficult to control the exact location of a turn. It is worth to note that all the connected leads have the same length and cross section area and thus the same impedance.

A fill factor of 0.6 is achieved for the VSW whilst only 0.52 is achieved for the RCW with the same number of turns. However, a fill factor of 0.56 can be achieved for the RCW in the case of complete slot fill where a good tension is employed using plastic wedges to place the winding. It is not necessary for the vertical conductors since they are more flexible to wind and handle the tension.

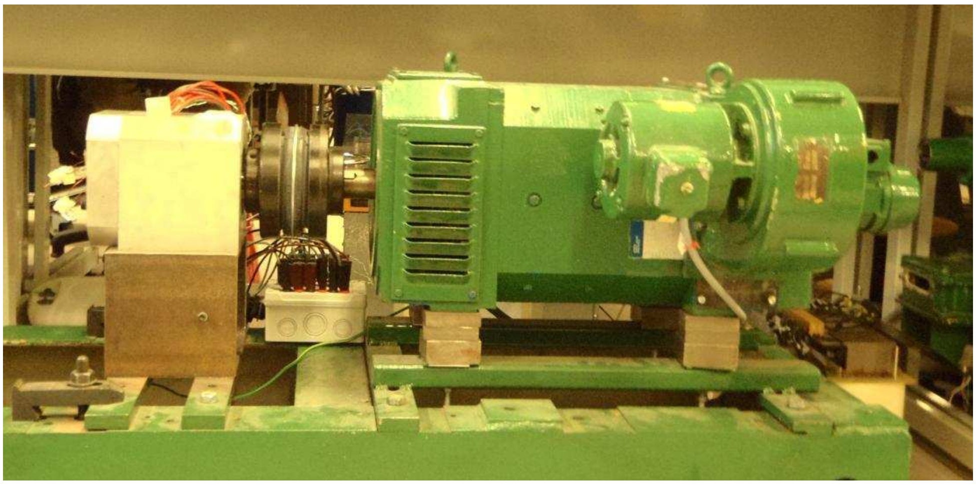

Figure 7.2 Experimental rig

Figure 7.2 shows the test rig used for experimental validations. Where, the FT-PM machine is driven by a DC motor which is controlled using a Eurotherm® industrial drive (590 series). Open circuit and short circuit tests are performed. Inter-turn SC fault test is carried out shorting the turns via external leads which are connected at the end-winding of the corresponding shorted turn. The obtained results are compared with the analytical and FE ones.

7.2.1. SC Current - VSW machine

Figure 7.3 shows the obtained steady state phase SC current for VSW wound FT-PM machine. From the results it can clearly be seen that measured phase SC current is in good agreement with both analytical and FE results. However, the magnitude of the analytically estimated phase SC current is slightly less than the measured ones whilst the FE calculated SC current is slightly higher. This is due to analytically estimated phase inductance are slightly higher than measured and FE calculated ones as discussed in chapter 3; consequently the analytical model slightly underestimates the SC current. Since the end winding inductance and resistance are not considered FE overestimates the SC current slightly.

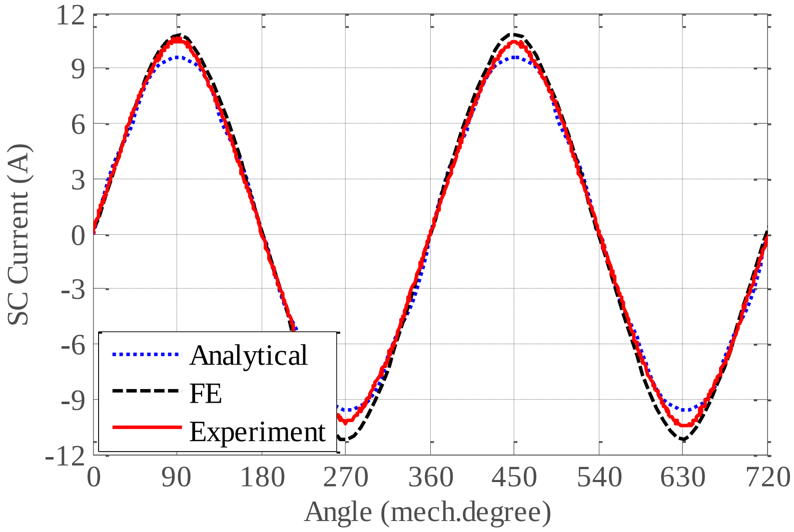

Figure 7.3 Measured and calculated phase SC current - VSW wound machine

Figure 7.4 compares the inter-turn SC current between the analytically estimated and measured results after application of the remedial action when the faulted turn is located at the middle of the slot. The SC current is calculated considering the measured impedance of both the end-windings and the external shorting connectors, since these impedances are larger than the single turn impedances.

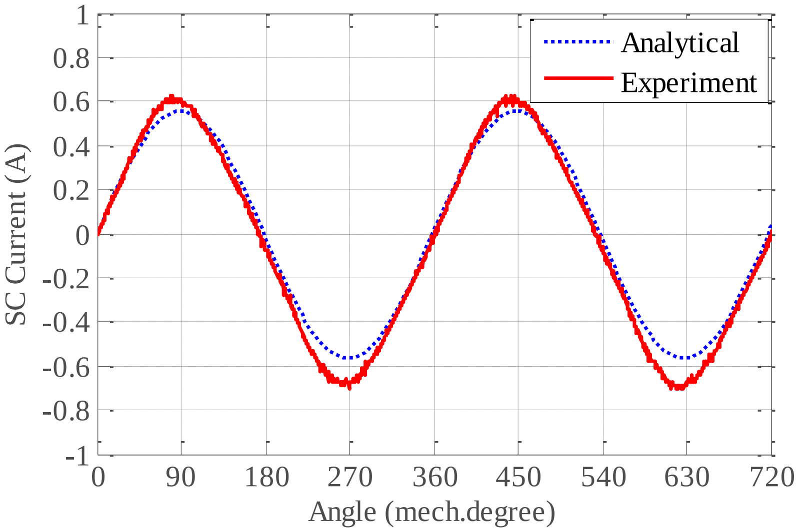

Figure 7.4 Inter-turn SC current comparison between analytical and experimented results considering external impedance of shorting connectors.

From Figure 7.4, it can be seen that the analytical results agree with the measured ones. From Table 7-2, it can also be seen that the induced current in a turn is not dependant on the position in the slot of the shorted turn. In fact the SC current slightly reduces with the turn position due to the progressive increase of the end-winding length. These experimental results confirm that the FT-PM machine having VSW limits SC current inherently regardless of the position in the slot of the shorted turn.

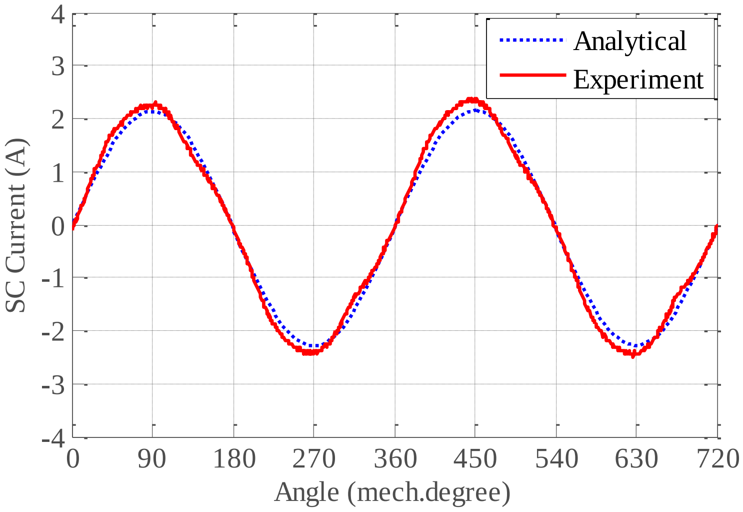

(a)

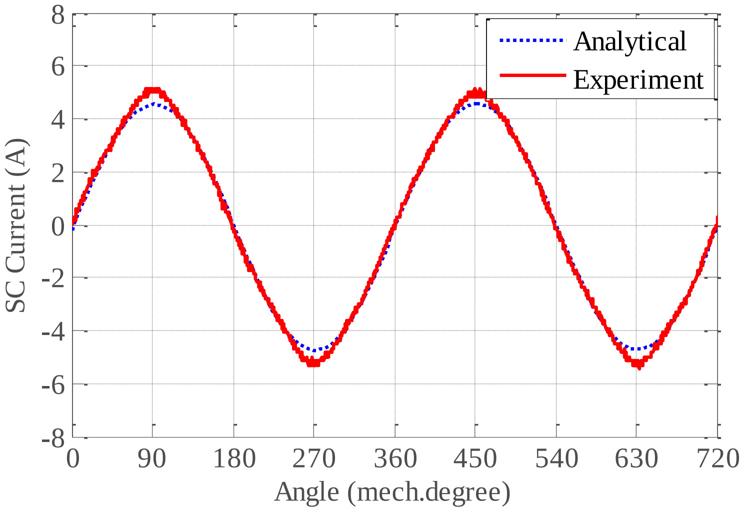

(b)

Figure 7.5 Comparison between simulation and experimental results considering the external impedance of the shorting connectors – (a) 10 turns fault (b) 20turns fault.

LOCATION OF THE FAULT	MAGNITUDE OF THE SC CURRENT	
	ESTIMATION	MEASURED
15th turn	0.593 A	0.602 A
20th turn	0.581 A	0.611 A
35th turn	0.467A	0.472 A

Table 7-2 Comparison of inter-turn SC fault current between analytical and measured results at 2000rpm

Figure 7.5 compares the analytically computed and measured SC current for different numbers of shorted turns, where the impedance of both the end-winding and the external shorting wires are accounted for. These results are in accordance with the predicted ones regardless of the number of shorted turns and their position in the slot.

7.2.2. SC Current - RCW machine

Figure 7.6 shows the obtained inter-turn SC fault current for three different positions (inner most, outer most and middle turns) after application of the remedial action. Form Figure 7.6, it can clearly be seen that the inter-turn SC current induced in the inner most turn is higher than others: middle and outer most. It can also be seen that there is a significant difference between the analytical and the measured SC current of the middle turn. This may come from the poor physical contact between the turns and shorting external leads. These results clearly explain that the RCW winding SC current amplitude is highly position-dependent and the winding is critical to inter-turn SC fault if the faulted turn is located closer to the slot opening region (inner most of the slot).

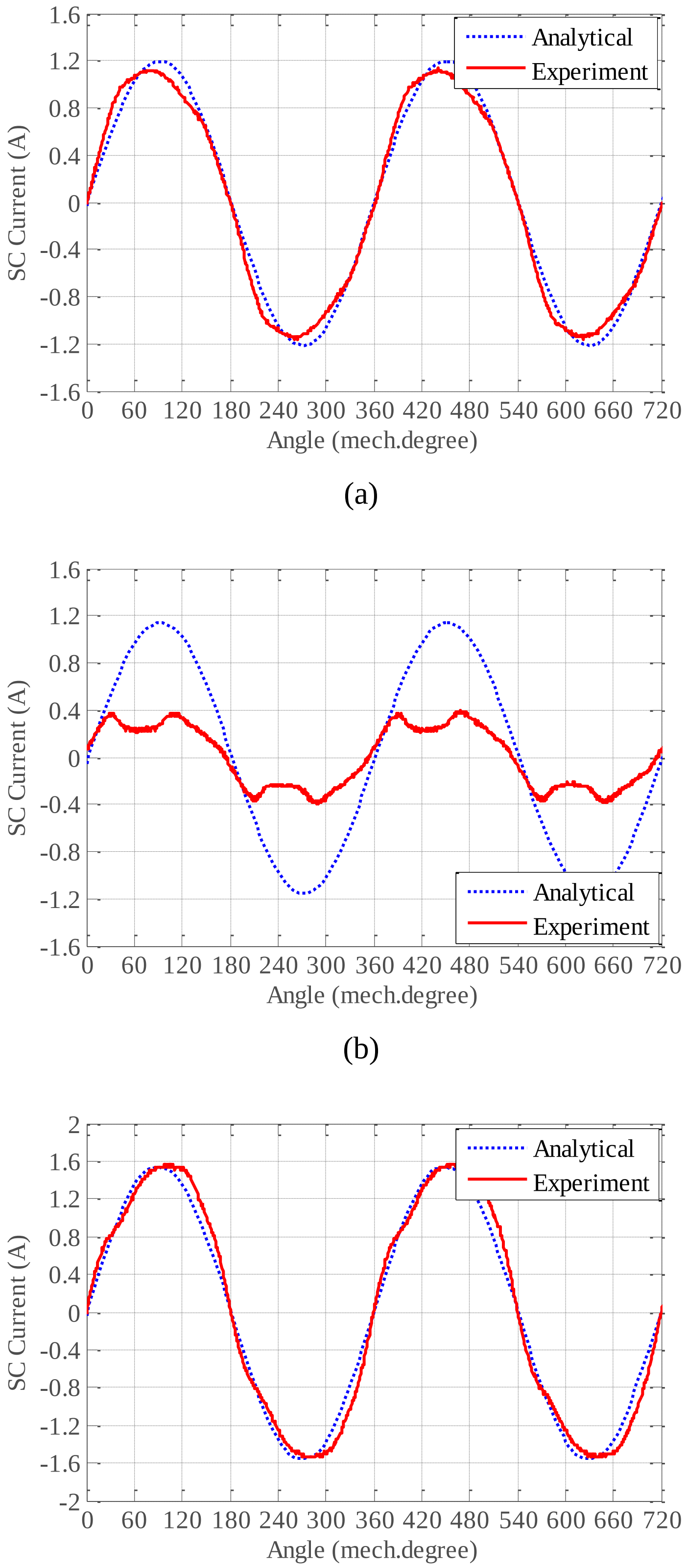

(a)

(b)

(c)

Figure 7.6 Inter-turn SC fault current at (a) outer most (b) middle (c) inner most of the slot

7.2.3. Copper losses

Figure 7.7 shows the measured AC to DC loss ratio against frequency. The analytically calculated results are in a good agreement with the measured ones. As expected, the AC loss of both windings increases considerably with frequency. At the rated condition (speed = 2000 rpm, current = 7.07 A_{rms}) the VSW's AC losses are around 1.4 times higher than the DC loss and it increases considerably with further frequency increase. Compared to the RCW the VSW's losses are ~27 % higher at rated condition and the rate of losses increase is also considerably higher. It is clear that a disadvantage of this winding topology is the increased AC copper losses unless the winding is designed to have optimal height.

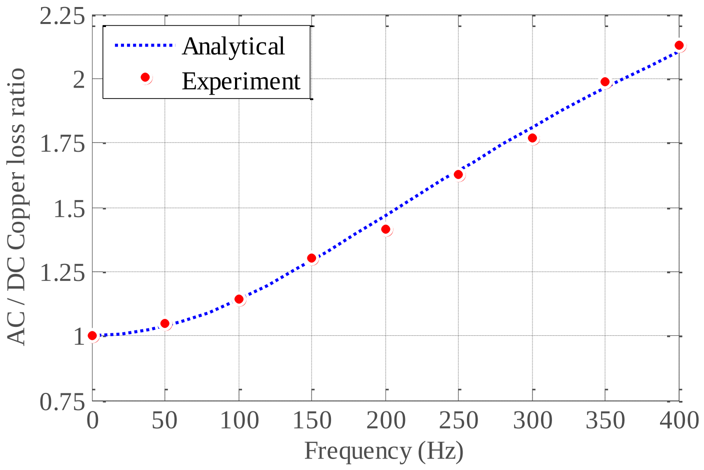

(a)

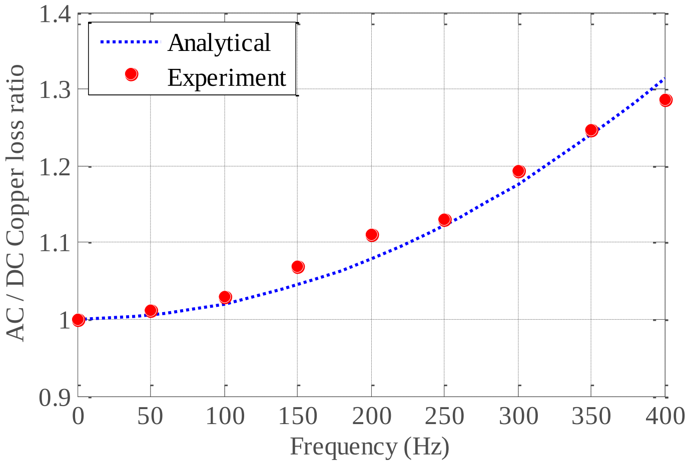

(b)

Figure 7.7 Total AC/DC loss ratio vs. Frequency: (a) VSW (b) RCW

7.2.4. Thermal behaviour of the windings

In order to measure the localised temperature in the outer surface and the bottom of the slot, two thermocouples are used with the Pico TC-08 thermocouple data logger. The temperatures measurement is carried out for both winding configurations whilst all phases are short-circuited at rated speed of 2000 rpm. The obtained results are given in Figure 7.8.

From the results, it can be seen that the magnitude of the phase SC current flowing through the winding of both machines is almost identical. From the results, it can clearly be seen that although the VSW's losses are 27.47 % higher than the RCW at rated condition, the thermal characteristic of the VSW wound machine is almost similar to the RCW ones. This result confirms that the VSW has a good thermal path to additional losses.

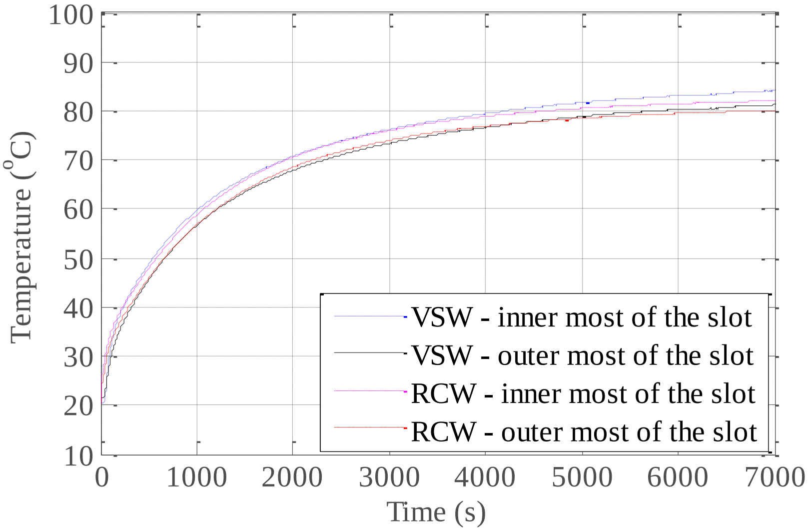

Figure 7.8 Temperature graph vs. time

7.3. **Conclusion**

An experimental validation has been carried out for two machine prototypes having VSW and RCW winding configurations. Inter-turn SC current, AC loss and temperature were measured. Obtained results were compared with the analytically calculated results. These results have further validated the proposed analytical model for the calculation of the SC current and AC copper losses in chapter 3 and 5, repectively. Also the results have confirmed that although the VSWs have higher AC copper losses than the RCWs, it has a better thermal path to the generated copper losses.

CHAPTER

8

Conclusion

Inter-turn SC fault behaviour in fault-tolerant permanent magnet synchronous machines adopting crude analytical approach was investigated in this thesis. The main objective was to develop a solution at the design stage in order to mitigate the position dependent inter-turn SC fault. An analytical model was developed to reduce the computation time and simplify the parametric study.

The problems of inter-turn SC faults in electrical machines and the necessity for their mitigation was discussed in chapter 1. A particular importance was subsequently given to explaining the merits/demerits as well as the trade-offs of the mitigation methods proposed in the literature; this is the subject of chapter 2. It covered the fault tolerance aspects in synchronous PM machines including various methods and strategies with more emphasis on inter-turn SC fault. Five different post-fault methodologies were discussed: phase terminals short-circuiting, current injection, auxiliary winding, mechanical and thermal design. It was concluded that shorting the phase terminals is the most attractive solution and this was adopted throughout this work.

In chapter 3, an analytical model that can be used to evaluate inductances and subsequently calculate the fault currents under faulted operation and also post-fault operation i.e. shorting terminals scheme, is proposed. It was shown that the analytical model is very effective in predicting the resulting SC currents once a fault-tolerant remedial control strategy is applied. The effectiveness of the analytical tool is verified by FE analysis and validated experimentally. Although this method, as any other analytical method, has some obvious limitations in terms of accuracy, it has a very fast computation time and can be effectively used at a design stage where much iteration is needed and where the modelling of individual turns in a finite element package under fault conditions would be prohibitively time consuming. Analysis made using the proposed analytical model has shown that for stranded coils a single turn-turn fault close to the slot opening results in a short circuit current magnitude more than three times the nominal current of the machine despite the machine being designed to be fault tolerant, i.e. phase SC current equal to its rated nominal value. Thus, a vertical winding concept was introduced as an alternative to stranded coils to minimize the position dependency of the SC currents resulting from turn-turn fault. An analytical model was developed for the vertical winding and was benchmarked against FE and validated experimentally. It is shown that the vertical winding configuration significantly improves the fault tolerance capability in terms of inherently limiting the inter-turn SC current regardless the fault position in the slot.

In chapter 4, the vertical winding design has been investigated in the context of losses and thermal behaviour. The obtained results confirmed that the vertical winding not only improves the fault tolerance capability in terms of inherently limiting the inter-turn SC current but it also has a better thermal behaviour compared to the conventional round conductors; whereas it was shown that there is always a trade-off between SC current limiting capability and eddy current losses. However, the proposed vertical winding is suitable for relatively low frequency applications, where eddy current losses are not critical. For high speed applications, design optimization is necessary to balance the eddy current losses with the resulting SC currents.

In order to investigate the influence of the eddy current losses in the vertical winding, 2-D field model was developed in chapter 5. The model consists of exact field computation using the separation of variables technique. This tool provides a considerable flexibility for parametric studies and design optimization of PM machines.

In chapter 6, feasible solutions to minimise the eddy current losses in the FT surface mounted PM machines wound with vertical conductors was investigated. As an initial solution, placement of the winding in the slot and their influence on AC copper losses and inter-turn SC current was investigated. As an alternative, a systematic parametric design was carried out based on two major key parameters: split ratio and tooth width ratio. The study was conducted using both FE and analytical tools proposed in chapter 3 and 5. FE analysis was used to estimate the required torque considering non-linearity of the material whilst the analytical tools were used to predict the SC fault current and the AC copper losses. It was shown that the split ratio has a significant influence not only on the DC copper losses and iron losses, but also on AC losses. The optimization process allows for improving the electrical machine fault tolerance capability by using vertical conductors whilst maintaining the additional losses at a reasonable level.

Finally, chapter 7 is dedicated to experimental validation tests on two machine prototypes having VSW and RCW winding configurations. Inter-turn SC current, AC losses and temperature were measured. The obtained results were compared with the analytically calculated ones. These results have further validated the proposed analytical models for the calculation of SC current and AC losses in chapter 3 and 5, repectively. Also the results have confirmed that although the VSW have higher AC losses than the RCW, it has a better thermal path to the generated extra copper losses.

8.1. **Future work**

Although much has been achieved in terms of concepts and their related tasks, there is scope for improvement and development:

- In section 5.9, it is shown that the sub domain field model has limitations due to non-convergence when the slot opening is very small. As a solution, altering harmonic series method that converge the solution conditionally could be considered.

- The sub domain field model proposed in chapter 5 is developed considering only the fundamental component of the supply current. The influence of high frequencies PWM harmonics could be considered as a further study.

- The proposed eddy current loss model is only applicable for surface mount PM machines. It would be interesting to apply the model for different PM machine topologies such as flux switching PM machine, inset PM machine, outer rotor PM machine, etc.

- The experimental study is only conducted at no-load condition. Operation of the two different prototypes under a controlled environment should be experimented with.

- The vertical winding concept has been proposed in the study to limit inter-turn SC current after application of the remedial action (terminals SC). However, alternative post-fault control algorithms could be investigated in PM machines adopting the new winding concept (VSW).

Appendixes

Appendix – A

PUBLICATIONS:

International Journals:

1. P. Arumugam, T. Hamiti, and C. Gerada, "Modeling of Different Winding Configurations for Fault-Tolerant Permanent Magnet Machines to Restrain Interturn Short-Circuit Current," IEEE Transactions on Energy Conversion, vol. 27, pp. 351-361, 2012

2. P. Arumugam, T. Hamiti, and C. Gerada, "Analysis of Vertical Strip wound Fault Tolernat Permnant Magnet Synchronous Machines," Industrial Electronics, IEEE Transactions on, in press.

3. P. Arumugam, T. Hamiti, and C. Gerada, "Analytical estimation of Eddy Current Loss in Semi-Closed Slot Vertical Conductor Permanent Magnet Synchronous Machines Considering Eddy Current Reaction Effect," Magnetics, IEEE Transactions on, in press.

International Conferences:

4. P. Arumugam, T. Hamiti, C. Gerada, "Analytical modelling of a vertically distributed winding configuration for Fault Tolerant Permanent Magnet Machines to suppress inter-turn short circuit current limiting," Electric Machines & Drives Conference (IEMDC), 2011 IEEE International , vol., no., pp.371-376, 15-18 May 2011.

5. P. Arumugam, T. Hamiti, and C. Gerada, "Fault tolerant winding design - A compromise between losses and fault tolerant capability," in Electrical Machines (ICEM), 2012 20th International Conference on, 2012, pp. 2559-2565.

Invited Presentation:

6. P. Arumugam, T. Hamiti, C. Gerada, "Permanent Magnet Synchronous Machine Design Optimization to Minimize Overall Electromagnetic Losses", UK Magnetic Society 2011, Sheffield, 8th November, 2011, United Kingdom.

Appendix – B

FLUX ESTIMATION - HORIZONTAL WINDING CONFIGURATION:

a) The flux (Ψ_x) linking the height of h_a which is related to the healthy turns N_a can be written as:

$$\Psi_x = \mu_o \, l_{stk} \, I \int_0^{h_a} \left(\frac{N}{h_s}\right)^2 \left[\frac{x^2}{S_w + 2(h_s - x)\tan(\beta)}\right] dx \qquad \text{(B-1)}$$

The flux (Ψ_y) linking the height of (h_s - h_b) which is associated with both healthy turns N_a and N_b can be described as:

$$\begin{aligned} \Psi_y &= P_{(hs-hb)} . (N_a + N_b)^2 . I \\ &= P_{(hs-hb)} . N_a{}^2 . I + 2.P_{(hs-hb)} . N_a \, N_b . I + P_{(hs-hb)} . N_b{}^2 . I \end{aligned} \qquad \text{(B-2)}$$

where, $P_{(hs-hb)}$ is the permeance associated to the height (h_s - h_b) and thus the flux linkage Ψ_y can be found as:

$$\begin{aligned} \Psi_y &= P_t . N_a{}^2 . I \\ &+ \mu_o \, l_{stk} \, I \left[\begin{array}{l} \left(\displaystyle\int_{h_b}^{h_s} \left(\frac{N}{h_s}\right)^2 \left[\frac{(x - h_b)^2}{S_w + 2(h_s - x)\tan(\beta)}\right] dx \right) \\ + \left(2 \displaystyle\int_{h_b}^{h_s} \left(\frac{N}{h_s}\right) \left[\frac{N_a (x - h_b)}{S_w + 2(h_s - x)\tan(\beta)}\right] dx \right) \end{array} \right] \end{aligned} \qquad \text{(B-3)}$$

Hence, the total slot leakage flux linking the healthy turns can be written as follows:

$$\Psi_h = P_s . N_h^2 . I + \Psi_x + . \Psi_y \tag{B-4}$$

b) The flux (Ψ_p) linking the height of (h_b - h_a) which is associated with both healthy N_a turns and shorted N_s turns can be expressed as:

$$\Psi_p = \mu_o \, l_{stk} \, I \int_{h_a}^{h_b} \left(\frac{N}{h_s} \right) \left[\frac{N_a \left(x - h_a \right)}{S_w + 2(h_s - x) \tan\left(\beta\right)} \right] dx \tag{B-5}$$

The flux (Ψ_q) linking the height of (h_b - h_s) which is associated with both healthy N_b turns and shorted N_s turns can be expressed as:

$$\Psi_q = \mu_o \, l_{stk} \, I \int_{h_b}^{h_s} \left(\frac{N}{h_s} \right) \left[\frac{N_s \left(x - h_b \right)}{S_w + 2(h_s - x) \tan\left(\beta\right)} \right] dx \tag{B-6}$$

Hence, the total slot leakage flux linking both healthy and shorted turns can be written as follows:

$$\Psi_m = P_s . N_h \, N_s . I + P_t . N_a \, N_s \, . I + \Psi_p + \Psi_q \tag{B-7}$$

where, the integration of the different flux components can be done numerically.

Appendix - C

FLUX ESTIMATION - VERTICAL WINDING CONFIGURATION:

Using the same process as for horizontal winding the different fluxes are given as follows:

a) The total leakage flux linking the healthy turns can be written as follows:

$$\begin{aligned}\Psi_h = \mu_o\, l_{stk}\, I \Bigg[& \left(\frac{h_t}{b_o} \left(N - N_s \right)^2 \right) \\ & + \left(\frac{1}{2} \left(\frac{2S_w h_s + 2S_w h_w - b_o h_w}{\left(h_s + h_w \right)\left(2h_s + h_w \right)} \right) \left(\frac{N^2}{4} + \left(N_a + N_b \right)^2 + \frac{N}{2}\left(N_a + N_b \right) \right) \right) \\ & + \left(\frac{S_w - 2W_a}{2\left(h_s + W_a \tan(\alpha) \right)} \right) N_a^{\,2} + \left(\int_0^{W_a} \left(\frac{N}{S_w} \right)^2 \left[\frac{x^2}{h_s + x \tan\left(\alpha \right)} \right] dx \right) \\ & + \left(\int_{W_b}^{\frac{1}{2}S_w} \left(\frac{N}{S_w} \right)^2 \left[\frac{\left(x - W_b \right)^2}{\left(h_s + x \tan(\alpha) \right)} \right] dx \right) + \left(2\int_{W_b}^{\frac{1}{2}S_w} \left(\frac{N}{S_w} \right) \left[\frac{N_a \left(x - W_b \right)^2}{\left(h_s + x \tan(\alpha) \right)} \right] dx \right) \Bigg] \end{aligned} \tag{C-1}$$

b) The total leakage flux linking both healthy and shorted turns can be written as follows:

$$\begin{aligned}\Psi_m = \mu_o\, l_{stk}\, I \Bigg[& \left(\frac{h_t}{b_o} \left(N - N_s \right) N_s \right) \\ & + \left(\frac{3N^2}{8} \left(\frac{2S_w h_s + 2S_w h_w - b_o h_w}{\left(h_s + h_w \right)\left(2h_s + h_w \right)} \right) \right) + \left(\frac{S_w - 2W_b}{2\left(h_s + W_b \tan(\alpha) \right)} \right) \left(N - N_s \right) N_s \\ & + \left(\int_{W_a}^{W_b} \left(\frac{N}{S_w} \right) \left[\frac{N_a \left(x - W_a \right)}{h_s + x \tan\left(\alpha \right)} \right] dx \right) + \left(\int_{W_b}^{\frac{1}{2}S_w} \left(\frac{N}{S_w} \right) \left[\frac{N_s \left(x - W_b \right)}{\left(h_s + x \tan(\alpha) \right)} \right] dx \right) \Bigg] \end{aligned} \tag{C-2}$$

Appendix - D

D.1 WINDING ARRANGEMENT IN THE SLOT AND ADOPTED MESH CONDITIONS IN FE SIMULATION

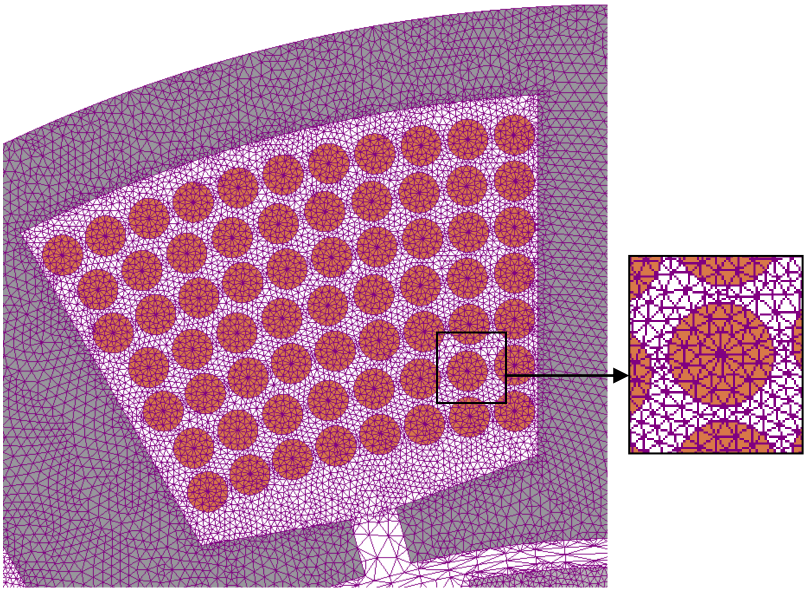

Figure D 1. Mesh refinement of the RCW

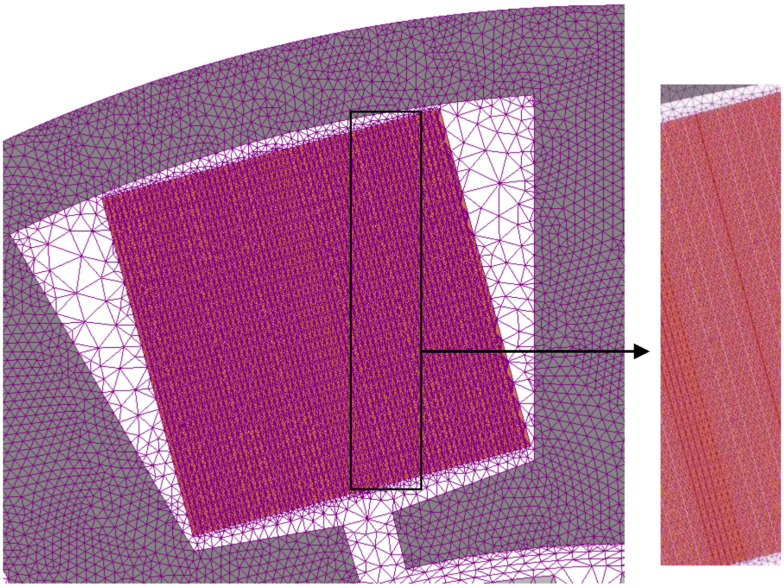

Figure D 2. Mesh refinement of the VSW

D.2 WINDING MANUFACTURING CONSIDERATIONS

From a manufactering standpoint, insering this type of winding in a lamination stack with semi-open slots is very difficult. However, a number of options can be adopted and two of them are illustrated in Figure D 3 which are self explanotary.

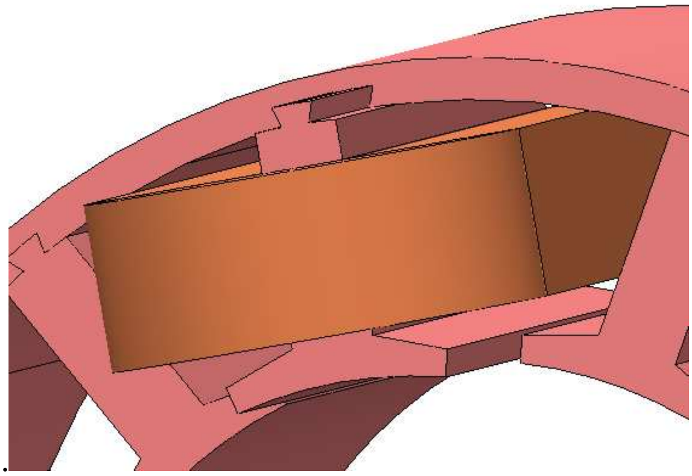

(a)

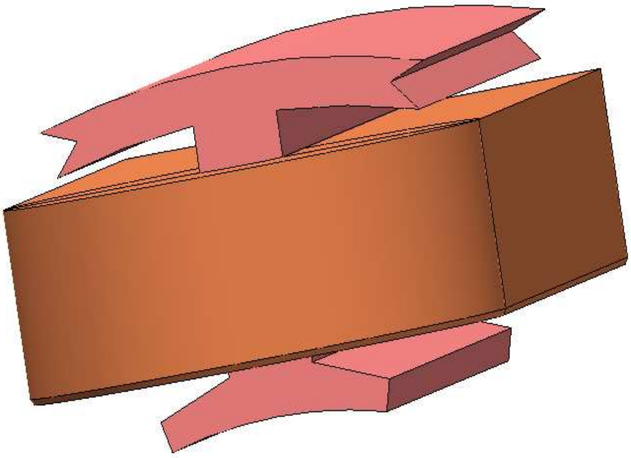

(b)

Figure D 3 Stator design with: (a) removable tooth, (b) separated tooth

Appendix - E

E.1 SOLUTION IN THE AIR GAP SUB-DOMAIN:

The magnetic vector potential in the airgap can be obtained by solving Laplace's equation:

$$\frac{\partial^2 A_{II}(r,\theta)}{\partial r^2} + \frac{1}{r}\frac{\partial A_{II}(r,\theta)}{\partial r} + \frac{1}{r^2}\frac{\partial^2 A_{II}(r,\theta)}{\partial \theta^2} = 0 \text{ for } \begin{cases} R_2 \le r \le R_3 \\ 0 \le \theta \le 2\pi \end{cases} \quad \text{(E-1)}$$

The interface condition between the PM sub-domain and the airgap at r = R_2 (Figure E. 1) is given from the continuity of the radial component of the magnetic flux density:

$$B_\theta^{II}(R_2,\theta) = B_\theta^{I}(R_2,\theta) \Leftrightarrow \left.\frac{\partial A_{II}}{\partial r}\right|_{r = R_2} = \left.\frac{\partial A_I}{\partial r}\right|_{r = R_2} \quad \text{(E-2)}$$

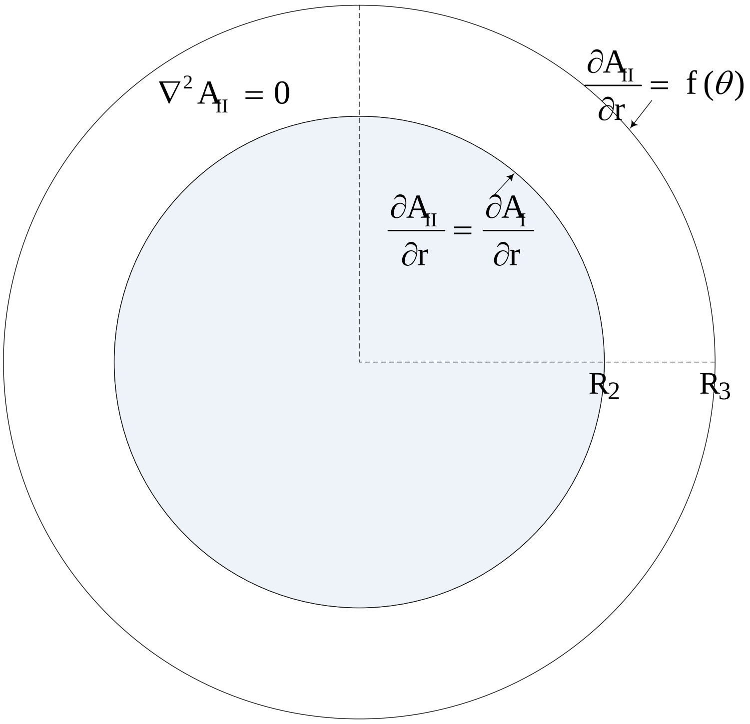

Figure E. 1 The airgap sub-domain and associated boundary conditions

The boundary condition at r = R3 is more complex because of the non-uniformity of the stator bore, i.e. slotting effect. Hence, the condition which takes into accounts both boundary and interface conditions can be written as follows:

$$f(\theta) = \begin{cases} \left.\dfrac{\partial A_I}{\partial r}\right|_{r=R_3} & \forall\ \theta \in [\theta_i, \theta_i + \beta] \\ 0 & \text{elsewhere} \end{cases} \tag{E-3}$$

Considering the boundary conditions (E-2) and (E-3), the general solution of the magnetic vector potential in the air gap sub domain can be obtained as

$$\begin{aligned} A_{II}(r,\theta) = {} & \sum_{n=1}^{\infty}\left(A_n^{II}\,\frac{R_2}{n}\,\frac{P_n(r,R_3)}{E_n(R_2,R_3)} \right. \\ & \left. + B_n^{II}\,\frac{R_3}{n}\,\frac{P_n(r,R_2)}{E_n(R_3,R_2)} \right) \times \cos(n\theta) \\ & + \sum_{n=1}^{\infty}\left(C_n^{II}\,\frac{R_2}{n}\,\frac{P_n(r,R_3)}{E_n(R_2,R_3)} \right. \\ & \left. + D_n^{II}\,\frac{R_3}{n}\,\frac{P_n(r,R_2)}{E_n(R_3,R_2)} \right) \times \sin(n\theta) \end{aligned} \tag{E-4}$$

Where, n is the harmonics term which is a positive integer. The constants A_n^{II}, B_n^{II}, C_n^{II} and D_n^{II} are evaluated using Fourier series expansions as follows:

$$A_n^{II} = \frac{1}{\pi}\int_0^{2\pi} \left.\frac{\partial A_I}{\partial r}\right|_{R_2} \cos(n\theta)\,d\theta \tag{E-5}$$

$$B_n^{II} = \frac{1}{\pi}\int_0^{2\pi} f(\theta)\,\cos(n\theta)\,d\theta \tag{E-6}$$

$$C_n^{II} = \frac{1}{\pi}\int_0^{2\pi} \left.\frac{\partial A_I}{\partial r}\right|_{R_2} \sin(n\theta)\,d\theta \tag{E-7}$$

$$D_n^{\,II} = \frac{1}{\pi}\int_0^{2\pi} f(\theta)\ \sin(n\theta)\,d\theta \qquad \text{(E-8)}$$

The expansions of the coefficients A_n^{II}, B_n^{II}, C_n^{II} and D_n^{II} are given in section E.4

E.2 SOLUTION IN THE SLOT SUB DOMAIN:

In order to get the magnetic vector potential, Poisson's equation is applied in the slot sub-domain. The superposition principle i.e. the general solution is sum of the general solution of corresponding Laplace's equation and a particular solution which satisfies the complete set of Poisson's equation (E-9), is considered in the solving process.

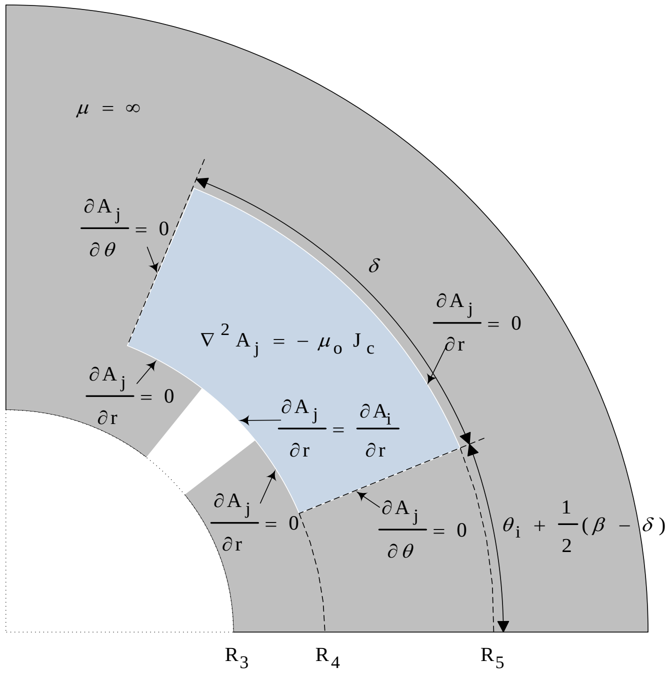

Figure E. 2 The slot sub-domain and associated boundary conditions

$$\frac{\partial^2 A_j(r,\theta)}{\partial r^2} + \frac{1}{r}\frac{\partial A_j(r,\theta)}{\partial r} + \frac{1}{r^2}\frac{\partial^2 A_j(r,\theta)}{\partial \theta^2} = -\mu_0 J_c$$

$$\text{for}\begin{cases} R_4 \le r \le R_5 \\ \theta_i + \frac{1}{2}(\beta - \delta) \le \theta \le \theta_i + \frac{1}{2}(\beta + \delta) \end{cases} \tag{E-9}$$

where, μo is permeability of the air. As shown in Figure E. 2, the tangential component of the magnetic field at side of the slot's wall and radial component of the magnetic field at the slot's wall at r = R5 are yields following boundary conditions.

$$\left.\frac{\partial A_j}{\partial \theta}\right|_{\theta = \theta_i + \frac{1}{2}(\beta - \delta)} = 0 \qquad \left.\frac{\partial A_j}{\partial \theta}\right|_{\theta = \theta_i + \frac{1}{2}(\beta + \delta)} = 0$$

$$\left.\frac{\partial A_j}{\partial r}\right|_{r = R_5} = 0 \tag{E-10}$$

At r = R4 the tangential component of the magnetic field in both and slot slot-opening sub-domains is equal and it becomes null elsewhere since the stator iron has infinite permeability as shown in Figure E. 2. Thus, the interface conditions between the slot sub-domain and slot-opening sub-domain are given by

$$\left.\frac{\partial A_j}{\partial r}\right|_{r=R_4} = \begin{cases} \left.\frac{\partial A_i}{\partial r}\right|_{r=R_4} & \forall\ \theta \in [\theta_i, \theta_i + \beta] \\ 0 & \text{elsewhere} \end{cases} \tag{E-11}$$

According to super position principle, considering the boundary conditions (E-10) and (E-11) the magnetic vector potential in the j^{th} slot is given by

$$A_j(r,\theta) = A_o^{\,j} + \frac{1}{2}\mu_o J_j\left(R_5^{\,2}\ln(r) - \frac{1}{2}r^2\right) + \sum_{m=1}^{\infty} A_m^{\,j}\,\frac{\delta R_4}{m\pi}\,\frac{P_{m\pi/\delta}(r,R_5)}{E_{m\pi/\delta}(R_4,R_5)} \times \cos\left(\frac{m\pi}{\delta}\left[\theta - \theta_i - \frac{1}{2}(\beta-\delta)\right]\right) \qquad \text{(E-12)}$$

where, m is the harmonics term which is a positive integer and J_j is current density in the j^th^ slot. The constants $A_o^{\,j}$ and $A_m^{\,j}$ are evaluated using Fourier series expansions of slot-opening interface over the slot interval at r = R_4 as follows:

$$A_0^{\,j} = \frac{1}{\delta}\int_{\theta_i}^{\theta_i+\beta} \left.\frac{\partial A_1}{\partial r}\right|_{R_4} d\theta \qquad \text{(E-13)}$$

$$A_m^{\,j} = \frac{2}{\delta}\int_{\theta_i}^{\theta_i+\beta} \left.\frac{\partial A_1}{\partial r}\right|_{R_4} \cos\left(\frac{m\pi}{\delta}\left(\theta - \theta_i - \frac{1}{2}(\beta-\delta)\right)\right) d\theta \qquad \text{(E-14)}$$

The expansions of the coefficients $A_o^{\,j}$ and $A_m^{\,j}$ are given in section E.4

E.3 SOLUTION IN THE PM SUB DOMAIN

The PM sub-domain and its associated boundary conditions are explained in Figure E. 3. In order to obtain the general solution in the PM sub-domain the following problem is solved.

$$\frac{\partial^2 A_1(r,\theta)}{\partial r^2} + \frac{1}{r}\frac{\partial A_1(r,\theta)}{\partial r} + \frac{1}{r^2}\frac{\partial^2 A_1(r,\theta)}{\partial \theta^2} = \frac{\mu_0}{r}\frac{\partial M}{\partial \theta} \qquad \text{(E-15)}$$

$$\text{for } \begin{cases} R_1 \le r \le R_2 \\ 0 \le \theta \le 2\pi \end{cases}$$

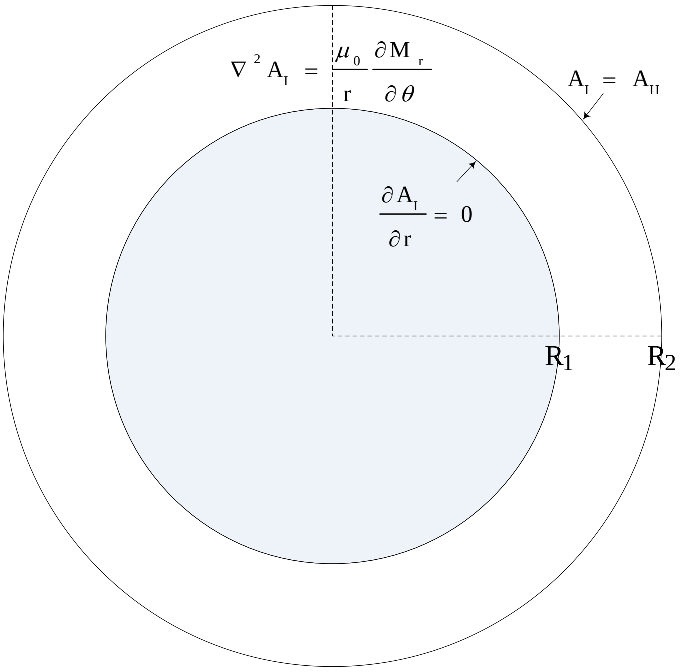

Figure E. 3 PM sub-domain and associated boundary conditions

where, $\overrightarrow{M}$ is the residual magnetization vector which amplitude is given as

$$M = \frac{B_r}{\mu_o} \tag{E-16}$$

where, B_r represents the remanence flux density and μ_o is permeability of the air. Thus, in polar coordinates, the magnetization of the magnet is given by

$$\overrightarrow{M} = M_r \vec{r} + M_\theta \vec{\theta} \tag{E-17}$$

Figure E. 4 shows the typical waveforms for M_r and M_θ, for radial magnetization and the components of which can be described over one pole pair p (with respect to the position θ) by

$$\begin{array}{ll}
\left.\begin{array}{l} M_r = 0 \\ M_\theta = 0 \end{array}\right\} & -\dfrac{\pi}{2p} \le \theta \le -\alpha\dfrac{\pi}{2p} \\
\left.\begin{array}{l} M_r = -\dfrac{B_r}{\mu_o} \\ M_\theta = 0 \end{array}\right\} & -\alpha\dfrac{\pi}{2p} \le \theta \le \alpha\dfrac{\pi}{2p} \\
\left.\begin{array}{l} M_r = 0 \\ M_\theta = 0 \end{array}\right\} & \alpha\dfrac{\pi}{2p} \le \theta \le (2-\alpha)\dfrac{\pi}{2p} \\
\left.\begin{array}{l} M_r = \dfrac{B_r}{\mu_o} \\ M_\theta = 0 \end{array}\right\} & (2-\alpha)\dfrac{\pi}{2p} \le \theta \le \alpha\dfrac{3\pi}{2p} \\
\left.\begin{array}{l} M_r = 0 \\ M_\theta = 0 \end{array}\right\} & \alpha\dfrac{3\pi}{2p} \le \theta \le \dfrac{3\pi}{2p}
\end{array} \tag{E-18}$$

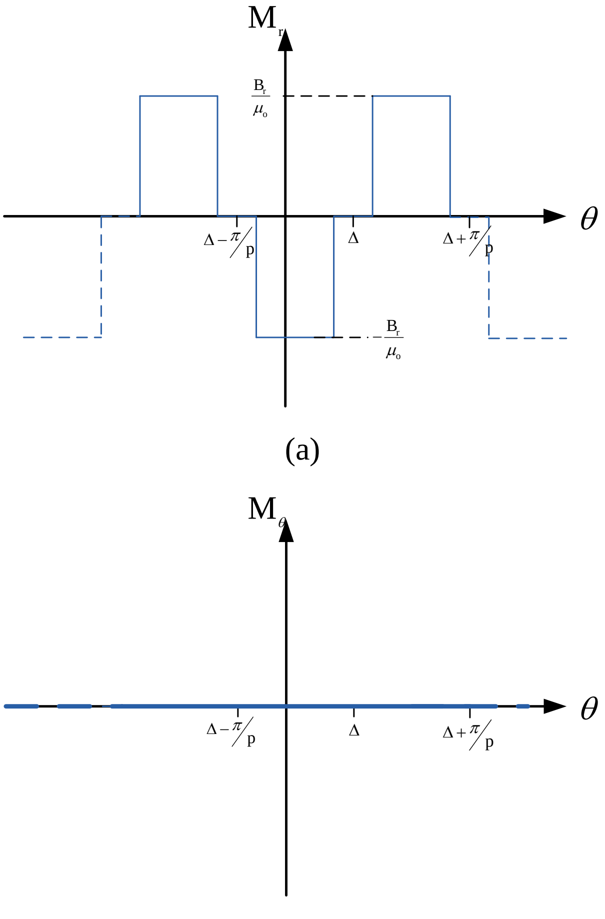

(a)

(b)

Figure E. 4 Illustration of the magnet's magnetization components (a) M_r and (b) M_θ along the θ direction

From the (E-18), it can be seen that the air space between the magnets is assumed to be occupied by unmagnetized permanent magnet material, i.e. $\overrightarrow{M} = 0$. Also for the magnet poles that are magnetised radially, M_{θ}, is zero. Thus, the radial magnetisation can be expressed in a Fourier series over a pole pair as [130]

$$M_r = \sum_{n=1,3,5...}^{\infty} M_{ar\,n} \cos(n\theta) + M_{br\,n} \sin(n\theta) \qquad \text{(E-19)}$$

where,

$$M_{ar\,n} = \sum_{n=1,2,3...}^{\infty} M_{r\,n} \cos(n\Delta) \qquad \text{(E-20)}$$

$$M_{br\,n} = \sum_{n=1,2,3...}^{\infty} M_{r\,n} \sin(n\Delta) \qquad \text{(E-21)}$$

where,

$$M_{r\,n} = \frac{2B_r}{\mu_o} \alpha \frac{\sin\left(\frac{n\pi\alpha}{2p}\right)}{\frac{n\pi}{2p}} \qquad \frac{n}{p} = 1, 3, 5..... \qquad \text{(E-22)}$$

where, n is harmonic terms which is positive integer and Δ represents the mechanical angular position of the rotor.

Associated PM sub-domains’ boundary conditions are:

$$\left.\frac{\partial A_I}{\partial r}\right|_{r = R_1} = 0$$

$$A_I(R_2, \theta) = A_{II}(R_2, \theta) \qquad \text{(E-23)}$$

Hence, considering boundary conditions (E-23), the obtained general solution of the magnetic vector potential in the PM sub-domain can be written as,

$$A_I(r,\theta) = \sum_{n=1}^{\infty}\left(A_n^{\,I}\,\frac{P_n(r,R_1)}{P_n(R_2,R_1)} + X_n(r)\,\cos(n\Delta)\right)\cos\left(n\theta\right)$$

$$+\sum_{n=1}^{\infty}\left(C_n^{\,I}\,\frac{P_n(r,R_1)}{P_n(R_2,R_1)} + X_n(r)\,\sin(n\Delta)\right)\sin\left(n\theta\right) \qquad \text{(E-24)}$$

where,

$$X_n(r) = -\frac{P_n(r,R_1)}{P_n(R_2,R_1)}\left(\frac{R_1}{n}\left(\frac{R_1}{R_2}\right)^n f_n{}'(R_1) + f_n(R_2)\right)$$

$$+\left(\frac{R_1}{n}\left(\frac{R_1}{r}\right)^n f_n{}'(R_1) + f_n(r)\right) \qquad \text{(E-25)}$$

and

$$f_n(r) = \begin{cases} \dfrac{4B_r\,p}{\pi\left(1-n^2\right)}\, r\cos\left(\dfrac{n\pi}{2p}\left(1-\alpha\right)\right) & \text{if } n = lp \ \text{ with } l = 1,3,5..... \\ \dfrac{2B_r}{\pi}\, r\ \ln(r)\ \cos\left(\dfrac{\pi}{2}\left(1-\alpha\right)\right) & \text{if } n = p = 1 \\ 0 & \text{otherwise} \end{cases} \qquad \text{(E-26)}$$

The constants $A_n^{\,I}$ and $C_n^{\,I}$ are evaluated using Fourier series expansions of airgap interface over the interval 2π at $r = R_2$ as follows:

$$A_n^{\,I} = \frac{1}{\pi}\int_0^{2\pi} A_{II}(R_2,\theta)\ \cos\left(n\theta\right)\,d\theta \qquad \text{(E-27)}$$

$$C_n^{\,I} = \frac{1}{\pi}\int_0^{2\pi} A_{II}(R_2,\theta)\ \sin\left(n\theta\right)\,d\theta \qquad \text{(E-28)}$$

The expansions of the coefficients $A_n^{\,I}$ and $C_n^{\,I}$ are given in next section.

E.4 COEFFICIENT COMPUTATION FOR MAGNETO STATIC PROBLEM:

For the simplification in the coputation of the coefficients, the following integral forms are calculated first and than included in the complete equation.

$$f_a\,(k,n,i) = \int_{\theta_i}^{\theta_i+\beta} \cos\left(n\theta\right) \times \cos\left(\frac{k\pi}{\beta}\left(\theta - \theta_i\right)\right) d\theta \tag{E-29}$$

$$g_a\,(k,n,i) = \int_{\theta_i}^{\theta_i+\beta} \sin\left(n\theta\right) \times \cos\left(\frac{k\pi}{\beta}\left(\theta - \theta_i\right)\right) d\theta \tag{E-30}$$

$$r_a\,(n,i) = \int_{\theta_i}^{\theta_i+\beta} \cos\left(n\theta\right)\, d\theta \tag{E-31}$$

$$s_a\,(n,i) = \int_{\theta_i}^{\theta_i+\beta} \sin\left(n\theta\right)\, d\theta \tag{E-32}$$

$$\begin{aligned} F_a\,(m,k) = \int_{\theta_i}^{\theta_i+\beta} \cos\left(\frac{m\pi}{\delta}\left[\theta - \theta_i - \frac{1}{2}(\beta - \delta)\right]\right) \\ \times\cos\left(\frac{k\pi}{\beta}\left(\theta - \theta_i\right)\right) d\theta \end{aligned} \tag{E-33}$$

The expansions of (5.16) and (5.17) for the slot-opening sub-domain are given as follows:

$$\begin{aligned} 0 = -A_o^{\,i} - B_o^{\,i}\ln(R_3) + \sum_{n=1}^{\infty} \Bigg(A_n^{\,II}\,\frac{R_2}{n\beta}\,\frac{2}{E_n\,(R_2,R_3)} \\ + B_n^{\,II}\,\frac{R_3}{n\beta}\,\frac{P_n\,(R_3,R_2)}{E_n\,(R_3,R_2)} \Bigg) \times r_a\,(n,i) \\ + \sum_{n=1}^{\infty} \Bigg(C_n^{\,II}\,\frac{R_2}{n\beta}\,\frac{2}{E_n\,(R_2,R_3)} \\ + D_n^{\,II}\,\frac{R_3}{n\beta}\,\frac{P_n\,(R_3,R_2)}{E_n\,(R_3,R_2)} \Bigg) \times s_a\,(n,i) \end{aligned} \tag{E-34}$$

$$
\begin{aligned}
0 = & -A_o^{\,i} - B_o^{\,i}\ln(R_4) + A_o^{\,j} \\
& + \frac{1}{2}\mu_o J_c^{\,j}\sin(\Delta_e)\left[R_5^{\,2}\ln(R_4) - \frac{R_4^{\,2}}{2}\right] \\
& + \sum_{m=1}^{\infty} A_m^{\,j}\left(\frac{2R_4}{\beta}\left(\frac{\delta}{m\pi}\right)^2 \frac{P_{m\pi/\delta}(R_4,R_5)}{E_{m\pi/\delta}(R_4,R_5)}\right. \\
& \qquad \left.\times\sin\left(\frac{m\pi\beta}{2\delta}\right)\cos\left(\frac{m\pi}{2}\right)\right)
\end{aligned}
\tag{E-35}
$$

where, Δ_e is angle of the excitation current density in the j^{th} slot with respect to position of the rotor (Δ). In order to perform the time stepping in the calculation, the angle for different slots is introduced in a matrix form. For instance, the matrix form of 12-slot/ 14-pole configurations is given below.

$$
A=\sin\left(\Delta_e\right) \qquad B=\sin\left(\Delta_e-\frac{2\pi}{3}\right) \qquad C=\sin\left(\Delta_e+\frac{2\pi}{3}\right)
$$

$$
M=\begin{bmatrix} A & -A & -B & B & C & -C & -A & A & B & -B & -C & C \end{bmatrix}
$$

Evaluation of (5.18) and (5.19) are given as follows:

$$
\begin{aligned}
0 = & -A_k^{\,i} + \sum_{n=1}^{\infty}\left(A_n^{\,II}\frac{2R_2}{n\beta}\frac{2}{E_n(R_2,R_3)}\right. \\
& \qquad \left. + B_n^{\,II}\frac{2R_3}{n\beta}\frac{P_n(R_3,R_2)}{E_n(R_3,R_2)}\right)\times f_a(k,n,i) \\
& + \sum_{n=1}^{\infty}\left(C_n^{\,II}\frac{2R_2}{n\beta}\frac{2}{E_n(R_2,R_3)}\right. \\
& \qquad \left. + D_n^{\,II}\frac{2R_3}{n\beta}\frac{P_n(R_3,R_2)}{E_n(R_3,R_2)}\right)\times g_a(k,n,i)
\end{aligned}
\tag{E-36}
$$

$$
0=-B_k^{\,i}+\sum_{m=1}^{\infty}A_m^{\,j}\left(\frac{2\delta R_4}{m\pi\beta}\frac{P_{m\pi/\beta}(R_4,R_5)}{E_{m\pi/\beta}(R_4,R_5)}\right)\times F_a(m,k) \tag{E-37}
$$

where, subscripts of coefficients (A_o^i, B_o^i, A_k^i and B_k^i) represents the order of the harmonics and superscripts are corresponding i^th^ slot-opening domain.

The expansions of coefficients A_n^{II}, B_n^{II}, C_n^{II} and D_n^{II} are:

$$0 = -A_n^{II} + A_n^{I}\frac{n}{R_2}\frac{E_n(R_2,R_1)}{P_n(R_2,R_1)} + X_n'(R_2)\cos(n\Delta) \tag{E-38}$$

$$0 = -C_n^{II} + C_n^{I}\frac{n}{R_2}\frac{E_n(R_2,R_1)}{P_n(R_2,R_1)} + X_n'(R_2)\sin(n\Delta) \tag{E-39}$$

where, X_n' is $(dX_n(r))/d_r|_{r = R2}$ and $X_n(r)$ is given in(E-25).

$$\begin{aligned} 0 = -B_n^{II} &+ \sum_{i=1}^{Q} B_o^i\left(\frac{1}{\pi R_3}\right) r_a(n,i) \\ &+ \sum_{i=1}^{Q}\sum_{k=1}^{\infty} A_k^i \frac{k}{\beta R_3}\frac{P_{k\pi/\beta}(R_3,R_4)}{E_{k\pi/\beta}(R_3,R_4)} \times f_a(k,n,i) \\ &- \sum_{i=1}^{Q}\sum_{k=1}^{\infty} B_k^i \frac{k}{\beta R_3}\frac{2}{E_{k\pi/\beta}(R_3,R_4)} \times f_a(k,n,i) \end{aligned} \tag{E-40}$$

$$\begin{aligned} 0 = -D_n^{II} &+ \sum_{i=1}^{Q} B_o^i\left(\frac{1}{\pi R_3}\right) s_a(n,i) \\ &+ \sum_{i=1}^{Q}\sum_{k=1}^{\infty} A_k^i \frac{k}{\beta R_3}\frac{P_{k\pi/\beta}(R_3,R_4)}{E_{k\pi/\beta}(R_3,R_4)} \times g_a(k,n,i) \\ &- \sum_{i=1}^{Q}\sum_{k=1}^{\infty} B_k^i \frac{k}{\beta R_3}\frac{2}{E_{k\pi/\beta}(R_3,R_4)} \times g_a(k,n,i) \end{aligned} \tag{E-41}$$

It is worth to note that the mutual coupling between the slots is included by the summing operation on Q number of slot as explained in (E-40) and (E-41).

The expansions of coefficients A_o^j and A_m^j for the slot sub-domain

$$0 = -A_o^{\,j} + B_o^{\,i}\frac{\beta}{\delta R_4} + \sum_{k=1}^{\infty}\left(A_k^{\,i}\frac{2}{E_{k\pi/\beta}(R_3,R_4)} - B_k^{\,i}\frac{P_{k\pi/\beta}(R_4,R_3)}{E_{k\pi/\beta}(R_3,R_4)}\right)\frac{2\sin(k\pi)}{\delta R_4} \qquad \text{(E-42)}$$

$$0 = -A_m^{\,j} + B_o^{\,i}\frac{4}{m\pi R_4}\sin\left(\frac{m\pi\beta}{2\delta}\right)\cos\left(\frac{m\pi}{2}\right) + \sum_{k=1}^{\infty}\left(A_k^{\,i}\frac{2}{E_{k\pi/\beta}(R_3,R_4)} - B_k^{\,i}\frac{P_{k\pi/\beta}(R_4,R_3)}{E_{k\pi/\beta}(R_3,R_4)}\right)\frac{2k\pi}{\delta\beta R_4}\times F_a(m,k) \qquad \text{(E-43)}$$

The expansions of coefficients A_n^I and C_n^I for the PM sub-domain:

$$0 = -A_n^{\,I} + A_n^{\,II}\frac{R_2}{n}\frac{P_n(R_2,R_3)}{E_n(R_2,R_3)} + B_n^{\,II}\frac{R_3}{n}\frac{2}{E_n(R_3,R_2)} \qquad \text{(E-44)}$$

$$0 = -C_n^{\,I} + C_n^{\,II}\frac{R_2}{n}\frac{P_n(R_2,R_3)}{E_n(R_2,R_3)} + D_n^{\,II}\frac{R_3}{n}\frac{2}{E_n(R_3,R_2)} \qquad \text{(E-45)}$$

In addition, the following relation is obtained between the coefficient B_o^i and the current density in the slot (J_c) by equating (5.15) and (E-12) according to the interface condition (E-11).

$$B_o^{\,i} = \frac{\delta}{2\beta}\mu_o J_c^{\,j}\sin(\Delta_e)\left(R_5^{\,2} - R_4^{\,2}\right) \quad \text{with } i = j \qquad \text{(E-46)}$$

From the system of linear equations given in above, the coefficients of different sub-domains are evaluated by solving the equation in a form of matrix numerically. The mathematical software Matlab® is used in the solving process.

E.5. COEFFICIENT COMPUTATION FOR TIME HARMONIC PROBLEM

Expansion of (5.35) given by,

$$\overline{C_o^{\,j}} = B_o^{\,i}\frac{\beta}{\delta R_4} + \sum_{k=1}^{\infty}\left(A_k^{\,i}\frac{2}{E_{k\pi/\beta}(R_3,R_4)} - B_k^{\,i}\frac{P_{k\pi/\beta}(R_4,R_3)}{E_{k\pi/\beta}(R_3,R_4)}\right) \times \frac{2\sin(k\pi)}{\delta R_4} \qquad \text{(E-47)}$$

Development of (5.36) can be expressed as follows:

$$\overline{C_m^{\,j}} = B_o^{\,i}\frac{4}{m\pi R_4}\sin\left(\frac{m\pi\beta}{\delta}\right)\cos\left(\frac{m\pi}{2}\right) + \sum_{k=1}^{\infty}\left(A_k^{\,i}\frac{2}{E_{k\pi/\beta}(R_3,R_4)} - B_k^{\,i}\frac{P_{k\pi/\beta}(R_4,R_3)}{E_{k\pi/\beta}(R_3,R_4)}\right) \times \frac{2k\pi}{\delta\beta R_4}F_a(m,k) \qquad \text{(E-48)}$$

E.6. BACK-EMF, FLUX DENSITY AND TORQUE CALCULATION:

Since the magnetic vector potential can be obtained everywhere in the sub-domains, the analytical tool also can be used to evaluate machine's performance such as back-EMF, torque, cogging torque, etc. The computation of back-EMF, torque and also flux density are described below.

E.6.1 FLUX DENSITY CALCULATION

The radial, tangential and magnitude of the flux density are:

$$B_r = \frac{1}{r}\frac{\partial A(r,\theta)}{\partial \theta} \tag{E-49}$$

$$B_\theta = -\frac{\partial A(r,\theta)}{\partial r} \tag{E-50}$$

$$B = \sqrt{B_r + B_\theta} \tag{E-51}$$

Hence, the radial and tangential flux density components in the different sub-domains can be obtained by differentiating the corresponding expression of vector potential A. Obtained flux density in the airgap sub-domain for 12-slot/14-pole machine is shown below.

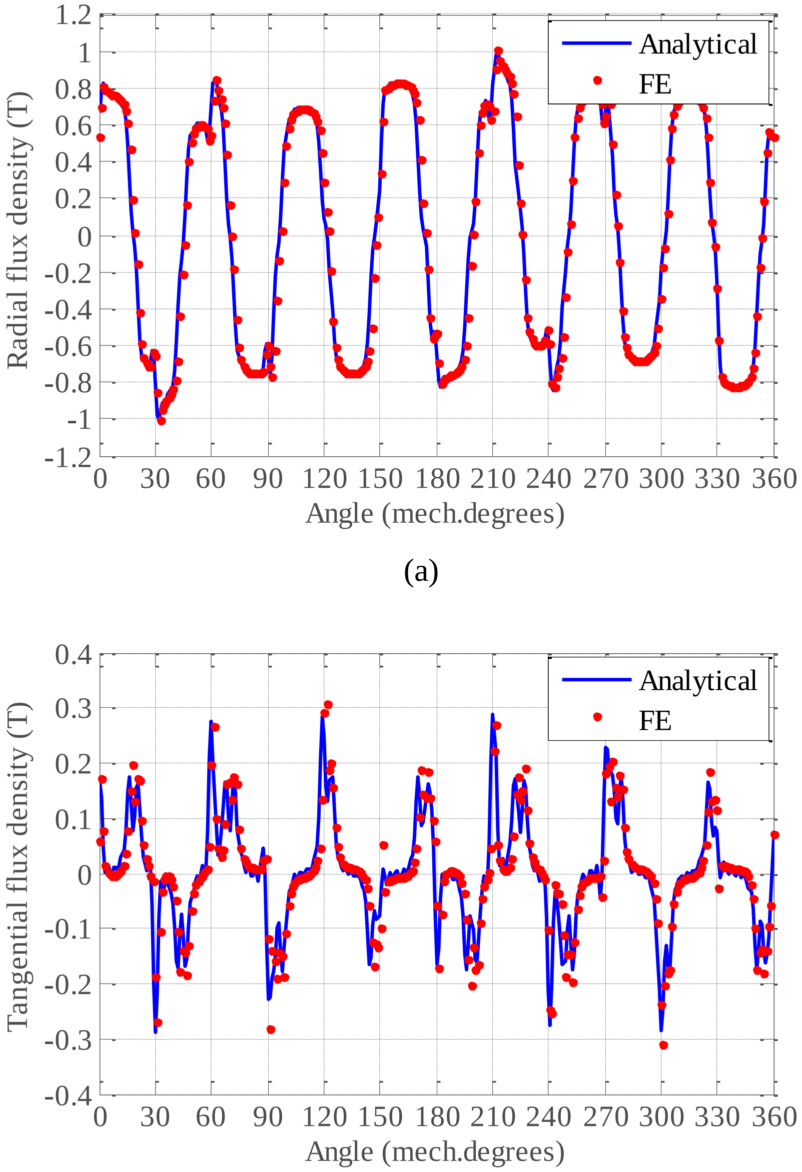

(a)

(b)

Figure E. 5 (a) Radial and (b) tangential component of the flux density in the middle (r = 31mm) of the airgap sub-domain at load condition

E.6.2 BACK-EMF CALCULATION

The back-EMF induced in the phase windings can be calculated by estimating total flux ϑ over the slot area A_s for given rotor position Δ. The total flux ϑ in a slot can be written as

$$\vartheta = \frac{l_{stk}}{A_s} \iint_{A_s} A_j(r,\theta)\ r\ dr d\theta \tag{E-52}$$

where, the trapezoidal slot area A_s given by

$$A_s = \delta \frac{\left(R_5{}^2 - R_4{}^2\right)}{2} \tag{E-53}$$

and the vector potential is averaged over the slot area since the slot has uniformly distributed current density. Hence, the back-EMF induced in a phase winding can be expressed as

$$e = \omega_{rm} \frac{\partial N\vartheta}{\partial \Delta} \tag{E-54}$$

where, ω_{rm} represents the rotor rotational speed in rad/s and N is number of per turns phase windings. Obtained back-EMF waveform for considered 12-slot/14-pole machine is given below.

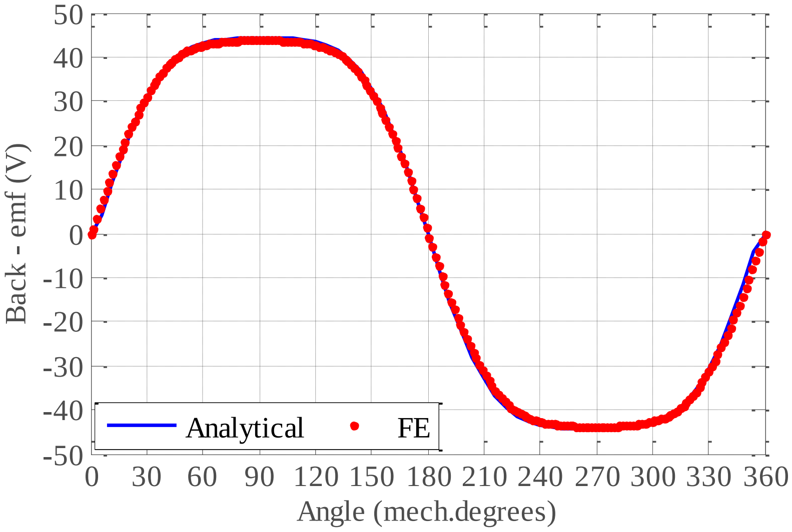

Figure E. 6 Comparison between analytically calculated and FE computed back-EMF

E6.3 TORQUE CALCULATION

Using well known Maxwell stress tensor the electromagnetic torque can be estimated as follows

$$T_e = \frac{l_{stk} R_c}{\mu_o} \int_0^{2\pi} B_r^{II}(R_c,\theta) B_\theta^{II}(R_c,\theta) \; d\theta \tag{E-55}$$

where, R_c is the radius in the airgap sub-domain and B_r, B_θ are radial and tangential component in the airgap sub-domain respectively. Obtained cogging torque, torque and torque-current waveform for considered 12-slot/14-pole machine is given below.

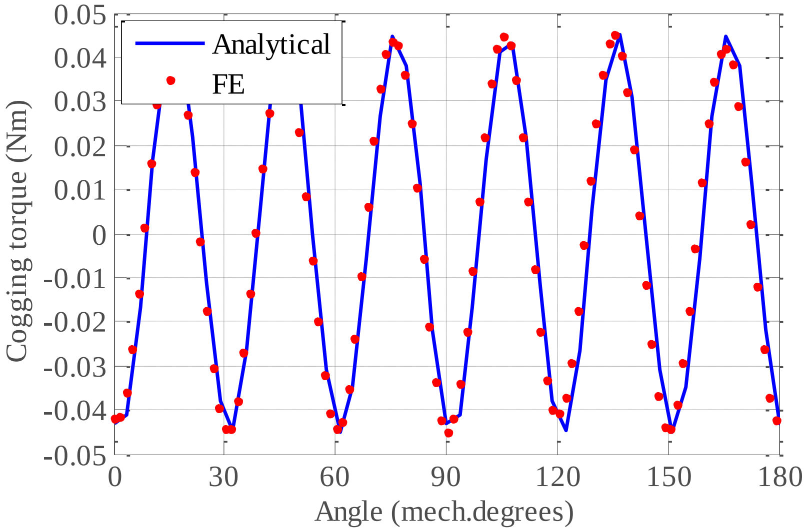

Figure E. 7 Comparison between analytically calculated and FE computed cogging torque

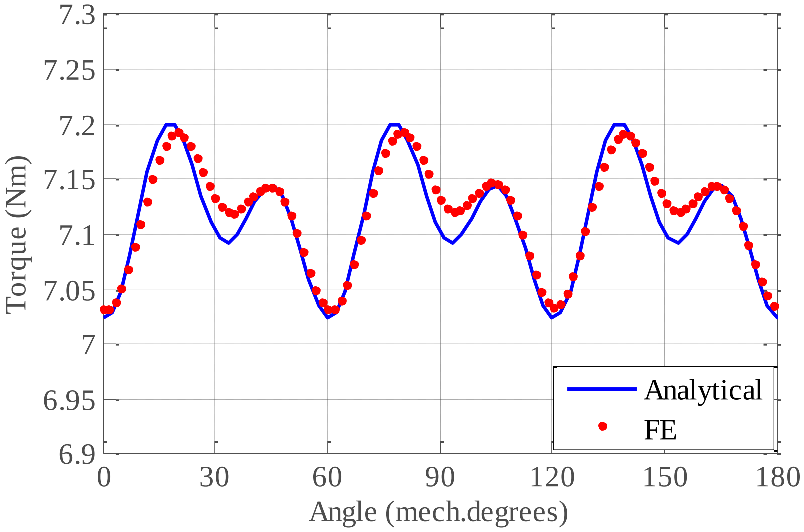

Figure E. 8 Comparison between analytically calculated and FE computed torque at rated condition

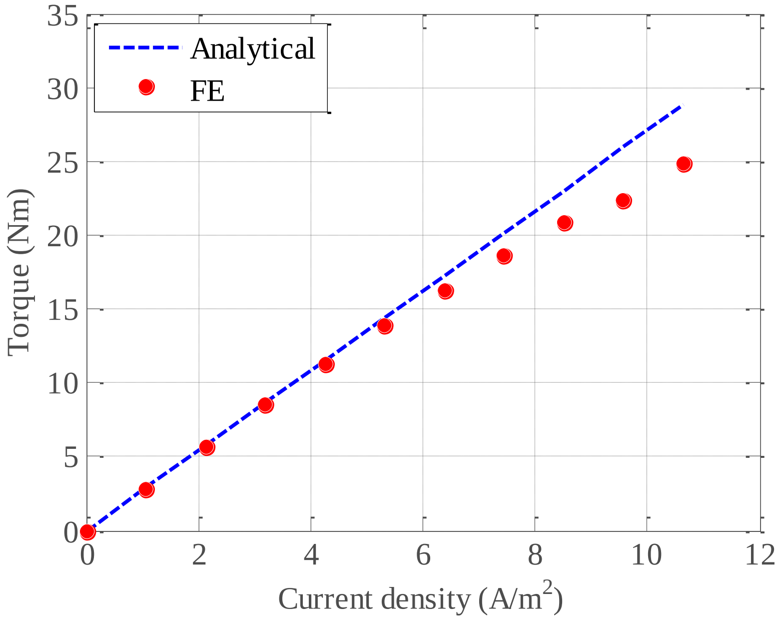

Figure E. 9 Torque – current characteristic of the machine

E.7 RESULTS FOR 12-SLOT/ 14-POLE PM MACHINE:

E.7.1 FIELD OBTAINED FROM MAGNETO STATIC PROBLEM

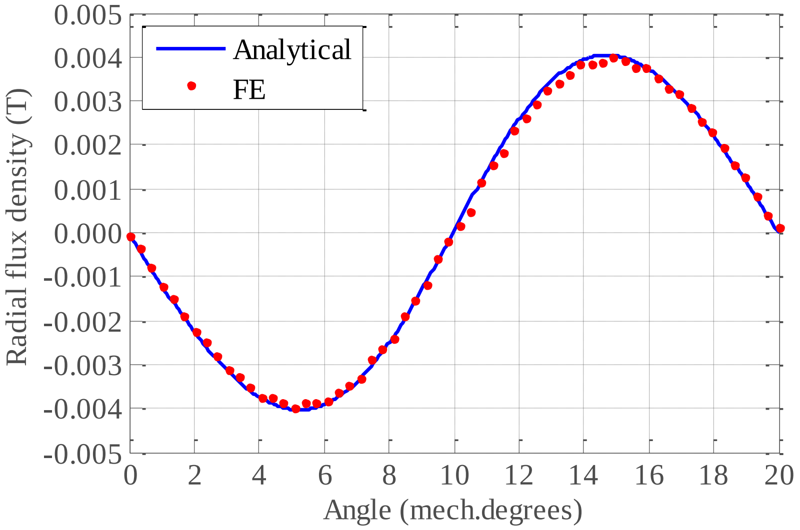

(a)

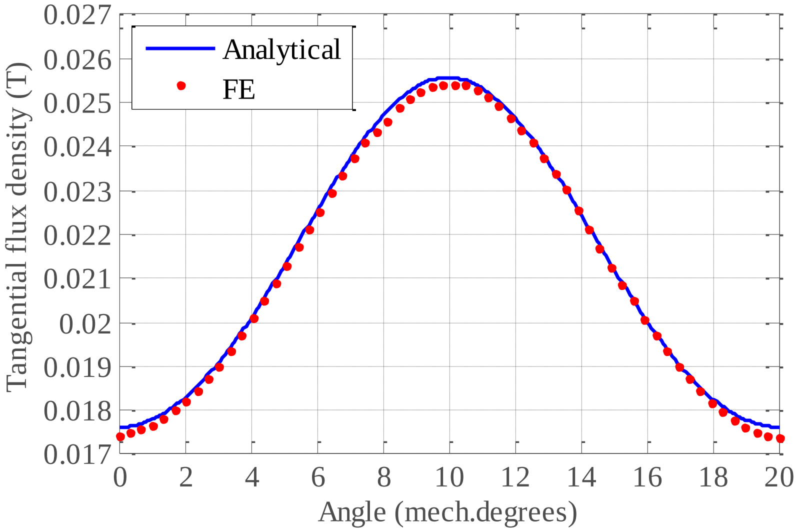

(b)

Figure E. 10 (a) Radial and (b) tangential component of the flux density in the middle (r = 40mm) of the slot sub-domain at load condition

E.7.2 FIELD OBTAINED FROM TIME-HARMONIC PROBLEM

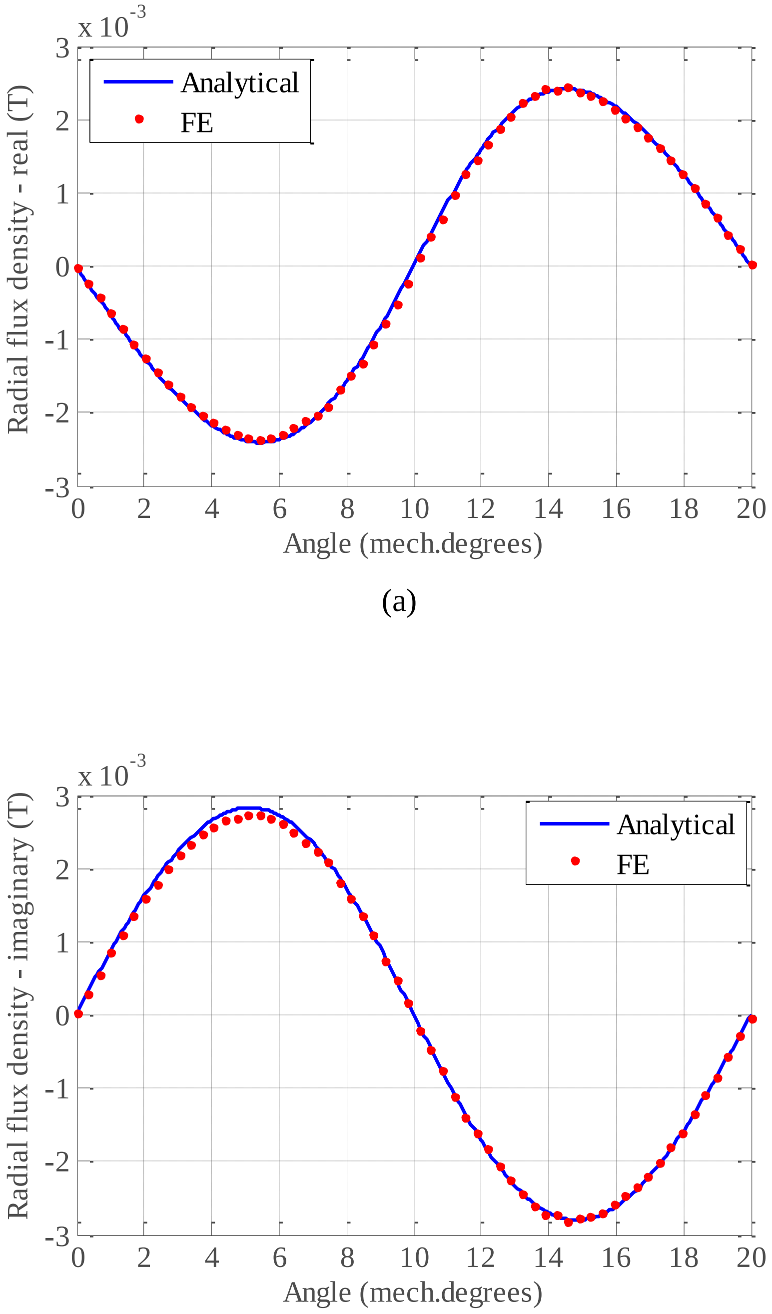

(a)

(b)

Figure E. 11 (a) Real and (b) imaginary parts of the radial flux density components in the middle of the slot (r = 40mm) at frequency f = 233.33 Hz

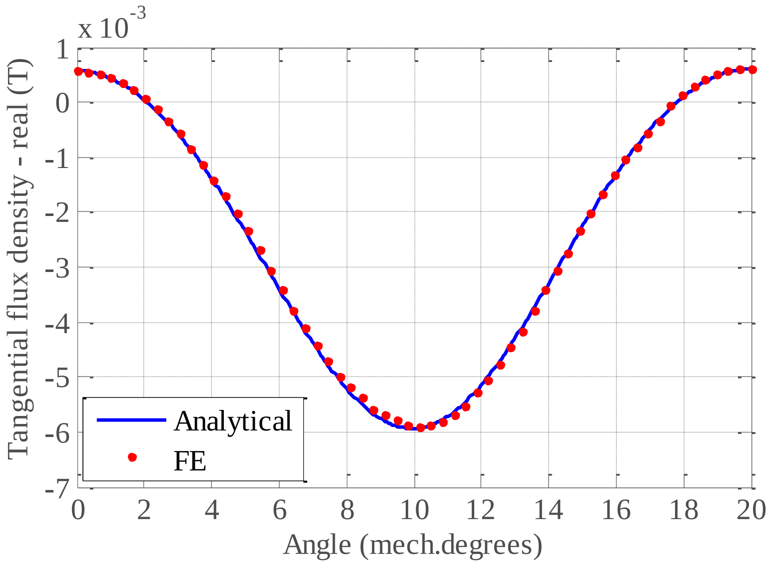

(a)

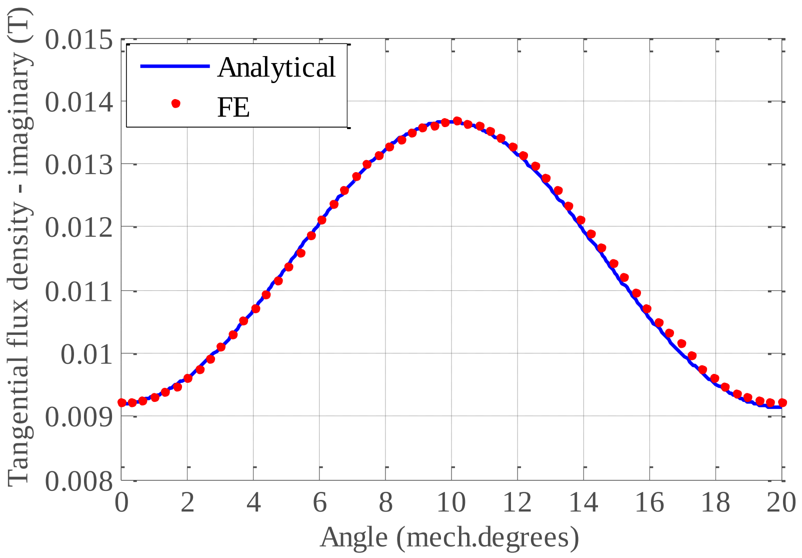

(b)

Figure E. 12 (a) Real and (b) imaginary parts of the tangential flux density components in the middle of the slot (r = 40mm) at frequency f = 233.33 Hz

E.8 EXAMPLE 2: 6-SLOT/ 4-POLE FT-PM MACHINE

As an example a 6-slot/ 4-pole concentrated winding PM machine is also considered; its parameters are given in

Table E -1. Obtained results are added below.

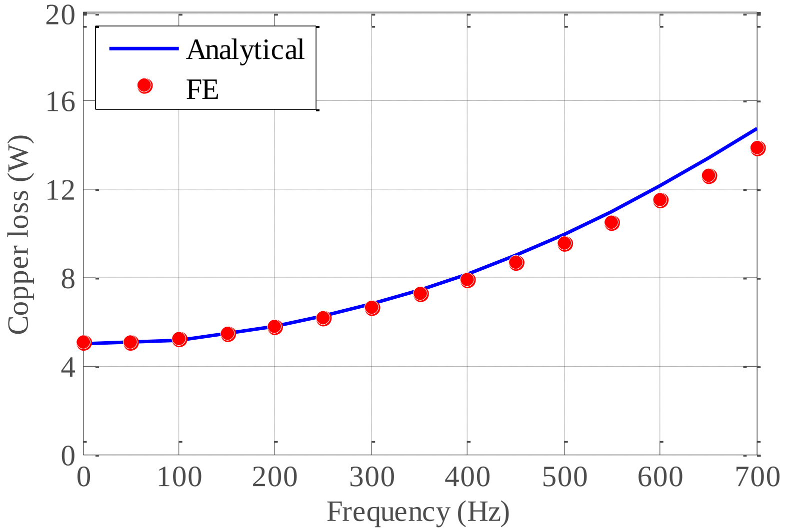

Figure E. 13 Magneto static field solution based and FE calculated RCW machine copper loss vs. frequency for the 6-slot 4-pole PM machine

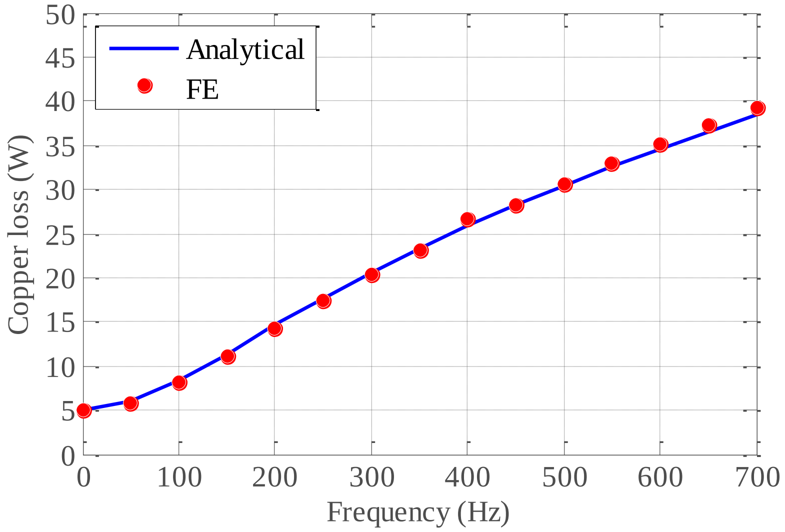

Figure E. 14 Time-harmonic field solution based and FE calculated VSW copper loss vs. frequency for the 6-slot 4-pole PM machine

SPECIFICATIONS	VALUE
Number of pole pairs (p)	2
Number of stator slots (Q)	6
Number of turns per phase (N_{ph})	42
Current density (J_{rms})	2.29 A/mm^2
Remanence flux density of the PM (B_{rem})	1.08 T
Inner radius of the rotor yoke (R_1)	20.00 mm
Stator inner radius (R_3)	28.00 mm
Stator outer radius (R_5)	45.00 mm
Magnet depth (R_2-R_1)	7.00 mm
Tooth-tip height (R_4-R_3)	2.00 mm
Depth of stator back iron	5.00 mm
Axial length (l_{stk})	100.00 mm
Slot width angle (δ)	30 mech.degrees
Slot opening angle (β)	12 mech.degrees
Magnet span (α)	0.833

Table E -1 Specifications of the 6-slot 4-pole PM machine

Appendix - F

Machine 1: Parallel slot configuration

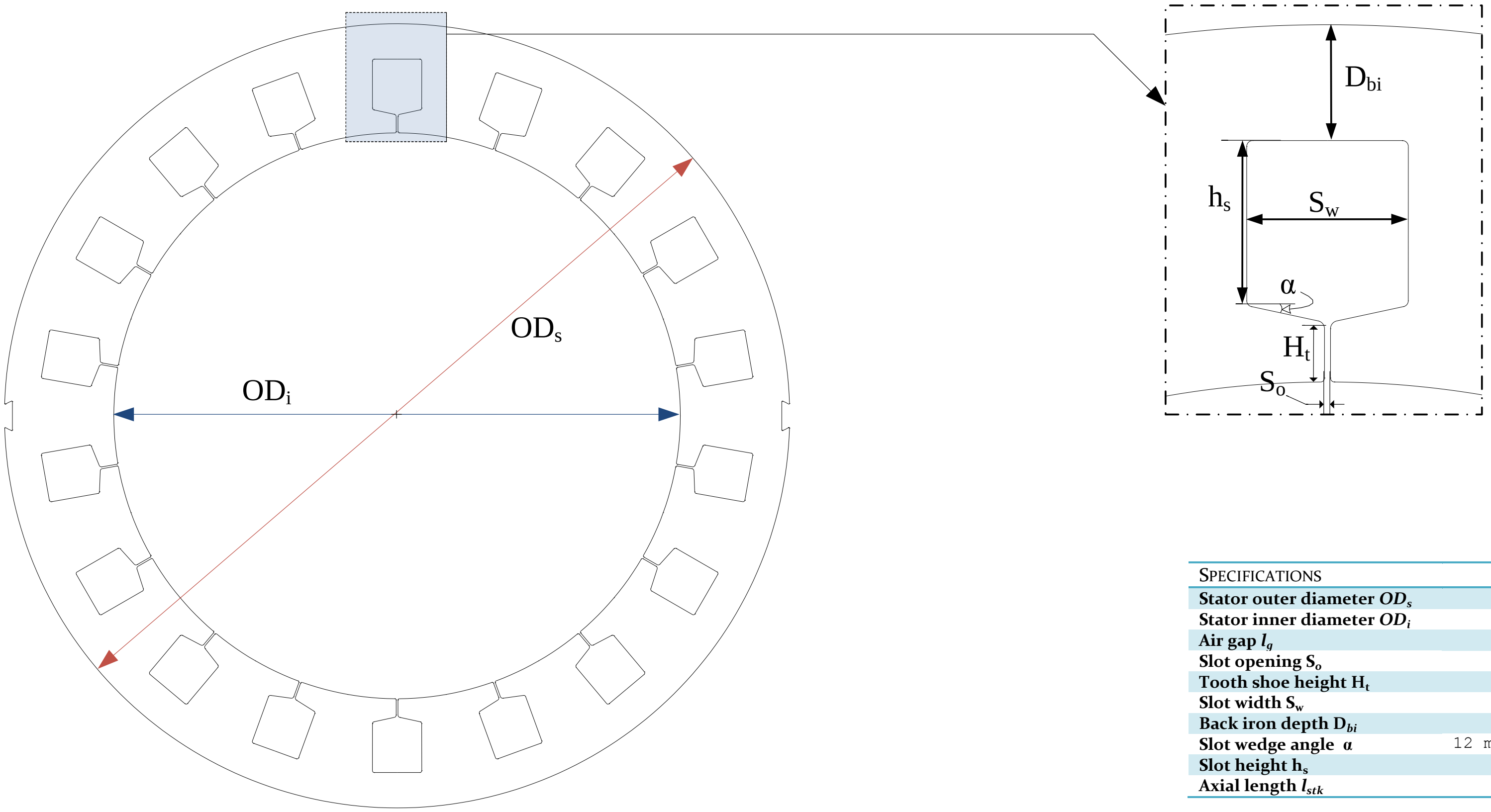

SPECIFICATIONS	VALUES
Stator outer diameter OD_s	128.9000 mm
Stator inner diameter OD_i	93.0000 mm
Air gap l_g	2.0000 mm
Slot opening S_o	0.3000 mm
Tooth shoe height H_t	3.0000 mm
Slot width S_w	8.0899 mm
Back iron depth D_{bi}	5.8206 mm
Slot wedge angle α	12 mech.degrees
Slot height h_s	8.0820 mm
Axial length l_{stk}	37.7200 mm

Machine 2: Parallel teeth configuration

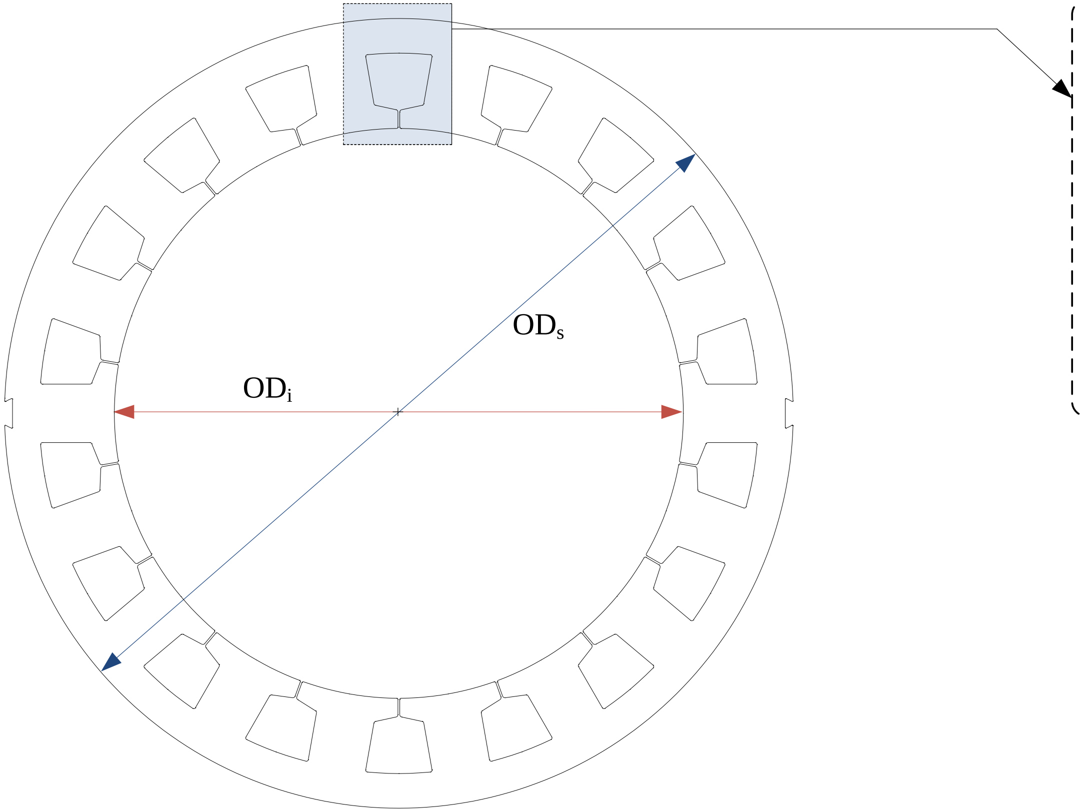

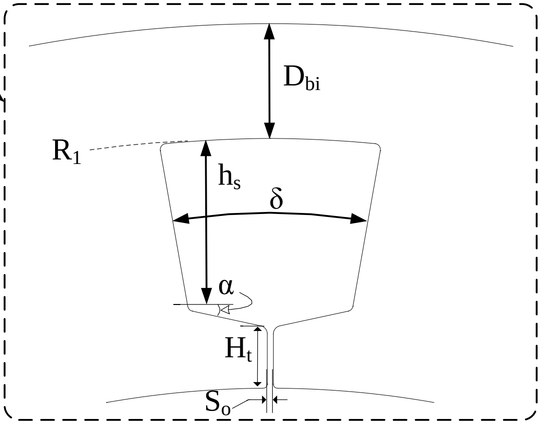

SPECIFICATIONS	VALUES
Stator outer diameter OD_s	128.9000 mm
Stator inner diameter OD_i	93.0000 mm
Air gap l_g	2.0000 mm
Slot opening S_o	0.3000 mm
Tooth shoe height H_t	3.0000 mm
Slot width angle δ	10.7 mech.degrees
Back iron depth D_{bi}	5.6130 mm
Slot wedge angle α	12 mech.degrees
Radius R_1	58.7829 mm
Slot height h_s	8.0820 mm
Axial length l_{stk}	37.7200 mm

Rotor

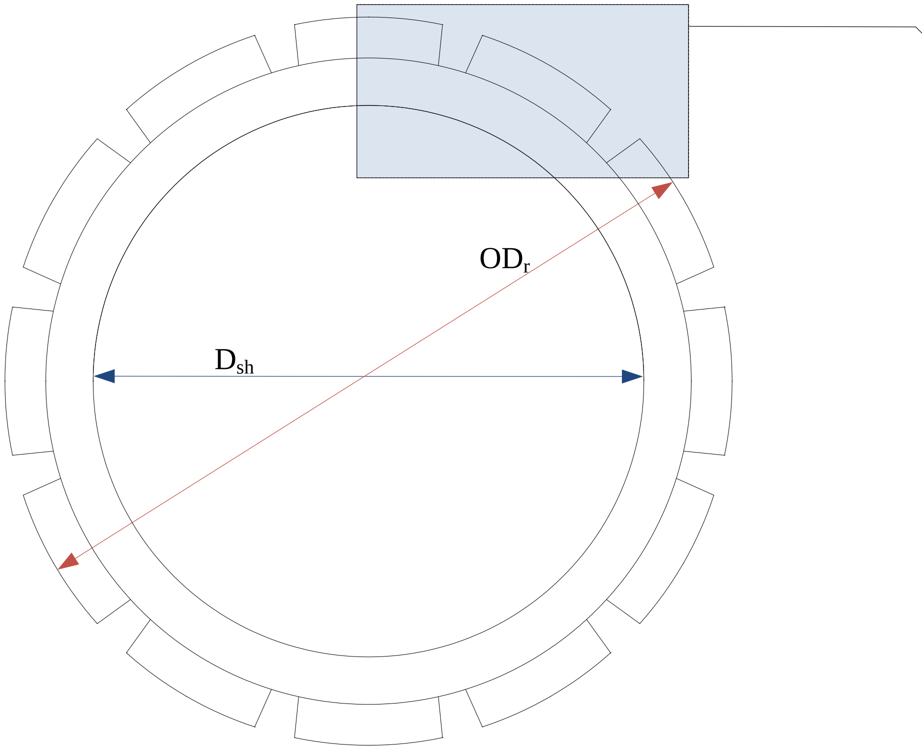

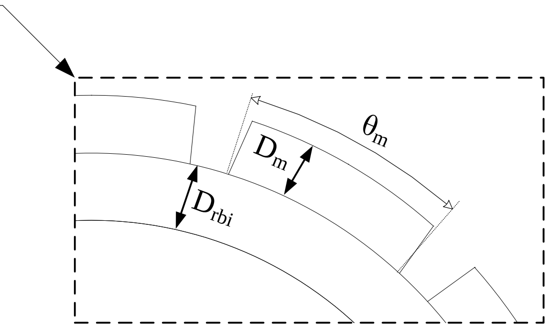

SPECIFICATIONS	VALUES
Rotor outer diameter OD_r	89.0000 mm
Shaft diameter D_{sh}	67.4000 mm
Rotor iron depth $\mathrm{D}_{\mathrm{rbi}}$	5.8000 mm
Magnet depth D_{m}	5.0000 mm
Magnet angle θ_{m}	25 mech.degrees
Magnet span	0.8333
Axial length l_{stk}	37.7200 mm

Appendix - G

G.1 EXPERIMENTAL PROTOTYPE OF FT-PM MACHINE

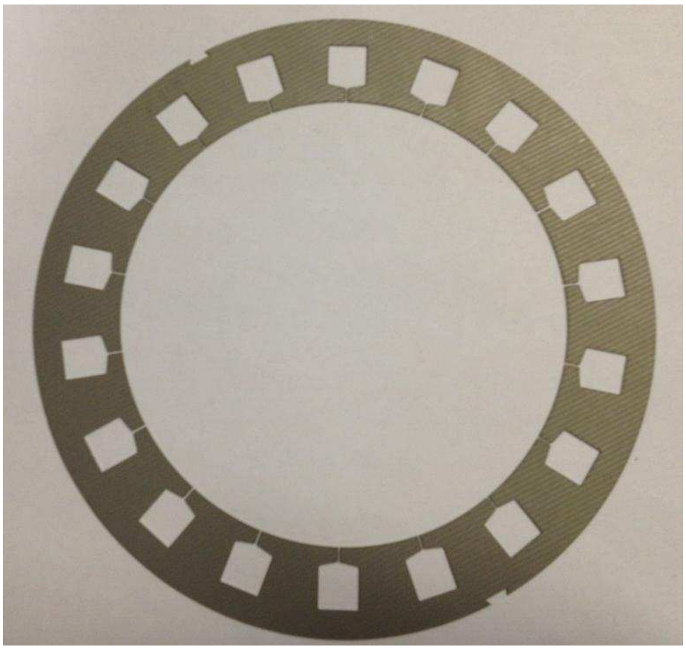

Figure G 1 A lamimation of the parallel slot design

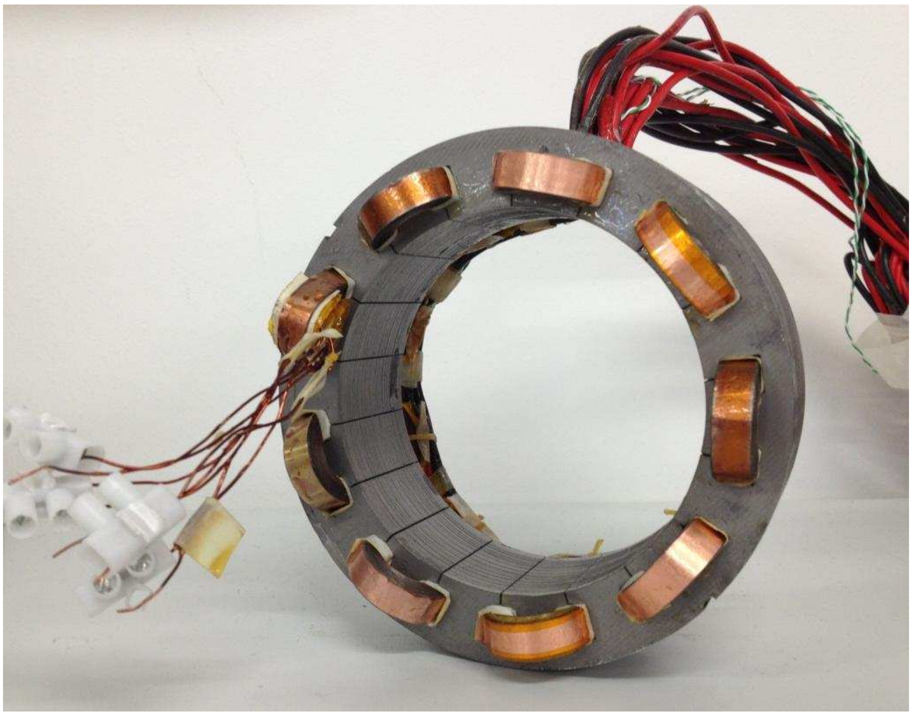

(a)

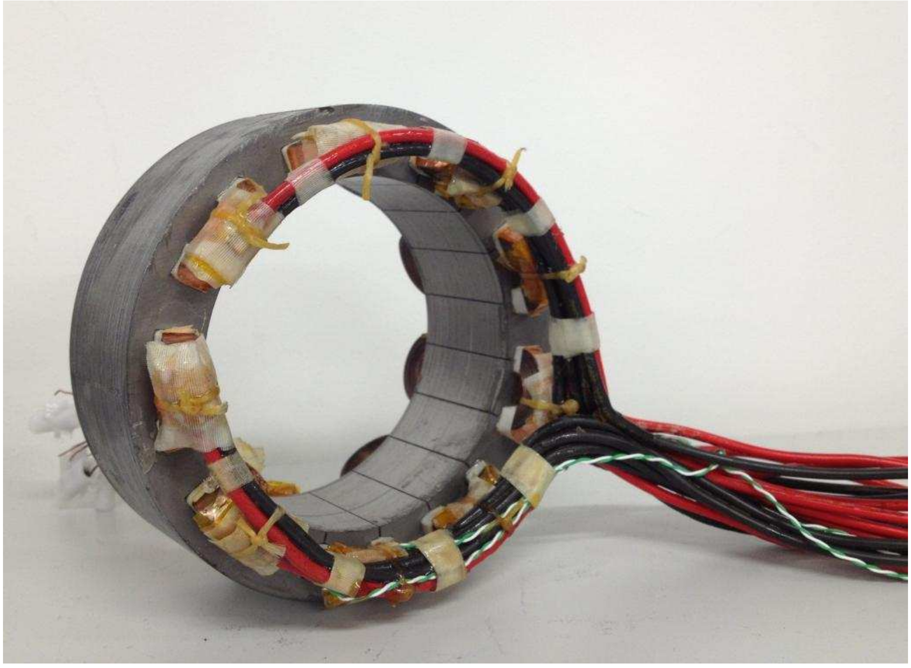

(b)

Figure G 2 VSW wound parallel slot stator: (a) view 1 and (b) view 2

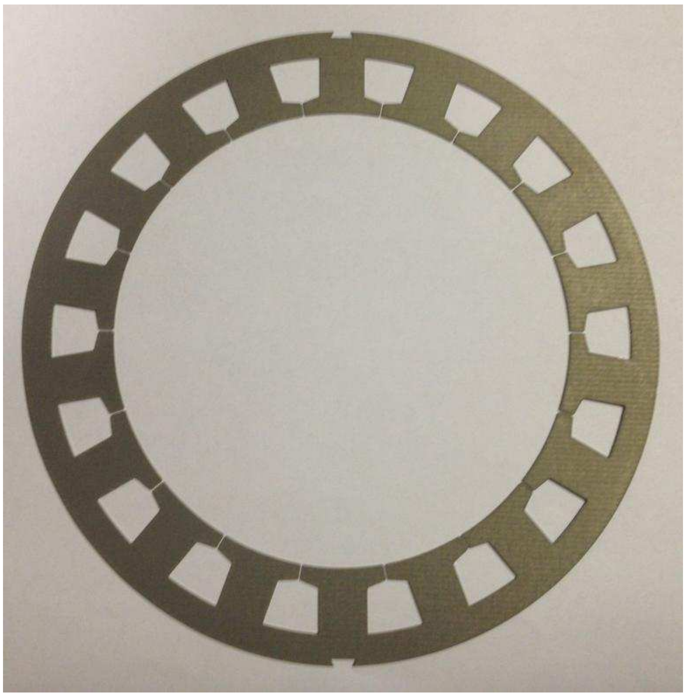

Figure G 3 A lamimation of the trapzoidal slot design

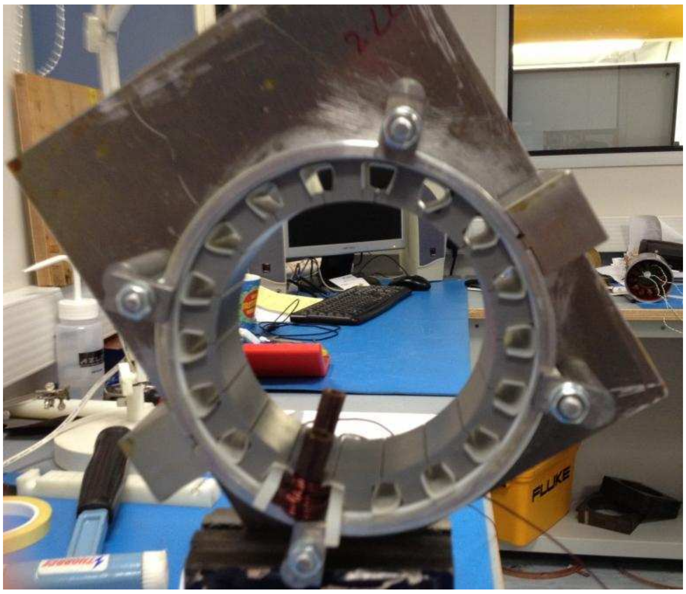

(a)

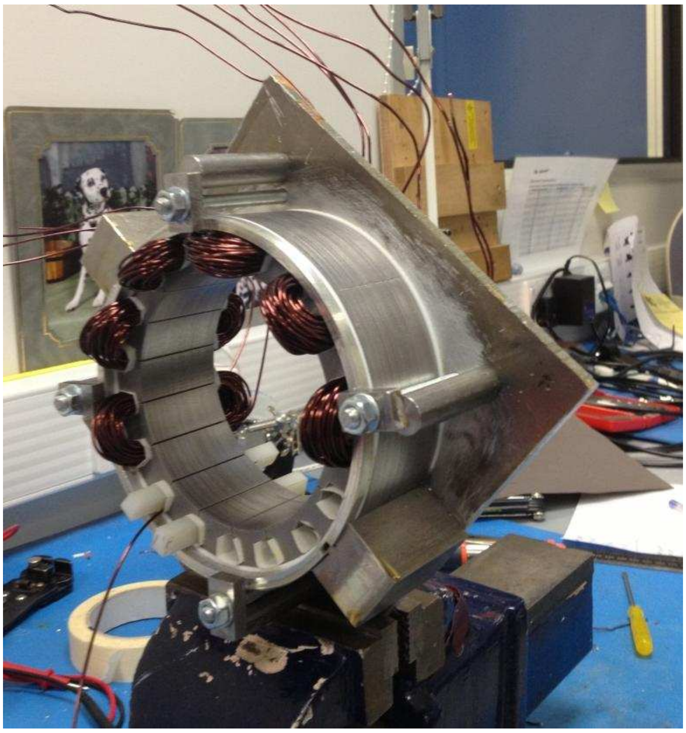

(b)

Figure G 4 (a), (b) Winding process of the trapzoidal slot stator using wedges

G1.1 EXPERIMENTAL RESULTS:

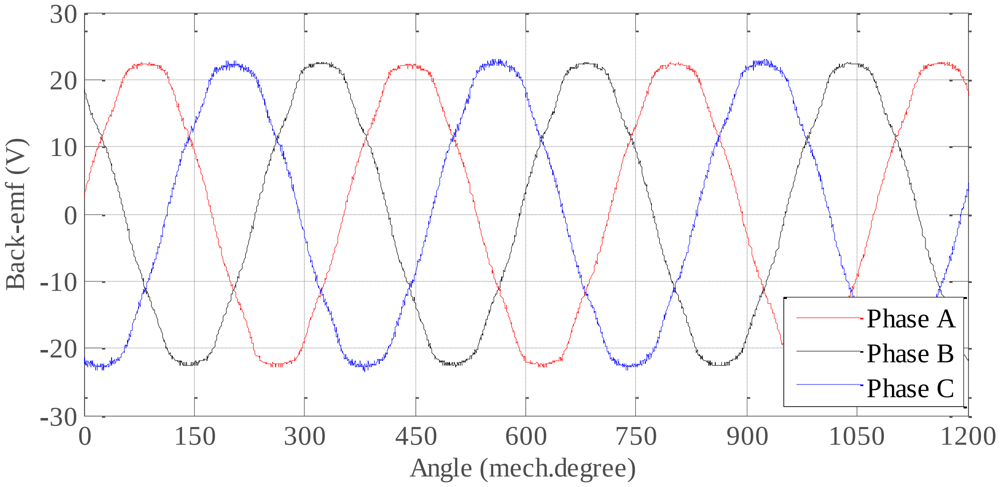

(a)

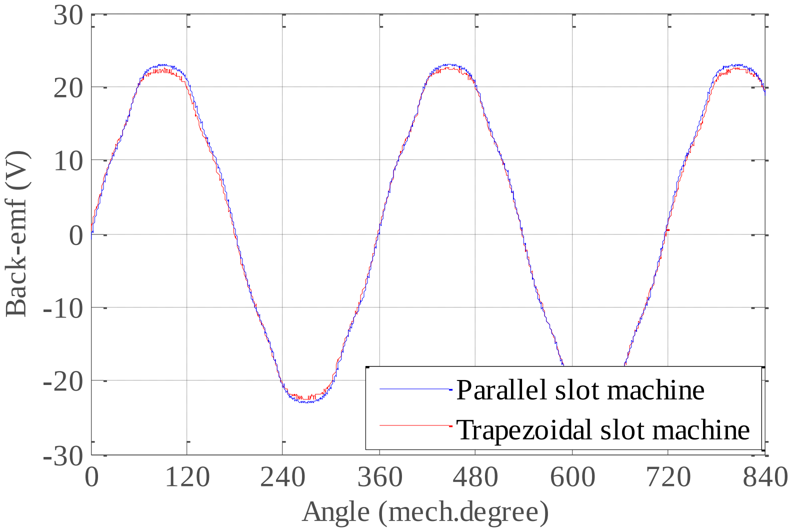

(b)

Figure G 5 (a) Three phase back-EMF waveform of a coil of a parallel slot machine (b) comparison with trapezoidal slot machine

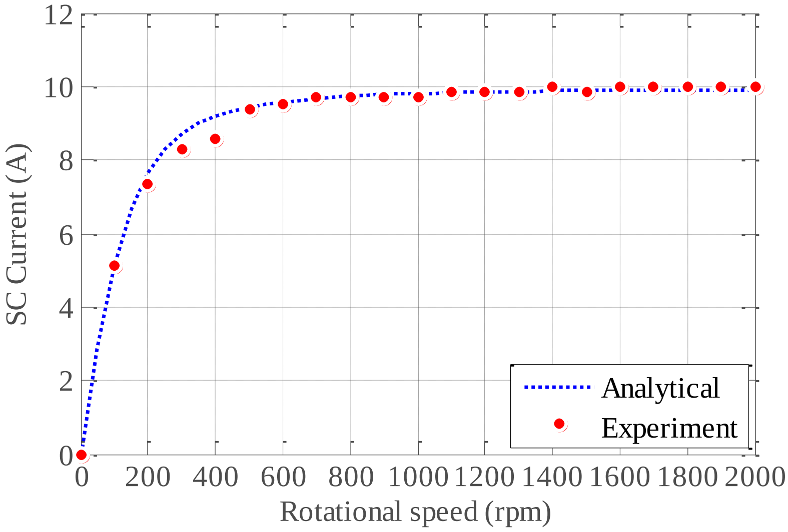

Figure G 6 Phase SC current vs. rotational speed

Bibliography

[1] A. J. Mitcham, G. Antonopoulos, and J. J. A. Cullen, "Implications of shorted turn faults in bar wound PM machines," Electric Power Applications, IEE Proceedings, vol. 151, pp. 651-657, 2004.

[2] A. G. Jack, B. C. Mecrow, and J. Haylock, "A comparative study of permanent magnet and switched reluctance motors for high performance fault tolerant applications," in Industry Applications Conference, 1995. Thirtieth IAS Annual Meeting, IAS '95., Conference Record of the 1995 IEEE, 1995, pp. 734-740 vol.1.

[3] A. M. El-Refaie, "Fault-tolerant permanent magnet machines: a review," Electric Power Applications, IET, vol. 5, pp. 59-74, 2011.

[4] B. C. Mecrow, A. G. Jack, J. A. Haylock, and J. Coles, "Fault-tolerant permanent magnet machine drives," Electric Power Applications, IEE Proceedings -, vol. 143, pp. 437-442, 1996.

[5] J. A. Haylock, B. C. Mecrow, A. G. Jack, and D. J. Atkinson, "Operation of fault tolerant machines with winding failures," Energy Conversion, IEEE Transactions on, vol. 14, pp. 1490-1495, 1999.

[6] S. Dwari and L. Parsa, "Disturbance Free Operation of Permanent Magnet Motor Drives Under Short Circuit Faults Using Center-Split Winding," in Industry Applications Conference, 2007. 42nd IAS Annual Meeting. Conference Record of the 2007 IEEE, 2007, pp. 1329-1334.

[7] B. A. Welchko, J. Wai, T. M. Jahns, and T. A. Lipo, "Magnet flux ing control of interior PM machine drives for improved response to short-circuit faults," in Industry Applications Conference, 2004. 39th IAS Annual Meeting. Conference Record of the 2004 IEEE, 2004, p. 267.

[8] J. Arellano-Padilla, M. Sumner, and C. Gerada, "Winding condition monitoring schemefor a permanent magnet machine using high-frequency injection," Electric Power Applications, IET, vol. 5, pp. 89-99, 2011.

[9] C. Li-an and Z. Peiming, "Detection and Protection of Short Circuit Fault Based on Morphology-wavelet," in Transmission and Distribution Conference and Exhibition: Asia and Pacific, 2005 IEEE/PES, 2005, pp. 1-5.

[10] B.-q. Xu, H.-m. Li, and L.-l. Sun, "Detection of stator winding inter-turn short circuit fault in induction motors," in Power System Technology, 2004. PowerCon 2004. 2004 International Conference on, 2004, pp. 1005-1009 Vol.2.

[11] B. Mahdi Ebrahimi and J. Faiz, "Feature Extraction for Short-Circuit Fault Detection in Permanent-Magnet Synchronous Motors Using Stator-Current Monitoring," Power Electronics, IEEE Transactions on, vol. 25, pp. 2673-2682, 2010.

[12] A. Yazidi, H. Henao, G. A. Capolino, F. Betin, and L. Capocchi, "Inter-turn short circuit fault detection of wound rotor induction machines using Bispectral analysis," in Energy Conversion Congress and Exposition (ECCE), 2010 IEEE, 2010, pp. 1760-1765.

[13] X. Boqiang, L. Heming, and S. Liling, "Negative sequence admittance average based detection of stator winding inter-turn short circuit fault in induction motors," in Electrical Machines and Systems, 2003. ICEMS 2003. Sixth International Conference on, 2003, pp. 867-870 vol.2.

[14] K. Min-Sub, P. Byoung-Gun, K. Rae-Young, and H. Dong-Seok, "A novel fault detection circuit for short-circuit faults of IGBT," in Applied Power Electronics Conference and Exposition (APEC), 2011 Twenty-Sixth Annual IEEE, 2011, pp. 359-363.

[15] M. O. Mustafa, G. Nikolakopoulos, and T. Gustafsson, "Stator winding short circuit fault detection based on set membership identification for three phase induction motors," in Control & Automation (MED), 2012 20th Mediterranean Conference on, 2012, pp. 290-296.

[16] M. Barcaro, N. Bianchi, and F. Magnussen, "Faulty Operations of a PM Fractional-Slot Machine With a Dual Three-Phase Winding," Industrial Electronics, IEEE Transactions on, vol. 58, pp. 3825-3832, 2011.

[17] M. Barcaro, N. Bianchi, and F. Magnussen, "Analysis and tests of a dual three-phase 12-slot 10-pole permanent magnet motor," in Energy Conversion Congress and Exposition, 2009. ECCE 2009. IEEE, 2009, pp. 3587-3594.

[18] B. S. Bernstein and J. Marks, "EPRI Report," Electrical Insulation Magazine, IEEE, vol. 3, pp. 21-21, 1987.

[19] B. M. Technology. Overheating Electric Motors: One Root Cause of Insulation Failure [Online]. Available: http://www.whitelegg.com/products/files/bcs_Overheating_Electric_Motors.pdf

[20] B. C. Mecrow, A. G. Jack, D. J. Atkinson, S. R. Green, G. J. Atkinson, A. King, et al., "Design and testing of a four-phase fault-tolerant permanent-magnet machine for an engine fuel pump," Energy Conversion, IEEE Transactions on, vol. 19, pp. 671-678, 2004.

[21] P. Arumugam, T. Hamiti, and C. Gerada, "Modeling of Different Winding Configurations for Fault-Tolerant Permanent Magnet Machines to Restrain Interturn Short-Circuit Current," Energy Conversion, IEEE Transactions on, vol. PP, pp. 1-11, 2012.

[22] S. Zhigang, W. Jiabin, D. Howe, and G. Jewell, "Analytical Prediction of the Short-Circuit Current in Fault-Tolerant Permanent-Magnet Machines," Industrial Electronics, IEEE Transactions on, vol. 55, pp. 4210-4217, 2008.

[23] M. S. Ballal, Z. J. Khan, H. M. Suryawanshi, and M. K. Mishra, "Detection of Inter-turn Short-circuit Fault in Induction Motor Using Theory of

Instantaneous Symmetrical Components," in Industrial Technology, 2006. ICIT 2006. IEEE International Conference on, 2006, pp. 460-464.

[24] A. Yazidi, H. Henao, G. A. Capolino, and F. Betin, "Rotor inter-turn short circuit fault detection in wound rotor induction machines," in Electrical Machines (ICEM), 2010 XIX International Conference on, 2010, pp. 1-6.

[25] J. Rosero, J. A. O. Romeral, L. Romeral, and E. Rosero, "Short circuit fault detection in PMSM by means of empirical mode decomposition (EMD) and wigner ville distribution (WVD)," in Applied Power Electronics Conference and Exposition, 2008. APEC 2008. Twenty-Third Annual IEEE, 2008, pp. 98-103.

[26] C. Gerada, K. J. Bradley, M. Sumner, P. Wheeler, S. Pickering, J. Clare, et al., "The results do mesh," Industry Applications Magazine, IEEE, vol. 13, pp. 62-72, 2007.

[27] P. Arumugam, T. Hamiti, and C. Gerada, "Modeling of Different Winding Configurations for Fault-Tolerant Permanent Magnet Machines to Restrain Interturn Short-Circuit Current," Energy Conversion, IEEE Transactions on, vol. 27, pp. 351-361, 2012.

[28] L. Alberti and N. Bianchi, "Experimental Tests of Dual Three-Phase Induction Motor Under Faulty Operating Condition," Industrial Electronics, IEEE Transactions on, vol. 59, pp. 2041-2048, 2012.

[29] B. Vaseghi, N. Takorabet, J. P. Caron, B. Nahid-Mobarakeh, F. Meibody-Tabar, and G. Humbert, "Study of Different Architectures of Fault-Tolerant Actuator Using a Two-Channel PM Motor," Industry Applications, IEEE Transactions on, vol. 47, pp. 47-54, 2011.

[30] G. Qi, L. Shi, S. Duan, L. Zhou, and D. Ma, "Analysis of Flux-Weakening Performances of Dual Three-Phase PM Brushless AC Motors with Alternate Winding Connections," in Electromagnetic Field Problems and Applications (ICEF), 2012 Sixth International Conference on, 2012, pp. 1-4.

[31] L. N. Tutelea, S. I. Deaconu, I. Boldea, F. Marignetti, and G. N. Popa, "Design and control of a single stator dual PM rotors axial synchronous machine for hybrid electric vehicles," in Power Electronics and Applications (EPE 2011), Proceedings of the 2011-14th European Conference on, 2011, pp. 1-10.

[32] B. A. Welchko, J. Wai, T. M. Jahns, and T. A. Lipo, "Magnet-flux-ing control of interior PM Machine drives for improved steady-state response to short-circuit faults," Industry Applications, IEEE Transactions on, vol. 42, pp. 113-120, 2006.

[33] A. J. Mitcham, G. Antonopoulos, and J. J. A. Cullen, "Favourable slot and pole number combinations for fault-tolerant PM machines," Electric Power Applications, IEE Proceedings -, vol. 151, pp. 520-525, 2004.

[34] C. Jie, W. Jiabin, K. Atallah, and D. Howe, "Performance Comparison and Winding Fault Detection of Duplex 2-Phase and 3-Phase Fault-Tolerant Permanent Magnet Brushless Machines," in Industry Applications Conference, 2007. 42nd IAS Annual Meeting. Conference Record of the 2007 IEEE, 2007, pp. 566-572.

[35] A. Mitcham, "Electrical machine," US 2005/0212374 A1, Dec 29, 2004.

[36] J. Wolmarans, H. Polinder, J. A. Ferreira, and D. Clarenbach, "Design of a fault tolerant permanent magnet machine for airplanes," in Electrical Machines and Systems, 2008. ICEMS 2008. International Conference on, 2008, pp. 2882-2887.

[37] J. A. Haylock, B. C. Mecrow, A. G. Jack, and D. J. Atkinson, "Operation of a fault tolerant PM drive for an aerospace fuel pump application," Electric Power Applications, IEE Proceedings -, vol. 145, pp. 441-448, 1998.

[38] J. W. Bennett, B. C. Mecrow, A. G. Jack, D. J. Atkinson, S. Sheldon, B. Cooper, et al., "A prototype electrical actuator for aircraft flaps and slats," in Electric Machines and Drives, 2005 IEEE International Conference on, 2005, pp. 41-47.

[39] M. Rottach, C. Gerada, T. Hamiti, and P. W. Wheeler, "Fault-tolerant electrical machine design within a Rotorcraft Actuation Drive System optimisation," in Power Electronics, Machines and Drives (PEMD 2012), 6th IET International Conference on, 2012, pp. 1-6.

[40] G. J. Atkinson, B. C. Mecrow, A. G. Jack, D. J. Atkinson, P. Sangha, and M. Benarous, "The Analysis of Losses in High-Power Fault-Tolerant Machines for Aerospace Applications," Industry Applications, IEEE Transactions on, vol. 42, pp. 1162-1170, 2006.

[41] B. C. Mecrow, A. G. Jack, D. J. Atkinson, S. Green, G. J. Atkinson, A. King, et al., "Design and testing of a 4 phase fault tolerant permanent magnet machine for an engine fuel pump," in Electric Machines and Drives Conference, 2003. IEMDC'03. IEEE International, 2003, pp. 1301-1307 vol.2.

[42] B. A. Welchko, T. M. Jahns, and T. A. Lipo, "Fault interrupting methods and topologies for interior PM machine drives," Power Electronics Letters, IEEE, vol. 2, pp. 139-143, 2004.

[43] M. T. Abolhassani and H. A. Toliyat, "Fault tolerant permanent magnet motor drives for electric vehicles," in Electric Machines and Drives Conference, 2009. IEMDC '09. IEEE International, 2009, pp. 1146-1152.

[44] C. Oprea and C. Martis, "Fault tolerant permanent magnet synchronous machine for electric power steering systems," in Power Electronics, Electrical Drives, Automation and Motion, 2008. SPEEDAM 2008. International Symposium on, 2008, pp. 256-261.

[45] N. Bianchi, S. Bolognani, M. Zigliotto, and M. Zordan, "Innovative remedial strategies for inverter faults in IPM synchronous motor drives," Energy Conversion, IEEE Transactions on, vol. 18, pp. 306-314, 2003.

[46] L. Alberti, M. Barcaro, Pre, x, M. D., A. Faggion, et al., "IPM Machine Drive Design and Tests for an Integrated Starter; Alternator Application," Industry Applications, IEEE Transactions on, vol. 46, pp. 993-1001, 2010.

[47] F. Tahami, H. Nademi, and M. Rezaei, "A sensor fault tolerant drive for interior permanent-magnet synchronous motors," in Power and Energy Conference, 2008. PECon 2008. IEEE 2nd International, 2008, pp. 283-288.

[48] L. Parsa and H. A. Toliyat, "Fault-Tolerant Interior-Permanent-Magnet Machines for Hybrid Electric Vehicle Applications," Vehicular Technology, IEEE Transactions on, vol. 56, pp. 1546-1552, 2007.

[49] M. T. Abolhassani, "A Novel Multiphase Fault Tolerant Permanent Magnet Motor Drive for Fuel cell Powered Vehicles," in Vehicle Power and Propulsion Conference, 2007. VPPC 2007. IEEE, 2007, pp. 160-167.

[50] J. F. Gieras, "PM synchronous generators with hybrid excitation systems and voltage control Capabilities: A review," in Electrical Machines (ICEM), 2012 XXth International Conference on, 2012, pp. 2573-2579.

[51] A. Shakal, Y. Liao, and T. A. Lipo, "A permanent magnet AC machine structure with true field weakening capability," in Industrial Electronics, 1993. Conference Proceedings, ISIE'93 - Budapest., IEEE International Symposium on, 1993, pp. 19-24.

[52] F. Leonardi, T. Matsuo, Y. Li, T. A. Lipo, and P. McCleer, "Design considerations and test results for a doubly salient PM motor with flux control," in Industry Applications Conference, 1996. Thirty-First IAS Annual Meeting, IAS '96., Conference Record of the 1996 IEEE, 1996, pp. 458-463 vol.1.

[53] J. F. G. e. al, "Permanent magnet electric generator with variable magnet flux excitation," US Patent: 7859231, Dec 28, 2010.

[54] W. Hua, Z. Q. Zhu, M. Cheng, Y. Pang, and D. Howe, "Comparison of flux-switching and doubly-salient permanent magnet brushless machines," in Electrical Machines and Systems, 2005. ICEMS 2005. Proceedings of the Eighth International Conference on, 2005, pp. 165-170 Vol. 1.

[55] Z. Xiaoyong, C. Ming, and L. Wenguang, "Design and analysis of a novel stator hybrid excited doubly salient permanent magnet brushless motor," in Electrical Machines and Systems, 2005. ICEMS 2005. Proceedings of the Eighth International Conference on, 2005, pp. 401-406 Vol. 1.

[56] K. T. Chau, Y. B. Li, J. Z. Jiang, and L. Chunhua, "Design and Analysis of a Stator-Doubly-Fed Doubly-Salient Permanent-Magnet Machine for Automotive Engines," Magnetics, IEEE Transactions on, vol. 42, pp. 3470-3472, 2006.

[57] Y. Gao and K. T. Chau, "Design of permanent magnets to avoid chaos in doubly salient PM machines," Magnetics, IEEE Transactions on, vol. 40, pp. 3048-3050, 2004.

[58] L. Yue and T. A. Lipo, "A doubly salient permanent magnet motor capable of field weakening," in Power Electronics Specialists Conference, 1995. PESC '95 Record., 26th Annual IEEE, 1995, pp. 565-571 vol.1.

[59] K. T. Chau, C. Ming, and C. C. Chan, "Nonlinear magnetic circuit analysis for a novel stator-doubly-fed doubly-salient machine," in Magnetics Conference, 2002. INTERMAG Europe 2002. Digest of Technical Papers. 2002 IEEE International, 2002, p. AU5.

[60] Y. Liao, F. Liang, and T. A. Lipo, "A novel permanent magnet motor with doubly salient structure," in Industry Applications Society Annual Meeting, 1992., Conference Record of the 1992 IEEE, 1992, pp. 308-314 vol.1.

[61] Z. Xiaoyong and C. Ming, "A novel stator hybrid excited doubly salient permanent magnet brushless machine for electric vehicles," in Electrical Machines and Systems, 2005. ICEMS 2005. Proceedings of the Eighth International Conference on, 2005, pp. 412-415 Vol. 1.

[62] C. Ming, H. Wei, X. Y. Zhu, W. X. Zhao, and H. Y. Jia, "A simple method to improve the sinusoidal static characteristics of doubly- salient PM machine for brushless AC operation," in Electrical Machines and Systems, 2007. ICEMS. International Conference on, 2007, pp. 665-669.

[63] Y. Chuang and G. Yu, "Performance analysis of new fault-tolerant flux-mnemonic doubly-salient permanent-magnet motor drive," in Power Electronics and Drive Systems, 2009. PEDS 2009. International Conference on, 2009, pp. 500-505.

[64] C. Sanabria-Walter, H. Polinder, J. A. Ferreira, P. Janker, and M. Hofmann, "Torque enhanced Flux-Switching PM machine for aerospace applications," in Electrical Machines (ICEM), 2012 XXth International Conference on, 2012, pp. 2585-2595.

[65] T. Raminosoa, C. Gerada, and M. Galea, "Design Considerations for a Fault-Tolerant Flux-Switching Permanent-Magnet Machine," Industrial Electronics, IEEE Transactions on, vol. 58, pp. 2818-2825, 2011.

[66] Z. Wenxiang, C. Ming, H. Wei, J. Hongyun, and C. Ruiwu, "Back-EMF Harmonic Analysis and Fault-Tolerant Control of Flux-Switching Permanent-Magnet Machine With Redundancy," Industrial Electronics, IEEE Transactions on, vol. 58, pp. 1926-1935, 2011.

[67] E. Sulaiman, T. Kosaka, Y. Tsujimori, and N. Matsui, "Design of 12-slot 10-pole Permanant Magnet Flux-Switching Machine with hybrid excitation for hybrid electric vehicle," in Power Electronics, Machines and Drives (PEMD 2010), 5th IET International Conference on, 2010, pp. 1-5.

[68] R. L. Owen, Z. Q. Zhu, A. S. Thomas, G. W. Jewell, and D. Howe, "Fault-Tolerant Flux-Switching Permanent Magnet Brushless AC Machines," in Industry Applications Society Annual Meeting, 2008. IAS '08. IEEE, 2008, pp. 1-8.

[69] H. Lei, Y. Haitao, H. Minqiang, Z. Shigui, and H. Li, "Fault-Tolerant Performance of a Novel Flux-Switching Permanent Magnet Linear Machine Based on Harmonic Current Injection," Magnetics, IEEE Transactions on, vol. 47, pp. 3224-3227, 2011.

[70] J. Meng-Jia, W. Can-Fei, S. Jian-Xin, and X. Bing, "A Modular Permanent-Magnet Flux-Switching Linear Machine With Fault-Tolerant Capability," Magnetics, IEEE Transactions on, vol. 45, pp. 3179-3186, 2009.

[71] A. S. Thomas, Z. Q. Zhu, R. L. Owen, G. W. Jewell, and D. Howe, "Multiphase Flux-Switching Permanent-Magnet Brushless Machine for Aerospace Application," Industry Applications, IEEE Transactions on, vol. 45, pp. 1971-1981, 2009.

[72] W. Yu and D. Zhiquan, "A Multi-Tooth Fault-Tolerant Flux-Switching Permanent-Magnet Machine With Twisted-Rotor," Magnetics, IEEE Transactions on, vol. 48, pp. 2674-2684, 2012.

[73] Z. Wenxiang, C. Ming, H. Wei, X. Lei, C. Ruiwu, and D. Yi, "Post-fault operation of redundant flux-switching permanent-magnet motors using harmonic injected current," in Electrical Machines and Systems (ICEMS), 2010 International Conference on, 2010, pp. 868-872.

[74] Z. Wenxiang, C. Ming, H. Wei, and J. Hongyun, "A redundant flux-switching permanent magnet motor drive for fault-tolerant applications," in Vehicle Power and Propulsion Conference, 2008. VPPC '08. IEEE, 2008, pp. 1-6.

[75] Y. Wen Wu, X. Wei, and X. Xian Yong, "Research on fault diagnosis and tolerant operation of redundant flux-switching permanent-magnet motors," in Applied Superconductivity and Electromagnetic Devices (ASEMD), 2011 International Conference on, 2011, pp. 164-168.

[76] Z. Wenxiang, C. Ming, K. T. Chau, H. Wei, J. Hongyun, J. Jinghua, et al., "Stator-Flux-Oriented Fault-Tolerant Control of Flux-Switching Permanent-Magnet Motors," Magnetics, IEEE Transactions on, vol. 47, pp. 4191-4194, 2011.

[77] G. J. Li, J. Ojeda, E. Hoang, and M. Gabsi, "Thermal-electromagnetic analysis of a fault-tolerant dual-star flux-switching permanent magnet motor for critical applications," Electric Power Applications, IET, vol. 5, pp. 503-513, 2011.

[78] A. R. Munoz, F. Liang, and M. W. Degner, "Evaluation of Interior PM and Surface PM Synchronous machines with distributed and concentrated windings," in Industrial Electronics, 2008. IECON 2008. 34th Annual Conference of IEEE, 2008, pp. 1189-1193.

[79] N. Bianchi, M. D. Pre, G. Grezzani, and S. Bolognani, "Design considerations on fractional-slot fault-tolerant synchronous motors," in Electric Machines and Drives, 2005 IEEE International Conference on, 2005, pp. 902-909.

[80] M. Barcaro, N. Bianchi, E. Fornasiero, and F. Magnussen, "Experimental comparison between two fault-tolerant fractional-slot multiphase PM motor drives," in Industrial Electronics (ISIE), 2010 IEEE International Symposium on, 2010, pp. 2160-2165.

[81] G. E. Horst, "Flux controlled permanent magnet dynamo-electric machine," 5530307, Jun 25, 1996.

[82] G. E. Horst, "Modular flux controllable permanent magnet dynamoelectric machine," 7057323, Jun 6, 2006.

[83] G. P. R. e. al, "Hybrid permanent magnet/homopolar generator and motor," 097124, Aug 1, 2000.

[84] J. A. Tapia, F. Leonardi, and T. A. Lipo, "Consequent-pole permanent-magnet machine with extended field-weakening capability," Industry Applications, IEEE Transactions on, vol. 39, pp. 1704-1709, 2003.

[85] J. A. Tapia, F. Leonardi, and T. A. Lipo, "A design procedure for a PM machine with extended field weakening capability," in Industry Applications Conference, 2002. 37th IAS Annual Meeting. Conference Record of the, 2002, pp. 1928-1935 vol.3.

[86] M. Aydin, S. Huang, and T. A. Lipo, "Performance evaluation of an axial flux consequent pole PM motor using finite element analysis," in Electric Machines and Drives Conference, 2003. IEMDC'03. IEEE International, 2003, pp. 1682-1687 vol.3.

[87] J. M. Miller, "Hybrid electric machine with two rotors, permanent magnet poles," 6531799, Mar 11, 2003.

[88] M. Aydin, H. Surong, and T. A. Lipo, "A new axial flux surface mounted permanent magnet machine capable of field control," in Industry Applications Conference, 2002. 37th IAS Annual Meeting. Conference Record of the, 2002, pp. 1250-1257 vol.2.

[89] K. A. Dooley, "Architecture for electric machine," 7126313, Oct 24, 2006.

[90] T. Hosoi, H. Watanabe, K. Shima, T. Fukami, R. Hanaoka, and S. Takata, "Demagnetization Analysis of Additional Permanent Magnets in Salient-Pole Synchronous Machines With Damper Bars Under Sudden Short Circuits," Industrial Electronics, IEEE Transactions on, vol. 59, pp. 2448-2456, 2012.

[91] A. F. e. al, "Flux shunt wave shape control arrangement for permanent magnet machines," 6750628, Jun 15, 2004.

[92] K. D. e. al, "Method and apparatus for controlling an electric machine," 7443070, Oct 28, 2008.

[93] J. W. Sadvary, "Regulatable permanent magnet alternator," 4766362, Aug 23, 1988.

[94] F. Caricchi, F. Crescimbini, F. G. Capponi, and L. Solero, "Permanent-magnet, direct-drive, starter/alternator machine with weakened flux linkage for constant-power operation over extremely wide speed range," in Industry Applications Conference, 2001. Thirty-Sixth IAS Annual Meeting. Conference Record of the 2001 IEEE, 2001, pp. 1626-1633 vol.3.

[95] L. P. Z. e. al, "Brushless permanent magnet wheel motor with variable axial rotor/stator," 6943478, Sep 13, 2005.

[96] T. F. G. e. al, "Permanent magnet generator with fault detection," 4641080, Feb 3, 1987.

[97] K. A. Dooley, "Method, apparatus and system for controlling an electric machine," 6873071, Mar 29, 2005.

[98] Z. Xu, H. Li, and S. Wan, "Analysis of generator rotor short circuit fault by reluctance network model," in Electrical Machines and Systems, 2003. ICEMS 2003. Sixth International Conference on, 2003, pp. 699-702 vol.2.

[99] S. Wan, A. Wang, Y. Li, and Y. Wang, "Reluctance network model of turbo-generator and its application in rotor winding inter-turn short circuit fault," in Electric Machines and Drives, 2005 IEEE International Conference on, 2005, pp. 386-390.

[100] O. A. Mohammed, S. Liu, and Z. Liu, "FE-based physical phase variable model of PM synchronous machines under stator winding short circuit faults," Science, Measurement & Technology, IET, vol. 1, pp. 12-16, 2007.

[101] O. A. Mohammed, S. Liu, and Z. Liu, "FE-based Physical Phase Variable Model of PM Synchronous Machines with Stator Winding Short Circuit Fault," Computational Electromagnetics (CEM), 2006 6th International Conference on, pp. 1-2, 2006.

[102] T. A. Lipo, Introduction to AC Machine Design: WisPERC, 2004.

[103] J. Pyrhönen, T. Jokinen, and V. Hrabovcová, Design of rotating electrical machines: Wiley, 2008.

[104] Infolytica - Magnet software. Available: http://www.infolytica.co.uk/ [09 March 2013]

[105] R. J. Distler, "Hysteresis Loop Analysis," Component Parts, IEEE Transactions on, vol. 10, pp. 115-118, 1963.

[106] O. Hellwig, S. Eisebitt, C. Guenther, F. Radu, J. Luening, W. F. Schlotter, et al., "Advanced Magnetic Nanostructure Characterization via Resonant Soft X-Ray Spectro Holography Imaging in Combination with Microscopic Hysteresis Loop Analysis," in Magnetics Conference, 2006. INTERMAG 2006. IEEE International, 2006, pp. 889-889.

[107] P. H. Mellor, R. Wrobel, and N. McNeill, "Investigation of Proximity Losses in a High Speed Brushless Permanent Magnet Motor," in Industry Applications Conference, 2006. 41st IAS Annual Meeting. Conference Record of the 2006 IEEE, 2006, pp. 1514-1518.

[108] A. Boglietti, A. Cavagnino, and M. Lazzari, "Computational Algorithms for Induction Motor Equivalent Circuit Parameter Determination—Part II: Skin Effect and Magnetizing Characteristics," Industrial Electronics, IEEE Transactions on, vol. 58, pp. 3734-3740, 2011.

[109] C. Gerada, "Advance electrical machines," University of Nottingham 2012.

[110] A. Boglietti, A. Cavagnino, D. Staton, M. Shanel, M. Mueller, and C. Mejuto, "Evolution and Modern Approaches for Thermal Analysis of Electrical Machines," Industrial Electronics, IEEE Transactions on, vol. 56, pp. 871-882, 2009.

[111] T. Sawata and D. Staton, "Thermal modeling of a short-duty motor," in IECON 2011 - 37th Annual Conference on IEEE Industrial Electronics Society, 2011, pp. 2054-2059.

[112] M. Mirzaei, A. Binder, and C. Deak, "3D analysis of circumferential and axial segmentation effect on magnet eddy current losses in permanent magnet synchronous machines with concentrated windings," in Electrical Machines (ICEM), 2010 XIX International Conference on, 2010, pp. 1-6.

[113] D. Maga, M. Zagirnyak, and D. Miljavec, "Additional losses in permanent magnet brushless machines," in Power Electronics and Motion Control Conference (EPE/PEMC), 2010 14th International, 2010, pp. S4-12-S4-13.

[114] P. B. Reddy, T. M. Jahns, and T. P. Bohn, "Transposition effects on bundle proximity losses in high-speed PM machines," in Energy Conversion Congress and Exposition, 2009. ECCE 2009. IEEE, 2009, pp. 1919-1926.

[115] P. B. Reddy, Z. Q. Zhu, H. Seok-Hee, and T. M. Jahns, "Strand-level proximity losses in PM machines designed for high-speed operation," in Electrical Machines, 2008. ICEM 2008. 18th International Conference on, 2008, pp. 1-6.

[116] P. B. Reddy, T. M. Jahns, and T. P. Bohn, "Modeling and analysis of proximity losses in high-speed surface permanent magnet machines with concentrated windings," in Energy Conversion Congress and Exposition (ECCE), 2010 IEEE, 2010, pp. 996-1003.

[117] Y. Amara, P. Reghem, and G. Barakat, "Analytical Prediction of Eddy-Current Loss in Armature Windings of Permanent Magnet Brushless AC Machines," Magnetics, IEEE Transactions on, vol. 46, pp. 3481-3484, 2010.

[118] A. Bellara, H. Bali, R. Belfkira, Y. Amara, and G. Barakat, "Analytical Prediction of Open-Circuit Eddy-Current Loss in Series Double Excitation Synchronous Machines," Magnetics, IEEE Transactions on, vol. 47, pp. 2261-2268, 2011.

[119] L. J. Wu, Z. Q. Zhu, D. Staton, M. Popescu, and D. Hawkins, "Analytical Model of Eddy Current Loss in Windings of Permanent-Magnet Machines Accounting for Load," Magnetics, IEEE Transactions on, vol. 48, pp. 2138-2151, 2012.

[120] T. Lubin, S. Mezani, and A. Rezzoug, "Analytic Calculation of Eddy Currents in the Slots of Electrical Machines: Application to Cage Rotor Induction Motors," Magnetics, IEEE Transactions on, vol. 47, pp. 4650-4659, 2011.

[121] A. T. Phung, O. Chadebec, G. Meunier, X. Margueron, and J. P. Keradec, "High Frequency Proximity Losses Determination for Rectangular Cross Section Conductors," in Electromagnetic Field Computation, 2006 12th Biennial IEEE Conference on, 2006, pp. 263-263.

[122] P. Anh-Tuan, G. Meunier, O. Chadebec, X. Margueron, and J. P. Keradec, "High-Frequency Proximity Losses Determination for Rectangular Cross-Section Conductors," Magnetics, IEEE Transactions on, vol. 43, pp. 1213-1216, 2007.

[123] A. S. Thomas, Z. Q. Zhu, and G. W. Jewell, "Proximity Loss Study In High Speed Flux-Switching Permanent Magnet Machine," Magnetics, IEEE Transactions on, vol. 45, pp. 4748-4751, 2009.

[124] N. Xi and C. R. Sullivan, "An improved calculation of proximity-effect loss in high-frequency windings of round conductors," in Power Electronics Specialist Conference, 2003. PESC '03. 2003 IEEE 34th Annual, 2003, pp. 853-860 vol.2.

[125] N. Xi and C. R. Sullivan, "Simplified high-accuracy calculation of eddy-current loss in round-wire windings," in Power Electronics Specialists Conference, 2004. PESC 04. 2004 IEEE 35th Annual, 2004, pp. 873-879 Vol.2.

[126] W. Leonhard, Control of Electrical Drives, 2nd edition ed.: Springer.

[127] S. A. Swann and J. W. Salmon, "Effective resistance and reactance of a solid cylindrical conductor placed in a semi-closed slot," Proceedings of the IEE - Part C: Monographs, vol. 109, pp. 611-615, 1962.

[128] S. A. Swann and J. W. Salmon, "Effective resistance and reactance of a rectangular conductor placed in a semi-closed slot," Electrical Engineers, Proceedings of the Institution of, vol. 110, pp. 1656-1662, 1963.

[129] T. Lubin, S. Mezani, and A. Rezzoug, "2-D Exact Analytical Model for Surface-Mounted Permanent-Magnet Motors With Semi-Closed Slots," Magnetics, IEEE Transactions on, vol. 47, pp. 479-492, 2011.

[130] Z. Q. Zhu, L. J. Wu, and Z. P. Xia, "An Accurate Subdomain Model for Magnetic Field Computation in Slotted Surface-Mounted Permanent-Magnet Machines," Magnetics, IEEE Transactions on, vol. 46, pp. 1100-1115, 2010.

[131] L. J. Wu, Z. Q. Zhu, D. Staton, M. Popescu, and D. Hawkins, "Analytical Modeling and Analysis of Open-Circuit Magnet Loss in Surface-Mounted Permanent-Magnet Machines," Magnetics, IEEE Transactions on, vol. 48, pp. 1234-1247, 2012.

[132] L. J. Wu, Z. Q. Zhu, D. Staton, M. Popescu, and D. Hawkins, "Analytical Model for Predicting Magnet Loss of Surface-Mounted Permanent Magnet Machines Accounting for Slotting Effect and Load," Magnetics, IEEE Transactions on, vol. 48, pp. 107-117, 2012.

[133] Sternberg, Nonlinear Partial Differential Equations in Engineering and Applied Science: Taylor & Francis, 1980.